Pulsed Plasma Enhanced Chemical Vapor Deposition of Fluorocarbon Thin Films for Dielectric Applications

by

Catherine B. Labelle
B.S., Chemical Engineering (1994)
Cornell University

M.S. in Chemical Engineering Practice (1996)
Massachusetts Institute of Technology

Submitted to the Department of Chemical Engineering
in Partial Fulfillment of the Requirements for the Degree of

Doctor of Philosophy in Chemical Engineering

at the

Massachusetts Institute of Technology

September, 1999

Signature of
Author..... .....
Catherine B. Labelle
Department of Chemical Engineering
July 28, 1999

Certified
by.....
Karen K. Gleason
Associate Professor of Chemical Engineering
Thesis Supervisor

Accepted
by.....
Robert E. Cohen
St. Laurent Professor of Chemical Engineering
Chairman, Committee for Graduate Students

Pulsed Plasma Enhanced Chemical Vapor Deposition of Fluorocarbon Thin Films for Dielectric Applications

By

Catherine B. Labelle

Submitted to the Department of Chemical Engineering
on July 28, 1999 in Partial Fulfillment of the
Requirements for the Degree of Doctorate in Philosophy in
Chemical Engineering

ABSTRACT

To enable evolutionary improvements in semiconductor device performance, new low dielectric constant (κ) materials are needed to replace silicon dioxide. Fluorocarbon films grown by pulsed plasma-enhanced chemical vapor deposition (pulsed PECVD) have been studied to evaluate their suitability as low κ materials. Pulsed plasma excitation mitigates several disadvantages of continuous plasma operation by modulating between pulse on and pulse off states. This thesis explores the effect of pulsed plasma excitation on resultant film composition and materials properties for a variety of precursors, including hexafluoropropylene oxide (HFPO), CHF_3, CH_2F_2, 1,1,2,2-$C_2H_2F_4$, and $CHClF_2$. Both a conventional rf PECVD system and an electron cyclotron resonance (ECR) high density plasma system have been used for deposition.

A series of films were deposited in the parallel plate plasma reactor from HFPO, CH_2F_2, and $C_2H_2F_4$, and analyzed using ellipsometry (deposition rates), electron spin resonance, carbon 1s x-ray photoelectron spectroscopy (XPS), Fourier Transform Infrared spectroscopy (FTIR), and atomic force microscopy (AFM). The films were also deposited on overhang test structures to determine dominant deposition mechanisms in the pulsed plasma environment. ESR measurements on a series of films from HFPO showed dangling bond concentrations decrease with increasing pulsed off time, a result of gas-phase healing reactions. XPS shows that films from $C_2H_2F_4$ and CH_2F_2 are dominated by C-CF structures, while those from HFPO are dominated by CF_2. FTIR shows a small amount of hydrogen incorporation for films from $C_2H_2F_4$ and CH_2F_2. The dielectric constants of these films are 2.4, 2.4, and 2.0 for $C_2H_2F_4$, CH_2F_2, and HFPO, respectively, with corresponding loss tangents of ~ 10^{-2}, ~10^{-2}, and 0.009. Gas-phase FTIR of the effluents from pulsed plasmas from HFPO, $C_2H_2F_4$, and CH_2F_2 shows that while the HFPO pulsed plasmas are dominated by an initial CF_2-producing dissociation, the other two precursors have competing dissociation pathways. For both $C_2H_2F_4$ and CH_2F_2, CF_2-production and HF elimination dissociation pathways compete, with the competition about 1:1 for $C_2H_2F_4$ pulsed plasmas, whereas HF elimination is dominant for CH_2F_2 pulsed plasmas. These dissociation mechanisms correlate with the observed deposited film compositions.

AFM measurements of the parallel plate deposited films show nodular growth ("cauliflower" appearance), with the size and distribution of the nodules dependent upon

both the precursor, the degree of surface modification to which the growing film is exposed, and the substrate surface. Advancing contact angles for all of the films were found to be higher than that of PTFE (108°), indicating both hydrophobic and rough surfaces.

Deposition of these same films onto overhang test structures revealed differences in the relative importance of mechanisms contributing to the overall fluorocarbon film growth process. Growth was dominated by direct or ion-induced deposition, but the role of the other mechanisms varied with the pulse conditions and precursor choice. In particular, deposition from neutral pathways becomes evident.

High/low (modulation between high and low power plasmas) and on/off (modulation between plasma and no plasma) pulsed ECR plasmas from $C_2H_2F_4$, CHF_3, and HFPO were used to deposit fluorocarbon films. Films deposited from $C_2H_2F_4$ by both pulsing techniques have similar compositions, but the on/off pulsed plasma films tend to be less fluorinated, and defluorination occurs within the high/low pulsed plasma films as precursor flow rate increases. High/low pulsed CHF_3 ECR plasma films are more heavily dominated by CF_2, while there is no detectable growth from high/low pulsed HFPO ECR plasmas. Optical emission spectroscopy (OES) of all of these plasmas shows high intensity peaks for H, C_2, and C_3, with lower intensity CF_2 and F peaks. The presence of etch-related species such as CO and F in the HFPO pulsed plasma likely accounts for lack of growth from that plasma. Gas-phase recombination reactions may be occurring between the OES sampling region and the deposition substrate, producing fluorocarbon molecular deposition species, and thus accounting for the high degree of fluorination seen in the deposited films. Comparison with the corresponding pulsed parallel plate plasma systems shows significant differences in both plasma species and deposited film composition. Parallel plate plasmas are characterized by high intensity CF_2 peaks, with only low intensity peaks for C_2 and H species.

FTIR was used to study structural changes in high/low and on/off pulsed $C_2H_2F_4$ ECR plasma deposited films upon thermal annealing. A significant increase in T_{stable} (~ 60°C) was achieved when the precursor flow rate was increased to 50 sccm for high/low pulsing, most likely due to reduction of a low temperature CF_3 loss mechanism. Shifts in asymmetric vs. symmetric CF_2 stretch intensities, as well as the appearance of CH stretches, were observed as a result of annealing. Systematic changes in peak intensity were observed in the 1400 – 2000 cm^{-1} range, where there is a shift from carbon-carbon double bonding structures to carbon-oxygen bonding structures. While the thermal stability of the low flow rate high/low pulsed plasma film appears to be dominated by a low temperature CF_3 loss mechanism, the thermal stability of the other films is dominated by oxygen uptake. Thus, minimizing both CF_3 and oxygen content of the deposited films would appear to be a valid strategy for increasing film thermal stability.

Thesis Supervisor: Karen K. Gleason

Title: Associate Professor of Chemical Engineering

Acknowledgments

I would like to thank my thesis advisor, Karen, who gave me much needed advice and guidance over the past five years and put up with my little music hobby. She has been extremely supportive of everything that I have tried to accomplish, while always knowing when to point me in a different direction. She also gave me the opportunity to build my own reactor and learn from every step of it along the way. I would also like to thank my thesis committee members, Prof. Herb Sawin, Prof. Paul Laibinis, and Prof. Klaus Jensen. They gave me guidance when I asked for it and let me follow my own path.

I extend my thanks to former and current members of my lab: Scott Limb, Mike Kwan, Leslie Loo, Kenneth Lau, Brett Cruden, Hilton Pryce-Lewis, and Daniel Burkey. I appreciate all of the technical and non-technical discussions we have had, which have lead to a very enjoyable 5 years. I especially appreciate all of your willingness to move my heavy pieces of equipment whenever I asked. Several parts of my thesis would never have happened without that help. A special thanks to Prof. Sawin's group, who let me wander through their lab at will, borrowing anything I might need, and discussing any problems I encountered.

I would also like to thank John Lee of Lucent Technologies Bell Laboratories for his continued mentoring throughout this thesis. Whether it consisted of offering donated equipment, career guidance, or just a friendly ear, he has always been extremely supportive and has helped me learn my way in this field. I look forward to working with him more when I start work at Lucent.

A special thanks to my piano teacher, David Deveau, and all of my music friends. Piano has always been my "other" profession, and being able to continue performing and following this path has kept me sane as I battled the treacherous waters of experimental research. It may have eaten up a big chunk of my time, but piano allowed me to be much more effective in my research than would have otherwise been possible.

Finally, I would like to thank my parents and siblings. It took them a while to get used to this "Ph.D" idea, but they have always been supportive of everything I do and they let me follow this path with their full encouragement. Special thanks to my sister Cindy who has listened to countless conversations about my reactor, and at this point, could probably build it herself.

Table of Contents

List of Figures

List of Tables

Chapter 1

Introduction & Background

Section 1.1: Motivation

One of the major challenges facing the semiconductor industry is the need to create faster microprocessors under increasingly more difficult conditions. An increase in processor speed is generally achieved by reducing the minimum chip feature size, but this strategy assumes that the main limitation on signal speed is due to intrinsic gate delay.[1] As the line width is reduced, the main contribution to signal delay is increasingly due to the "RC" delay, which is proportional to both the metal resistivity (ρ_m) and the interlayer dielectric constant (κ).[1,2] To reduce the RC delay, it is necessary to decrease the metal resistivity, the dielectric constant, or both. The standard metal and dielectric materials currently used are aluminum ($\rho_{Al} = 2.8 \times 10^{-8}$ Ω·m)[3] and silicon dioxide ($\kappa_{SiO2} \sim 4.0$).[2,4] A decrease in resistivity would require a metal such as copper or silver ($\rho_m = 1.7 \times 10^{-8}$ and 1.6×10^{-8} Ω·m, respectively).[3] Indeed, recently, several semiconductor companies have announced the successful implementation of copper interconnect integration processes and the general manufacturing shift from aluminum to copper is in progress.[5,6]

The substitution of a new low dielectric constant (low κ) material for the traditional SiO_2 has proven to be more complicated than the metal replacement problem. SiO_2 has always been the insulator of choice for semiconductor processing due to its good chemical, thermal, mechanical, and electrical characteristics, as well as its compatibility with the silicon substrate.[4,7] Ideally, a replacement dielectric material would have many of the same properties as SiO_2, but with a dielectric constant < 4.0. Unfortunately, many of the non-porous materials with dielectric constants < 4.0 (and especially, < 3.0), are polymeric, and thus have properties which are vastly different

from that of SiO_2.[8] This switch from an inorganic to an organic material has proven to be a major challenge in low κ development, as a reduction in κ can lead to reduced thermal stability (T_{stable}, defined by SEMATECH as the T at which there is < 1% weight loss in vacuum after an 8 hour anneal)[9] and adhesion. These three properties, κ, T_{stable}, and adhesion, are often used as benchmarks to accept or dismiss a particular material, since if the requirements for these properties are not met, subsequent integration steps will not be successful. In addition to these difficulties, it is not clear which low κ material should be used. In response to the demand for new low κ materials, several different classes of materials are currently under investigation, with a specific range of dielectric constants associated with each class.[8,9] Finally, it is still not clear which process will be used to deposit the new dielectric material: spin-on, chemical vapor deposition (CVD), or plasma-enhanced CVD (PECVD).

Proposed low κ materials range from fluorinated SiO_2 (Si_xOF_y, κ = 3.4 – 4.1) to porous materials, based on either SiO_2 or another low κ material (κ_{min} = 1 for air gaps).[8] Adding fluorine to SiO_2 lowers the material's dielectric constant, while the Si-O structure retains most of the materials properties of SiO_2.[4] The degree of fluorination contributes to lowering the dielectric constant, but as the fluorine concentration increases, the film becomes increasingly unstable, although the stability is also dependent upon the exact deposition conditions.[4] Thus, fluorinated SiO_2 is merely a short-term solution to the dielectric constant problem. Porous materials represent the other end of the dielectric constant spectrum, leading to films with κ < 2.0, and possibly, 1.0 for air gaps.[8,10-12] However, along with the low κ that porosity provides, there also arise concerns with

mechanical strength, low thermal conductivity, and the stability of the surface passivation of the pores.[10,11]

In between fluorinated SiO_2 and porous films, several other materials are being considered. As outlined in a recent review (see reference #8), these include hydrogen silsesquioxane (HSQ, $\kappa = 2.9$), organic-inorganic hybrids of HSQ ($\kappa < 3.0$), fluorinated polyimide ($\kappa = 2.6 - 2.9$), poly(arylene) ether ($\kappa = 2.6 - 2.8$), divinyl siloxane bis-benzocyclobutene (DVS-BCB, $\kappa = 2.65$), aromatic hydrocarbons ($\kappa = 2.65$), Parylene AF4 (aliphatic tetrafluorinated poly-p-xylylene, $\kappa = 2.5$), and fluorocarbons ($\kappa = 1.9 - 2.6$,[13] $\kappa_{PTFE} = 1.9$).[8] Porous SiO_2 and most of the organic polymers are deposited via spin-on processing, while fluorocarbons, Si_xOF_y, hydrocarbons, and parylenes are deposited via CVD or PECVD processes. Table 1-1 lists each class of proposed low κ material with several key properties.[8]

This thesis focuses on the deposition of fluorocarbon thin films via PECVD and high density plasma CVD (HDP CVD). Fluorocarbon films have the lowest bulk dielectric constants of any material, and therefore are the logical choice for dielectric replacement before moving to porous materials. PECVD and HDP CVD versus spin-on processing will be used since they can produce conformal films with uniform properties in a solventless environment. The lack of solvents in these processes is significant since environmental, safety, and health issues are becoming increasing important to the semiconductor industry.[14] In addition, many of the current semiconductor fabrication tools for SiO_2 are plasma-based, and so these deposition processes would be compatible with existing processing tools.

Table 1-1. Low κ materials classification

Material	Dielectric constant (κ)[8,13]	Type of material	Deposition process
Si_xOF_y	3.4 – 4.1	Inorganic	CVD, PECVD
HSQ	2.9	Inorganic	Spin-on
MSQ	< 3.0	Inorganic/organic hybrid	Spin-on
Fluorinated polyimide	2.6 – 2.9	Organic	Spin-on
Poly(arylene) ether	2.6 – 2.8	Organic	Spin-on
Black diamond	2.7	Inorganic/organic hybrid	PECVD
DVS-BCB	2.65	Organic	Spin-on
Aromatic hydrocarbons	2.65	Organic	Spin-on
Parylene AF4	2.5	Organic	CVD
Fluorocarbons	1.9 – 2.6	organic	PECVD
PTFE	1.9	Organic	Spin-on
Nanoporous silica	1.3 – 2.5	Inorganic	Spin-on

Section 1.2: PECVD and HDP CVD

A plasma can be defined as a partially ionized gas in which highly reactive neutrals and ions are produced by collisions of free electrons with neutral gas molecules.[15] A plasma can be created by applying an electric field across a gas-filled volume. The generated electrical potential from such a field will accelerate electrons in the gas, giving them energy which can then be passed to neutrals through collisions. Due to the low rate of energy exchange between the much heavier neutrals and the light electrons, the electrons will have a significantly higher average temperature, often exceeding 10,000 K, than the other gas species, which are often not significantly above room temperature. Thus the plasma is able to produce significant concentrations of ions, radicals, and other excited species without appreciable gas heating.[15] In PECVD, the plasma is used to generate reactive species which then deposit on a substrate placed in the reactor.

Many different types of plasmas can be generated, but there are typically two categories under which semiconductor processing plasmas fall. First, there is the conventional low density, capacitively-coupled plasma, which is generally produced by using a 13.56 MHz radio frequency (rf) generator to apply an electrical field between two parallel electrodes. The size, shape, and distance between these electrodes can vary, but the plasmas produced share many of the same characteristics. Table 1-2 lists typical properties of a conventional rf discharge.[16] A parallel plate plasma reactor was used to deposit many of the films studied in this thesis. Figure 1-1 shows a schematic of the parallel plate reactor used.

The second category is that of high density plasmas (HDPs), which typically have

Table 1-2. Typical plasma conditions in conventional rf and high density discharges

Plasma Characteristic	Conventional rf Discharge	High Density Discharge
Plasma density	$10^{8} - 10^{11}$ cm^{-3}	$10^{11} - 10^{12}$ cm^{-3}
Neutral pressure	0.02 – 2 Torr	0.001 – 0.05 Torr
Plasma potential	$\sim 10^{2}$ V	$\sim$ 10 V
Ion flux to walls	1 – 50 A·m^{-2}	50 – 500 A·m^{-2}
Electron temperature	1 – 5 eV	2 – 10 eV
Fractional ionization	$10^{-6} - 10^{-3}$	$10^{-4} - 10^{-1}$

(reproduced from Graves, IEEE Transactions on Plasma Science, Vol. 22, No. 1, 1994)

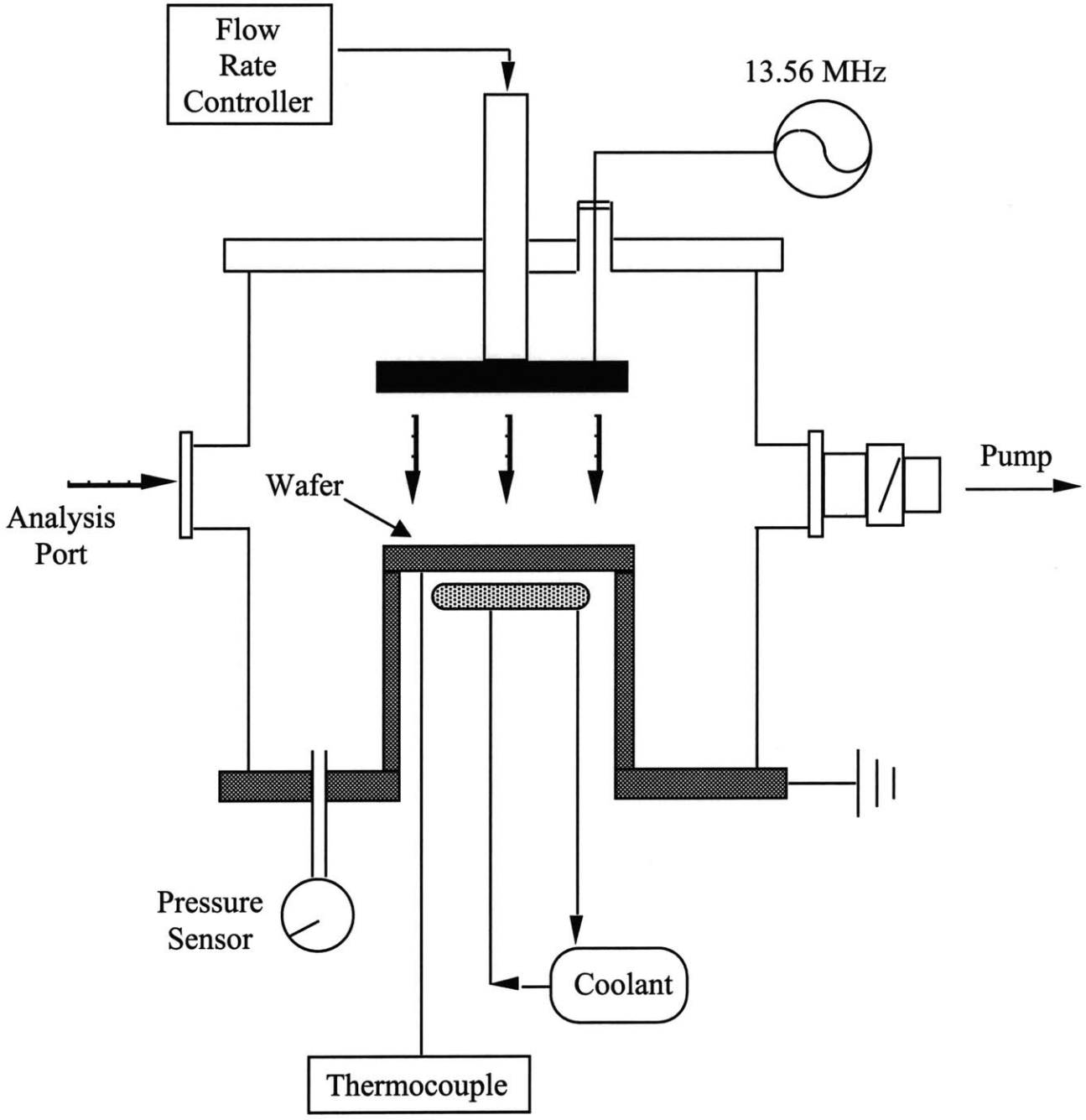

Figure 1-1: Parallel plate reactor schematic

an electron density of $10^{11} - 10^{12}$ cm^{-3}, as opposed to $10^{8} - 10^{11}$ cm^{-3} for conventional rf plasmas (see Table 1-2).[16] A relatively recent review of plasma processing in microelectronics (see reference #16) discusses conventional and HDP sources and compares many of their properties.[16] The higher electron density of HDPs results in a higher degree of fracturing of the neutral molecules, with fractional ionizations typically increasing 100x from conventional to high density plasmas. One of the major advantages of high density sources is the independent control of ion flux (proportional to ion density) and ion energy (proportional to the dc potential between the plasma and the substrate). High density plasmas use generation techniques that do not involve the substrate, and therefore it is possible to apply a separate rf bias on the substrate which can control the energy of ions approaching the substrate surface. A second advantage of high density sources is the low pressure under which they operate. Typical HDP sources operate between 1 and 50 mTorr, which is significantly lower than operating pressures for most conventional rf plasma systems (20 mTorr – 2 Torr). The pressure affects the mean free path of the reactant molecules:

$$\lambda = \frac{k_B T}{\sqrt{2}\sigma P} \qquad (1)$$

where k_B = Boltzmann's constant, T = species temperature, σ = collision cross section of species, and P = system pressure.[17] Typical mean free paths for room temperature species at the HDP pressures are on the order of millimeters, and therefore result in collisionless sheaths; i.e., no collisions occur between molecules traveling from the plasma region to the substrate surface. The lack of collisions means that, through the independent substrate bias, the energy and direction of the impinging ions can be controlled, a major advantage when wanting to achieve anisotropic etching profiles.

Collisionless sheaths can not be achieved in conventional rf plasmas, where the higher pressures lead to mean free paths on the order of microns, a dimension much smaller than the sheath height.

There are several different types of HDP sources, including inductively coupled plasmas (ICP), helicons, helical resonators, and electron cyclotron resonance (ECR) plasmas.[18] An ECR plasma source was used to deposit the HDP films in this thesis and will be described here in more detail.

The phenomenon of electron cyclotron resonance occurs when microwave energy is coupled to the natural resonance frequency of the electron gas in the presence of a static magnetic field. This resonance frequency occurs when the electron cyclotron frequency equals the excitation frequency, and is given by Equation 2,

$$f_{ce} = \frac{1}{2\pi}\frac{eB}{m_e} \qquad (2)$$

where f_{ce} = electron cyclotron frequency, e = electron charge, B = strength of the static magnetic field, and m_e = electron mass.[19] For an applied microwave frequency of 2.45 GHz, the most commonly used ECR frequency, the required static magnetic field for electron cyclotron resonance is 875 G. An ECR plasma is generated by utilizing the ECR phenomenon to generate high energy electrons, which then interact with the process gas to produce reactive ions and neutrals. Physically, at electron cyclotron resonance, the electrons are accelerated perpendicular to the static magnetic field by the applied electric field ($\vec{E}$), resulting in an outward spiraling motion along a magnetic field line.[19] This process is shown in Figure 1-2 for both $\vec{E} = 0$ and $\vec{E} > 0$. The key to ensuring a high degree of ECR coupling is to reduce the probability of collisions while the electrons are

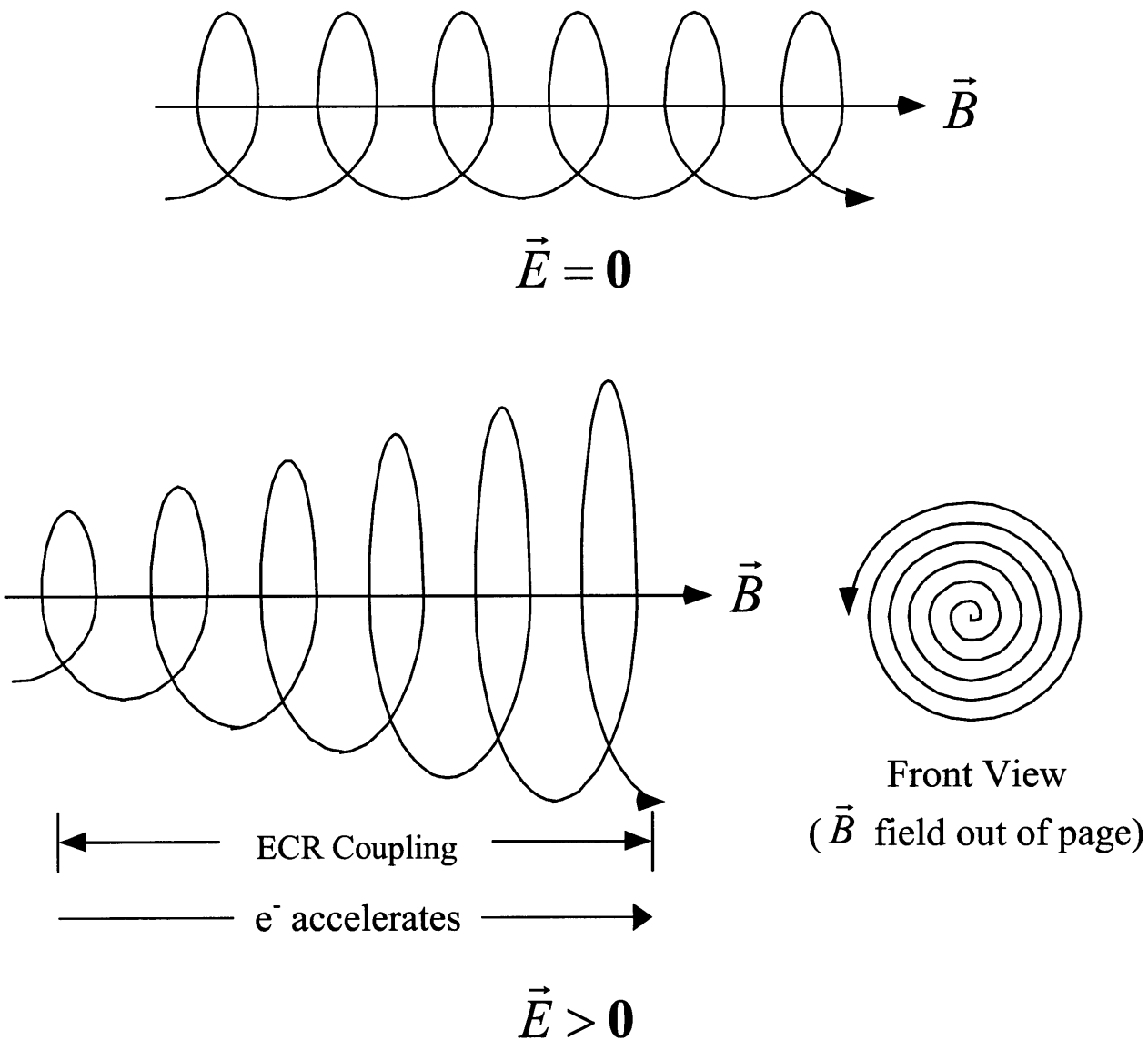

Figure 1-2: Mechanism of e^- acceleration via ECR coupling. At the ECR resonance frequency, for an applied electric field > 0, the e^- will accelerate until it collides with another body or falls out of the ECR region of the plasma.

gaining energy through the ECR coupling. Hence, optimal ECR coupling occurs at low pressure, usually between 0.2 – 10 mTorr.[19,20] ECR plasma sources are high density plasma sources since their efficient coupling of energy into electrons results in electron densities of $10^{11} - 10^{12}$ cm^{-3}.[19-21]

Several different categories of ECR plasma sources are currently in use, and many more are still being developed. The source used in this thesis was a Wavemat Microwave Plasma Disk Reactor (MPDR) 325i, which utilizes a cavity tuning configuration (see Figure 1-3 and Appendix A). A sliding short adjusts the length of the cavity, while a tunable microwave coupling probe controls the coupling of microwave energy into the cavity. It should be noted that the cavity resonance is a separate phenomenon from that of electron cyclotron resonance. Cavity resonance is a function of both the length of the cavity (determined by the sliding short) and the tuning probe position for a particular cavity diameter, and hence, these parameters are used to tune a plasma to a particular resonance mode. There are an infinite number of natural resonance frequencies for a particular cavity, which can be limited by fixing the applied microwave frequency. As cavity diameter increases for a fixed excitation frequency, it is known that the density of resonance modes increases, making it difficult to isolate one resonance mode in the cavity.[20] Thus, for large diameter cavities, it is common to observe multimode or mode-hopping behavior. The MPDR 325i has a cavity diameter of 25 cm, which is large enough to result in mode-hopping under some process conditions. For more detail on cavity resonance modes, please refer to reference #20.

ECR systems have only recently come into widespread research and industrial use (starting in the late 1980s). One of its major advantages is its electrodeless design,

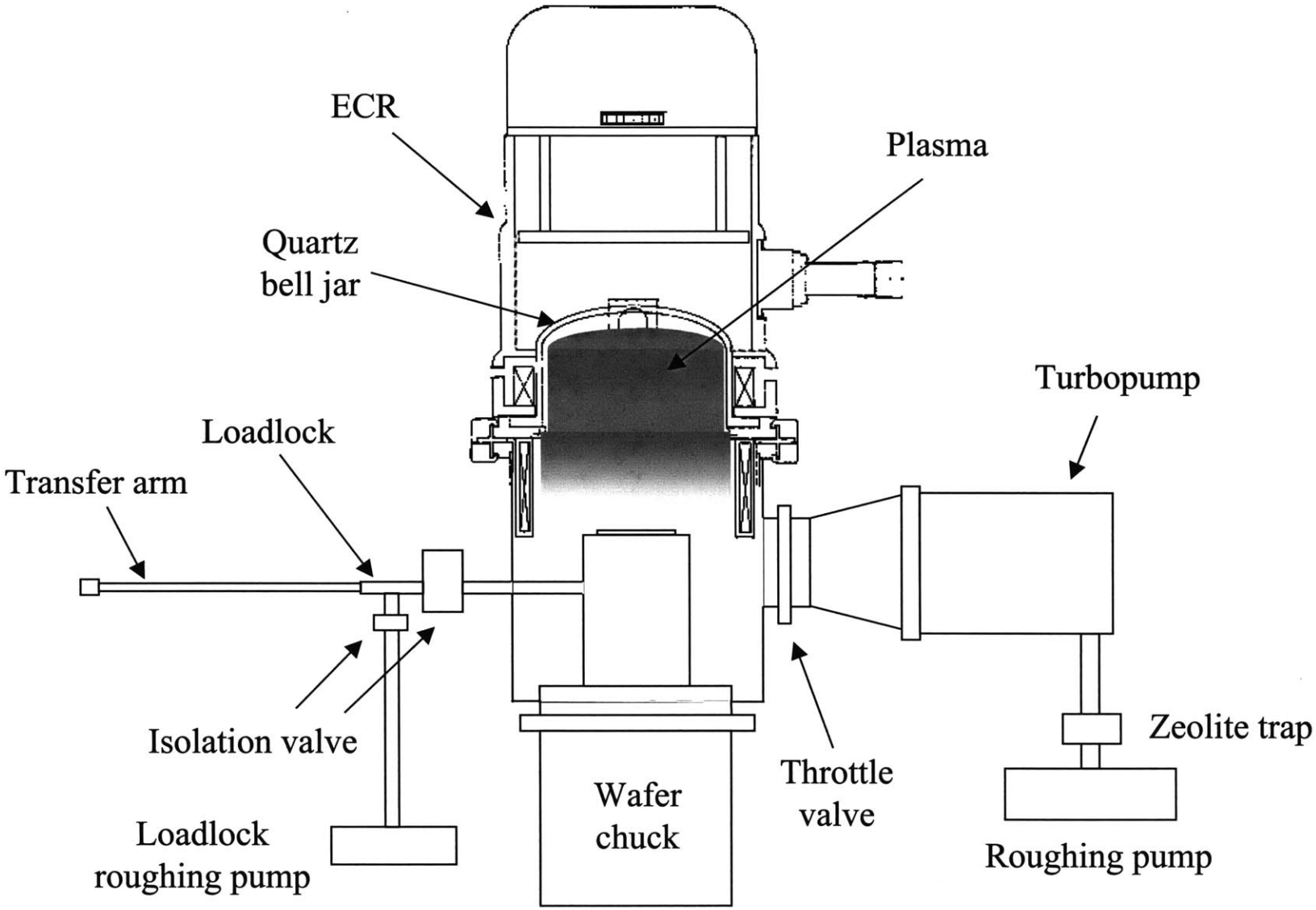

Figure 1-3: Schematic of ECR Deposition System

whereby ion energy and ion flux are uncoupled, allowing for independent control. ECR plasmas have found use in many applications, including silicon oxidation,[22] silicon nitride deposition,[22,23] diamond deposition,[24,25] and sputtering.[21,22,26] Recently, Samukawa,[27,28] Oehrlein,[29] and Goto[30-33] have used ECR sources to deposit fluorocarbon thin films.

Section 1.3: Fluorocarbon Films

Fluorocarbon plasmas, both conventional and high density, are used extensively throughout the semiconductor industry in both etching and cleaning processes.[2,4,34] In addition, it has been found that the deposition of a fluorocarbon film during plasma etching of SiO_2 is key to the successful etching of anisotropic features with no undercut.[29,35] The plasma deposition of fluorocarbon films has been studied for many years,[36,37] and only recently has been considered for use in low κ applications.[38] A variety of different precursors are currently in use, including CF_4, C_2F_4, C_2F_6, C_3F_8, c-C_4F_8, C_6F_6, CHF_3, CH_2F_2, $C_2H_2F_4$, and C_3F_6O (hexafluoropropylene oxide), to name a few.[13,36,39,40] In general, it has been found that there is a boundary between etching and deposition which is dependent on the F:C ratio of the precursor (see Figure 1-4).[37] This boundary can be shifted by the addition of H_2 or O_2, as indicated in Fig. 1-4. If the precursor contains hydrogen or oxygen, the etching vs. deposition regions are similarly shifted.

The choice of a deposition precursor is particularly important in determining the composition and properties of the fluorocarbon films deposited. Process parameters during the deposition (e.g., pressure, temperature, input power, etc.) also affect the film

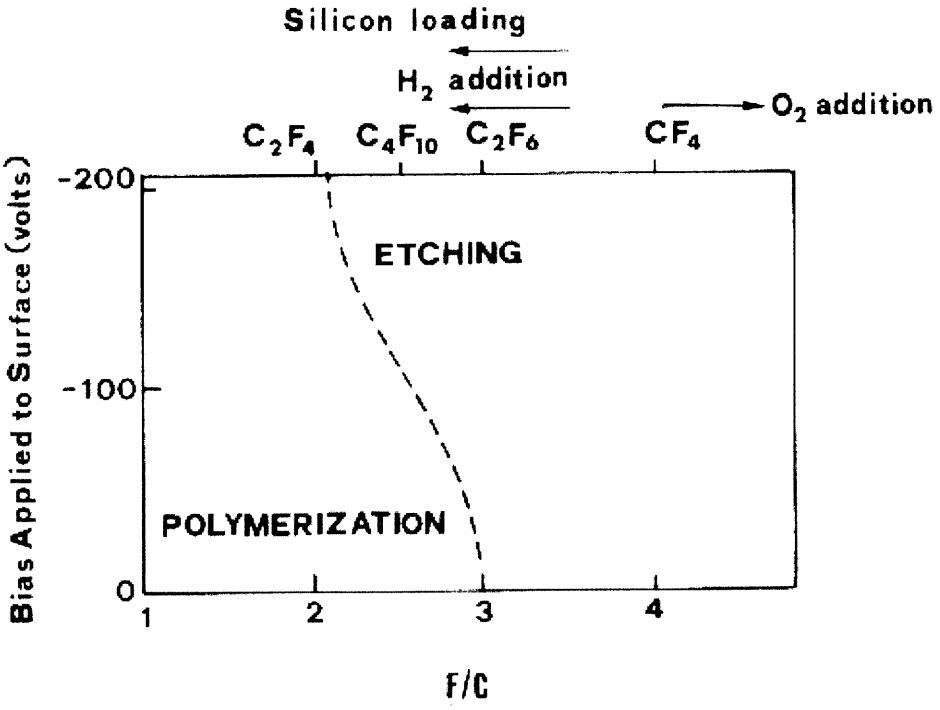

Figure 1-4: Etching versus polymerization regimes as a function of precursor F:C ratio. Increasing the precursor F:C ratio leads to etching for a constant substrate bias. The addition of H_2 or O_2 shifts the boundary curve for a particular precursor as indicated in the plot.

formed. Surprisingly, films of similar composition can be deposited from dissimilar precursors (see Table 1-3). Films having F:C ratios between 1.0 and 1.3 have been grown from CF_4, C_2F_6, C_4F_8, C_9F_{18}, and CHF_3 using both conventional and high density plasma sources.[29,33,39,41,42] Many researchers have investigated gas mixtures in order to tailor film composition. One of the most common additives is H_2, which has been shown to scavenge free F in the plasma.[27,31,43-47] For PECVD of C_2F_6/H_2 gas mixtures, controlling the H_2 concentration allows one to control the concentration of cross-linking C-CF groups in the deposited film.[47] In ECR HDP CVD, it has been found that H_2 addition to c-C_4F_8 plasmas leads to film deposition where before there was only an etching environment (i.e., Fig. 1-4) and there is an increase in gas phase CF concentration (via HF extraction from CF_2 groups), while CF_3 concentration decreases (also due to HF extraction to form CF_2).[43] Other precursor mixtures usually incorporate a hydrofluorocarbon with a pure fluorocarbon (e.g., $C_4F_8 + CH_4$)[45,48] or a linear fluorocarbon with a cyclic fluorocarbon (e.g., $C_2F_6 + C_6F_6$) to attempt to incorporate the stability of cyclic structure into fluorocarbon matrix.[46,49]

Several observations can be made about fluorocarbon plasma deposition for both conventional and high density systems (includes ICP and helicon systems as well as ECR). First, upon exposure to atmosphere, fluorocarbon plasma films generally absorb a small amount of oxygen, most likely by attachment to dangling bonds left on the surface by ion bombardment during plasma exposure.[41,47,50] Second, a majority of the deposition is due to growth from activated surface sites.[29,33,47,51] Growth from neutral species is present, but at a much slower rate than the ion-induced surface activation path.[29] Third, CF_2 is one of the primary deposition species, although its dominance is

Table 1-3. Summary of fluorocarbon films studied in the literature.

Author	Reference	Plasma	Precursor	F:C
Samukawa	(27)	Pulsed ECR	CHF_3	0.79
		ECR	CHF_3	0.86
Takahashi	(44)	Pulsed ECR	CHF_3/H_2	0.25 – 2.1
Takahashi	(75)	Pulsed ECR	CHF_3/O_2	0.05 – 2.1
Takahashi	(33)	Pulsed ECR	CHF_3	1.2 – 1.4
Miyata	(30)	ECR	C_4F_8	2.2
		ECR	C_4F_8/H_2	2.1
Oehrlein	(29)	ECR	CF_4	0.97 – 1.14
Endo	(39)	Helicon	C_4F_8	1.06
		Helicon	C_2F_6	1.10
		Helicon	CF_4	1.12
Endo	(41)	Helicon	C_2F_6	1.15
		Helicon	CF_4	1.21
		PECVD	CF_4/CH_4	1.14
Endo	(59)	Helicon	C_4F_8	0.53 – 0.75
Mountsier	(46)	ICP	C_2F_6, C_3F_6, C_3F_8, C_4F_8, C_6F_6, C_7F_{14}, C_2F_6/C_6F_6, C_6F_6/H_2	< 1.5
Wang	(42)	Pulsed PECVD	C_9F_{18}	1.18 – 1.72
Limb	(62)	Pulsed PECVD	C_3F_6O	1.46 – 2.06
d'Agostino	(47)	PECVD	C_2F_6/H_2	0.4 – 2.0
Amyot	(50)	PECVD	C_4F_8, CF_4	1.3 – 1.7
Mackie	(74)	Pulsed ICP	C_2F_6/H_2	0.1 – 0.7
		Pulsed ICP	CF_4/H_2	0.1 – 0.3
Hynes	(68)	Pulsed ICP	perfluoroallylbenzene	0.9 – 1.5

dependent upon precursor and plasma conditions.[29,31,43,47] Finally, it has been shown for conventional PECVD that polymerization can occur in the gas phase, producing molecules with up to nine carbons for some precursors.[52]

The properties of fluorocarbon plasma films can be generalized in some aspects. Most plasma deposited fluorocarbon films have a F:C < 1.8 (see Table 1-3), and in that composition range, an increase in the F:C leads to films with lower dielectric constants. For example, helicon deposited films from C_4F_8, C_2F_6, and CF_4 have F:C ratios from 1.06 $\rightarrow$ 1.12, respectively, while their dielectric constants decrease from 2.3 $\rightarrow$ 2.1, respectively.[39] However, this lower κ is usually achieved at the expense of lower thermal stability. For the above example, this translates into a reduction in % residual thickness after a 1 hour vacuum anneal at 350°C from 98 $\rightarrow$ 50%, respectively.[39] Bulk polytetrafluoroethylene (PTFE, F/C=2) has a dielectric constant of 1.9 with a thermal stability (T_{stable}) > 400°C,[53,54] which would make it ideal for low κ applications, but this combination of properties has not yet been achieved via plasma processing. Low κ with high thermal stability is the goal for all plasma-deposited fluorocarbon systems, and many different experimental approaches have be attempted including H_2 addition,[46,47] gas mixtures,[45,46,48,49] HDP CVD,[55-59] conventional PECVD,[47,60] and high substrate temperatures.[45,48] Another major property issue is adhesion, both by the fluorocarbon film to an underlying substrate, and by a film deposited on top of the fluorocarbon film. This property is not quite as crucial as κ and T_{stable} since it can be mitigated through the use of liner layers and surface treatments,[57,58] but it is essential to the eventual complete integration scheme. A host of other materials properties need to be addressed for the

complete integration scheme,[8,9] but these three are generally acknowledged as the deciding factors for the success or failure of a particular film.

Section 1.4: Pulsed Plasma Deposition

Another technique that allows for control over the types of films deposited is pulsed plasma deposition, where the plasma is cycled between "on" and "off" states.[36,40] In this process, rf power is applied for a specified "on" time, followed by an "off" period during which no excitation is used. During the "on" time, both ions and reactive neutrals are produced. However, since ions often have shorter lifetimes than neutrals, during the "off" time the ratio of neutrals to ions will increase, and thus, the process equilibrium will be shifted to favor film deposition from reactive neutrals. Therefore, the overall chemistry of these plasmas should be much more sensitive to the original precursor molecules than their continuous counterparts, and it should be possible to develop a range of fluorocarbon films with different film properties.

Pulsed plasmas are usually operated in two regimes: millisecond (ms) pulsing or microsecond (μs) pulsing. For conventional rf plasmas, ms pulsing is the primary mode, with typical on times of 2 – 50 ms, and off times ranging from 10 – 1000 ms.[40,61-63] For high density plasmas, the mode of pulsing is usually dependent on whether etching or deposition is being done. For etching, it has been found that μs pulsing is very effective at reducing notching effects, both in ECR[27,64,65] and ICP[66] systems, and pulsing times are on the order of 10 – 100 μs for both on and off times. For deposition, some researchers use μs pulsing (usually with ICP sources),[67,68] while others use ms pulsing (ECR sources).[33,69] Pulse times for the deposition processes range from 10 – 400 μs and 10 –

20 ms for on times, and 5 – 400 μs and 10 – 100 ms for off times. Pulse rise and fall times were all lower than the minimum pulse on or off time.

There are several benefits associated with pulsed plasmas. It has been shown to provide a degree of compositional control over films deposited from a particular precursor which is dependent on the pulse on/off conditions.[61-63,70] The chemistry of the chosen precursor also has a greater impact in pulsed systems since the off period utilizes more of the traditional neutral-based chemistry of these precursors and their derivatives. The specific functional groups within the precursors are also more likely to be incorporated into the growing film due to the reduced applied power. In continuous plasma systems, there is an excess of energy available to dissociate precursors and any of their derivatives, resulting in a predominance of small molecules in the plasma gas. By pulsing the plasma, the probability of the gas phase species being reduced to their basic constituents is reduced, and thus, more of the precursor functionalities can potentially be retained in the depositing film. The reduction in ion bombardment due to the pulsing also allows for less surface damage and a reduction in substrate heating.[18,36]

Pulsed plasma deposition of fluorocarbon thin films has been studied in both conventional rf PECVD systems as well as ICP and ECR high density systems. Savage, Timmons, and Lin[40,61] first looked at the pulsed plasma deposition of hexafluoropropylene oxide (HFPO) in a conventional PECVD system and found that the % CF_2 in the film could be controlled by pulse conditions. Further studies by Limb and Gleason[62,71] examined this control in more detail, and the variation in CF_2 concentration was linked to the dominant precursor decomposition $C_3F_6O \rightarrow CF_2 + CF_3CFO$, whose extent could be controlled by the pulse conditions. Other pulsed fluorocarbon PECVD

systems have also been investigated, including C_3F_6,[40] C_2F_4,[72] C_9F_{18},[42] CF_4,[70] and CHF_3.[70] Similar types of compositional control have been reported.

Fluorocarbon films deposited by pulsed HDP CVD have been studied by several groups.[67,69,73,74] Pulsed ICP has been used to investigate deposition from CF_4,[74] C_2F_6,[74] C_6F_{12},[67] and perfluoroallylbenzene.[68] In addition, Takahashi et. al.,[32,33,44,69,73,75] using pulsed ECR, have closely examined the gas phase CF_x radical concentrations for ms-pulsed plasmas of CHF_3 using infrared diode laser absorption spectroscopy. They found that CF_2 was the primary deposition species for the pulsed ECR CHF_3 plasma, and that while electron impact dissociation of CHF_3 was the primary source of CF_3 and CF_2 radicals, CF was formed through secondary electron impact dissociations of CF_3 and CF_2. Films deposited in the ECR system also displayed a variation in composition due both to pulse conditions and the addition of either H_2 or O_2 to the feed gas.[44,75]

Section 1.5: Thesis Goals

This thesis will explore the effect of pulsing the plasma excitation on resultant film composition and materials properties for a variety of precursors, including HFPO, CHF_3, CH_2F_2, $C_2H_2F_4$, and $CHClF_2$. Both a conventional rf PECVD system and an ECR high density plasma system will be used for deposition, and the films obtained from each reactor will be compared. The systematic effects of pulsing on film deposition rate and composition will be explored. In addition, the effect of pulsing on properties such as dangling bond concentration, film morphology, gap-fill behavior, and electrical characteristics, including dielectric constant and dissipation factor, will be examined. The role of the precursor chemistry in the film compositions created will also be

investigated by gas phase Fourier Transform Infrared Spectroscopy (FTIR) of the pulsed plasma system effluents. In general, a relationship between the precursors and plasma conditions used and the resulting films will be investigated in more detail in order to provide a clearer understanding of the complexities involved in trying to tailor a film for a particular application.

Section 1.6: References

1. W. W. Lee and P. S. Ho, *MRS Bull.* **22**(10), 19 (1997).

2. S. Wolf, *Silicon Processing for the VLSI Era*, Vol. 2 (Lattice Press, Sunset Beach, CA, 1990).

3. D. Halliday, R. Resnick, and J. Merrill, *Fundamentals of Physics*, 3rd ed. (Wiley & Sons, New York, 1988).

4. *Handbook of Semiconductor Interconnection Technology*, G. C. Schwartz, K. V. Srikrishnan, and A. Bross, Eds. (Marcel Dekker, New York, 1998).

5. P. Singer, *Semicond. Intl.* **20**(13), 67 (1997).

6. P. Singer, *Semicond. Intl.* **21**(6), 90 (1998).

7. S. Wolf and R. N. Tauber, *Silicon Processing for the VLSI Era*, Vol. 1 (Lattice Press, Sunset Beach, CA, 1986).

8. L. Peters, *Semicond. Intl.* **21**(10), 64 (1998).

9. P. Singer, *Semicond. Intl.* **19**(5), 88 (1996).

10. C. Jin, J. D. Luttmer, D. M. Smith, and T. A. Ramos, *MRS Bull.* **22**(10), 39 (1997).

11. M. B. Anand, M. Yamada, and H. Shibata, *IEEE Trans. Electron Devices* **44**(11), 1965 (1997).

12. P. Singer, *Semicond. Intl.* **22**(3), 38 (1999).

13. K. K. Gleason, *History and Future of Fluorocarbon CVD Low k DielectricThin Films* (DUMIC, Santa Clara, CA, 1999), p. 11.

14. R. Chiarello, A. Muscat, D. Boning, K. Gleason, S. Karecki, and S. Raghavanl, *Semicond. Intl.* **22**(2), 62 (1999).

15. B. Chapman, *Glow Discharge Processes* (Wiley & Sons, New York, 1980).

16. D. B. Graves, *IEEE Trans. Plasma Sci.* **22**(1), 31 (1994).

17. P. W. Atkins, *Physical Chemistry*, 4th ed. (W. H. Freeman and Company, New York, 1990).

18. S. V. Nguyen, *IBM J. Res. Develop.* **43**(1/2), 109 (1999).

19. J. Asmussen, "Electron Cyclotron Resonance Microwave Discharges for Etching and Thin Film Deposition," in *Handbook of Plasma Processing Technology*, Eds: S. M. Rossnagel, J. J. Cuomo, and W. D. Westwood (Noyes, Park Ridge, NJ, 1990).

20. *High Density Plasma Sources: Design, Physics and Performance*, O. A. Popov, Ed. (Noyes Publications, Park Ridge, NJ, 1995).

21. J. Musil, *Vacuum* **47**(2), 145 (1996).

22. J. Asmussen, Jes, T. A. Grotjohn, P. Mak, and M. A. Perrin, *IEEE Trans. Plasma Sci.* **25**(6), 1196 (1997).

23. S. Leclerc, A. Lecours, M. Caron, E. Richard, G. Turcotte, and J. F. Currie, *J. Vac. Sci. Technol. A* **16**(2), 881 (1998).

24. M. Kadono, T. Inoue, A. Miyanaga, and S. Yamazaki, *Appl. Phys. Lett.* **61**(7), 773 (1992).

25. A. Hatta, K. Kadota, Y. Mori, T. Ito, T. Sasaki, and A. Hiraki, *Appl. Phys. Lett.* **66**(13), 1602 (1995).

26. G. A. Dixit, *Vacuum* **51**(4), 723 (1998).

27. S. Samukawa, *Jpn. J. Appl. Phys. Pt. 1* **32**(12B), 6080 (1993).

28. S. Samukawa, *Jpn. J. Appl. Phys. Pt. 1* **33**(4B), 2133 (1994).

29. G. S. Oehrlein, Y. Zhang, D. Vender, and M. Haverlag, *J. Vac. Sci. Technol. A* **12**(2), 323 (1994).

30. K. Miyata, M. Hori, and T. Goto, *J. Vac. Sci. Technol. A* **14**(4), 2083 (1996).

31. K. Takahashi, M. Hori, M. Inayoshi, and T. Goto, *Jpn. J. Appl. Phys. Pt. 1* **35**(6A), 3635 (1996).

32. K. Takahashi, M. Hori, and T. Goto, *Jpn. J. Appl. Phys. Pt. 1* **33**(8), 4745 (1994).

33. K. Takahashi, M. Hori, S. Kishimoto, and T. Goto, *Jpn. J. Appl. Phys. Pt. 1* **33**(7B), 4181 (1994).

34. S. M. Sze, *VLSI Technology* (McGraw-Hill Book Company, New York, 1983).

35. M. Inayoshi, M. Ito, M. Hori, and T. Goto, *J. Vac. Sci. Technol. A* **16**(1), 233 (1998).

36. H. Yasuda, *Plasma Polymerization* (Academic Press, New York, 1985).

37. *Plasma Deposition, Treatment, and Etching of Polymers*, R. d'Agostino, Ed. (Academic Press, Boston, 1990).

38. D. R. Cote, S. V. Nguyen, A. K. Stamper, D. S. Armbrust, D. Tobben, R. A. Conti, and G. Y. Lee, *IBM J. Res. Develop.* **43**(1/2), 5 (1999).

39. K. Endo, *MRS Bull.* **22**(10), 55 (1997).

40. C. R. Savage, R. B. Timmons, and J. W. Lin, "Spectroscopic Characterization of Films Obtained in Pulsed Radio-Frequency Plasma Discharges of Fluorocarbon Monomers," in *Structure-Property Relations in Polymers: Spectroscopy and Performance*, Advances in Chemistry Series Vol. 236, Eds: M. W. Urban and C. D. Craver (ACS, Washington, 1993), p. 745.

41. K. Endo and T. Tatsumi, *Appl. Phys. Lett.* **68**(20), 2864 (1996).

42. J.-H. Wang, J.-J. Chen, and R. B. Timmons, *Chem. Mater.* **8**(9), 2212 (1996).

43. K. Miyata, K. Takahashi, S. Kishimoto, M. Hori, and T. Goto, *Jpn. J. Appl. Phys. Pt. 2* **34**(4A), L444 (1995).

44. K. Takahashi, M. Hori, and T. Goto, *J. Vac. Sci. Technol. A* **14**(4), 2011 (1996).

45. S. Takeishi, H. Kudo, R. Shinohara, M. Hoshino, S. Fukuyama, J. Yamaguchi, and M. Yamada, *J. Electrochem. Soc.* **144**(5), 1797 (1997).

46. T. W. Mountsier and J. A. Samuels, *Thin Solid Films* **332**, 362 (1998).

47. R. d'Agostino, R. Cramarossa, F. Fracassi, E. Desimoni, L. Sabbatini, P. G. Zambonin, and G. Caporiccio, *Thin Solid Films* **143**, 163 (1986).

48. Y. Ma, H. Yang, J. Guo, C. Sathe, A. Agui, and J. Nordgren, *Appl. Phys. Lett.* **72**(25), 3353 (1998).

49. K. Endo and T. Tatsumi, *Appl. Phys. Lett.* **70**(19), 2616 (1997).

50. N. Amyot, J. E. Klemberg-Sapieha, M. R. Wertheimer, Y. Segui, and M. Moisan, *IEEE Trans. Elect. Insul.* **27**(6), 1101 (1992).

51. R. d'Agostino, F. Cramarossa, V. Colaprico, and R. d'Ettole, *J. Appl. Phys.* **54**(3), 1284 (1983).

52. W. W. Stoffels, E. Stoffels, and K. Tachibana, *J. Vac. Sci. Technol. A* **16**(1), 87 (1998).

53. F. Rodriguez, *Principles of Polymer Systems*, 3rd ed. (Hemisphere Publishing Corp., New York, 1989).

54. *Thermal Stability of Polymers*; *Vol. 1*, R. T. Conley, Ed. (Marcel Dekker, Inc., New York, 1970).

55. J. A. Theil, G. Kooi, F. Mertz, G. Ray, and K. Seaward, *The Effect of Thermal Cycling on a-C:F,H Low Dielectric Constant Films Deposited by ECR Plasma Enhanced Chemical Vapor Deposition* (IITC, San Francisco, CA, 1998).

56. J. A. Theil, F. Mertz, M. Yairi, K. Seaward, G. Ray, and G. Kooi, *Thermal Stability of a-C:F,H Films Deposited by Electron Cyclotron Resonance Plasma Enhanced Chemical Vapor Deposition* (MRS Symp. Proc., San Francisco, CA, 1997).

57. K. Endo, T. Tatsumi, Y. Matsubara, and T. Horiuchi, *Jpn. J. Appl. Phys. Pt. 1* **37**(4A), 1809 (1998).

58. K. Endo, T. Tatsumi, and Y. Matsubara, *Jpn. J. Appl. Phys. Pt. 2* **35**(10B), L1348 (1996).

59. K. Endo and T. Tatsumi, *Jpn. J. Appl. Phys. Pt. 2* **36**(11B), L1531 (1997).

60. K. Endo and T. Tatsumi, *J. Appl. Phys.* **78**(2), 1370 (1995).

61. C. R. Savage, R. B. Timmons, and J. W. Lin, *Chem. Mater.* **3**(4), 575 (1991).

62. S. J. Limb, D. J. Edell, E. F. Gleason, and K. K. Gleason, *J. Appl. Polym. Sci.* **67**, 1489 (1998).

63. X. Chen, K. Rajeshwar, R. B. Timmons, J.-J. Chen, and O. M. R. Chyan, *Chem. Mater.* **8**(5), 1067 (1996).

64. N. Fujiwara, T. Maruyama, and H. Miyatake, *Jpn. J. Appl. Phys. Pt. 1* **37**(4B), 2302 (1998).

65. S. Samukawa, *Appl. Phys. Lett.* **64**(25), 3398 (1994).

66. T. H. Ahn, K. Nakamura, and H. Sugai, *Plasma Sources Sci. Technol.* **5**(2), 139 (1996).

67. A. M. Hynes, M. J. Shenton, and J. P. S. Badyal, *Macromolecules* **29**(12), 4220 (1996).

68. A. Hynes and J. P. S. Badyal, *Chem. Mater.* **10**(8), 2177 (1998).

69. K. Takahashi, M. Hori, and T. Goto, *Jpn. J. Appl. Phys. Pt. 2* **32**(8A), L1088 (1993).

70. M. Haverlag, W. W. Stoffels, E. Stoffels, G. M. W. Kroesen, and F. J. de Hoog, *J. Vac. Sci. Technol. A* **14**(2), 384 (1996).

71. S. J. Limb, K. K. Gleason, D. J. Edell, and E. F. Gleason, *J. Vac. Sci. Technol. A* **15**(4), 1814 (1997).

72. K. Nakajima, A. T. Bell, and M. Shen, *J. Appl. Polym. Sci.* **23**, 2627 (1979).

73. K. Takahashi, M. Hori, K. Maruyama, S. Kishimoto, and T. Goto, *Jpn. J. Appl. Phys. Pt. 2* **32**(5A), L694 (1993).

74. N. M. Mackie, N. F. Dalleska, D. G. Castner, and E. R. Fisher, *Chem. Mater.* **9**(1), 349 (1997).

75. K. Takahashi, M. Hori, and T. Goto, *J. Vac. Sci. Technol. A* **14**(4), 2004 (1996).

Chapter 2

Electron Spin Resonance of Pulsed PECVD Fluorocarbon Films

(Published in Journal of Applied Physics, Vol. 82, Issue 4, pg. 1784 in 1997 as "Electron Spin Resonance of Pulsed Plasma Enhanced Chemical Vapor Deposited Fluorocarbon Films," Catherine B. Labelle, Scott J. Limb, and Karen K. Gleason.)

Section 2.1: Abstract

Pulsed-rf excitation of hexafluoropropylene oxide (HFPO) has been used to deposit poly(tetrafluoroethylene)-like (PTFE-like) thin films. Films were deposited at pulse rates of 10/20, 10/50, 10/200, and 10/400 ms on/ms off and analyzed using electron spin resonance spectroscopy (ESR). All four films produced similar broad ESR spectra, with an average width at maximum slope of ~60 G and a g-value of 2.0045. The number of free electrons in a sample decreased with increasing pulse off time. This behavior can be modeled by the reaction of a free radical with a gas species, assuming that free radicals are generated only during the pulse on time.

Section 2.2: Introduction

Low dielectric constant (κ) materials are needed for interlayer dielectric (ILD) applications in the semiconductor industry.[1-6] Specifically, new ILDs with dielectric constants of less than 4 will be needed to implement new design rules. The move to lower dielectric constant materials would allow for reductions in propagation delay (i.e., RC time constant), power consumption (i.e., $\propto CV^2$), and cross-coupling noise between adjacent lines,[6,7] and it is generally agreed that with smaller design rules, these reductions will be needed for higher performance.[1-4,6]

Most organic polymers and aerogels currently under study for ILD applications have been deposited using spin-on processes. However, several drawbacks are associated with this technique. First, achieving gap-fill when dealing with sub-0.25 μm technology is difficult with spin-on processes. Second, the spin-on films usually have anisotropic properties due to partial alignment of the polymeric chains during the

process. Finally, spin-on technologies employ solvents, and thus, waste disposal and worker exposure to the chemicals must be considered.

Chemical vapor deposition (CVD) of low κ materials would have several potential advantages over spin-on processes. These include: better gap-fill, generally amorphous films (isotropic dielectric properties), compatibility with conventional silicon-based IC processing and equipment, conformal coatings, *in situ* administration of adhesion promoters and/or plasma surface modifications to enhance substrate/dielectric or dielectric/metal interfaces, and, finally, no solvents. Despite these advantages, however, CVD processes have received little attention as approaches to deposit polymeric ILD materials.

In plasma-enhanced CVD (PECVD), energetic neutrals and ionized species are created in a glow discharge and subsequently deposit on a substrate. Many polymeric films can be deposited in this manner, and without the high temperatures inherent in thermal CVD processes. However, PECVD films have often been ruled out as potential ILDs due to their concentration of dangling bonds (i.e., unpaired electrons), which are detrimental to the dielectric properties of a PECVD film. Specifically, dangling bonds are suspected to give rise to dielectric loss, and, since they are reactive free radicals, their reactions with atmospheric oxygen and/or water may account for some of the observed aging effects which produce undesirable variations in film properties over time.[8,9] Thus, it is desirable to keep the dangling bond concentration to a minimum. Typical dangling bond concentrations for PECVD polymers are 10^{18} to 10^{20} spins/cm^3.[10] These concentrations can sometimes be reduced by low temperature annealing.[11]

Pulsed, rather than continuous, plasma excitation may be a viable compromise between thermal CVD and continuous PECVD. In this deposition process, which is a modification of traditional continuous PECVD, rf power is applied only for a specified "on" time, followed by an "off" period during which no excitation is used. During the "on" time, both ions and reactive neutrals are produced. However, since ions often have shorter lifetimes than neutrals, during the "off" time the ratio of neutrals to ions will increase, and thus, the competition between growth and etching reactions at the surface will be altered to favor film deposition from reactive neutrals. Also, by pulsing the plasma in this manner, some degree of control over the amount of ion bombardment to which a substrate is exposed can be maintained. By reducing ion bombardment during film growth, the density of dangling bonds remaining in the films should decrease.[10,12] Yasuda et al. have done an extensive analysis comparing materials deposited by pulsed vs. continuous plasma excitation for a variety of hydrocarbons and fluorocarbons.[10,12]

Pulsed plasma excitation has been reported to dramatically change the nature of the deposited fluorocarbon film.[13,14] For hexafluoropropylene oxide (HFPO) monomer, it was found that, for a constant pulse on time, the deposition rate per pulse cycle initially increases rapidly with increasing pulse off time, and then levels off at longer off times,[15] indicating that a significant portion of the deposition polymerization occurs during the pulse off time. This result also implies that the overall deposition rate (nm/s) will go through a maximum at short pulse off times, decreasing as the pulse off time increases.[15] In addition, it was found that the film composition changes with pulse off time. Specifically, while films deposited at very short pulse off times (10 ms on, 20 - 60 ms off time) contain significant fractions of CF_3, CF_2, CF, and quaternary carbon, as the pulse

off time is increased, the films' composition becomes increasingly dominated by CF_2, with the concentration of other bond configurations becoming negligible.[13-15] At long pulse off times, these films bear a closer chemical resemblance to Teflon™ than most continuous PECVD fluorocarbon films. Our lab has confirmed these results, and has investigated the effect of several other process parameters.[15]

The same general behavior of deposition per cycle was observed as pressure was varied. More importantly, the F/C ratio and % CF_2 content were found to increase with pressure, with the F/C ratio increasing from 1.7 to 1.9 and the % CF_2 content increasing from 49 to 64% as the pressure was changed from 400 to 1000 mTorr.[15]

Finally, it is worth noting that XPS and FTIR spectra detect only a few atomic % of oxygen in the films.[13-16] These results indicate that the majority of oxygen which enters the plasma via the HFPO reactive monomer exits the deposition chamber without depositing on the film surface. A study of the thermal decomposition of HFPO indicates that HFPO decomposes primarily into a CF_2 radical (difluorocarbene) plus a stable carbonyl:[17]

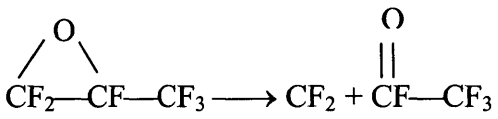

A similar decomposition activation energy (29 ± 4 kcal/mole) has been measured for HFPO thermal CVD.[18] In addition, the lack of significant oxygen in the pulsed plasma films indicates that this decomposition mechanism may be occurring in the plasma system as well.

The dangling bond concentration of a film can be measured directly by electron spin resonance spectroscopy (ESR), a technique which provides direct chemical identification of these defects.[19-21] The integrated ESR signal intensity is proportional to the number of dangling bonds in a sample, and thus, by comparison to a known standard, the number of dangling bonds in a sample can be determined. In addition, the hyperfine structure of ESR spectra can give structural information about the defect since nuclei with non-zero spin surrounding the ESR-active defect will affect the resonance field of the defect for a fixed frequency measurement.

Pulsed-rf excitation of hexafluoropropylene oxide (HFPO) has been used to deposit poly(tetrafluoroethylene)-like (PTFE-like) thin films.[14-16] Films similar to bulk PTFE (Teflon™) would be desirable as ILD materials since not only does bulk PTFE have a low dielectric constant (~2.0), but it also has a very low dielectric loss and is an excellent moisture barrier. Films were deposited at different pulsing rates and analyzed using ESR spectroscopy.

Section 2.3: Experimental Methods

Films ~5 μm thick were deposited on silicon wafers at pulse cycle conditions of 10/20, 10/50, 10/200, and 10/400 ms on/ms off using 23 cm^3/min (STP) HFPO (PCR Inc., 99% purity) with a source power of 2.7 W/cm^2 (ENI Power Systems, Inc., Model HF-300) at 1000 mTorr in a parallel-plate plasma reactor. The wafers were cooled on the backside with water at ~23°C. Cycling conditions were set using a pulse generator (Systron-Donner Corp. Datapulse 100A) and monitored with an oscilloscope (Leader,

Model 1041). A manually operated matching network (Heathkit Antenna Tuner, Model SA-2060A) was used to minimize reflected power during the pulse.

After deposition, each film was scraped off the silicon wafer with a razor blade and placed in a 0.375 inch O.D., 7 inch long ESR tube. Quartz wool was packed above and below the sample in the tubes. The weight of sample in each tube was measured to ± 0.0001 g with a Mettler AJ100 balance.

An ESR reference sample was prepared by dissolving 0.0008 g α,γ–bisdiphenylene-β-phenylallyl (BDPA) (Aldrich, 1:1 complex with benzene) and 1.0045 g polystyrene in 10 mL of chloroform mixed by a magnetic stir bar. The solution was then spread out on glass plates and air dried (to remove chloroform) in a hood for over 24 hours. The solidified mixture of BDPA and polystyrene was then scraped off of the glass plates, and 0.0301 g of the mixture was placed in an ESR tube with quartz wool packed above and below the sample. The ESR tube was then sealed under vacuum. The sealed sample was calculated to have $(2.9 \pm 0.4) \times 10^{16}$ spins.

ESR measurements were made using a 9.8 GHz Bruker ESP-300 ESR spectrometer with a maximum sweep width of 8000 Gauss. All samples were measured at 83.4 s sweep time, 600 G sweep width, 0.974 G modulation amplitude and 100 kHz modulation frequency. Depending on the sample, microwave excitation was performed at either 0.2 or 2.0 mW. The BDPA standard was used to calibrate the observed integrated intensity under these conditions.

For the 10/400 sample, variation in ESR intensity was also measured for power levels from 0.1 to 20 mW.

Section 2.4: Results and Discussion

Figure 2-1 shows the ESR spectrum for a 10 ms on/50 ms off pulsed plasma polymerized film derived from HFPO. The spectrum is broad, having a peak-to-peak linewidth of 60.5 ± 1.7 G, and a g-value of 2.0037 ± 0.0005 (g-value of a free electron = 2.0023). Similar linewidths and g-values were observed for films deposited at pulse rates of 10/20, 10/200, and 10/400 (ms on/ms off). These linewidths are rather large compared to pulsed plasma polymerized hydrocarbons (~10-20 G),[10] but are typical of pulsed plasma polymerized fluorocarbons (~40-70 G).[12] The lack of any discernible hyperfine structure can be attributed to the amorphous nature of the film. The broadness of the spectrum is most likely due to the proximity of ^{19}F nuclei, which can give rise to large hyperfine coupling constants. There was no broadening of the spectra with increasing dangling bond concentration, since the same linewidth (± 4 G) was found for all of the pulsed samples. This result indicates that the dipolar couplings between paramagnetic centers (i.e., free electron to free electron) produce a negligible broadening effect.

A single Lorentzian with a peak to peak distance, d, of 54.6 G was found to fit the 10/50 spectrum with a coefficient of determination, r^2, of 0.98. This fit captures the main features of the spectrum, namely the position of the centerpoint and the two peaks, but the outer tails do not drop off as rapidly as the measured spectra. The fit was not improved by using either a single Gaussian, a combination of two different Gaussians, or a combination of two different Lorentzians. A combination of a single Gaussian and a single Lorentzian produced a slightly better fit than the single Lorentzian, but the improvement was deemed insufficient to justify the increased complexity of the model.

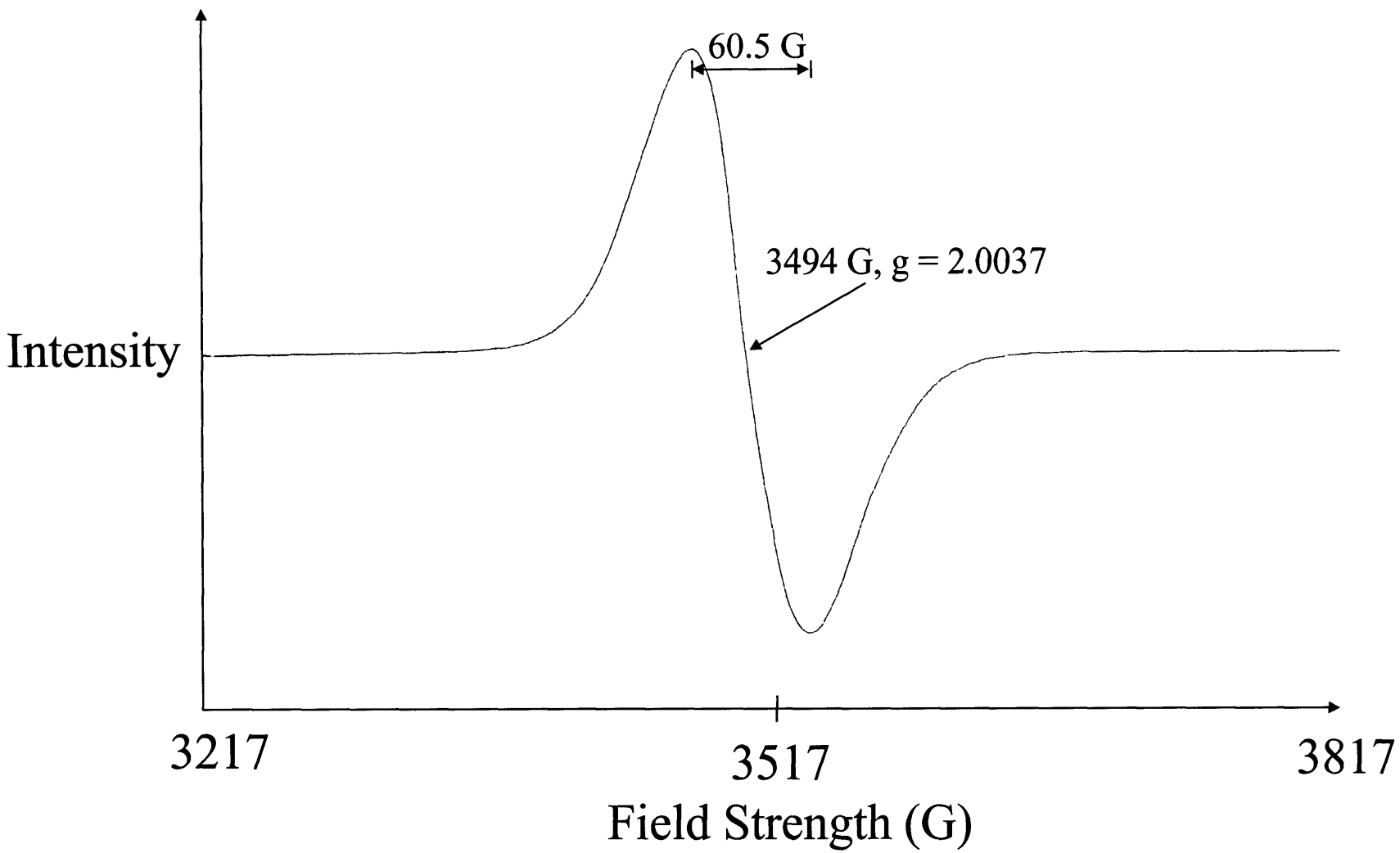

Figure 2-1: ESR spectra for 10/50 pulsed sample. Peak-to-peak linewidth = 60.5 G and g-value = 2.0037.

Figure 2-2 shows the integrated ESR intensity versus the square root of the applied power for a 10/400 pulsed plasma film. The linear behavior shown in Figure 2-2 indicates that saturation did not occur at the given spectrometer conditions with the tested samples. Thus, the signal intensity is directly proportional to the number of dangling bonds in the sample. In addition, this result indicates that the spectral linewidth is not a result of saturation broadening.

The number of dangling bonds in each pulsed sample was calculated by comparison to the BDPA standard. Figure 2-3 shows the calculated number of dangling bonds per gram of material as a function of pulse off time. Increasing the pulse off time results in a decrease in the number of dangling bonds formed during deposition.

The dependence of dangling bond concentration on pulse off time can be modeled by considering an individual layer deposited during a single pulse cycle. First, assume that dangling bonds are created only during the pulse on time. During the pulse off time, several mechanisms are possible: (1) none of the created dangling bonds recombine, (2) the created dangling bonds diffuse over the film surface and recombine via a simple radical termination reaction:

$$M\bullet + M\bullet \xrightarrow{k} 2M \qquad (2)$$

and, (3) dangling bonds are removed from the surface by interaction with a gas phase species:

$$M\bullet + N(g) \xrightarrow{k_1} Q \qquad (3)$$

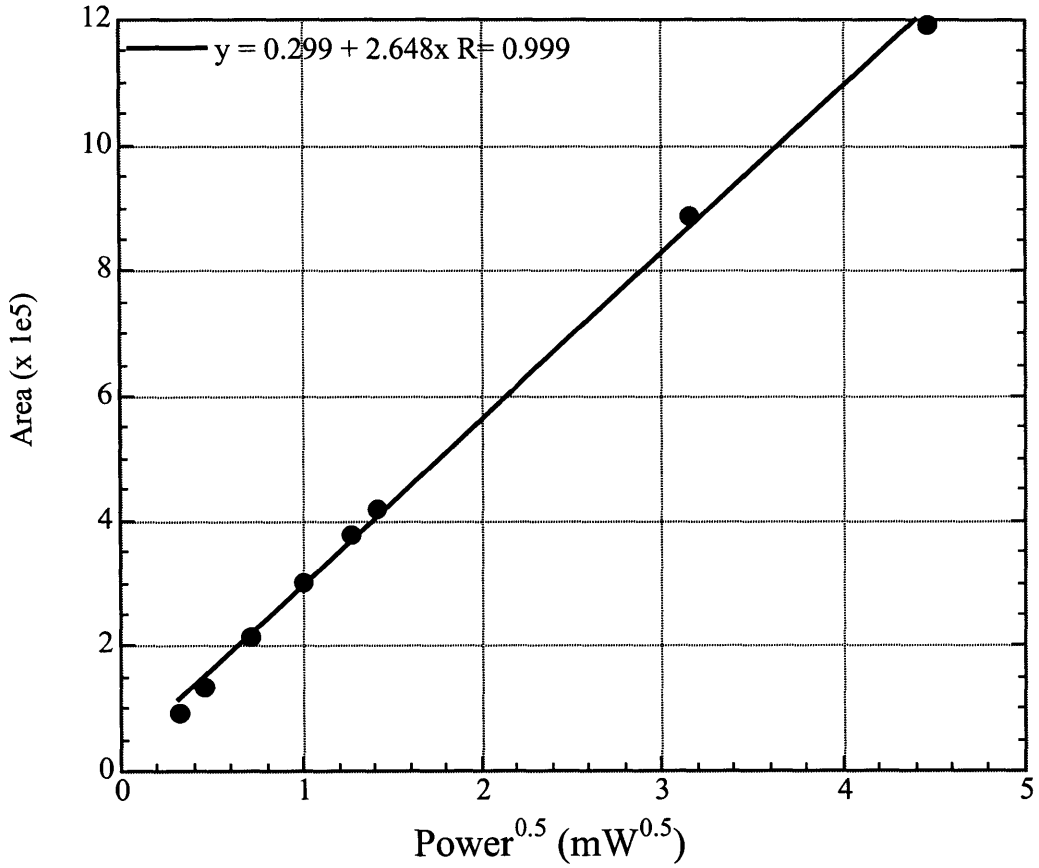

Figure 2-2: Integrated ESR area versus square root of microwave power. Linear relationship indicates saturation has not occurred.

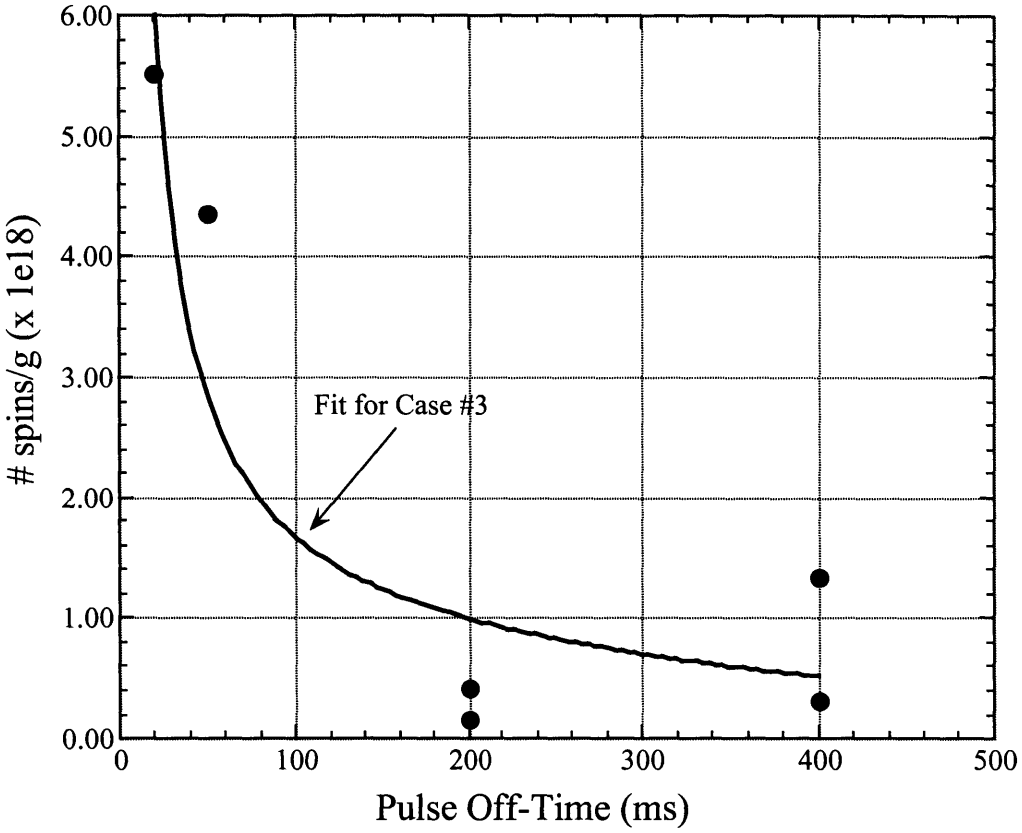

Figure 2-3: Dangling bond concentration vs. pulse off time. Curve fits are non-linear least square regressions of Eqns. 6 (Case #2) and 7 (Case #3), which represent two different pathways for dangling bond reduction. In Case #2, it is assumed that during the pulse off time dangling bonds diffuse over the film surface and recombine. In Case #3, dangling bond reduction during the pulse off time is assumed to be due to interaction with a gas phase species. Statistical analysis indicates that Case #3 is the more valid of the two.

where Q represents whatever structures (gas and/or solid) remain after the reaction.

In each case, the final dangling bond concentration (spins/g) can be calculated by:

$$[M\bullet]_f = \frac{[M\bullet]_1}{\rho_{film} d} \tag{4}$$

where $[M\bullet]_f$ = final dangling bond concentration at end of off-time (spins/**g**),
$[M\bullet]_1$ = dangling bond concentration per unit area at end of off time (spins/**cm^2**),
ρ_{film} = density of film (~2.20 g/cm^3)[22], and
d = thickness of film deposited in one pulse cycle (cm).

The thickness, d, is just the deposition rate per cycle, r_p, times 1 cycle. The dependence of r_p on pulse off time, t_1, is known ($r_p = 0.18\left(1 - e^{-14t_1}\right)$, in nm/cycle),[15] so it can be substituted in for d. The resulting models have a zero, second, and first order dependence on the concentration of dangling bonds, $[M\bullet]$, respectively (assuming the reactions proceed in the forward direction only). The resulting equations for $[M\bullet]_f$ are:

Case (1): $$[M\bullet]_f = \frac{\left(1 \text{ x } 10^8\right)[M\bullet]_0}{2.20\left(1.8\left(1 - e^{-14t_1}\right)\right)} \tag{5}$$

Case (2): $$[M\bullet]_f = \left[\frac{1 \text{ x } 10^8}{2.20\left(1.8\left(1 - e^{-14t_1}\right)\right)}\right]\left[\frac{[M\bullet]_0}{1 + 2kt_1[M\bullet]_0}\right]. \tag{6}$$

Case (3): $$[M\bullet]_f = \frac{\left(1 \text{ x } 10^8\right)[M\bullet]_0 e^{-k_1 P_N t_1}}{2.20\left(1.8\left(1 - e^{-14t_1}\right)\right)} \tag{7}$$

where $[M\bullet]_0$ = initial dangling bond concentration present at end of on time (spins/cm^2),
t_1 = pulse off time (s), and
P_N = pressure of gas species (~ 1 Torr).

These models contain the adjustable parameters $[M\bullet]_0$ (Case 1), $[M\bullet]_0$ and k (Case 2), and $[M\bullet]_0$ and k_1 (Case 3). A least squares regression was used to fit each model to the data. From observation, Case 1 did not model the data satisfactorily. However, both Cases 2 and 3 produced good fits (Figure 2-3), indicating that some dangling bonds are eliminated during the off time. Both models predicted that $[M\bullet]_0 \sim 10^{10}$ spins/cm^2. This value for $[M\bullet]_0$ is reasonable since for a typical plasma charge density of 1 mA/cm^2, the typical number of ions striking the surface in the 10 ms on time would be $\sim 6.25 \times 10^{12}$ ions/cm^2. This analysis indicates that only a small fraction (~ 0.011) of incident ions produce dangling bonds. In addition, there are $\sim 10^{15}$ surface sites/cm^2, and thus, only 1×10^{-5} of the sites have dangling bonds. This low density of dangling bond sites indicates that the probability of two dangling bonds meeting and recombining in the given time is small, and therefore, the Case 2 recombination reaction probably does not occur significantly. Thus, Case 3 seems the most reasonable model.

The lowest measured dangling bond concentration was on the order of 10^{17} spins/g. The model indicates that if the pulse off time was increased, an even lower dangling bond concentration would be found. However, according to this model, even to lower the dangling bond concentration to 10^{16} spins/g, the pulse off time would have to be increased to ~1900 ms. The overall deposition rate (nm/min) corresponding to such a large pulse off time would be excessively slow, and therefore, unacceptable. Thus, if films with lower dangling bond concentrations are desired, other options must be considered. Assuming most of the dangling bonds are formed by ion bombardment during the pulse on-time, one possible solution may be to reduce the pulse on-time or average ion energy during the on period. These modifications will affect other

parameters such as film composition and deposition rate, but a pulsing rate may be found such that film composition, deposition rate, and dangling bond concentration are all acceptable.

Section 2.5: Summary and Conclusions

ESR measurements were made on PTFE-like films deposited at pulse rates of 10/20, 10/50, 10/200, and 10/400 ms on/ms off. The spectra were broad, with an average linewidth of ~60 G, which correlates well with published values of linewidths for other pulsed plasma polymerized fluorocarbons,[12] and an average g-value of 2.0045. The dangling bond concentration decreased with increasing pulse off-time. A model which allows for radical reduction through interaction with a gas phase species during the pulse off time was found to best fit the data.

The presence of free electrons in films which are used in semiconductor applications is generally undesirable. The fact that the dangling bond concentration can be controlled by the pulse rate of the plasma during deposition is key to the possible future use of these films in semiconductor applications, since the deposition process can be tailored to produce a film with a desired concentration of dangling bonds.

Section 2.6: Acknowledgments

We would like to gratefully acknowledge the NIH for support of this work under contract NO1-NS-3-2301. We would also like to thank the Office of Naval Research and Lucent Technologies Bell Laboratories for their support of this project.

Section 2.7: References

1. P. Singer, Semiconductor Intl. **17,** 52-56 (1994).

2. R. K. Laxman, Semiconductor Intl. **18,** 71-74 (1995).

3. P. Singer, Semiconductor Intl. **17,** 34 (1994).

4. S. P. Murarka, Solid State Tech. **39,** 83-90 (1996).

5. J. Paraszczak, D. Edelstein, S. Cohen, E. Babich, and J. Hummel, IEDM Technical Digest, 261-264 (1993).

6. P. Singer, Semiconductor Intl. **19,** 88-96 (1996).

7. J. Wary, R. Olson, and W. Beach, Semiconductor Intl. **19,** 211-216 (1996).

8. H. Yasuda, J. Macromol. Sci.--Chem. **A10,** 383-420 (1976).

9. N. Morosoff, B. Crist, M. Bumgarner, T. Hsu, and H. Yasuda, J. Macromol. Sci.--Chem. **A10,** 451-471 (1976).

10. H. Yasuda and T. Hsu, J. Poly. Sci.: Poly. Chem. Ed. **15,** 81-97 (1977).

11. S. Morita, G. Sawa, and M. Ieda, J. Macromol. Sci.--Chem. **A10,** 501-517 (1976).

12. H. Yasuda and T. S. Hsu, J. Poly. Sci.: Poly. Chem. Ed. **15,** 2411-2425 (1977).

13. C. R. Savage, R. B. Timmons, and J. W. Lin, Chem. Mater. **3,** 575-577 (1991).

14. C. R. Savage, R. B. Timmons, and J. W. Lin, in *Advances in Chemistry Series*; *Vol. 236* (American Chemical Society, 1993), p. 745-768.

15. S. J. Limb (Personal communication).

16. S. J. Limb, K. K. Gleason, D. J. Edell, and E. F. Gleason, J. Vac. Sci. Technol. A **A15,** to be published in August (1997).

17. M. B. Knickelbein, D. A. Webb, and E. R. Grant, in *New Devices for the Production of Intense Pulsed Jets of CF_2: Laser Spectroscopic Characterization*, Boston, MA, 1984 (Materials Research Society), p. 23-33.

18. S. J. Limb, C. B. Labelle, K. K. Gleason, D. J. Edell, and E. F. Gleason, Appl. Phys. Lett. **68,** 2810-2812 (1996).

19. H. M. Assenheim, *Introduction to Electron Spin Resonance* (Plenum Press, New York, 1966).

20. P. W. Atkins and M. C. R. Symons, *The Structure of Inorganic Radicals* (Elsevier Publishing Company, New York, 1967).

21. J. E. Wertz and J. R. Bolton, *Electron Spin Resonance: Elementary Theory and Practical Applications* (McGraw-Hill Book Company, New York, 1972).

22. F. Rodriguez, *Principles of Polymer Systems*, 3 ed. (Hemisphere Publishing Corporation, New York, 1989).

Chapter 3

Pulsed Plasma Enhanced Chemical Vapor Deposition from CH_2F_2, $C_2H_2F_4$, and $CHClF_2$

(Published in Journal of Vacuum Science and Technology A, Vol. 17, Issue 2, pg. 445 in 1999 as "Pulsed Plasma Enhanced Chemical Vapor Deposition from CH_2F_2, $C_2H_2F_4$, and $CHClF_2$," Catherine B. Labelle and Karen K. Gleason.)

Section 3.1: Abstract

Pulsed plasma enhanced chemical vapor deposition films have been grown from $C_2H_2F_4$, CH_2F_2, and $CHClF_2$. C-1s x-ray photoelectron spectroscopy (XPS) indicates a prevalence of C-CF species in the films from $C_2H_2F_4$ and CH_2F_2, whereas CF_2 species dominate the films from $CHClF_2$. The CF_x species distributions for the films are largely controlled by the competition between CF_2-producing and HF elimination reactions in the pulsed plasmas. Dominance by HF elimination produces films with high C-CF and CF concentrations (e.g., CH_2F_2), whereas dominance by CF_2-producing reactions leads to films with higher CF_2 concentrations (e.g., $CHClF_2$). The % CF_3 in the film is lowest for the precursor having the lowest F:H ratio, CH_2F_2. Little or no hydrogen was detected in the deposited films. Pulsed plasma films from all three precursors gave dielectric constants of 2.4, with loss tangents on the order of 10^{-2}. Dielectric measurements of pulsed plasma films from hexafluoropropylene oxide (HFPO) gave a dielectric constant of 2.0 ± 0.1 with a loss tangent of 0.009.

Section 3.2: Introduction

Materials with low dielectric constants ($\kappa < 3$) are needed as interlayer dielectrics (ILDs) in order to implement new integrated circuit (IC) design rules.[1-3] The move to lower dielectric constant materials would result in reductions in propagation delay (i.e., RC time constant), power consumption (i.e., $\propto CV^2$), and cross-coupling noise between adjacent lines, which would allow for higher performance with smaller design rules.[1-3]

Fluorocarbon films are excellent potential ILD materials.[4-9] The lowest dielectric constant of this class of materials has been predicted to be 2.0.[6,7,10] Fluorocarbon

plasmas are used extensively to anisotropically etch silicon and silicon dioxide.[11] During etching, fluorocarbon films are often formed along the feature sidewalls.[11] By modifying the plasma conditions, the plasma equilibrium can be shifted to deposition rather than etching, and these films can be deposited preferentially.[12] Typical precursors include CF_4, C_2F_4, C_2F_6, CHF_3, C_4F_8, and C_2F_6O.[13-17] Fluorocarbon films deposited by plasma-enhanced chemical vapor deposition (PECVD) have long been studied because of their promising electrical, optical, and chemical characteristics.[12,18,19] However, PECVD films have often been ruled out as potential ILDs due to their incorporation of dangling bonds (i.e., unpaired electrons), which are suspected to give rise to dielectric loss and aging effects. [20,21] High dielectric loss is unacceptable for some circuit applications, while aging effects lead to instability of the film properties. Typical dangling bond concentrations for PECVD polymers are 10^{18} to 10^{20} spins/cm^3,[22] which can sometimes be reduced by low temperature annealing.[23]

Pulsed, rather than continuous, plasma excitation can reduce dangling bond concentrations in fluorocarbon films.[24] Thus, pulsing has the potential to improve the electrical properties of the films. In this process, rf power is applied for a specified "on" time, followed by an "off" period during which no excitation is used. During the "on" time, both ions and reactive neutrals are produced. However, since ions often have shorter lifetimes than neutrals, during the "off" time the ratio of neutrals to ions will increase, and thus, the process equilibrium will be shifted to favor film deposition from reactive neutrals.

Pulsed plasma excitation has been reported to dramatically change the nature of the deposited fluorocarbon film.[4,5,25] The composition of films from HFPO changes

dramatically with pulse off time. At very short pulse off times (10 ms on, 20 - 60 ms off time) films contain significant fractions of CF_3, CF_2, CF, and quaternary carbon (C-CF). As the pulse off time is increased, the film composition becomes increasingly dominated by CF_2.[4,5,17,25] The maximum F:C ratio was 1.9, with a corresponding CF_2 fraction of 64%.[17,25]

It is also worth noting that x-ray photoelectron spectroscopy (XPS) and Fourier-transform infrared spectroscopy (FTIR) spectra detect only a few atomic % of oxygen in HFPO pulsed plasma films.[4,5,17,25] These results indicate that the majority of oxygen which enters the pulsed plasma via the HFPO reactive precursor exits the deposition chamber without depositing on the film surface. A study of the thermal decomposition of HFPO indicates that HFPO decomposes primarily into a CF_2 radical (difluorocarbene) plus a stable carbonyl:[26]

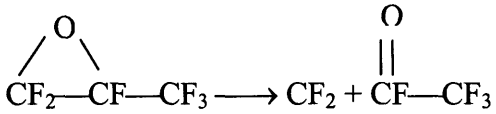

(1)

A similar decomposition activation energy (29 ± 4 kcal/mole) has been measured for thermal CVD from HFPO.[27] The lack of significant oxygen and the high % CF_2 in the pulsed plasma films indicates that this decomposition mechanism may also be occurring during pulsed plasmas from HFPO. Gas phase FTIR of the reactor effluents confirms the formation of $CFOCF_3$ in the pulsed plasma.[28]

This paper reports results from three new gases selected for use in the pulsed PECVD system: CH_2F_2 (HFC-32), $C_2H_2F_4$ (HFC-134), and $CHClF_2$ (Freon 22). These

reactants were all reported to thermally decompose into CF_2.[29-35] In addition, feed gases containing hydrogen were selected for their low global warming and ozone depletion potentials. Dielectric measurements of the films from HFPO and from the new precursors will be presented.

Section 3.3: Experimental

Films were deposited on silicon (Si) wafers at a variety of pulse cycle conditions using pulse on times of 5, 10, 20, 30 and 40 ms, and pulse off times of 20, 50, 100, 200 and 400 ms. A flow rate of 12.5 sccm was used for all four precursors, with a source power of 2.7 W/cm^2 at 1000 mTorr in a parallel plate reactor. The wafers were cooled on the backside with water at ~23°C.

Carbon-1s x-ray photoelectron spectroscopy (C-1s XPS, Physical Electronics Model 5200C employing a Mg $K\alpha_{1,2}$ exciting radiation source) was used to determine the relative areas of CF_3, CF_2, CF, and C-CF for a 10 ms on/100 ms off film deposited from each gas. The resulting spectra were analyzed using the same techniques as Limb et al.[25]

For the three precursors containing hydrogen, which is not detected by XPS, Fourier Transform Infrared Spectroscopy (FTIR) was used to determine if hydrogen species were present in the resulting films. The FTIR spectra (Nicolet Magna-IR 860) were obtained for films as-deposited on Si wafers, with the Si wafer spectrum being subtracted from the sample spectrum. Each spectrum was obtained from an average of 32 scans, taking special precautions to evacuate any water out of the spectrometer with a continuous N_2 purge. The final spectra were all normalized to a film thickness of 1500 Å using the Beer-Lambert law.[36]

Film thicknesses and refractive indices were determined using both spectroscopic and single-wavelength ellipsometry (Woolham Variable Angle Spectroscopic Ellipsometer, Rudolph Research AutoEl II Ellipsometer, Gaertner Scientific Corporation L116A Ellipsometer). Approximate thicknesses were determined by profilometry (Tencor P-10 Surface Profilometer), with final values measured by ellipsometry. Single wavelength ellipsometry was done with a He-Ne laser (6328 Å) at an angle of incidence of 70°. For the spectroscopic ellipsometry, psi and delta were measured between 3000 and 8000 Å at 50 Å increments at angles of incidence of 30, 45, and 60°, with 10 repetitions at each point. The resulting psi and delta curves were modeled by assuming the refractive index followed a Cauchy dispersion:

$$n = A_n + \frac{B_n}{\lambda^2} + \frac{C_n}{\lambda^4} \qquad (2)$$

where n is the refractive index, λ is the wavelength (Å), and A_n, B_n, and C_n are fitted parameters. The amplitude of k (imaginary part of refractive index) was also allowed to vary. Excellent fits were obtained, from which the indices of refraction at 6328Å were determined.

Dielectric constants and loss tangents were determined through capacitance-voltage (C-V) measurements of metal-insulator-metal (MIM) structures, using a Hg probe (Materials Development Corporation Model 811) as the top metal structure. Films with a target thickness of 5000Å were deposited on Al-covered Si (~1000 Å), which served as the rest of the MIM structure. Capacitance was measured from -20 to +20 V at 1 MHz. Backside contact was used during the measurements, so the MIM structure was modeled as a parallel plate capacitor, and the dielectric constant obtained from:

$$C_0 = \frac{\kappa \varepsilon_0 A}{d} \tag{3}$$

where C_0 is the observed capacitance, κ is the dielectric constant of film, ε_0 is the free permittivity (8.854×10^{-14} F/cm), A is the contact area with dielectric film, and d is the film thickness.[11]

Standard deviations for the dielectric constant are given for all four films. The actual area of the Hg dot contacting the film was not directly measured, leading to one potential source of error. However, thin film capacitors fabricated from films deposited from HFPO[10] gave dielectric constants similar to those determined by the Hg probe method.

A second source of error in these measurements was in the determination of the film thickness between the metal contacts used in the capacitance-voltage (C-V) measurements. Both ellipsometry and profilometry were utilized in measuring the film thicknesses. A discrepancy of a several hundred angstroms was observed when comparing the two measurement techniques (Figure 3-1), and that discrepancy was factored into the error calculations. Another difficulty was in determining the films' refractive indices using a single wavelength, single angle ellipsometer. This issue was ultimately resolved by using a variable angle spectroscopic ellipsometer to measure psi and delta at three angles of incidence over a wavelength range of 3000-8000 Å. By modeling the refractive index using a Cauchy dispersion and allowing the film to be slightly absorbing (typical $k_{amplitude} \sim 10^{-3}$), film thicknesses were determined with great confidence, and refractive indices were determined over a wide range of wavelengths.

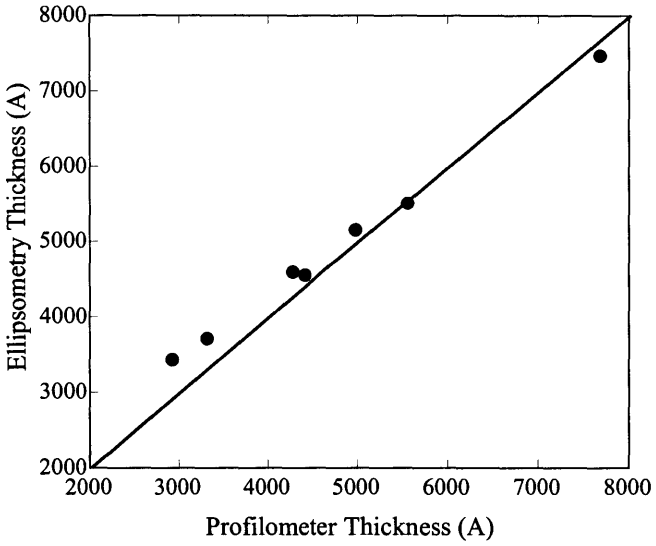

Figure 3-1: Comparison of thickness measurements given by single wavelength ellipsometry (6328 Å, 70° angle of incidence) versus profilometry. Ellipsometry measurements consistently predicted a higher thickness than that indicated by profilometry by several hundred angstroms.

Figure 3-2 shows the resulting calculated thicknesses compared to profilometry measurements. There is still a discrepancy on the order of ~200 Å, with the ellipsometer predicting higher than the profilometer, but the goodness of the ellipsometry fits of psi and delta over the wide range of wavelengths and angles of incidence indicates that the spectroscopic ellipsometer gives the more accurate measurement.

Section 3.4: Results and Discussion

Section 3.4.1: Deposition Rates

Figure 3-3 shows the film deposition rates per pulse cycle for CH_2F_2, $C_2H_2F_4$, $CHClF_2$, and HFPO as a function of pulse off time for a constant pulse on time of 10 ms. All four precursors show an initial increase in deposition rate/cycle as pulse off time is increased, indicating that deposition is occurring during the off period. As has been seen previously, the deposition rate/cycle increases steadily, and then levels off around 200 ms for HFPO.[37] However, the other three gases all show an initial increase in deposition rate/cycle, peak, and then decline. Thus, the deposition mechanisms for these three precursors appear to be significantly different from those of HFPO.

Overall, it is important to note that $C_2H_2F_4$ gives the highest deposition rates/cycle of the four precursors, with a peak of 2.8 Å/cycle at a pulse cycle of 10 ms on/100 ms off. Several factors may contribute to this result. First, $C_2H_2F_4$ contains 2 Cs per molecule of gas, which may allow the film to form longer-chain segments at a faster rate than when using gases like CH_2F_2 and $CHClF_2$. HFPO has three Cs per molecule, but tends to break down into smaller one- and two-C segments (Eqn. 1). The two-C segment is most likely

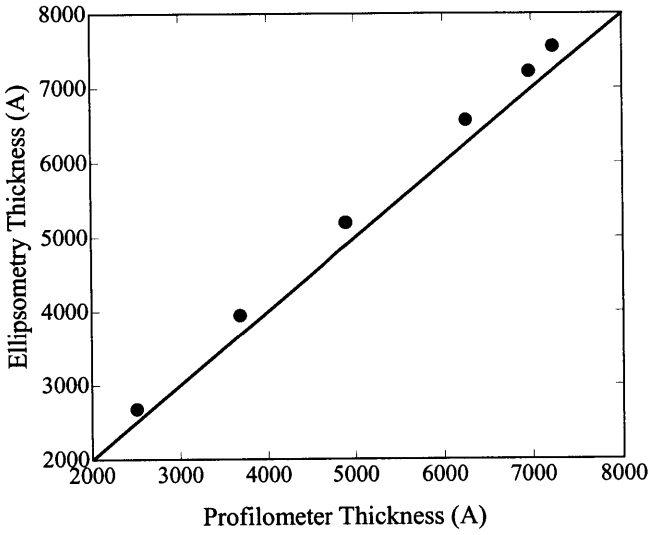

Figure 3-2: Comparison of thickness measurements given by variable angle spectroscopic ellipsometry (3000 - 8000 Å; 30, 45, 60° angles of incidence) versus profilometry. Excellent fits of psi and delta from the ellipsometry measurements were obtained by assuming a Cauchy dispersion for the refractive indices, and allowing the films to be slightly absorbing. Again, ellipsometry measurements indicate a slightly higher thickness than the profilometry. However, due to the excellence of the ellipsometry fits over the wide range of measurement conditions, the ellipsometry calculations are taken as correct.

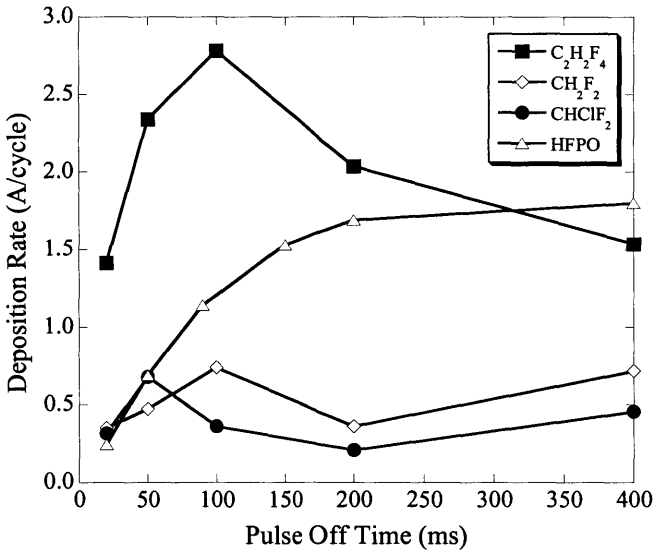

Figure 3-3: Deposition rate per pulse cycle versus pulse off time for a constant pulse on time of 10 ms. Hydrogen containing gases show a maximum in the deposition rate as compared to the plateau reached by HFPO. These trends indicate that a different deposition mechanism is prevalent for the hydrogen-containing precursors than for the HFPO.

split further into one-C species or exhausted from the reactor since negligible oxygen is found in the deposited film.[17,25] Regardless, the deposition mechanism would involve single-carbon additions (as with CH_2F_2 and $CHClF_2$), resulting in a slower deposition rate than $C_2H_2F_4$.

Another factor in the deposition rates is the presence of hydrogen versus oxygen in the feed gas. Coburn and Winters have shown that there is a balance between etching and polymerization from continuous plasmas based on the F:C ratio of the precursor.[12] $C_2H_2F_4$ and HFPO both have the same F:C ratio (= 2), but the first contains hydrogen, whereas the second contains oxygen. Hydrogen has been shown to increase fluorocarbon deposition rates by scavenging fluorine atoms to form HF.[12,38] This reaction reduces the etching of the growing fluorocarbon film by fluorine atoms, pushing the plasma further toward the polymerization regime. In contrast, oxygen tends to promote etching by tying up carbon in CO and CO_2 and thus, releasing free fluorine to etch the growing film.[12,38] This suggests that $C_2H_2F_4$ would be expected to have higher deposition rates than HFPO, all other factors aside.

Finally, the deposition rates are also influenced by the ease of forming the depositing precursors during the pulse on time. The relative levels of the deposition rates may simply be due to the fact that it is easier for the plasma to dissociate $C_2H_2F_4$ and HFPO than CH_2F_2 and $CHClF_2$.

Figures 3-4(a,b) show the deposition rates per pulse cycle for the four precursors as a function of pulse on time for a constant pulse off time of 400 ms. All of the precursors show a general increase in deposition rate/cycle with pulse on time, although the rate of increase is different for each gas. For HFPO and $CHClF_2$ (Fig. 3-4a), the data

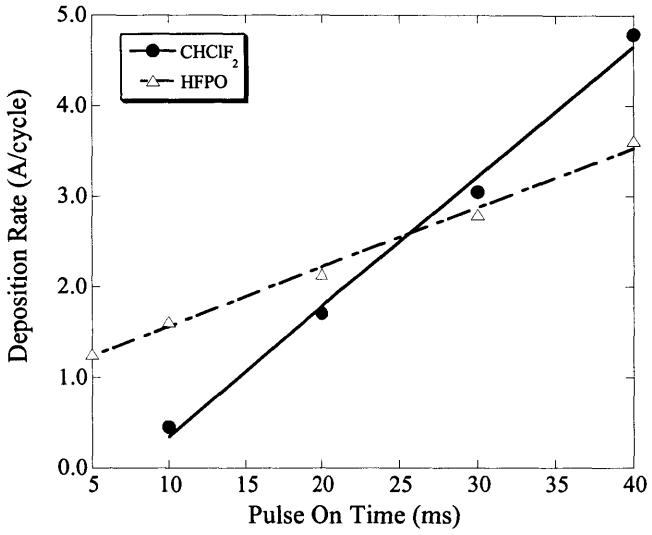

(a)

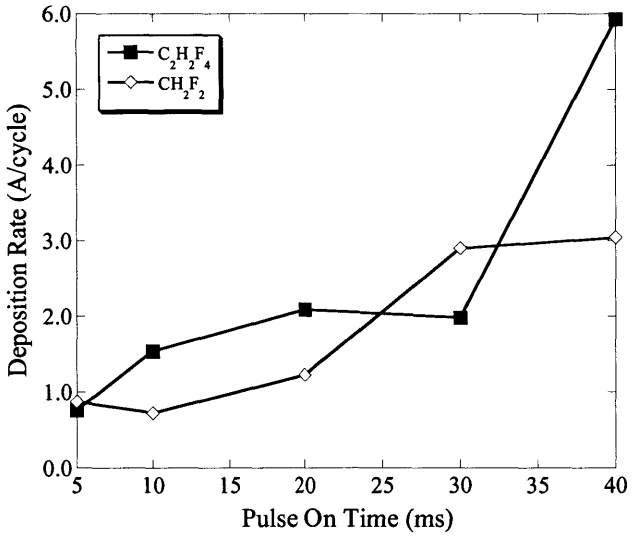

(b)

Figure 3-4: Deposition rate per pulse cycle versus pulse on time for a constant pulse off time of 400 ms. All four precursors show a general increase in deposition rate/cycle with pulse on time, although the rate of increase is different for each gas. (a) HFPO and $CHClF_2$ show a strict linear increase ($r^2 > 0.99$), as would be expected if the sole effect of increasing on time is to excite a larger fraction of the gas through one dominant reaction pathway. (b) $C_2H_2F_4$ and CH_2F_2 show nonlinear increases in deposition rate with pulse on time, indicating a more complex response to pulse on time, perhaps due to the effect of competing CF_2-producing and HF elimination reactions during deposition.

can be fitted by linear least squares regressions with coefficients of determination (r^2) > 0.99. This linear increase is expected if the sole effect of increasing on time is to excite a larger fraction of the gas through one dominant reaction pathway. However, competing reactions would result in more complex behavior. Such may be the case for $C_2H_2F_4$ and CH_2F_2 (Fig. 3-4b), which show nonlinear increases in deposition rate with pulse on time.

Figure 3-5 shows the overall deposition rates (Å/***min. process time***) of $C_2H_2F_4$ as a function of duty cycle. The deposition rate/min. increases with duty cycle, with a maximum at 2800 Å/min. However, the pulsed plasma is not just producing an average power effect. For instance, the 10/200 and the 20/400 conditions result in different film deposition rates even though the duty cycle is 0.048 for both. This difference indicates that the kinetics of the plasma during the on period and neutral reactions during the off period play a crucial role in determining the concentration of species in the pulsed PECVD reactor. The 10/100 and 40/400 films also have different deposition rates even though the duty cycle is 0.091 for both.

Section 3.4.2: Film Composition

Figure 3-6 shows the C-1s XPS spectra for films deposited from $C_2H_2F_4$, CH_2F_2, and $CHClF_2$, all at a pulse condition of 10/100. Table 3-1 lists the concentration of each species in the films, along with the overall F:C ratios calculated from the areas under the peaks. Films deposited from both $C_2H_2F_4$ and CH_2F_2 have low F:C ratios (0.91 and 0.60, respectively), whereas the film deposited from $CHClF_2$ has a higher F:C ratio (1.22). These ratios reflect the relative distribution of the CF_x species in the films. The dominant species for films from both $C_2H_2F_4$ and CH_2F_2 is C-CF, with the film from $C_2H_2F_4$

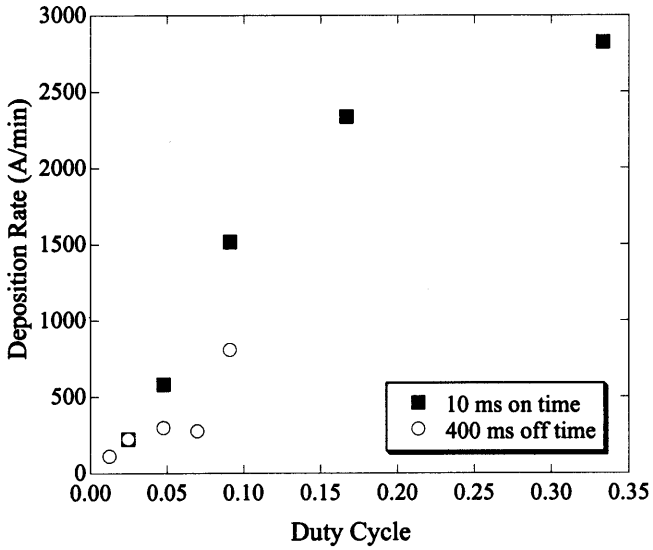

Figure 3-5: Deposition rate (Å/***min. process time***) of $C_2H_2F_4$ as a function of pulse duty cycle (on time/(on time + off time)). Deposition rate generally increases with duty cycle. However, it is clear from the duplicate points at 0.048 (10/200 and 20/400) and 0.091 (10/100 and 40/400) that the pulsing is not producing an average power effect. Rather, the specific pulse on and off times, and the resulting species concentrations established by those pulse conditions, are important.

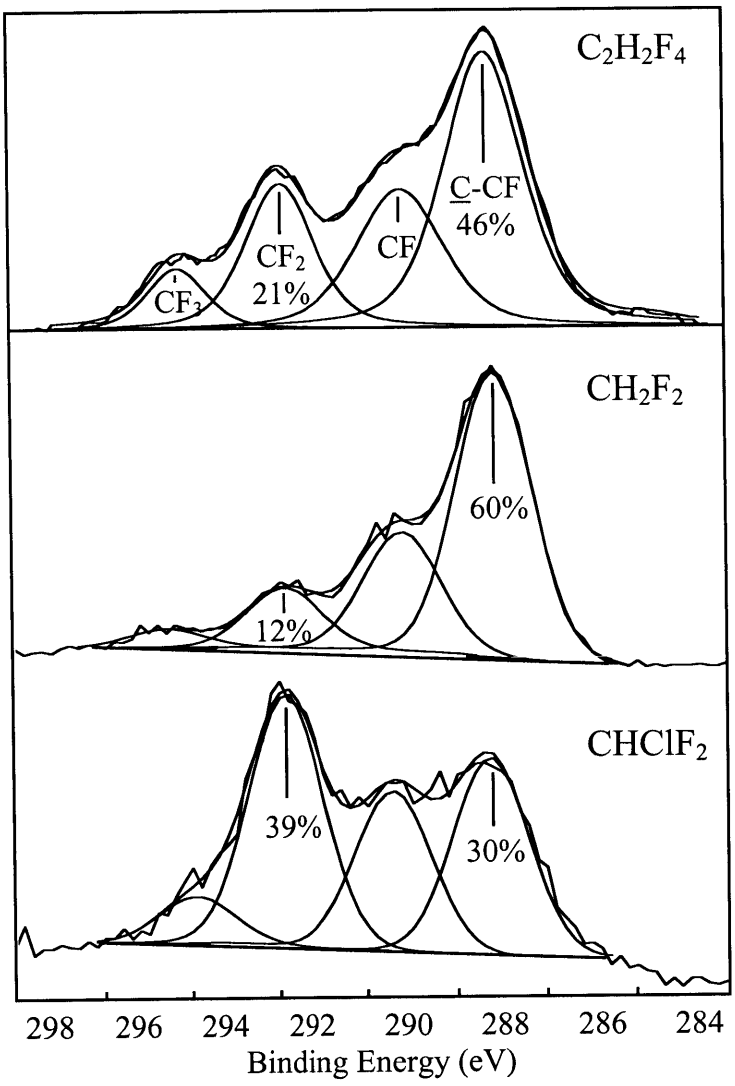

Figure 3-6: C-1s XPS of 10/100 films deposited from $C_2H_2F_4$, CH_2F_2, and $CHClF_2$. The strength of the competition between the CF_2-producing reaction and HF elimination reaction for each precursor determines the distribution of CF_2, CF, and C-CF species, with domination of the HF elimination reaction leading to reduced CF_2 concentrations and higher CF and C-CF concentrations. The prevalence of free fluorine atoms, as determined by the F:H ratio of each precursor, influences the concentration of CF_3 species in the films.

Table 3-1. Percentages of CF_3, CF_2, CF, and C-CF species and F:C ratios as obtained from C-1s XPS for 10/100 pulsed films deposited from $C_2H_2F_4$, CH_2F_2, and $CHClF_2$. The C-CF species dominate for the films from $C_2H_2F_4$ and CH_2F_2, whereas CF_2 dominates in the film from $CHClF_2$. Almost equal concentrations of CF species are present in all the films, but the CF_3 concentration in the film from CH_2F_2 is roughly half of that in the films from $C_2H_2F_4$ and $CHClF_2$. The species distributions are dominated by the competition between CF_2-producing and HF elimination reactions, along with the role that the precursor F:H ratio plays in the concentration of free fluorine available to produce CF_3 species.

Precursor	% CF_3	% CF_2	% CF	% C-CF	F:C ratio
$C_2H_2F_4$	8	21	25	46	0.91
CH_2F_2	4	12	24	60	0.60
$CHClF_2$	7	39	24	30	1.22

consisting of approximately 46% C-CF, whereas the film from CH_2F_2 has approximately 60% C-CF. The film from $CHClF_2$ also shows a strong concentration of C-CF (~ 30%), but is dominated more by CF_2 (~ 39%), and in addition, contains a small fraction of Cl (~9%, excluded from calculated CF_x fractions). CF_2 species were also present in films from $C_2H_2F_4$ and CH_2F_2, but to a much smaller degree (21% and 12%, respectively). Finally, all three precursors produced films with approximately the same fraction of CF species, but films from CH_2F_2 had approximately half the number of CF_3 moieties as films from the other gases. These species distributions are significantly different from those obtained for films from HFPO (%CF_3 = 18, %CF_2 = 55, %CF = 14, %C-CF = 13, F:C = 1.78),[25] again highlighting the difference in deposition mechanisms between HFPO and these precursors.

While plasma decomposition mechanisms can differ from thermal ones, in some cases similar pathways are observed. For example, HFPO decomposition to CF_2 (Eqn. 1) occurs both upon heating[39] and in a plasma[26]. Indeed, films with high CF_2 fractions can be deposited from thermal and plasma CVD using HFPO as a precursor.[40] The three precursors studied here were chosen partly due to their reported ability to produce CF_2 species upon thermal decomposition:[29-35]

$$C_2H_2F_4 \longleftrightarrow H_2 + \left[C_2F_4 \longleftrightarrow 2CF_2\right] \quad (4)$$

$$CH_2F_2 \longleftrightarrow H_2 + CF_2 \quad (5)$$

$$CHClF_2 \longleftrightarrow HCl + CF_2 \quad (6)$$

In addition, HF elimination is a competing thermal decomposition pathway. For example,

$$CH_2F_2 \longrightarrow CHF + HF \qquad (7)$$

occurs in parallel with reaction (5).[41]

If similar reactions occur under plasma excitation, the higher ratios of CF_2:CF in the films deposited from $C_2H_2F_4$ and $CHClF_2$ suggest that the difluorocarbene forming reactions (4, 6) are favored over the HF elimination reactions for these two precursors. However, the high concentration of C-CF species in the films deposited from $C_2H_2F_4$ suggests that HF elimination also competes at a significant rate for this precursor:

$$C_2H_2F_4 \longrightarrow HF + C_2HF_3. \qquad (8)$$

In the case of CH_2F_2 the situation is reversed: the films' CF and C-CF concentrations are clearly dominant, suggesting that HF elimination is the primary decomposition pathway.

It is interesting to note that the two precursors for which HF elimination appears to be significant, $C_2H_2F_4$ and CH_2F_2, also give non-linear responses to increasing pulse on time (Fig. 3-4b). This non-linear behavior would be anticipated for complex reaction networks. In contrast, the precursors yielding CF_2-rich films, HFPO and $CHClF_2$, have linear increases in deposition rate with pulse on time (Fig. 3-4a).

The concentration of CF_3 groups in the films corresponds to the expected ease of generating free fluorine atoms in the pulsed plasma. Such free fluorine is capable of adding to CF_2 in the gas phase or at the surface to create CF_3.[42] CH_2F_2 pulsed plasmas would be expected to have the least free fluorine because of this precursor's low F:H

ratio. This assumption agrees with the observation that films from CH_2F_2 have the lowest CF_3 concentrations of the three films.

The role of the F:H ratio is also apparent from looking at the CH_x stretch region of the FTIR spectra of the three films. Figure 3-7 shows the FTIR spectra for the 10/100 pulsed films. CF_x species generally absorb from 980 - 1450 cm^{-1},[17] and CF_2 and CF stretches can be identified in each of the spectra. Of particular interest, however, is the C-H stretch region, which generally extends from 2850 - 2960 cm^{-1} for saturated hydrocarbons.[43] Figure 3-7 shows that the CH_x stretches are weak, indicating hydrogen concentrations in the films are low.

Figure 3-8 shows an expansion of the CH_x region for all three spectra. Doublets in both the $C_2H_2F_4$ and CH_2F_2 pulsed plasma films spectra indicate hydrogen incorporation into the films during deposition. The peaks are centered around 3093 and 2983 cm^{-1} for the film from $C_2H_2F_4$ and 3113 and 3008 cm^{-1} for the film from CH_2F_2, all of which are outside of the typical C-H stretch region for saturated hydrocarbons. However, the C-H stretch region for hydrofluorocarbons has been reported to be ~2879 - 2994 cm^{-1}.[44] Due to the high electronegativity of fluorine atoms, any C-H bond near a C-F bond (e.g., CF_x-CFH-CF_x) will be strengthened, resulting in an increase in the vibrational frequency, and thus, the absorption peak will be shifted to higher wavenumbers.[45] In addition, double-bonded carbons with hydrogen attachments (=C-H) absorb from 3020 - 3100 cm^{-1}.[43] Thus, the incorporated hydrogen is likely near fluorine or is attached to an unsaturated carbon. The CH_x signal for the film from $C_2H_2F_4$ is about half that of the film from CH_2F_2, consistent with the lower F:H ratio of the CH_2F_2. Even on the expanded scale of Figure 3-8, the film from $CHClF_2$ has no detectable H,

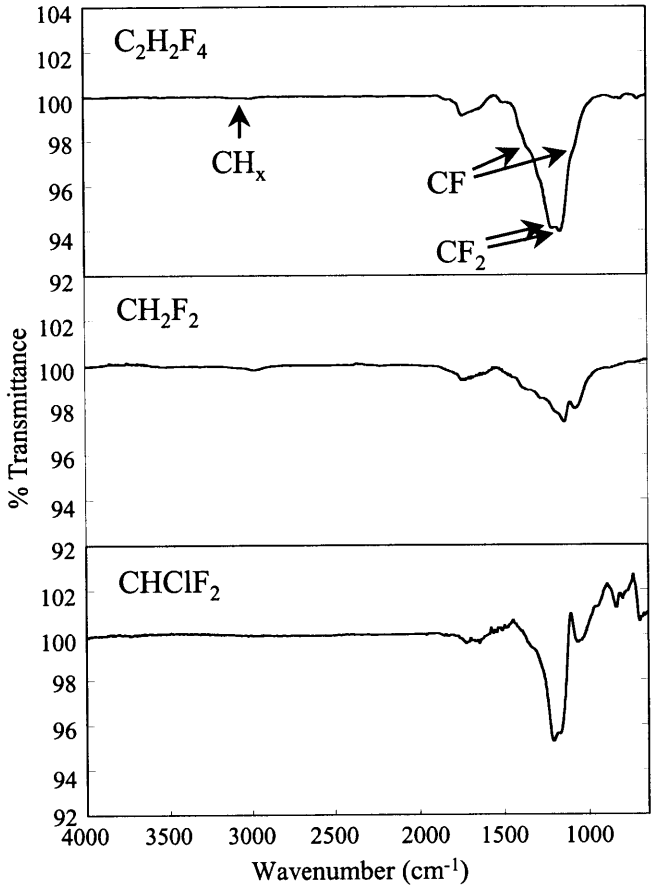

Figure 3-7: FTIR spectra of 10/100 films deposited from $C_2H_2F_4$, CH_2F_2, and $CHClF_2$. CF and CF_2 species are easily identified in all three spectra. CH_x stretches are only observed in pulsed plasma films from $C_2H_2F_4$ and CH_2F_2. All spectra were normalized to a film thickness of 1500 Å.

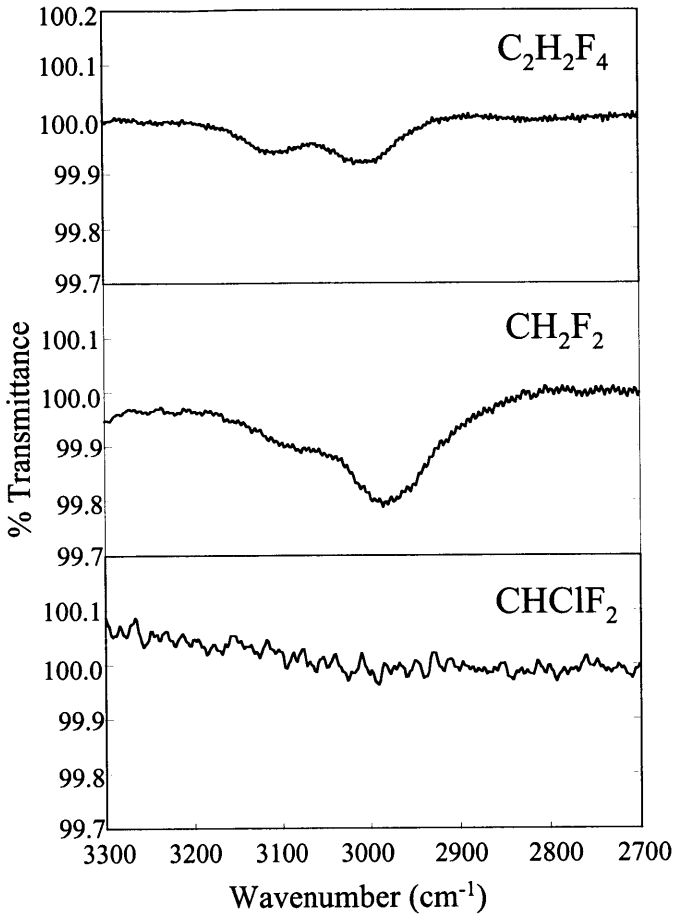

Figure 3-8: Expansion of CH_x region of FTIR spectra from Figure 3-7. The $C_2H_2F_4$ and CH_2F_2 spectra indicate the presence of hydrogen incorporated into the pulsed plasma films. The peaks are shifted to higher wavenumbers than typical saturated hydrocarbon C-H stretches due to the presence of fluorine and/or C=C double bonds.

indicating the HCl formation may strongly drive the formation of difluorocarbene from this precursor (Eqn. 6). This reasoning is also supported by the high $\%CF_2$ observed in the XPS of the film from $CHClF_2$ (Fig. 3-6).

Section 3.4.3: Electrical Properties

Table 3-2 lists the square of the refractive index (n^2), the dielectric constant (κ), and the loss tangent (tan δ) for films from HFPO, $C_2H_2F_4$, CH_2F_2, and $CHClF_2$. The dielectric constant of films from HFPO show a slight dependence on pulse conditions, decreasing slightly with increasing pulse off time for a constant on time,[10] but all give a dielectric constant of 2.0 ± 0.1. This value is very close to the minimum possible value as determined by the square of the refractive index.[46] For the films from HFPO, $n^2 = 1.84 \pm 0.02$. The dielectric constant for the HFPO pulsed plasma films is the same as that of bulk polytetrafluoroethylene (PTFE),[47] and is most likely due to the high CF_2 fractions in these films, also indicated by the high F:C ratio of these films (1.78).[17,25] The other three precursors give films with dielectric constants of 2.4, once again highlighting the difference in structure between the films from HFPO versus the other precursors. These dielectric constants are also quite close to their minimum values, as given by n^2.

All four precursors give films with loss tangents on the order of 10^{-2}, with the films from HFPO having the minimum loss out of the four (0.009). Minimizing tan δ is important since it reflects the loss of energy from an applied electric field due to defects and traps in the films.[19] Low dielectric loss, corresponding to low values of tan δ, is desired for high performance integrated circuit operation. The loss tangent of bulk PTFE is 0.0002,[47] so the tan δ of the films from HFPO is surprisingly close to that of bulk

Table 3-2. Electrical properties of films deposited from HFPO, $C_2H_2F_4$, CH_2F_2, and $CHClF_2$. The dielectric constants (κ) from films from all four precursors are close to their minimums, as given by the squares of their refractive indices (n^2). The loss tangents ($\tan \delta$) are all on the order of 10^{-2}, with the films from HFPO having the lowest $\tan \delta$. $\tan \delta$ of bulk PTFE is 0.0002, which is quite close to that of the pulsed HFPO films (0.009). These values of $\tan \delta$ are all quite low when considering that continuous plasma films usually give higher values due to the plasma damage incurred during processing.[48,49]

Precursor	n^2	κ	$\tan \delta$
HFPO	1.84 ± 0.02	2.0 ± 0.1	0.009
$C_2H_2F_4$	2.07 ± 0.04	2.4 ± 0.1	0.018
CH_2F_2	2.24 ± 0.02	2.4 ± 0.3	0.012
$CHClF_2$	2.25 ± 0.06	2.4 ± 0.2	0.012

PTFE when considering that the films from HFPO were plasma-polymerized versus deposited using traditional polymer synthesis techniques. Loss tangents from continuous plasma films tend to be higher than those of conventionally prepared polymer films (0.08 - 0.10 vs. 10^{-3} - 10^{-4}).[19,48,49] The pulsed plasma films improve upon the loss tangents of the continuous plasma films with tan δ's of 0.009 - 0.02.

Section 3.5: Conclusions

Films were deposited by pulsed-PECVD using three new precursors: $C_2H_2F_4$, CH_2F_2, and $CHClF_2$. All three precursors showed a dependence of deposition rate on pulse cycling conditions, with $C_2H_2F_4$ having the highest deposition rates (2800 Å/min. max.). Films from $C_2H_2F_4$ and CH_2F_2 were dominated by C-CF structures, with the relevant concentrations being 46 and 60%, respectively, for 10 /100 pulsed films. Films from $CHClF_2$ were almost equally composed of CF_2 and C-CF (39 and 30%, respectively), with lesser concentrations of CF_3 and CF. A small percentage (~9%) of Cl was also found in these films. Although the precursors were selected partially for their CF_2-forming ability, the competition between that reaction and HF elimination appears to be key in determining the distribution of CF_2, CF, and C-CF species. For these precursors, HF elimination appears to dominate strongly in CH_2F_2 pulsed plasmas (high C-CF concentration), and has decreasing importance for $C_2H_2F_4$ and $CHClF_2$ pulsed plasmas (in that order). In addition, the precursor F:H ratios play an important role in determining the concentration of free F in the pulsed plasma, and thus, the concentration of CF_3, as well as any incorporation of hydrocarbon species into the films. FTIR spectra of these same films show that a small amount of hydrogen was incorporated in films from

both $C_2H_2F_4$ and CH_2F_2, with the film from $C_2H_2F_4$ having a smaller absorbance than that from CH_2F_2. No hydrogen was detected in the films from $CHClF_2$. Finally, films from all three precursors were found to have dielectric constants of 2.4 with loss tangents on the order of 10^{-2}. Films from HFPO were found to have a slightly lower dielectric constant (2.0 ± 0.1) and loss tangent (0.009).

Section 3.6: Acknowledgments

The authors gratefully acknowledge the support of the Office of Naval Research, Lucent Technologies Bell Laboratories Graduate Research Program for Women, DuPont, and the NSF/SRC Engineering Research Center for Environmentally Benign Semiconductor Manufacturing. We would also like to thank Helen Maynard of Lucent Technologies Bell Laboratories for her help with the spectroscopic ellipsometry. This work made use of MRSEC Shared Facilities supported by the National Science Foundation under Award Number DMR-9400334.

Section 3.7: References

[1]P. Singer, Semicond. Intl. **17,** 52 (1994).

[2]R. K. Laxman, Semicond. Intl. **18,** 71 (1995).

[3]P. Singer, Semicond. Intl. **19,** 88 (1996).

[4]C. R. Savage, R. B. Timmons, and J. W. Lin, Chem. Mater. **3,** 575 (1991).

[5]C. R. Savage, R. B. Timmons, and J. W. Lin, in *Structure-Property Relations in Polymers: Spectroscopy and Performance*, Advances in Chemistry Series Vol. 236, Eds: M. W. Urban and C. D. Craver (ACS, Washington, 1993), p. 745.

[6]K. Endo, MRS Bull. **22,** 55 (1997).

[7]K. Endo and T. Tatsumi, J. Appl. Phys. **78,** 1370 (1995).

[8]K. Endo and T. Tatsumi, Appl. Phys. Lett. **68,** 2864 (1996).

[9]W. W. Lee and P. S. Ho, MRS Bull. **22,** 19 (1997).

[10]C. B. Labelle, S. J. Limb, K. K. Gleason, and J. A. Burns, *Characterization of Pulsed-Plasma Enhanced Chemical Vapor Deposited Fluorocarbon Thin Films* (DUMIC, Santa Clara, CA, 1997), p. 98.

[11]S. Wolf and R. N. Tauber, *Silicon Processing for the VLSI Era*, Vol. 2 (Lattice Press, Sunset Beach, CA, 1990).

[12]J. W. Coburn and H. F. Winters, J. Vac. Sci. Technol. **16,** 391 (1979).

[13]E. Kay, J. Coburn, and A. Dilks, in *Plasma Chemistry III*, Topics in Current Chemistry Vol. 94, Eds: S.Veprek and M. Venugopalan (Springer-Verlag, New York, 1980), p. 1.

[14]H. Yasuda and T. S. Hsu, J. Polym. Sci.: Polym. Chem. Ed. **15,** 2411 (1977).

[15]M. A. Butler, R. J. Buss, and A. Galuska, J. Appl. Phys. **70,** 2326 (1991).

[16]R. d'Agostino, F. Cramarossa, F. Fracassi, E. Desimoni, L. Sabbatini, P. G. Zambonin, and G. Caporiccio, Thin Solid Films **143,** 163 (1986).

[17]S. J. Limb, K. K. Gleason, D. J. Edell, and E. F. Gleason, J. Vac. Sci. Technol. A **15,** 1814 (1997).

[18]R. d'Agostino, P. Capezzuto, G. Bruno, and F. Cramarossa, Pure Appl. Chem. **57,** 1287 (1985).

[19]H. Yasuda, *Plasma Polymerization* (Academic Press, New York, 1985).

[20]H. Yasuda, J. Macromol. Sci.--Chem. **A10,** 383 (1976).

[21]N. Morosoff, B. Crist, M. Bumgarner, T. Hsu, and H. Yasuda, J. Macromol. Sci.--Chem. **A10,** 451 (1976).

[22]H. Yasuda and T. Hsu, J. Polym. Sci.: Polym. Chem. Ed. **15,** 81 (1977).

[23]S. Morita, G. Sawa, and M. Ieda, J. Macromol. Sci.--Chem. **A10,** 501 (1976).

[24]C. B. Labelle, S. J. Limb, and K. K. Gleason, J. Appl. Phys. **82,** 1784 (1997).

[25]S. J. Limb, D. J. Edell, E. F. Gleason, and K. K. Gleason, J. Appl. Polym. Sci. **67,** 1489 (1998).

[26]M. B. Knickelbein, D. A. Webb, and E. R. Grant, *New Devices for the Production of Intense Pulsed Jets of CF_2: Laser Spectroscopic Characterization* (MRS Symp. Proc., Boston, MA, 1984), Vol. 38, p. 23.

[27]S. J. Limb, C. B. Labelle, K. K. Gleason, D. J. Edell, and E. F. Gleason, Appl. Phys. Lett. **68,** 2810 (1996).

[28]C. B. Labelle, S. Karecki, R. Reif, and K. K. Gleason, J. Vac. Sci. Technol. A, (submitted) (1999).

[29]R. Martinez, F. Castano, M. N. S. Rayo, and R. Pereira, Chem. Phys. **172,** 349 (1993).

[30]G. E. Millward, R. Hartig, and E. Tschuikow-Roux, J. Phys. Chem. **75,** 3195 (1971).

[31]M.-C. Su, S. S. Kumaran, K. P. Lim, J. V. Michael, and A. F. Wagner, J. Phys. Chem. **100,** 15827 (1996).

[32]J. W. Edwards and P. A. Small, Nature, 1329 (1964).

[33]J. W. Edwards and P. A. Small, Ind. Eng. Chem. Fundam. **4,** 396 (1965).

[34]F. Gozzo and C. R. Patrick, Tetrahedron **22,** 3329 (1966).

[35]G. R. Barnes, R. A. Cox, and R. F. Simmons, J. Chem. Soc. B. Phys. Org. **6,** 1176 (1971).

[36]P. W. Atkins, *Physical Chemistry*, 4th ed. (W. H. Freeman and Company, New York, 1990).

[37]S. J. Limb, D. J. Edell, E. F. Gleason, and K. K. Gleason. (submitted to Chemistry of Materials).

[38]*Plasma Deposition, Treatment, and Etching of Polymers*, edited by R. d'Agostino (Academic Press, Boston, 1990).

[39]R. C. Kennedy and J. B. Levy, J. Fluorine Chem. **7,** 101 (1976).

[40]S. J. Limb, K. K. S. Lau, D. J. Edell, E. F. Gleason, and K. K. Gleason, Plasmas and Polymers, (submitted) (1999).

[41]S. F. Politanskii and V. U. Shevchuk, Kinet. Katal. **9,** 496 (1968).

[42]A. D. Tserepi, J. Derouard, J. P. Booth, and N. Sadeghi, J. Appl. Phys. **81,** 2124 (1997).

[43]J. McMurry, *Organic Chemistry*, 3rd ed. (Brooks/Cole, Pacific Grove, CA, 1992).

[44]M. J. Danilich, D. J. Burton, and R. E. Marchant, Vib. Spectrosc. **9,** 229 (1995).

[45]R. M. Silverstein, G. C. Bassler, and T. C. Morrill, *Spectroscopic Identification of Organic Compounds*, 5th ed. (Wiley, New York, 1991).

[46]L. Solymar and D. Walsh, *Lectures on the Electrical Properties of Materials* (Oxford University, New York, 1984).

[47]A. T. DiBenedetto, *The Structure and Properties of Materials* (McGraw-Hill, New York, 1967).

[48]J. A. Theil, F. Mertz, M. Yairi, K. Seaward, G. Ray, and G. Kooi, *Thermal Stability of a-C:F,H Films Deposited by Electron Cyclotron Resonance Plasma Enhanced Chemical Vapor Deposition* (MRS Symp. Proc., San Francisco, CA, 1997).

[49]J. A. Theil, G. Kooi, F. Mertz, G. Ray, and K. Seaward, *The Effect of Thermal Cycling on a-C:F,H Low Dielectric Constant Films Deposited by ECR Plasma Enhanced Chemical Vapor Deposition* (IITC, San Francisco, CA, 1998).

Chapter 4

FTIR of Effluents from Pulsed Plasmas of 1,1,2,2-$C_2H_2F_4$, HFPO, and CH_2F_2

(In press at Journal of Vacuum Science and Technology A in 1999 as "Fourier Transform Infrared Spectroscopy of Effluents from Pulsed Plasmas of 1,1,2,2-Tetrafluoroethane, Hexafluoropropylene Oxide, and Difluoromethane," by Catherine B. Labelle, Simon M. Karecki, Rafael Reif, and Karen K. Gleason)

Section 4.1: Abstract

Gas-phase Fourier Transform Infrared Spectroscopy (FTIR) has been used to analyze the effluents from $C_2H_2F_4$, hexafluoropropylene oxide (CF_3CFOCF_2, HFPO), and CH_2F_2 pulsed plasmas. A series of reference spectra for possible effluent species was used to identify the major species in each. The major species in pulsed $C_2H_2F_4$ plasmas were found to be: $C_2H_2F_4$, HF, C_2F_4, C_2HF_5, CHF_3, and SiF_4 (formed from free fluorine). For HFPO pulsed plasmas, the major effluents are: HFPO, CF_3COF, COF_2, C_2F_4, C_2F_6, CO, CF_4, and C_3F_8, whereas for CH_2F_2 pulsed plasmas the major effluents are: CH_2F_2, HF, SiF_4, and CHF_3. Reaction sets were postulated for each precursor to account for the observed effluents, and these sets were used to explain the trends of species concentrations with pulse on and pulse off time. In each case, most of the effluent concentration trends could be traced back to competition between dissociation pathways of a particular molecule. For both $C_2H_2F_4$ and CH_2F_2, the main reactions were the competition between CF_2-production and HF elimination from the original precursor. For $C_2H_2F_4$ pulsed plasmas, the competition between these pathways was found to be ~ 1:1, whereas for CH_2F_2 pulsed plasmas, the HF elimination pathway is dominant. For HFPO, the key reactions are the three dissociation pathways of CF_3COF, a main product of the initial dissociation of HFPO into CF_2 + CF_3COF. The global warming impact of each of the pulsed PECVD processes was gauged by the MMTCE (million metric tons of carbon equivalent) metric. CH_2F_2 pulsed plasmas were found to have the lowest MMTCE (min. = 2.1×10^6), whereas HFPO pulsed plasmas had the highest MMTCE (max = 7.7×10^7). For all three precursors, the MMTCE impact is reduced by decreasing the degree of plasma excitation through increasing the off time at a fixed on time.

Section 4.2: Introduction

Fluorocarbon plasmas are used extensively throughout the semiconductor industry in both etching and cleaning processes. [1,2] In addition, fluorocarbon plasmas are also being considered to deposit fluorocarbon thin films that can potentially be used as new, lower κ ($\kappa < 3$), interlayer dielectric materials.[3-5] These low-κ materials would yield reductions in propagation delay, power consumption, and cross-coupling noise between adjacent lines, all of which would enable the implementation of future generations of integrated circuit design rules. [6-9] In order to implement these new materials, however, a host of film property and processing requirements, many of which are often conflicting, must be met. [6-8] Therefore, an understanding of the plasma which generates a particular film is crucial in determining how that film forms and what properties will result from that formation pathway.

Typically, continuous plasma enhanced chemical vapor deposition (PECVD) is used to deposit films from a variety of fluorocarbon precursors. However, it has been observed that for continuous PECVD the effect of various processing parameters on film properties is minimal.[10,11] Additionally, very similar films can be obtained from a range of different fluorocarbon precursors, indicating that the choice of precursor is not as critical as would be assumed.[10,11] Rather, the excitation state of the plasma is sufficient to fracture various precursors into similar small components, regardless of the size of the original molecule (i.e., C_4F_8 vs. CF_4). Thus, similar films can be obtained from different precursor chemistries. This mode of operation makes it difficult to obtain a range of different film compositions and properties from the available fluorocarbon precursors.

An alternative to continuous PECVD is pulsed-PECVD, where the plasma is cycled between "on" and "off" states. In this process, rf power is applied for a specified "on" time, followed by an "off" period during which no excitation is used. During the "on" time, both ions and reactive neutrals are produced. However, since ions often have shorter lifetimes than neutrals, during the "off" time the ratio of neutrals to ions will increase, and thus, the process equilibrium will be shifted to favor film deposition from reactive neutrals. Therefore, the overall chemistry of these plasmas should be much more sensitive to the original precursor molecules than their continuous counterparts, and it should be possible to develop a range of fluorocarbon films with different film properties.

Pulsed plasma excitation has been reported to dramatically change the nature of deposited fluorocarbon films.[12-14] The composition of films from hexafluoropropylene oxide (CF_3CFOCF_2, HFPO) changes dramatically with pulse off time. At very short pulse off times (10 ms on, 20 - 60 ms off time) films contain almost equal fractions of CF_3, CF_2, CF, and quaternary carbon (C-CF), whereas at longer pulse off times, the film composition becomes increasingly dominated by CF_2.[12-15] These pulse-dependent changes in film composition might be attributed to the reduction in ion bombardment as the pulse duty cycle is decreased. However, it has been shown that the extent of these changes cannot be fully accounted for by ion bombardment alone. Rather, the changes in pulsed plasma chemistry must also be taken into account.[14]

The choice of precursor is also important for pulsed PECVD systems. It is known that the addition of hydrogen to a pure fluorocarbon system shifts the boundary between etching and deposition regimes.[11] 1,1,2,2-Tetrafluoroethane ($C_2H_2F_4$) and difluoromethane (CH_2F_2) both have the same absolute F:C ratio, but their F:H ratios are

different, and therefore distinctly different pulsed plasma films are obtained from these two precursors. Both pulsed PECVD films are dominated by C-CF (46 and 60%, respectively), but films from $C_2H_2F_4$ have almost double the CF_3 and CF_2 content of films from CH_2F_2 (CF_3 = 8 and 4%, CF_2 = 21 and 12%, respectively).[16] These changes are due to both pulse conditions and precursor choice (i.e., F:C,H ratios), and reflect the increased importance of neutral chemistry in the deposition process. Hence, an understanding of this neutral chemistry is extremely important in determining what types of films will result from a particular precursor.

The effluents of three different pulsed plasma systems (1,1,2,2-$C_2H_2F_4$, HFPO, and CH_2F_2) have been analyzed using gas-phase Fourier Transform Infrared Spectroscopy (FTIR). The main species in each effluent have been identified and the pulsed plasma chemistry has been inferred from them. Large differences in gas-phase effluent species have been found between the three precursors, highlighting the importance of the precursor choice for a process when using pulsed PECVD. The global warming impact of each of the pulsed deposition processes studied has been evaluated using the MMTCE (million metric tons of carbon equivalent) metric, which weights the effluent species by their respective global warming potentials. Differences in MMTCE are observed not only between processes using different precursors, but also as a function of the level of plasma excitation (i.e., pulse conditions) for processes using the same precursor.

Section 4.3: Experimental

Pulsed plasmas having on times of either 10 or 40 ms and pulse off times of 50, 100, or 400 ms were struck from pure $C_2H_2F_4$, HFPO, or CH_2F_2 in a parallel plate reactor system.[14,15] The powered electrode (11.4 cm diameter aluminum disk) and grounded electrode (11.4 cm aluminum cylinder) were spaced 1 inch apart, with samples placed on the grounded electrode. The total reactor volume excluding the electrode volume is 5100 cm^3, and the effective volume between the electrodes is 261 cm^3. An applied peak power of 280 W (2.7 w/cm^2) at 13.56 MHz was delivered to the powered electrode. Impedance matching was achieved with a manually adjusted LC network. A flow rate of 12.5 sccm was used for all three feed gases, with a pressure of 1000 mTorr. At each pulse condition, the reactor effluents were sampled from the final pump exhaust and fed through a gas-phase Fourier Transform Infrared Spectrometer (FTIR, see Figure 4-1). This FTIR spectrometer has previously been used to analyze effluents from plasma etching chemistries.[17] Duplicate measurements were taken at the pulse condition 10/100 ms on/ms off to check for reproducibility. Under all pulse conditions the residence time of the reactor (~1.5 s) was greater than the time for a single pulse.

Reactor effluents were diluted with N_2 to approximately 1600 ppm of the unreacted feed gas and fed into a Midac I-2000 FTIR spectrometer equipped with an absorption cell with zinc selenide windows having an optical path length of 1 cm. Data was acquired continuously at a rate of 9 spectra/min. over a range of 450-4500 cm^{-1} at room temperature and a cell pressure of ~ 600 Torr. Each spectrum consisted of an average of 4 scans. The FTIR signal was allowed to stabilize before striking the plasma, and the plasma was maintained until the new effluent signal stabilized. Due to the use of a wet pump, average times for stabilization of the effluent signal were approximately 10-

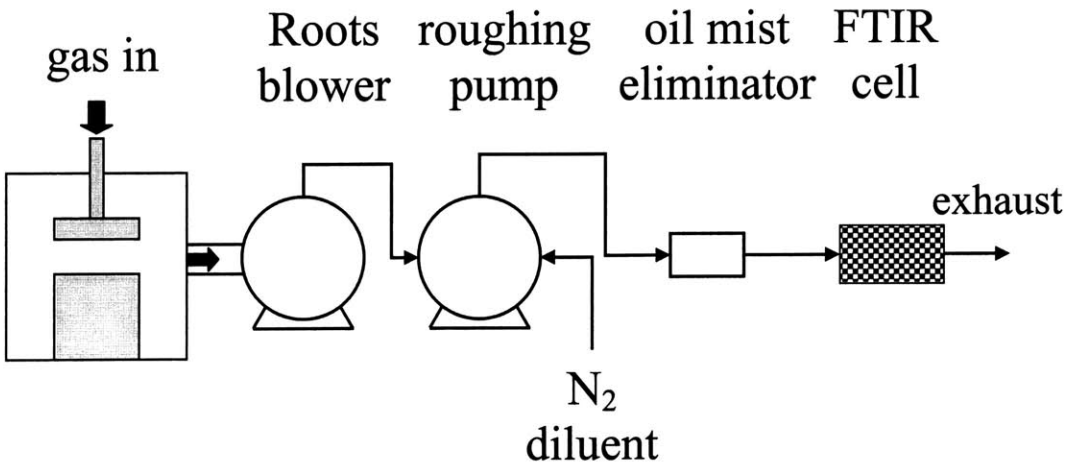

Figure 4-1: Schematic of pulsed PECVD system with effluent FTIR apparatus in place. Effluent from the pulsed plasma exits the chamber, exhausts through both a Roots blower and a roughing pump, and is fed to an FTIR absorption cell with an optical path length of 1 cm. N_2 diluent is added at the roughing pump to reduce effluent concentrations to ~ 1600 ppm. An oil mist eliminator was added before the FTIR cell to prevent hydrocarbons from the pump oil from contaminating the FTIR cell.

15 minutes. The effluent concentrations reported here are for the stabilized signal. MMTCE numbers reported are for a 1 minute sampling of the pulsed plasma effluent after stabilization.

The results were analyzed using reference spectra obtained in our lab or from libraries maintained by Midac, Hanst, Aldrich, and DuPont. For each of the three feed gases studied the set of species expected in the effluent was identified. The corresponding set of reference spectra served as the input to AutoQuant, a gas phase FTIR analysis program available from Midac, which would then perform a least squares regression to determine the concentration of each species in the effluent. Results were only accepted if the residual differences between the experimental and the regressed spectral intensities were 1 - 3 orders of magnitude below the original spectral intensities. In some cases, it was necessary to add species to the analysis method in order to achieve a satisfactory fit. Reference spectra found to not contribute to the statistical goodness of the fit were removed from the analysis method. For example, molecules containing oxygen were found to be insignificant in the analysis of the $C_2H_2F_4$ and CH_2F_2 pulsed plasma effluent spectra. Table 4-1 lists the species used in the final regressions for $C_2H_2F_4$, HFPO and CH_2F_2 pulsed plasma effluents. Note that several anticipated effluents, such as H_2 and F_2, are not IR active and thus can not be detected by this methodology.

The reference FTIR spectra measured for $C_2H_2F_4$, HFPO, and CH_2F_2 are shown in Figure 4-2. The flow rates and dilution levels in N_2 for Figs. 4-2a-c are 12.5 sccm $C_2H_2F_4$ diluted to1638 ppm, 23 sccm HFPO diluted to 4998 ppm, 12.5 sccm CH_2F_2 diluted to 5386 ppm, respectively. At these conditions, each spectrum has a maximum

Table 4-1. Set of species considered as potential effluents from pulsed plasmas of $C_2H_2F_4$, HFPO, and CH_2F_2. For each species, the source of the reference spectrum is listed.

$C_2H_2F_4$		**HFPO**		**CH_2F_2**	
Effluent	Source	Effluent	Source	Effluent	Source
$C_2H_2F_4$	this work	HFPO	this work	CH_2F_2	this work
CH_2F_2	this work	CO	Hanst	C_2F_4	DuPont
C_2F_4	DuPont	CO_2	Hanst	C_3F_6	Midac
C_3F_6	Midac	C_3F_6O	Aldrich	HF	Midac
HF	Midac	C_2F_4	DuPont	C_2F_6	Midac
C_2HF_5	Midac	CF_3COF	DuPont	CF_4	Midac
C_2F_6	Midac	COF_2	Midac	C_3F_8	Midac
CF_4	Midac	C_3F_6	Midac	SiF_4	Midac
C_3F_8	Midac	HF	Midac	CHF_3	Midac
SiF_4	Midac	C_2F_6	Midac		
CHF_3	Midac	CF_4	Midac		
		C_3F_8	Midac		
		SiF_4	Midac		

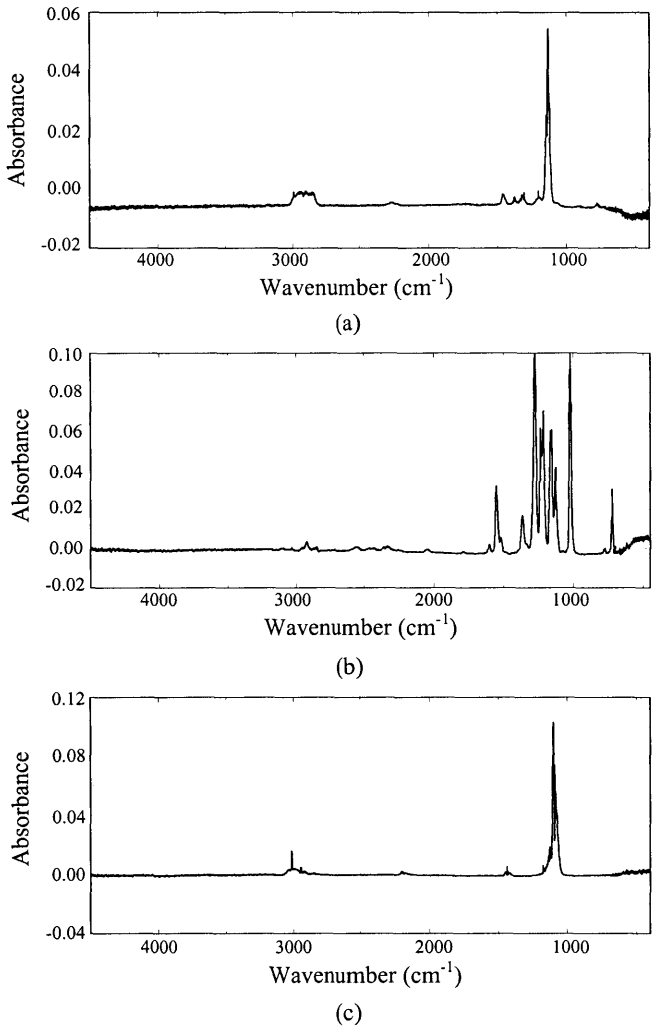

Figure 4-2: Reference spectra for pure (a) 1,1,2,2-$C_2H_2F_4$, (b) HFPO, and (c) CH_2F_2. The flow rates and dilution levels in N_2 are 12.5 sccm $C_2H_2F_4$ diluted to 1638 ppm, 23 sccm HFPO diluted to 4998 ppm, 12.5 sccm CH_2F_2 diluted to 5386 ppm. At these conditions, each spectrum has a maximum absorbance of ~ 0.1.

absorbance of ≤ 0.1. The global warming impact of the effluent was determined by calculating the MMTCE (million metric tons of carbon equivalent) metric for each pulsed plasma condition. The MMTCE is a standard metric defined by the Environmental Protection Agency (EPA) and is used in the reporting of perfluorocompound (PFC) emissions in the semiconductor industry.[17-19] It is defined as:

$$MMTCE = \frac{(\text{kg effluent X})\left(\frac{\text{MW C}}{\text{MW CO}_2}\right)(\text{GWP100 effluent X})}{1 x 10^9} \qquad (1)$$

where MW = molecular weight and GWP100 = global warming potential (GWP) at an integrated time horizon of 100 years. GWP data can be obtained from the literature.[20] The MMTCE of each effluent stream was calculated by summing the contributions from each species in the stream.

Section 4.4: Results

Figures 4-3 and 4-4 show the effluent concentrations for six different pulsed $C_2H_2F_4$ plasma conditions. The major effluents, in approximate order of high to low concentration, are: $C_2H_2F_4$, HF, C_2F_4, C_2HF_5, CHF_3, and SiF_4. Minor effluents (maximum concentration < 5% of initial $C_2H_2F_4$ concentration) consist of CF_4, C_2F_6, and C_3F_8. SiF_4 was detected due to the presence of a Si wafer fragment in the reactor during the sampling period, and will be considered as a measure of the free F present in the pulsed plasmas.

Increasing off time at a fixed on time corresponds to reducing the power input to the reactor. Thus, as expected, increasing off time for a pulse on time of 10 ms, results in more unreacted $C_2H_2F_4$ and less decomposition products in the effluent (Fig. 4-3a).

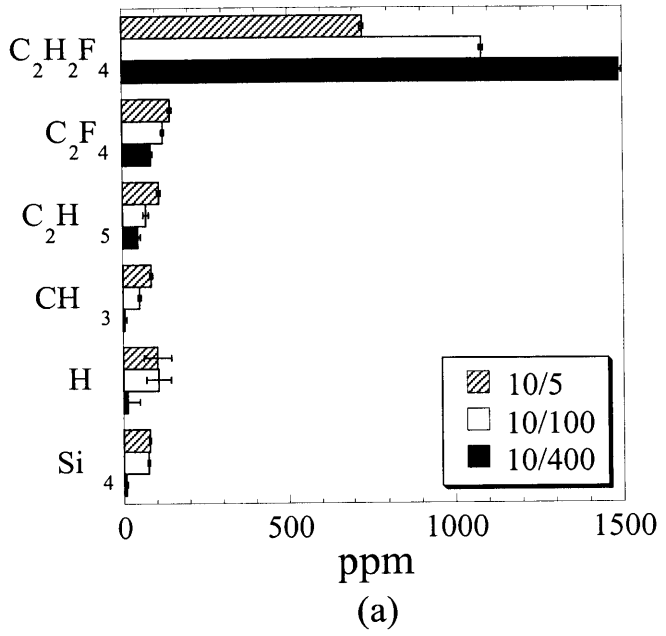

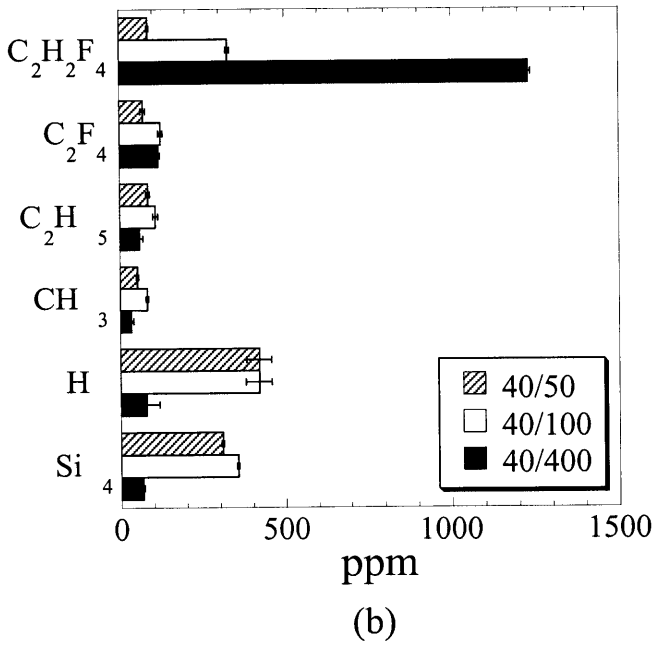

Figure 4-3: $C_2H_2F_4$ pulsed plasma effluent concentrations shown as a function of pulse off time for on times of (a) 10 ms, and (b) 40 ms. Major effluents are: $C_2H_2F_4$, HF, C_2F_4, C_2HF_5, CHF_3, and SiF_4. Minor effluents consist of CF_4, C_2F_6, and C_3F_8. SiF_4 was detected due to the presence of a Si wafer fragment in the reactor during the sampling period, and will be considered as a measure of the free F present in the pulsed plasmas. Increasing off time at a fixed on time corresponds to reducing the power input to the reactor, and hence, results in more unreacted $C_2H_2F_4$ and less decomposition products in the effluent (Fig. 4-3a). However, at the longer 40 ms on time, the response of the non-$C_2H_2F_4$ effluents change, with each concentration going through a maximum before decreasing at longer pulse off times (Fig. 4-3b).

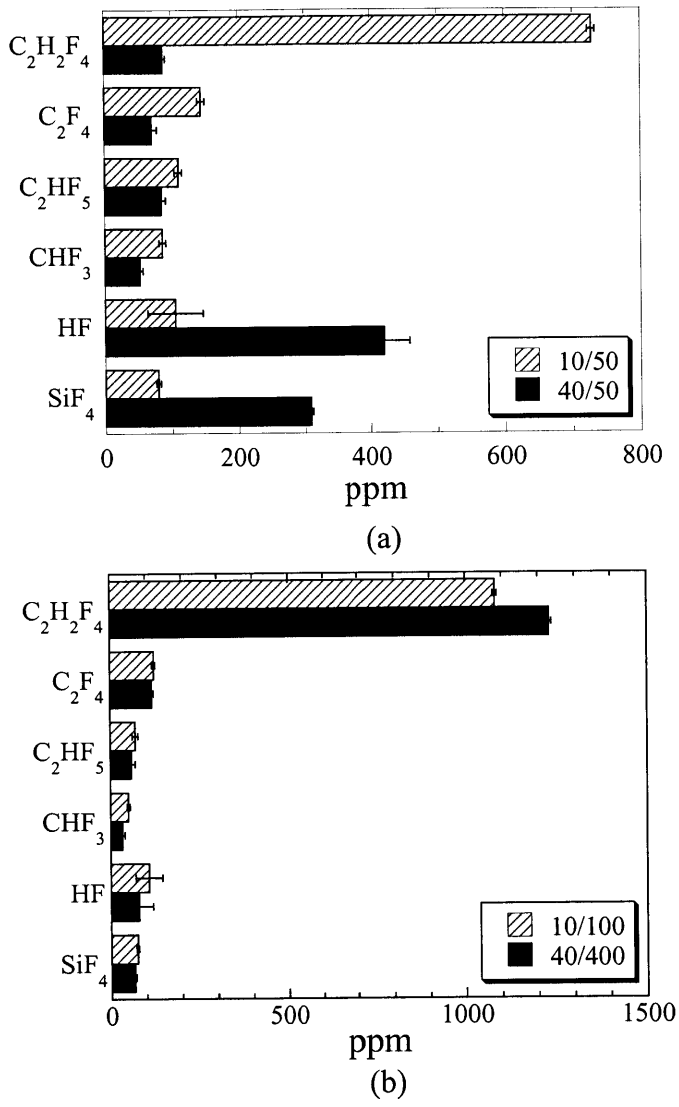

Figure 4-4: (a) $C_2H_2F_4$ pulsed plasma effluent concentrations shown as a function of pulse on time for a pulse off times of 50 ms. Increased on time leads to increased dissociation of $C_2H_2F_4$, as well as increased fracturing of secondary products of the initial dissociation ($[C_2F_4]$ decreases, but [HF] increases). (b) Pulsed plasma effluents for two different pulse conditions with the same duty cycle. Differences in effluent concentrations indicate the pulsing is not producing solely an average power effect. Rather, the duration of the pulse cycle itself is critical.

However, at the longer 40 ms on time, the response of the non-$C_2H_2F_4$ effluents changes, with each concentration going through a maximum before decreasing at longer pulse off times (Fig. 4-3b). The effect of increasing pulse on time is seen explicitly in Fig. 4-4a, where [C_2F_4], [C_2HF_5], and [CHF_3] all decrease, while [HF] and [SiF_4] increase. Effluent concentrations differed at two conditions having the same plasma duty cycle, 10/100 and 40/400 (Fig. 4-4b). Thus, average power is not the only variable controlling the plasma decomposition kinetics. The duration of the pulse cycle is also a critical factor in determining pulsed plasma composition.

Figures 4-5 and 4-6 show the effluent concentrations from five of the six pulsed HFPO plasma conditions measured. Under all conditions, the major effluents are HFPO, CF_3COF, COF_2, C_2F_4, C_2F_6, CO, CF_4, and C_3F_8. Minor effluents (max. concentration < 5% of initial HFPO concentration) consisted of C_3F_6 and, for the 10/50 and 40/50 conditions, CO_2.

For a constant on time of 10 ms, most of the decomposition product concentrations vary inversely with the effluent [HFPO] as pulse off time is increased, but [C_2F_4] and [CF_3COF] show more complex behavior. Identical trends were observed when the pulse on time was held constant at 40 ms (not shown). In contrast, when pulse on time is increased at a constant off time, most of the concentrations vary in proportion with the effluent [HFPO] (Fig. 4-6a). Again, [C_2F_4] and [CF_3COF] behave differently, varying inversely with effluent [HFPO] as pulse on time is increased. These same trends were observed for all three pulse off times. Furthermore, as was seen in the $C_2H_2F_4$ results, pulsed HFPO plasmas with the same duty cycle do not produce the same effluent

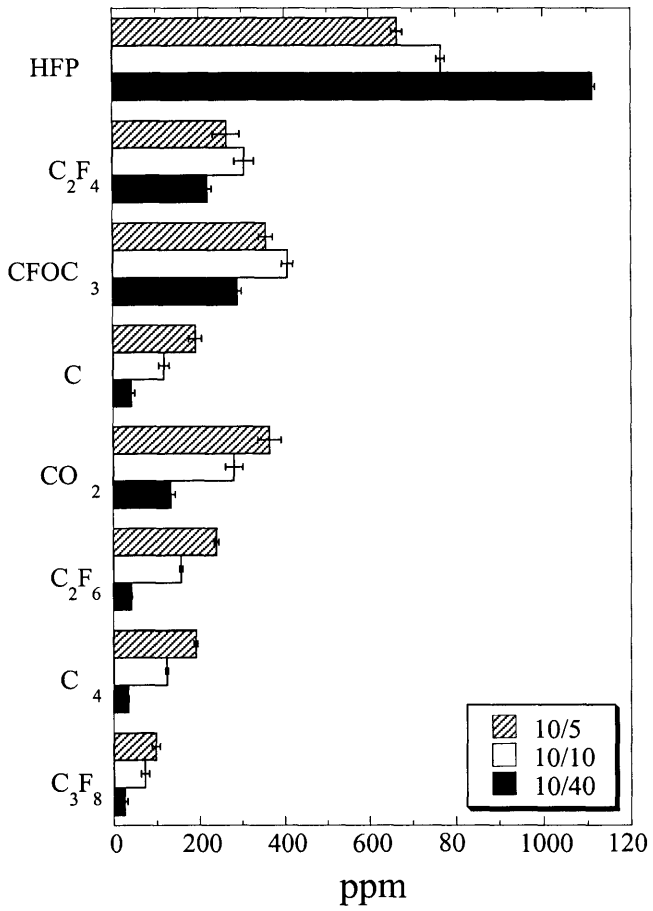

Figure 4-5: HFPO pulsed plasma effluent concentrations shown as a function of pulse off time for an on time of 10 ms. Major effluents are: HFPO, CF_3COF, COF_2, C_2F_4, C_2F_6, CO, CF_4, and C_3F_8. Minor effluents consisted of C_3F_6 and, for the 10/50 and 40/50 conditions, CO_2. Most of the decomposition product concentrations vary inversely with the effluent HFPO concentration as pulse off time is increased, but [C_2F_4] and [CF_3COF] show more complex behavior. Identical trends were observed when the pulse on time was held constant at 40 ms (not shown).

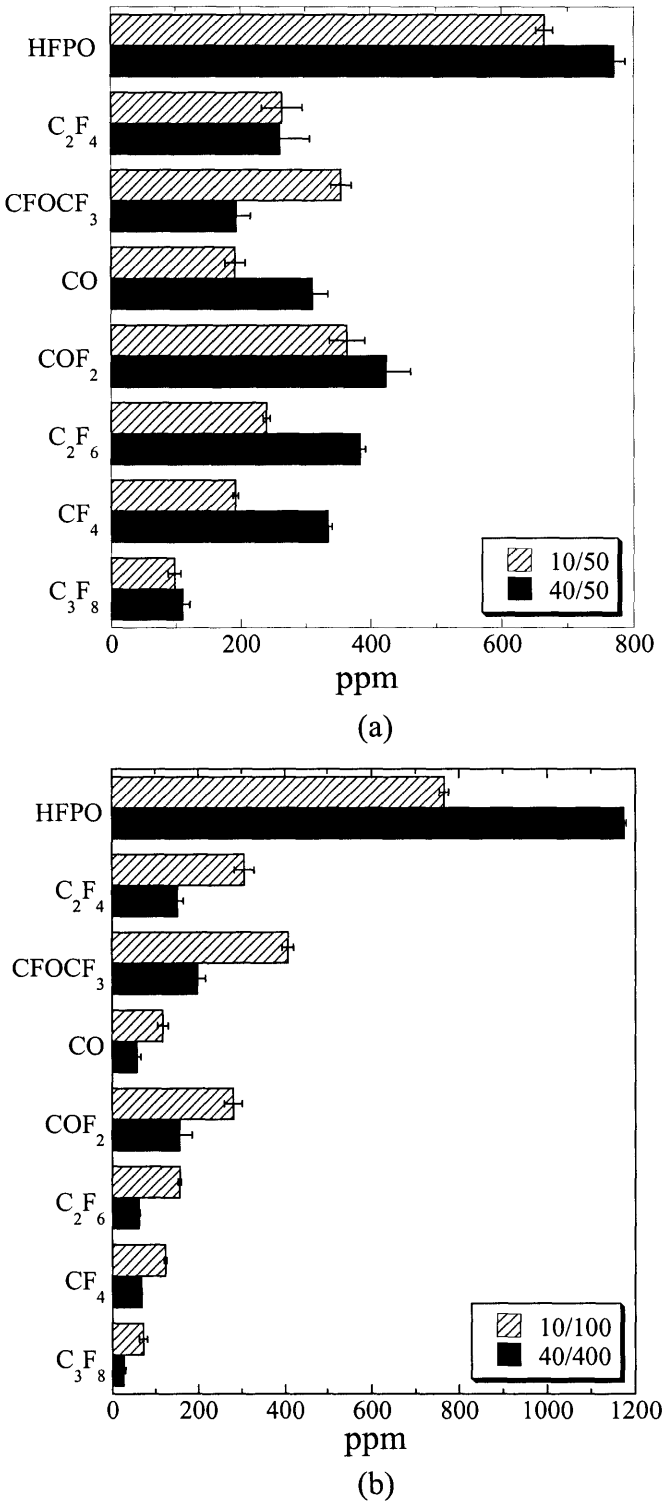

Figure 4-6: (a) HFPO pulsed plasma effluent concentrations shown as a function of pulse on time for a pulse off time of 50 ms. Most of the concentrations vary in proportion with the effluent [HFPO], but, as in Fig. 4-5, [C_2F_4] and [CF_3COF] behave differently, varying inversely with effluent [HFPO] as pulse on time is increased. These same trends were observed for all three pulse off times. (b) Pulsed plasma effluent concentrations shown for two different pulse conditions with the same duty cycle. As with $C_2H_2F_4$, pulsed HFPO plasmas with the same duty cycle do not produce the same effluent concentrations, indicating that the duration of the pulse on and off times are important in determining the overall pulsed plasma chemistry.

concentrations (Fig. 4-6b), indicating that the duration of the pulse on and off times are important in determining the overall pulsed plasma chemistry.

Finally, Figure 4-7 shows the effluent concentrations for three CH_2F_2 pulsed plasma conditions. For all three, the major effluents consisted of CH_2F_2, HF, SiF_4, and CHF_3. Minor effluents (max. concentration < 4% of initial CH_2F_2 concentration) included C_3F_6 and CF_4.

When pulse off time is increased at a constant on time, both [HF] and [CHF_3] vary inversely with the effluent [CH_2F_2], while [SiF_4] shows a slight increase (Fig 4-7a). In contrast, [HF] and [SiF_4] vary inversely with [CH_2F_2], while [CHF_3] is proportional to [CH_2F_2] when pulse on time is increased at a constant pulse off time (Fig. 4-7b).

Section 4.5: Discussion

Section 4.5.1: $C_2H_2F_4$

Based on the effluent species identified via FTIR, a minimal reaction set can be formulated to account for the presence of each compound. Table 4-2 shows the reaction set for the $C_2H_2F_4$ pulsed plasmas (effluent species identified by FTIR are in **bold**). The table lists each postulated reaction along with literature references for studies of that particular reaction under thermal or photolytic conditions. It is assumed that if a reaction occurs under thermal or photolytic conditions, it is also feasible under the excitation conditions present in a pulsed plasma. This assumption has been tested and holds for at least one reaction (decomposition of HFPO to CF_2 + CF_3COF).[21]

The primary reactions in the $C_2H_2F_4$ scheme are the two competing dissociation pathways of $C_2H_2F_4$, producing either C_2F_4 + H_2 or C_2HF_3 + HF (reactions (2-1) and (2-

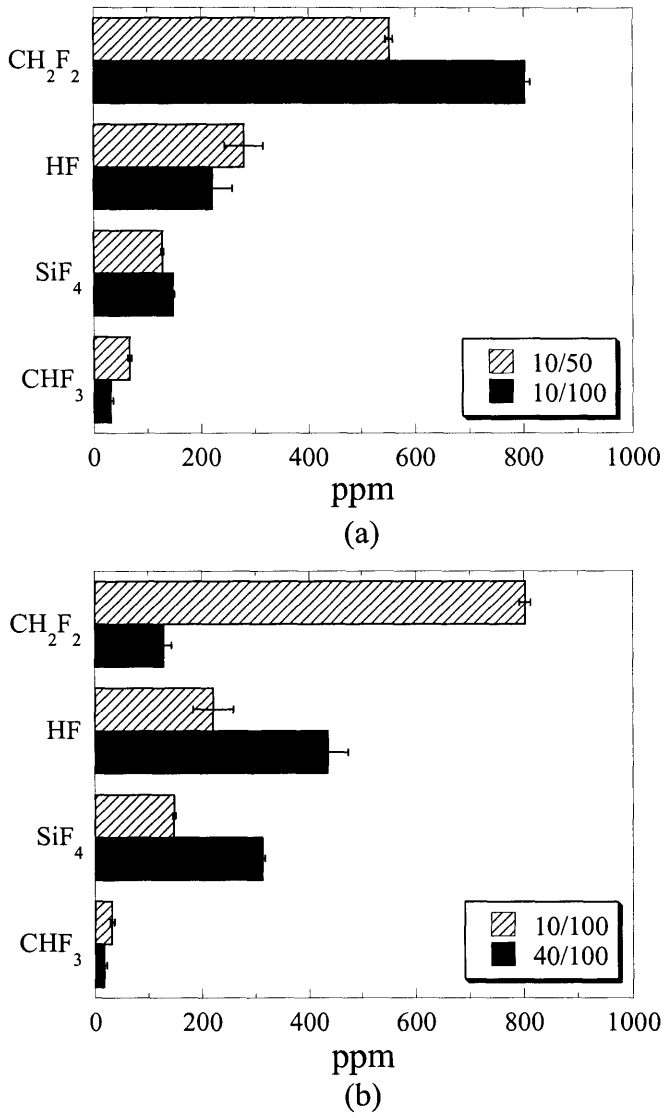

Figure 4-7: CH_2F_2 pulsed plasma effluent species concentrations as a function of (a) pulse off time (t_{on} = 10 ms) and (b) pulse on time (t_{off} = 100 ms). Major effluents consisted of CH_2F_2, HF, SiF_4, and CHF_3. Minor effluents included C_3F_6 and CF_4. Both [HF] and [CHF_3] vary inversely with the effluent [CH_2F_2], while [SiF_4] shows a slight increase with increasing pulse off time (t_{on} = constant, Fig. 4-7a). In contrast, [HF] and [SiF_4] vary inversely with [CH_2F_2], while CHF_3 is proportional to [CH_2F_2] when pulse on time is increased at a constant pulse off time (Fig. 4-7b).

Table 4-2. Reaction set for $C_2H_2F_4$. Effluent species detected via FTIR are shown in **bold**. The table lists each postulated reaction along with literature references for studies of that particular reaction under thermal or photolytic conditions.[22,25-36] It is assumed that if a reaction occurs under thermal or photolytic conditions, it is also feasible under the excitation conditions present in a pulsed plasma.

Reaction	Reference		Equation No.
$C_2H_2F_4 \rightarrow H_2 + \mathbf{C_2F_4}$	Millward	(25)	(2-1)
$C_2H_2F_4 \rightarrow \mathbf{HF} + C_2HF_3$	Burgess	(22)	(2-2)
	Tschuikow-Roux	(26)	
	Millward	(25)	
$C_2F_4 \rightarrow 2CF_2$	Burgess	(22)	(2-3)
	Kennedy & Levy	(27)	
	Batey & Trenwith	(28)	
	Dalby	(29)	
	Politanskii	(30)	
	Schug	(31)	
	Edwards	(32)	
	Atkinson & Trenwith	(33)	
	Hidaka	(34)	
	Millward	(25)	
$HF \rightarrow H + \mathbf{F}$	Burgess	(22)	(2-4)
$C_2F_4 + HF \rightarrow \mathbf{C_2HF_5}$	Burgess	(22)	(2-5)
	Tschuikow-Roux	(26)	
$CF_2 + HF \rightarrow \mathbf{CHF_3}$	Burgess	(22)	(2-6)
	Politanskii	(30)	
	Schug	(31)	
	Hidaka	(34)	
	Plumb & Ryan	(35)	
$CF_2 + F \rightarrow CF_3$	Plumb & Ryan	(35)	(2-7)
$CF_3 + F \rightarrow \mathbf{CF_4}$	Burgess	(22)	(2-8)
	Plumb & Ryan	(35)	
$2CF_3 \rightarrow \mathbf{C_2F_6}$	Burgess	(22)	(2-9)
	Weibel	(36)	
	Dalby	(29)	
	Hidaka	(34)	
	Tschuikow-Roux	(26)	
$C_2F_6 + CF_2 \rightarrow \mathbf{C_3F_8}$	Batey & Trenwith	(28)	(2-10)

2)). Figure 4-8 shows the calculated % conversion of $C_2H_2F_4$ increases linearly with duty cycle for all the pulse conditions investigated here. This suggests that these two dissociation reactions occur primarily in the forward direction during the on period. All of the remaining effluent species are then formed by secondary or tertiary reactions of the products of these initial dissociations.

The reaction set can also be used to suggest the origins of the observed trends with both pulse off and on time. A schematic of the major reactions in the $C_2H_2F_4$ reaction set is shown in Figure 4-9. The degree of competition between pathways I and II can be judged by looking at Fig. 4-3a. At a given off time, the ratio of $[C_2F_4]$ to [HF], the main observable products of the dissociation pathways, is about one (taking into account error bars) for all of the 10 ms on pulse conditions. Therefore, the ratio of pathways I:II is ~1:1. $[HF] >> [C_2F_4]$ at a pulse on time of 40 ms (Fig. 4-4a), but increasing on time should not change the degree of competition between pathways I and II. Rather, an additional HF source must be present. This source can be identified as the further dissociation of C_2HF_3 (dotted pathway in Fig. 4-9):[22]

$$C_2HF_3 \rightarrow C_2F_2 + HF\,. \qquad (2\text{-}11)$$

Reaction (2-11) was not included in Table 4-2 since a reference spectrum for C_2F_2 was not available during analysis, and thus, C_2F_2 was not measured directly. Since Rxn. (2-11) requires the dissociation of first $C_2H_2F_4$ and then C_2HF_3, during the brief on time of 10 ms, the second dissociation may not occur to an appreciable extent. When the on time is increased, however, Rxn. (2-11) can proceed to a greater degree, thus producing the observed increase in [HF].

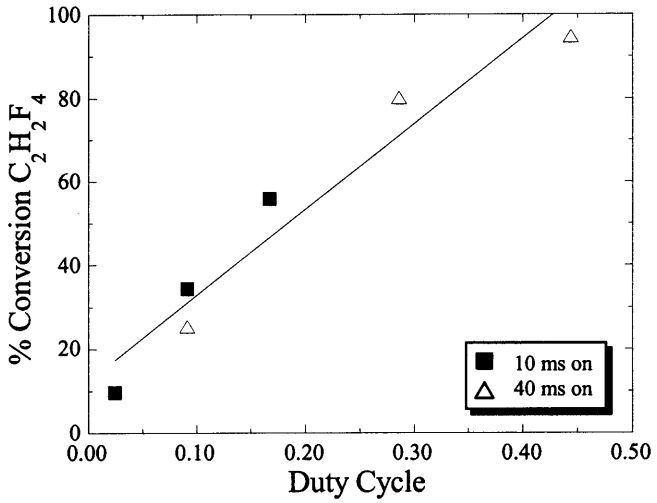

Figure 4-8: Percent conversion of $C_2H_2F_4$ as a function of duty cycle. Although the fractional conversion is not numerically equal to duty, it is linear with duty cycle. This suggests that these two dissociation reactions ((2-1) & (2-2)) occur primarily in the forward direction during the on period.

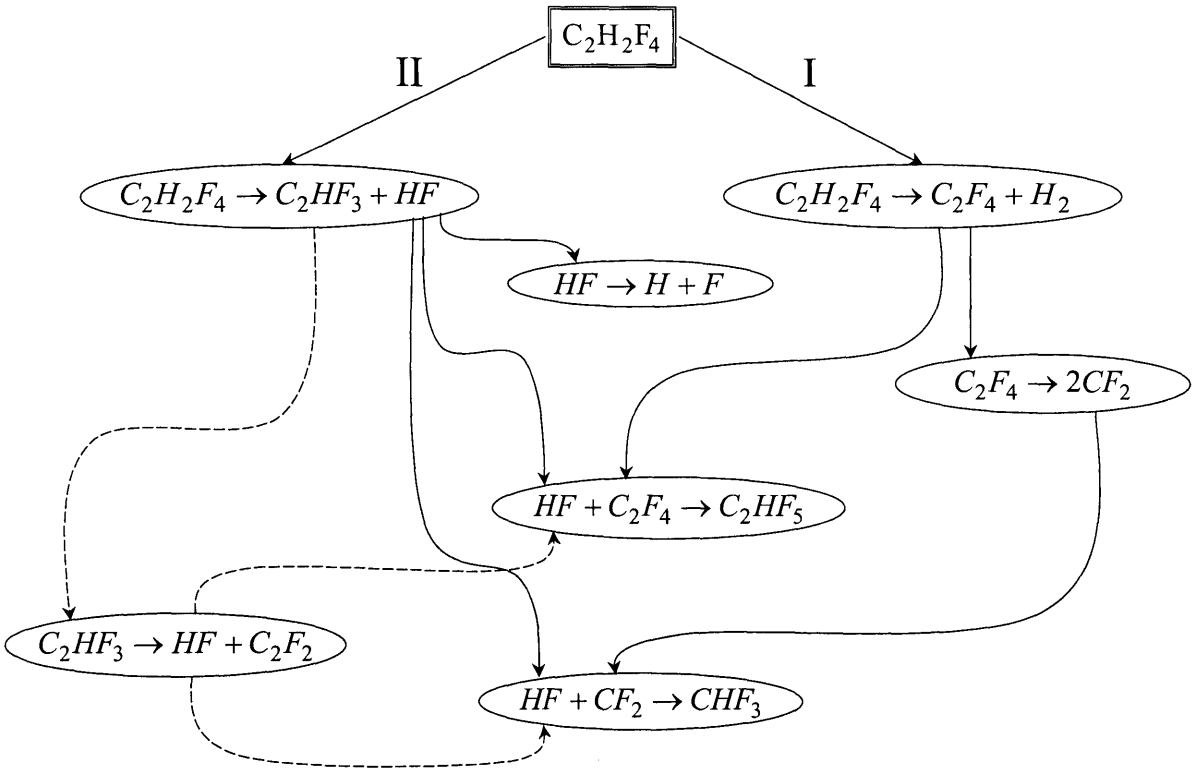

Figure 4-9: Schematic of the major reaction pathways for $C_2H_2F_4$ pulsed plasma species. Pathway I leads to CF_2-dependent species, whereas pathway II leads to HF-dependent species. Both C_2HF_5 and CHF_3 are dependent on pathways I and II. The further dissociation of C_2HF_3 (dotted lines) only occurs during long on times and is partly responsible for the large increase in [HF] observed at t_{on} = 40 ms. Comparison of [HF]/[C_2F_4] at a short on time indicates that the competition between pathways I and II is ~1:1.

After the initial dissociations via I and II, all other effluent products rely on reactions involving C_2F_4 and/or HF. At 10 ms on, many of these secondary and tertiary reactions can not proceed to a significant extent, and so most product concentrations will be inversely proportional to $[C_2H_2F_4]$ (i.e., Fig. 4-3a). However, at increased on times, these reactions will become more important (i.e., Rxn. (2-11)), leading to intermediates which are not only produced, but consumed in significant quantities. Thus, the concentrations of these intermediates will go through a maximum (Fig. 4-3b).

Section 4.5.2: HFPO

As with $C_2H_2F_4$, a reaction scheme can be assembled to account for the HFPO pulsed plasma effluents, and it is presented in Table 4-3. In contrast with $C_2H_2F_4$, there is only one primary dissociation pathway for HFPO (Rxn. 3-1; Rxn. 3-14 is minimal). However, Figure 4-10 shows that % HFPO conversion versus duty cycle is not linear, and therefore, Rxn. 3-1 must be reversible:

$$C_3F_6O \leftarrow CF_2 + CFOCF_3 \qquad (3\text{-}1')$$

Due to this reversibility, $[CF_3COF]$ and $[C_2F_4]$ (formed from CF_2, Rxn. (3-2)) will have a more complex response to pulse conditions than the other species (i.e., maxima observed in response to increased pulse off time).

The main reactions of interest in this scheme are the three dissociation pathways for CF_3COF (Rxn. (3-3) $\rightarrow$ (3-5)), which are in competition with each other. Figure 4-11 shows the % change in [CO], $[C_2F_6]$, and $[CF_4]$ as pulse off time is increased. All three species show almost identical concentration changes when comparing 50 with 100 ms off and 100 with 400 ms off, indicating that one particular reaction underlies all of their

Table 4-3. Reaction set for HFPO. Effluent species detected via FTIR are shown in **bold**. The table lists each postulated reaction along with literature references for studies of that particular reaction under thermal or photolytic conditions.[21,22,25-38]

Reaction	Reference		Equation No.
$C_3F_6O \rightarrow CF_2 + CF_3COF$	Kennedy & Levy	(27)	(3-1)
	Knickelbein	(21)	
$2CF_2 \rightarrow \mathbf{C_2F_4}$	Burgess	(22)	(3-2)
	Kennedy & Levy	(27)	
	Batey & Trenwith	(28)	
	Dalby	(29)	
	Politanskii	(30)	
	Schug	(31)	
	Edwards	(32)	
	Atkinson & Trenwith	(33)	
	Millward	(25)	
$CF_3COF \rightarrow CFO + CF_3$	Weibel	(36)	(3-3)
$CF_3COF \rightarrow \mathbf{COF_2} + CF_2$	Batey & Trenwith	(28)	(3-4)
$CF_3COF \rightarrow \mathbf{CO} + \mathbf{CF_4}$	Weibel	(36)	(3-5)
$2CF_3 \rightarrow \mathbf{C_2F_6}$	Burgess	(22)	(3-6)
	Weibel	(36)	
	Dalby	(29)	
	Hidaka	(34)	
	Tschuikow-Roux	(26)	
$CF_4 + CF_2 \rightarrow \mathbf{C_2F_6}$	Burgess	(22)	(3-7)
$C_2F_6 + CF_2 \rightarrow \mathbf{C_3F_8}$	Batey & Trenwith	(28)	(3-8)
$C_2F_4 + CF_2 \rightarrow \mathbf{C_3F_6}$	Batey & Trenwith	(28)	(3-9)
	Atkinson & Atkinson	(37)	
$CF_2 + F \rightarrow CF_3$	Plumb & Ryan	(35)	(3-10)
$CF_3 + F \rightarrow \mathbf{CF_4}$	Burgess	(22)	(3-11)
	Plumb & Ryan	(35)	
$CFO \rightarrow \mathbf{CO} + F$	Burgess	(22)	(3-12)
$CFO + F \rightarrow \mathbf{COF_2}$	Burgess	(22)	(3-13)
$C_3F_6O \rightarrow \mathbf{C_3F_6} + O$	Shapovalov	(38)	(3-14)
$CO + O \rightarrow \mathbf{CO_2}$	Burgess	(22)	(3-15)

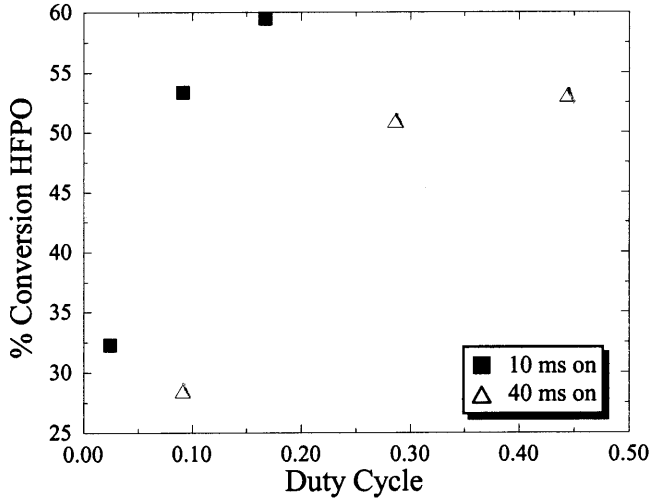

Figure 4-10: Percent conversion of HFPO as a function of duty cycle. The response with duty cycle is clearly non-linear, indicating that the initial dissociation of HFPO (Rxn. 3-1) must be reversible. Due to this reversibility, [CF_3COF] and [C_2F_4] (formed from CF_2, Rxn. (3-2)) will have a more complex response to pulse conditions than the other species (i.e., maxima observed in response to increased pulse off time).

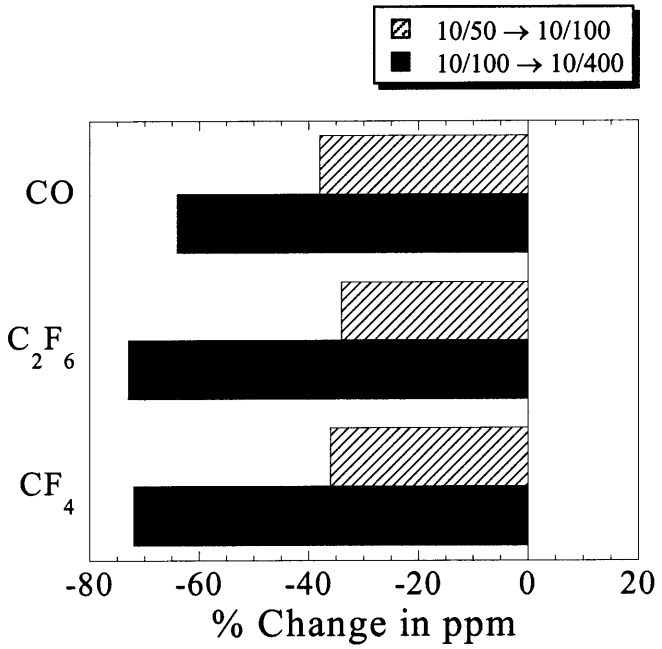

Figure 4-11: Percent change in [CO], [C_2F_6], and [CF_4] as pulse off time is increased. All three species show almost identical concentration changes when comparing 50 with 100 ms off and 100 with 400 ms off, indicating that one particular reaction underlies all of their formation pathways. This common reaction is Rxn. (3-3), one of the dissociation pathways of CF_3COF.

formation pathways. Looking at Table 4-3, it is evident that all three species are possible derivatives of either CFO or CF_3, which are the products of CF_3COF dissociation pathway (3-3). Therefore, Rxn. (3-3) must be one of the dominant pathways out of the three. In contrast, Rxn. (3-5) must be a minor dissociation pathway since, although it produces CO and CF_4, this pathway does not disrupt the correlation between CO, CF_4, and C_2F_6. [COF_2] is generally higher than [CO], [C_2F_6], and [CF_4], indicating that although COF_2 can be formed from the products of Rxn. (3-3), there must be a secondary source; namely, Rxn. (3-4). Rxn. (3-4) also produces CF_2, which can then contribute to many of the secondary and tertiary reactions in the system. The interaction between these dissociation pathways can also be observed via C_3F_8: [C_3F_8] follows the same general trend as CO, C_2F_6, and CF_4, but since it is also dependent on CF_2 for its formation (Rxn. (3-8)), it does not show exactly the same response as displayed in Fig. 4-11.

From this discussion, it is possible to explain the concentration trends observed for both pulse on and pulse off times. From Fig. 4-6a, it is evident that increased on time leads to an increase in recombination reaction (3-1') to form HFPO. Therefore, [CF_3COF] will decrease due to both consumption in Rxn. (3-1') and increased dissociation via Rxns. (3-3) $\rightarrow$ (3-5) due to the increased on time. [C_2F_4] decreases (more evident at 100 and 400 ms off times, not shown) for similar reasons. All of the other species formed from CF_3COF and CF_2 show increased concentrations with pulse on time due to the increased dissociation of CF_3COF.

From Fig. 4-5, most of the effluent concentrations are inversely proportional to [HFPO]. However, since Rxn. (3-1') is present, this behavior is actually more closely linked to the dissociation of CF_3COF. At short off times, CF_3COF dissociation proceeds

to a significant degree, leading to large concentrations of its secondary products. As off time is increased (i.e., 100 ms), the pulses will still be frequent enough to promote HFPO dissociation with ease, but the secondary reactions do not proceed as readily, and thus, [CF_2] and [CF_3COF] decrease. If the off time becomes sufficiently long, the overall reduction in HFPO dissociation will then dominate the observed effluent concentrations, leading to even lower concentrations of secondary products.

Section 4.5.3: CH_2F_2

The reaction set for CH_2F_2 is presented in Table 4-4. Similar to $C_2H_2F_4$, there are two competing dissociation pathways for CH_2F_2 (Rxns. (4-1) and (4-2)). Figure 4-12 shows the % CH_2F_2 conversion versus duty cycle. As with $C_2H_2F_4$, although the fractional conversion is not equal to duty, the response is linear, indicating that neither Rxn. (4-1) or (4-2) proceeds significantly in the reverse direction.

It is clearly evident from Fig. 4-7a,b that Rxn. (4-1) is the dominant pathway. C_2F_4, the most definitive measure of the production of significant [CF_2] for both HFPO and $C_2H_2F_4$, is not present in any of the measured CH_2F_2 pulse effluents. The only evidence that reaction (4-2) is proceeding at all is the slight concentrations of CHF_3 observed, which is formed by combination of CF_2 and HF (Rxn. 4-4). The trends with pulse on and off time follow simply from these observations. Increased off time leads to less dissociation of CH_2F_2, and therefore a decrease in [HF] and [CHF_3]. Longer on times allow for increased dissociation of CH_2F_2, leading to increased [HF]. Note that the [HF] increases ~10% more than [CH_2F_2] decreases in Fig. 4-7b. This may be due to the further reaction of CHF,[23]

Table 4-4. Reaction set for CH_2F_2. Effluent species detected via FTIR are shown in **bold**. The table lists each postulated reaction along with literature references for studies of that particular reaction under thermal or photolytic conditions.[22,28,30,31,34,35,37,39]

Reaction	Reference		Equation No.
$CH_2F_2 \rightarrow CHF + \mathbf{HF}$	Burgess	(22)	(4-1)
	Politanskii	(30)	
	Schug	(31)	
$CH_2F_2 \rightarrow CF_2 + H_2$	Burgess	(22)	(4-2)
	Martinez	(39)	
$HF \rightarrow H + \mathbf{F}$	Burgess	(22)	(4-3)
$CF_2 + HF \rightarrow \mathbf{CHF_3}$	Burgess	(22)	(4-4)
	Politanskii	(30)	
	Schug	(31)	
	Hidaka	(34)	
	Plumb & Ryan	(35)	
$C_2F_4 + CF_2 \rightarrow \mathbf{C_3F_6}$	Batey & Trenwith	(28)	(4-5)
	Atkinson & Atkinson	(37)	
$CF_2 + F \rightarrow CF_3$	Plumb & Ryan	(35)	(4-6)
$CF_3 + F \rightarrow \mathbf{CF_4}$	Burgess	(22)	(4-7)
	Plumb & Ryan	(35)	

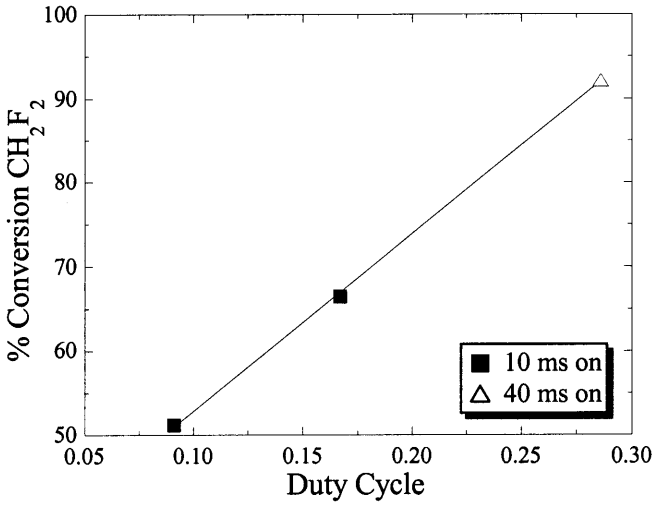

Figure 4-12: Percent conversion of CH_2F_2 as a function of duty cycle. As with $C_2H_2F_4$, although the % conversion is not equal to the duty, the response is linear, indicating that reactions (4-1) and (4-2) are not proceeding significantly in the reverse direction.

$$CHF \rightarrow C + HF \qquad (4\text{-}8)$$

which would provide a secondary source of HF to the system. The decrease in [CHF_3] with on time may be due to Rxns. (4-6) and (4-7), which consume CF_2 and lead to the formation of CF_4, seen only at 40 ms on time.

Reaction (4-8) could also account for the lack of C detected in the effluent (CHF_3 is the only non-CH_2F_2 C-containing product observed by the FTIR). Films deposited from CH_2F_2 pulsed plasmas are predominately composed of quaternary carbon (C-CF), which can also account for some of the missing gas phase carbon.[16] Optical emission spectroscopy measurements also indicate the presence of C_2 species in the pulsed plasma, which would not be detectable via FTIR.[24]

Section 4.5.4: MMTCE

Figure 4-13 shows the calculated MMTCE metrics for the pulse conditions observed for each feed gas. In each plot the contribution of each global warming gas in the effluent is shown. Although the concentrations of many of the identified global warming components are minor compared to other species in the effluent, their large global warming potentials translate into large contributions to the overall MMTCE. The total MMTCE for $C_2H_2F_4$ pulsed plasmas varied from 2.1×10^7 to 1.6×10^7, with the major contributors shifting from $C_2H_2F_4$ and CHF_3 at 10 ms on, to CHF_3 and C_2F_6 at 40 ms on. For HFPO, there are only three contributing species to the MMTCE (C_2F_6, CF_4, and C_3F_8), and the C_2F_6 contribution is dominant at all conditions. The total MMTCE for HFPO pulsed plasmas varied from 7.7×10^7 to1.0×10^7. For CH_2F_2, the major contributing species is CHF_3, leading to total MMTCE's varying from 7.0×10^6 to 2.1 x

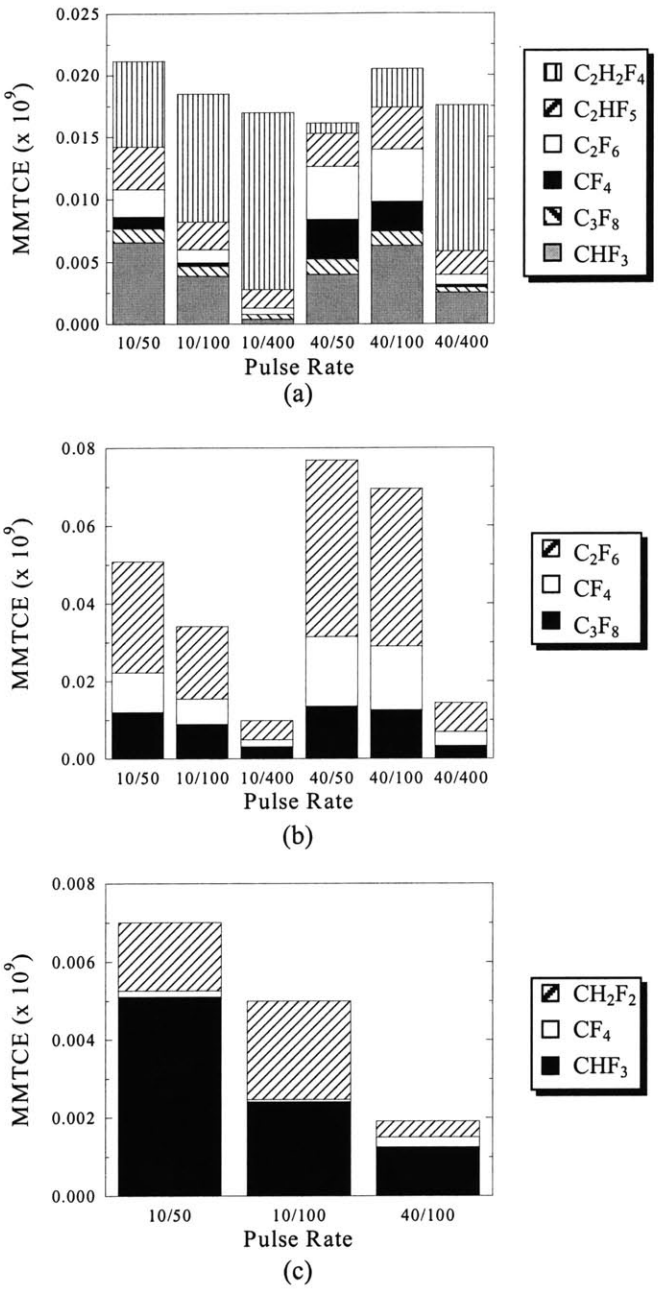

Figure 4-13: Calculated MMTCE metrics for the pulse conditions observed for (a) $C_2H_2F_4$, (b) HFPO, and (c) CH_2F_2. In each plot the contribution of each global warming gas in the effluent is shown. The total MMTCE for $C_2H_2F_4$ pulsed plasmas varied from 2.1×10^7 to 1.6×10^7, those for HFPO varied from 7.7×10^7 to1.0×10^7, whereas those for CH_2F_2 varied from 7.0×10^6 to 2.1×10^6. CH_2F_2 pulsed plasmas produce the most environmentally friendly effluents of the three feed gases, although, for all three precursors, the MMTCE impact is reduced by decreasing the degree of plasma excitation through increasing the off time at a fixed on time.

10^6. Comparing the three sets of MMTCE's, it is evident that CH_2F_2 pulsed plasmas produce the most environmentally friendly effluents of the three feed gases. For all three precursors, the MMTCE impact is reduced by decreasing the degree of plasma excitation through increasing the off time at a fixed on time. Note that all of the MMTCE values reported here are less than those reported for a typical C_3F_8 etch process (1 minute process time),[18] and several orders of magnitude less than those reported for a standard C_2F_6 cleaning process.[17]

Section 4.6: Conclusions

Gas-phase Fourier Transform Infrared Spectroscopy (FTIR) has been used to analyze the effluents of pulsed plasmas from $C_2H_2F_4$, HFPO, and CH_2F_2. The major species in pulsed $C_2H_2F_4$ plasmas were found to be: $C_2H_2F_4$, HF, C_2F_4, C_2HF_5, CHF_3, and SiF_4 (produced by free fluorine). For HFPO pulsed plasmas, the major effluents are: HFPO, CF_3COF, COF_2, C_2F_4, C_2F_6, CO, CF_4, and C_3F_8, whereas for CH_2F_2 pulsed plasmas the major effluents are: CH_2F_2, HF, SiF_4, and CHF_3. Reaction sets were postulated for each precursor to account for the observed effluents, and these sets were used to explain the trends of species concentrations with pulse on and pulse off time. In each case, most of the effluent concentration trends could be traced back to competing dissociation pathways for a particular molecule. For both $C_2H_2F_4$ and CH_2F_2, the main reactions were the competition between CF_2-production and HF elimination from the original precursor (Rxns. (2-1) & (2-2), (4-1) & (4-1)), with the competition about 1:1 for $C_2H_2F_4$ pulsed plasmas, whereas HF elimination is dominant for CH_2F_2 pulsed plasmas.

For HFPO, the key reactions are the dissociation pathways of CF_3COF (Rxns. (3-3) $\rightarrow$ (3-5)). The order of dominance was found to be: (3-3) >> (3-4) > (3-5). The global warming impact of each of the pulsed PECVD processes was evaluated via the MMTCE metric. CH_2F_2 pulsed plasmas were found to have the lowest MMTCE (min. = 2.1 x 10^6), whereas HFPO pulsed plasmas had the highest MMTCE (max = 7.7 x 10^7). For all three precursors, the MMTCE impact is reduced by decreasing the degree of plasma excitation through increasing the off time at a fixed on time.

Thus, precursor decomposition can be limited by controlling pulsed plasma conditions. This accentuates the impact of precursor selection on the gas phase composition within the pulsed-PECVD reactor. Average power is not the only variable controlling the plasma decomposition kinetics. The dynamics resulting from the chemical kinetics of the competing serial and parallel decomposition pathways over the duration of the pulse cycle are also crucial.

Section 4.7: Acknowledgments

The authors gratefully acknowledge the financial support of the Office of Naval Research, Lucent Technologies Bell Laboratories Graduate Research Program for Women, and the NSF/SRC Engineering Research Center for Environmentally Benign Semiconductor Manufacturing. We would also like to thank DuPont for donation of the feed gases used in this study.

Section 4.8: References

[1]S. Wolf, *Silicon Processing for the VLSI Era*, Vol. 2 (Lattice Press, Sunset Beach, CA, 1990).

[2]S. M. Sze, *VLSI Technology* (McGraw-Hill Book Company, New York, 1983).

[3]K. Endo and T. Tatsumi, Appl. Phys. Lett. **68,** 2864 (1996).

[4]K. Endo, MRS Bull. **22,** 55 (1997).

[5]J. A. Theil, G. Kooi, F. Mertz, G. Ray, and K. Seaward, *The Effect of Thermal Cycling on a-C:F,H Low Dielectric Constant Films Deposited by ECR Plasma Enhanced Chemical Vapor Deposition* (IITC, San Francisco, CA, 1998).

[6]P. Singer, Semicond. Intl. **17,** 52 (1994).

[7]R. K. Laxman, Semicond. Intl. **18,** 71 (1995).

[8]P. Singer, Semicond. Intl. **19,** 88 (1996).

[9]L. Peters, Semicond. Intl. **21,** 64 (1998).

[10]H. Yasuda, *Plasma Polymerization* (Academic Press, New York, 1985).

[11]*Plasma Deposition, Treatment, and Etching of Polymers*, edited by R. d'Agostino (Academic Press, Boston, 1990).

[12]C. R. Savage, R. B. Timmons, and J. W. Lin, Chem. Mater. **3,** 575 (1991).

[13]C. R. Savage, R. B. Timmons, and J. W. Lin, in *Structure-Property Relations in Polymers: Spectroscopy and Performance*, Advances in Chemistry Series Vol. 236, Eds: M. W. Urban and C. D. Craver (ACS, Washington, 1993), p. 745.

[14]S. J. Limb, D. J. Edell, E. F. Gleason, and K. K. Gleason, J. Appl. Polym. Sci. **67,** 1489 (1998).

[15]S. J. Limb, K. K. Gleason, D. J. Edell, and E. F. Gleason, J. Vac. Sci. Technol. A **15,** 1814 (1997).

[16]C. B. Labelle and K. K. Gleason, J. Vac. Sci. Technol. A **17,** 445 (1999).

[17]L. C. Pruette, S. M. Karecki, R. Reif, J. G. Langan, S. A. Rogers, R. J. Ciotti, and B. S. Felker, J. Vac. Sci. Technol. A **16,** 1577 (1998).

[18]S. Karecki, L. Pruette, R. Reif, L. Beu, T. Sparks, and V. Vartanian, J. Vac. Sci. Technol. A **16,** 2722 (1998).

[19]EPA, "National Air Pollutant Emission Trends, 1900-1996," Report No. EPA-454/R-97-011 (1997).

[20]AFEAS, "Alternative Fluorocarbons Environmental Acceptability Study," (1996).

[21]M. B. Knickelbein, D. A. Webb, and E. R. Grant, *New Devices for the Production of Intense Pulsed Jets of CF_2: Laser Spectroscopic Characterization* (MRS Symp. Proc., Boston, MA, 1984), Vol. 38, p. 23.

[22]D. R. Burgess, Jr., M. R. Zachariah, W. Tsang, and P. R. Westmoreland, Prog. in Energy Comb. Sci. **21,** 453 (1996).

[23]C.-p. Tsai and D. L. McFadden, J. Phys. Chem. **93,** 2471 (1989).

[24]C. B. Labelle and K. K. Gleason. (Work in progress).

[25]G. E. Millward, R. Hartig, and E. Tschuikow-Roux, J. Phys. Chem. **75,** 3195 (1971).

[26]E. Tschuikow-Roux, G. E. Millward, and W. J. Quiring, J. Phys. Chem. **75,** 3493 (1971).

[27]R. C. Kennedy and J. B. Levy, J. Fluorine Chem. **7,** 101 (1976).

[28]W. Batey and A. B. Trenwith, J. Chem. Soc. **28,** 1388.

[29]F. W. Dalby, J. Chem. Phys. **41,** 2297 (1964).

[30]S. F. Politanskii and V. U. Shevchuk, Kinet. Katal. **9,** 496 (1968).

[31]K. P. Schug, H. G. Wagner, and F. Zabel, Ber. Bunsenges. Phys. Chem. **83,** 167 (1979).

[32]J. W. Edwards and P. A. Small, Nature**,** 1329 (1964).

[33]B. Atkinson and A. B. Trenwith, J. Chem. Soc., 2082 (1953).

[34]Y. Hidaka, T. Nakamura, and H. Kawano, Chem. Phys. Lett. **187,** 40 (1991).

[35]I. C. Plumb and K. R. Ryan, Plasma Chem. Plasma Process **6,** 11 (1986).

[36]D. E. Weibel, C. M. d. Vohringer, E. H. Staricco, and E. R. d. Staricco, J. Photochem. Photobiol. A: Chem. **63,** 1 (1992).

[37]B. Atkinson and V. A. Atkinson, J. Chem. Soc., 2086 (1957).

[38]V. V. Shapovalov, V. A. Poluektov, and N. A. Ryabinin, Kinetics and Catalysis **32,** 947 (1992).

[39]R. Martinez, F. Castano, M. N. S. Rayo, and R. Pereira, Chem. Phys. **172,** 349 (1993).

Chapter 5

Surface Morphology of PECVD Fluorocarbon Thin Films from HFPO, 1,1,2,2-$C_2H_2F_4$, and CH_2F_2

(In press at Journal of Applied Polymer Science in 1999 as "Surface Morphology of PECVD Fluorocarbon Thin Films from Hexafluoropropylene Oxide, 1,1,2,2-Tetrafluoroethane, and Difluoromethane," Catherine B. Labelle and Karen K. Gleason.)

Section 5.1: Abstract

Atomic Force Microscopy (AFM) measurements have been made on a series of fluorocarbon films deposited from pulsed plasmas of hexafluoropropylene oxide (HFPO), 1,1,2,2-tetrafluoroethane ($C_2H_2F_4$), and difluoromethane (CH_2F_2). All of the films give images showing nodular growth ("cauliflower" appearance), with the size and distribution of the nodules dependent upon both the precursor, the degree of surface modification to which the growing film is exposed, and the substrate surface. Films deposited from $C_2H_2F_4$ showed clusters of smaller nodules around larger nodules, whereas films deposited from CH_2F_2 were characterized by a uniform distribution of smaller nodules, and films deposited from HFPO had the largest observed nodules. Movchan and Demchishin's structure zone model was applied to the observed films, which were all found to be zone 1 structures, indicating that film growth is dominated by shadowing effects. Increased substrate temperature and incident power per nm of film deposited results in decreased rms roughness, consistent with greater atomic mobility during deposition. Larger nodules in the fluorocarbon films developed on silicon wafer substrates than on rougher Al-coated substrates. Advancing contact angles for all of the films were found to be higher than that of PTFE (108°), indicating both hydrophobic and rough surfaces. Specifically, contact angles of films deposited from HFPO were found to increase with pulse off time, the same trend observed for both the CF_2 fraction of the film and the rms roughness.

Section 5.2: Introduction

Fluorocarbon thin films are currently under investigation for a variety of applications, including biomaterials and semiconductor dielectrics.[1-4] All of these applications would benefit from analysis of the deposited films' surface structure and morphology. Surface morphology influences parameters such as wettability and adhesion, and can affect both the conformality of a particular coating and its etching characteristics (i.e., preferential etching in a particular direction).

Atomic force microscopy (AFM) has been used extensively to study the surfaces of polymers, plasma-deposited polymers, and plasma-modified polymers.[5-13] AFM is especially suited to polymer analysis due to the low applied forces in contact mode, which can be further reduced by using tapping mode. These low forces allow the film surface to be imaged without modification by the force of the AFM tip on the surface.[14] The surfaces of bulk polymers including poly(tetrafluoroethylene), polypropylene, polysulfone, and polyimides, as well as organic thin films grown by a variety of deposition techniques, have been studied using AFM.[5,7,9-11,13]

This paper focuses on fluorocarbon films deposited using a pulsed-modulated radio frequency plasma (pulsed-plasma enhanced chemical vapor deposition, pulsed-PECVD). Recent work with pulsed fluorocarbon plasmas has shown that significant compositional control can be achieved for deposition from some precursors, and in all cases, the role of the precursor chemistry is significantly more important than for continuous plasma PECVD.[15-17] The range of fluorocarbon film compositions achieved

through pulse modulation leads to a range of film materials properties, resulting in the possibility of a range of surface morphologies and surface properties.

AFM measurements have been made on films deposited from pulsed plasmas of hexafluoropropylene oxide (HFPO), 1,1,2,2-tetrafluoroethane ($C_2H_2F_4$), and difluoromethane (CH_2F_2). Roughness analyses have been performed on the resulting data, and the effect of the pulse modulation on the surface features has been explored. Contact angles measurements have also been performed to test the wettability of the fluorocarbon films as a function of both deposition precursor and the pulse conditions.

Section 5.3: Experimental

Pulsed PECVD films were deposited on both silicon (Si) and sputtered aluminum-coated (~1000 Å) Si wafers. The pulse on time was either 10 or 40 ms, and the pulse off time was in the range between 20 and 400 ms. A flow rate of 12.5 sccm was used for 1,1,2,2-$C_2H_2F_4$ and CH_2F_2, whereas 23 sccm was used for HFPO, all with a peak rf power of 2.7 W/cm^2 at 1000 mTorr in a parallel plate reactor. Previous work shows changing the HFPO flow rate from 12.5 to 23 sccm has little impact on film deposition rate and composition.[15] The wafers were cooled on the backside with water at ~23°C.

Atomic force microscopy (AFM) was used to determine surface roughness, the height of surface features, and the overall appearance of the surface. A Digital Instruments Dimension 3000 AFM was used in tapping mode with a standard etched silicon tip to study 2 μm x 2 μm areas on the surface of each film. Tapping mode was employed in order to prevent possible surface damage due to continuous contact of the tip with the surface.

Advancing contact angles were measured on static drops of water using a Ramé-Hart manual goniometer equipped with video camera and computer monitor for viewing the drops. Contacting liquids were advanced and retreated (1 μL/s) prior to measurement with a Micro-Electrapette syringe (Matrix Technologies, Lowell, MA). The pipet tip remained in the drop during measurement. Measurements of the ~ 5 μL drops were taken at five different locations on a sample.

Section 5.4: Results & Discussion

Figures 5-1(a) – (c) show 2D AFM surface images of 10 ms on/100 ms off (10/100) pulsed plasma films from $C_2H_2F_4$, CH_2F_2, and HFPO. The three films are of comparable thickness: 516, 364, and 438 nm for the $C_2H_2F_4$, CH_2F_2, and HFPO precursors, respectively. All three films show growth of spherical nodules, with the height and diameter of the nodules dependent upon the precursor. Table 5-1 lists the deposition conditions, root mean square roughness (R_{rms}), maximum feature height, and nodule diameters (*d*) for all of the films discussed in this work.

Growth from $C_2H_2F_4$ (Fig. 5-1a) displays clusters of nodules, where smaller nodules (d ~ 20 – 50 nm) group around larger nodules (d ~ 100 – 150 nm), often referred to as a "cauliflower" appearance.[18] The larger nodules may have formed through agglomeration of several smaller nodules over the deposition period. Alternatively, the larger nodules could result from initial growth from a nucleation site on the silicon surface, with subsequent nucleation of additional nodules from the larger one, thus producing arrays of smaller nodules on the larger ones. The maximum feature height is ~

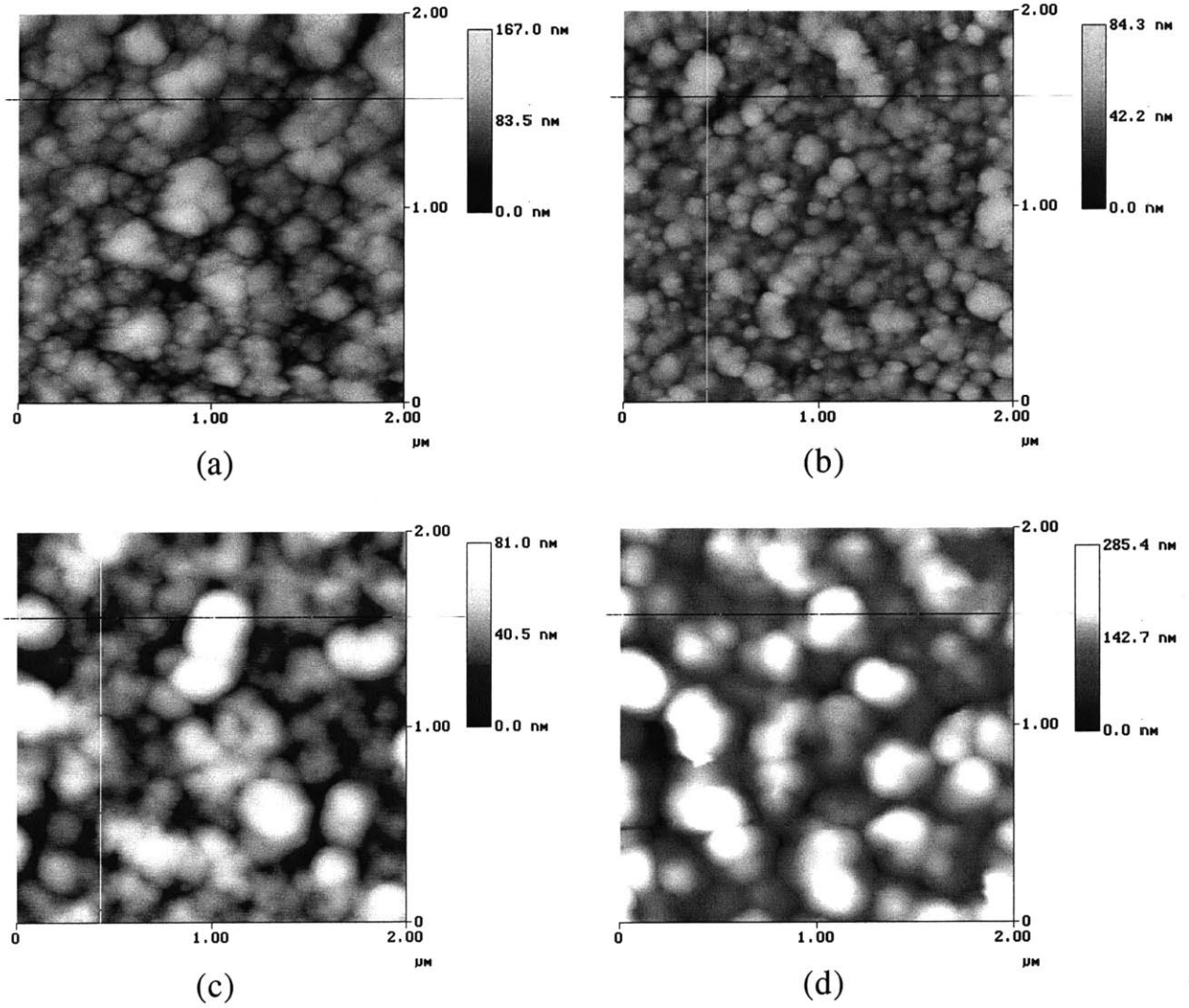

Figure 5-1: 2D AFM surface images of pulsed plasma films deposited from 1,1,2,2-$C_2H_2F_4$, CH_2F_2, and HFPO. All films show nodular growth, with the size and distribution of nodules dependent upon the pulse cycling condition and precursor, which in turn determine the energy input to the growing surface per nm of deposited film and the pulsed plasma chemistry. (a) 10/100 $C_2H_2F_4$, (b) 10/100 CH_2F_2, (c) 10/100 HFPO, (d) 10/400 HFPO.

Table 5-1. Deposition conditions, film thickness, root mean square roughness (R_{rms}), maximum feature height, and nodule diameters (*d*) for all of the films discussed in this work.

Precursor	Pulse	Substrate	Film Thickness (nm)	Dep. T (C)	R_{rms} (nm)	Max. Feature Height (nm)	*d* (nm)
HFPO	10/20	Si	399	25	0.88	11.63	20 – 40
	10/50	Si	515	25	4.04	44.04	85 – 150
	10/100	Si	438	25	12.3	80.88	130 – 260
	10/200	Si	484	25	31.7	217.07	120 – 190
	10/400	Si	422	25	28.4	285.44	180 – 270
	10/400	Si	687	60	12.5	80.68	140 – 250
	10/400	Si	556	110	10.7	65.71	130 – 200
	10/400	Al/Si	470	25	26.9	171.41	170 – 260
$C_2H_2F_4$	10/100	Si	516	25	22.3	166.70	20 – 50 100 – 150
	40/400	Si	~340	25	41.1	337.62	70 – 110
	10/100	Al/Si	564	25	21.5	181.66	20 – 80
	40/400	Al/Si	~430	25	67.1	431.06	50 – 90
CH_2F_2	10/100	Si	364	25	11.8	84.31	30 – 100
	40/400	Si	770	25	47.8	338.91	60 – 100
	10/100	Al/Si	356	25	15.2	151.99	30 – 50
	40/400	Al/Si	~540	25	32.8	250.24	40 – 80

167 nm, which is nearly 33% of the total 516 nm film, and a large rms surface roughness (R_{rms}) is also seen (22.3 nm).

Deposition from CH_2F_2 (Fig. 5-1b) rather than $C_2H_2F_4$ (Fig. 5-1a) results in smaller nodules of $d \sim 30 - 100$ nm, distributed uniformly over the scanned area. The nodules are also shorter, with a maximum feature height of ~ 84 nm. This change is reflected in the R_{rms}, which is 11.8 nm, approximately half the R_{rms} observed for the film deposited from $C_2H_2F_4$. The AFM image for the film grown from HFPO (Fig. 5-1c) reveals nodules that are significantly larger than those seen in either Fig. 5-1a or 5-1b. The nodule diameters in Fig. 5-1c range from 130 to 260 nm, and there is also a distribution of nodule heights. Indeed, those taller, larger nodules could be physically blocking the supply of growth species to the lower nodules, otherwise known as "shadowing."[19,20] Surprisingly, however, in comparison to the film grown from CH_2F_2, the maximum feature height is slightly lower (81 nm). Also, the corresponding rms roughnesses are similar (12.3 nm). The shadowing effect observed for the HFPO precursor is even more apparent when a longer pulse off time is used. Figure 5-1d shows a 2D AFM surface image of a 10/400 pulsed plasma film deposited from HFPO (422 nm thick). The nodules are a bit larger ($d \sim 180 - 270$ nm) and now the maximum height has jumped to ~ 285 nm. The rms roughness reflects these changes, increasing to 35.6 nm.

In CH_2F_2 pulsed plasmas, HF and free fluorine are the dominant products.[17] These species are also present in lesser concentrations in $C_2H_2F_4$ pulsed plasmas, but are absent in HFPO pulsed plasmas. More HF and free fluorine in the plasma correlates to smaller nodule sizes in films produced at the same excitation conditions (e.g., 10/100, Figs. 5-1a-c). This suggests F ions and atoms aid the nucleation of new nodules.

However, many variables are coupled in the plasma environment, so it difficult to make definitive statements. In creating HF and free fluorine in the plasma, carbon-rich species must be made and these may also play a role in nucleation. In support of this hypothesis, note that the percentage of unfluorinated carbon in the films decreases with reduced tendency of the precursor to undergo HF elimination.[16,17]

It is known that the CF_x fractions for films grown from HFPO pulsed plasmas are dependent upon the absolute pulse on and off times.[15] HFPO pulsed plasmas are known to have high concentrations of CF_2 in the gas phase due to the initial decomposition of HFPO into CF_2 + $CFOCF_3$, with those concentrations also dependent upon the absolute pulse on and off times.[17] For a fixed pulse on time, the % CF_2 in the deposited film increases with increasing pulse off time, while other CF_x species decrease, reflecting both the change in the available CF_2 and the decrease in surface modification due to ion bombardment, chemical etching, and other plasma-induced surface damage mechanisms as pulse off time is increased.[15] These changes in plasma chemistry (i.e., available depositing species) and surface modification likely control the geometry of nodule formation during film growth as well. The degree to which a growing surface will be subjected to surface modification is dependent upon both the pulse on time and the film growth rate. Figure 5-2a plots R_{rms} and the incident power/deposition rate per pulse cycle (J*cycle/nm), Q, as a function of the pulse off time for a series of films deposited from HFPO (pulse on time fixed at 10 ms). The incident power is calculated as the peak power (280 W) multiplied by the length of the pulse on time. Fig. 5-2a shows a decrease in Q as pulse off time increases, while R_{rms} increases. Thus, at short off times the growing

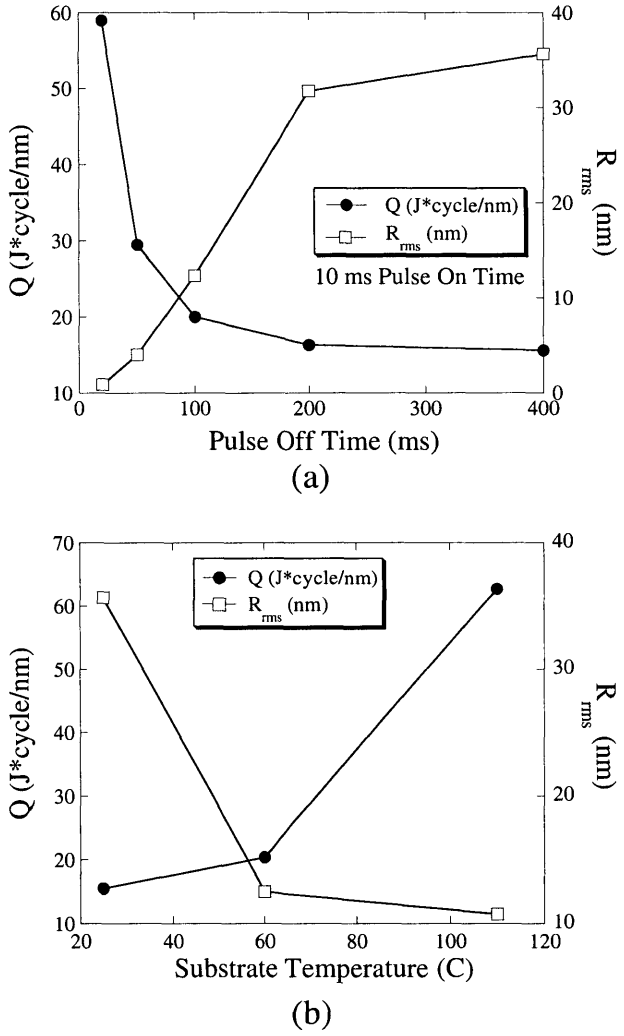

Figure 5-2: (a) R_{rms} and the incident power/deposition rate per pulse cycle (J*cycle/nm), Q, as a function of the pulse off time for a series of films deposited from HFPO. At short off times the growing surface is subjected to the most modification, leading to smoother surfaces. As pulse off time is increased, less modification occurs, resulting in a rougher surface. (b) R_{rms} and Q as a function of the substrate deposition temperature for a series of 10/400 HFPO pulsed plasma films. Q increases with increasing substrate temperature, whereas R_{rms} decreases, indicating that at higher temperatures, the growing film is subjected to increased modification. The changes in R_{rms} observed here are directly due to the increased surface modification, since the CF_x distribution does not change significantly for these films as substrate temperature is increased.[15]

surface is subjected to the most modification, leading to smoother surfaces; whereas, as pulse off time is increased, less modification occurs, resulting in a rougher surface.

The degree of surface modification to which a growing film is subjected also accounts for the decrease in R_{rms} as the substrate temperature during deposition is increased. Figure 5-2b shows R_{rms} and Q as a function of the substrate deposition temperature for a series of 10/400 HFPO pulsed plasma films. As the substrate temperature increases, Q also increases, whereas R_{rms} decreases, indicating that at higher temperatures, the growing film is subjected to increased modification, leading to the decrease in R_{rms}. It is especially important to note that the CF_x distribution does not change significantly for these films as substrate temperature is increased.[15] Therefore, the changes in R_{rms} observed here are directly due to the increased surface modification, as opposed to the data presented in Fig. 5-2a, where both % CF_2 and Q increase with pulse off time.

The results obtained for films deposited from $C_2H_2F_4$ and CH_2F_2 can also be partially explained in terms of surface modification mechanisms. Comparing R_{rms} and Q for 10/100 pulsed plasma films from all three precursors (Table 5-2), R_{rms} is once again inversely related to Q. However, the power factor, Q, does not account for the jump in R_{rms} when comparing 10/100 and 40/400 films deposited from $C_2H_2F_4$ and CH_2F_2. For $C_2H_2F_4$, Q actually increases, whereas R_{rms} doubles. For CH_2F_2, there is a slight decrease in Q, but this decrease is not sufficient to explain the increase in R_{rms}. Clearly, another mechanism must be in effect. Unfortunately, the data presented here is not sufficient to postulate this additional mechanism.

Table 5-2. Comparison of R_{rms}, maximum feature height, nodule diameter (*d*), and incident power factor (Q) for 10/100 films deposited from all three precursors. Data for 40/400 films deposited from $C_2H_2F_4$ and CH_2F_2 are also present for comparison with the 10/100 condition.

Precursor	Pulse	Thickness (nm)	Dep. Rate (nm/cycle)	R_{rms} (nm)	Max. Feature Height (nm)	*d* (nm)	Q (J*cycle/nm)
HFPO	10/100	438	0.14	12.3	80.88	130 – 260	20.0
$C_2H_2F_4$	10/100	516	0.278	22.3	166.70	20 – 50 100 – 150	10.1
	40/400	~340	0.593	41.1	337.62	70 – 110	18.9
CH_2F_2	10/100	364	0.074	11.8	84.31	30 – 100	37.9
	40/400	770	0.304	47.8	338.91	60 – 100	36.8

Figure 5-3 shows a 2D AFM surface image of a 10/100 pulsed plasma film deposited from CH_2F_2 onto an Al-coated Si substrate (film = 356 nm thick). In comparison with Fig. 5-1b, in which the film was deposited on a bare Si substrate, it can be seen that the surface morphology has changed as a result of the Al coating. The nodules are generally much smaller (d ~ 30 – 50 nm), but the maximum feature height has almost doubled, to 152 nm. Despite this increase in feature height, due to the smaller distribution of nodule sizes, the rms roughness is only slightly larger (15.2 nm). In general, the nodule sizes were found to decrease for all of the films deposited on the Al-coated Si vs. bare Si substrates (all precursors). The maximum feature heights also changed, but they did not all follow the same trend. The rms roughness generally followed the maximum feature height, since those changes were usually larger than the change in nodule size (see Table 5-1). These changes in surface morphology can be traced directly to the surface properties of the substrate. Bare Si is extremely smooth, with R_{rms} = 0.53 nm and a maximum feature height of 9.47 nm. In contrast, the Al-coated Si substrate has clearly distinguished finger-like structures (d ~ 60-100 nm), leading to R_{rms} = 7.48 nm and a maximum feature height of 57.26 nm. These finger-like structures clearly influence the size and distribution of the fluorocarbon film nodules which grow from them.

It is of interest to make a connection between the surface structures seen here, and those observed in the literature for various types of deposited films. Movchan and Demchishin were the first to propose a generalized structure zone model (SZM) which correlated observed film morphology with a normalized process parameter, in this case T/T_m, where T is the deposition temperature and T_m is the melting point of the deposited

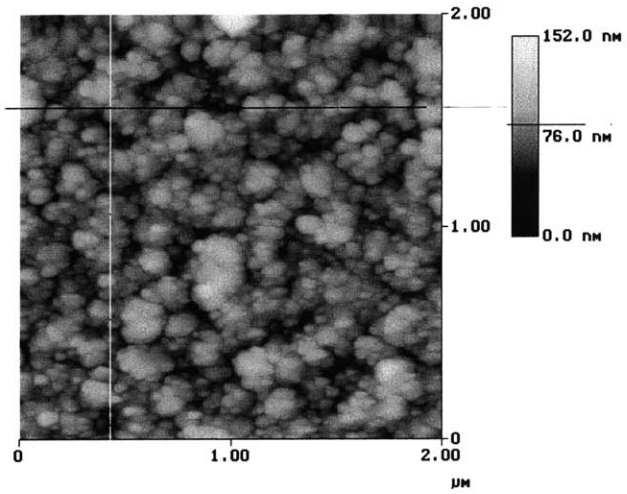

Figure 5-3: 2D AFM surface image of 10/100 CH_2F_2 pulsed plasma film deposited on an Al-coated Si substrate. In comparison with Fig. 5-1b, the nodule diameter has decreased, whereas the maximum feature height has almost doubled. Despite the increase in maximum feature height, due to the smaller nodule size distribution, R_{rms} is not significantly changed from the sample deposited on bare Si (15.2 nm vs. 11.8 nm).

film.[19] They identified three different growth regimes based on the observed microstructure of the films. Thornton later added to this model by proposing a transitional region between Movchan and Demchishin's zones 1 and 2.[20] According to this model, microstructural development is in turn controlled by shadowing effects (zone 1), surface diffusion (zone T and zone 2), and bulk diffusion (zone 3) as T/T_m increases.[19-21] Each zone has particular materials properties associated with it, and thus, by identifying the relevant growth zone for a particular material, it was possible to infer some of its material properties. It is important to note that these studies were based on both evaporated and sputtered metals and metal oxides.[19,20] Hence, it can not be automatically assumed that covalently bonded PECVD films would necessarily conform to the SZM. However, several covalently bonded systems have been studied, and the SZM has been successfully applied to these systems.[18] All of the films investigated here were found to be zone 1 growth structures. This categorization is evident from the AFM images in Figs. 5-1 and 5-3, and can also be seen clearly in Fig. 5-4, which shows a SEM micrograph of a 10/50 pulsed plasma film from HFPO deposited over a polysilicon resistor structure. The nodules observed with the AFM are clearly seen in the open areas, as well as columnar growths over the device structures. The ability to smooth the film microstructure by increased plasma exposure suggests this energy input to the surface promotes atomic rearrangements, analogous to the manner in which increasing temperature allows for increased surface and bulk diffusion. Thus, the dominance of a shadowing effect proposed earlier for the films from HFPO is confirmed with the identification of these films (as well as those from $C_2H_2F_4$ and CH_2F_2) as zone 1 growth structures.

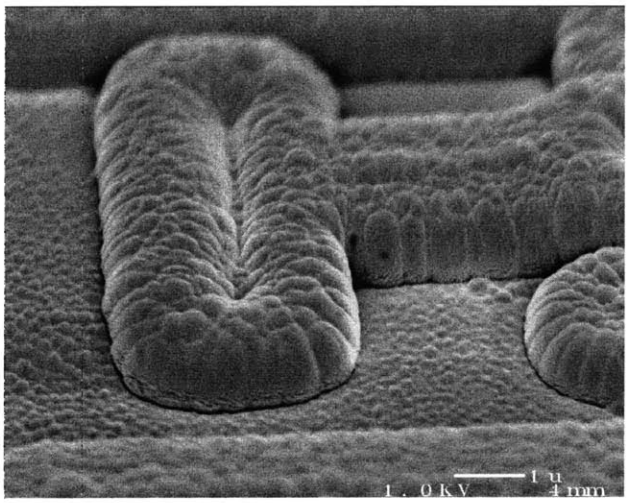

Figure 5-4: SEM micrograph of a 10/50 HFPO pulsed plasma film deposited over a polysilicon resistor structure. The nodules observed with the AFM are clearly seen in the open areas, as well as columnar growths over the device structures. The observed surface morphology emphasizes the zone 1 nature of the deposited film.

All of the advancing contact angles measured for pulsed plasma films from HFPO, as well as those from $C_2H_2F_4$ and CH_2F_2, are well above 90°. A contact angle > 90° indicates a non-wetting surface, whereas one < 90° is indicative of a wetting surface.[22] For reference, the advancing contact angle for polytetrafluoroethylene (PTFE) is ~ 108°.[22] Measured contact angles can be affected by a film's surface roughness, fluorine to carbon ratio, and degree of oxidation.[3,4,22] Oxidation occurs through the formation of C=O, OH, and COOH groups by reaction of dangling bonds formed during the pulsed plasma deposition with ambient water and oxygen.[4] It is assumed for all of these measurements that the differences in degrees of oxidation between samples do not significantly affect the observed contact angles.

All of the HFPO pulsed plasma films were found to have contact angles between 105 and 130°. 10/100 pulsed plasma films from $C_2H_2F_4$ and CH_2F_2 had contact angles of 107 and 101°, respectively, whereas their 40/400 films had contact angles of 144° each. The large increase in contact angles between these two pulse conditions is most likely a function of the increased roughening of the surface at the 40 ms on time. AFM measurements show that R_{rms} at least doubles between these pulse conditions for both precursors (see Table 5-1).

Figure 5-5 shows the advancing contact angle for a drop of water on a series of pulsed plasma films, all deposited from HFPO, as a function of the pulse off time (pulse on time = 10 ms). Fig. 5-5 highlights two aspects of the HFPO pulsed plasma films. First, there is a general increase in contact angle with pulse off time. This increase can be attributed to two effects: composition and surface roughness. First, it is known that the % CF_2 in the deposited films increases with pulse off time.[15] It is also known that CF_x

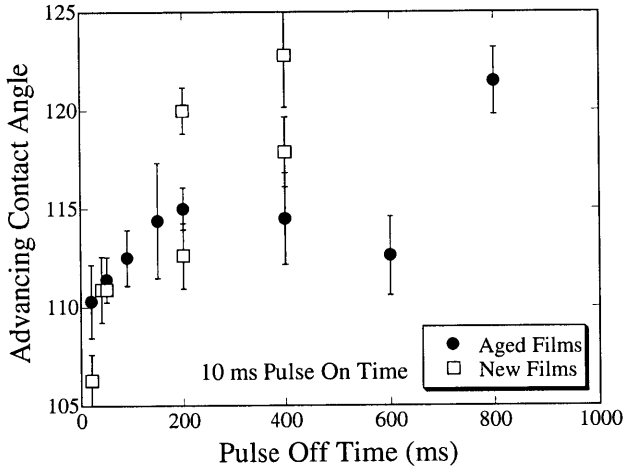

Figure 5-5: Advancing contact angle for a drop of water on a series of HFPO pulsed plasma films as a function of the pulse off time (pulse on time = 10 ms). Two aspects of the HFPO pulsed plasma films are highlighted. First, there is a general increase in contact angle with pulse off time which can be attributed to two effects: change in CF_x composition and increased surface roughness. For this series of films, % CF_2 generally increases with pulse off time while % CF_3 stays relatively the same. The increase in % CF_2 will lead to an increase in hydrophobicity, contributing to the increase in contact angles. Second, freshly grown films deposited at longer pulse off times have higher contact angles than their aged counterparts, while those at short off times have similar or smaller contact angles. These types of trends have been seen in other PECVD fluorocarbon systems and were expected since general handling of the older films would result in contamination and alteration of the surface. Oxidation of free radicals and unsaturated carbon bonds after plasma deposition can also contribute to a decrease in contact angle.

groups are increasingly hydrophobic as x = 1 → 3.[22] The composition of these films tends to decrease CF and C-CF groups while increasing CF_2, with only minor variations in % CF_3 as pulse off time is increased.[15] Therefore, an increase in the % CF_2 for these films should indicate an increasingly hydrophobic environment, which would result in a higher contact angle. Most of the contact angles observed here are slightly over 108°, the contact angle for water on PTFE. Since PTFE presents a CF_2-only surface, it can be assumed that the ~ 15% CF_3 also present in these films contributes to the higher contact angles. The second contribution to the increasing contact angles can be traced to the increase in surface roughness as pulse off time is increased (Fig. 5-2a). Roughness is known to increase any observed contact angles,[4,22] and therefore since R_{rms} increases with pulse off time for these films, an increase in contact angle is also expected.

The second trend which Fig. 5-5 emphasizes is that freshly deposited films (contact angles measured within 2 days of deposition) can give different results than films aged for several months (> 6 months). In general, newly grown films deposited at longer pulse off times have higher contact angles than their aged counterparts, while those at short off times have similar or smaller contact angles. These types of trends have been seen in other PECVD fluorocarbon systems[23] and were expected since general handling of the older films would result in contamination and alteration of the surface. Oxidation of free radicals and unsaturated carbon bonds after plasma deposition has also been seen widely in the literature.[3,4] The introduction of C=O groups into the films increases the surface energy of the plasma polymer, resulting in a decrease in the contact angle.[4,22,24] This mechanism most likely also plays a role in the long pulse off time trend seen here.

Significant hysteresis was also observed for all of the pulsed plasma films measured, with retreating contact angles generally 89-92°. The trends observed with the advancing contact angle do not translate to the retreating angle, as the retreating contact angles are less susceptible to effects such as roughness.[4]

Section 5.5: Conclusions

AFM measurements have been made on a series of fluorocarbon films deposited from pulsed plasmas of HFPO, 1,1,2,2-$C_2H_2F_4$, and CH_2F_2. All of the films give images showing nodular growth ("cauliflower" appearance), with the size and distribution of the nodules dependent upon both the precursor, the degree of surface modification to which the growing film is exposed, and the substrate surface. Films deposited from $C_2H_2F_4$ showed clusters of smaller nodules around larger nodules, whereas films deposited from CH_2F_2 were characterized by a uniform distribution of smaller nodules, and films deposited from HFPO had the largest observed nodules. For films deposited from HFPO, it was found that the rms roughness increased with increasing pulse off time, while for a fixed pulse condition, the roughness decreased with increasing substrate temperature. These changes can be partially attributed to the change in incident power per nm of film deposited as either pulse off time or substrate temperature is varied. Films from all of the precursors were also sensitive to the surface structure of the deposition substrate, with the rougher Al-coated Si surface affecting both the nodule size and distribution for all of the deposited films. Movchan and Demchishin's structure zone model was applied to the observed films, which were all found to be zone 1 structures, indicating that film growth is dominated by shadowing effects. Advancing contact angles for all of the films were

found to be higher than that of PTFE (108°), indicating both hydrophobic and rough surfaces. Specifically, contact angles of films deposited from HFPO were found to increase with pulse off time, the same trend observed for both the CF_2 fraction of the film and the rms roughness.

Section 5.6: Acknowledgments

The authors gratefully acknowledge the financial support of the Office of Naval Research, Lucent Technologies Bell Laboratories Graduate Research Program for Women, and the NSF/SRC Engineering Research Center for Environmentally Benign Semiconductor Manufacturing. We would also like to thank DuPont for donation of the feed gases used in this study, and Emily Sung for her work with the contact angle measurements.

Section 5.7: References

1. K. Endo, *MRS Bull.*, **22**(10), 55 (1997).

2. K. Endo and T. Tatsumi, *Appl. Phys. Lett.*, **68**(20), 2864 (1996).

3. H. Yasuda, *Plasma Polymerization*, Academic Press, New York, 1985.

4. *Plasma Deposition, Treatment, and Etching of Polymers*, R. d'Agostino, Ed., Academic Press, Boston, 1990.

5. J. Hopkins, R. D. Boyd, and J. P. S. Badyal, *J. Phys. Chem.*, **100**(16), 6755 (1996).

6. J. D. Miller, S. Veeramasuneni, J. Drelich, M. R. Yalamanchili, and G. Yamauchi, *Poly. Engr. Sci.*, **36**(14), 1849 (1996).

7. J.-H. Jou, C.-L. Cheng, E. C.-Y. Jou, and A. C.-M. Yang, *J. Polym. Sci.: B: Polym. Phys.*, **34**, 2239 (1996).

8. G. Beamson, D. T. Clark, D. E. Deegan, N. W. Hayes, D. S.-L. Law, J. R. Rasmusson, and W. R. Salaneck, *Surf. and Interface Anal.*, **24**, 204 (1996).

9. P. Dietz, K. Hansma, K. J. Ihn, F. Motamedi, and P. Smith, *J. Mater. Sci.*, **28**, 1372 (1993).

10. H. Hansma, F. Motamedi, P. Smith, P. Hansma, and J. C. Wittman, *Polymer*, **33**(3), 647 (1992).

11. M. C. Coen, G. Dietler, S. Kasas, and P. Groning, *Appl. Surface Sci.*, **103**, 27 (1996).

12. B. Nysten, R.-C. Roux, S. Flandrois, C. Daulan, and H. Saadaoui, *Phys. Rev. B*, **48**(17), 12527 (1993).

13. J. Hopkins and J. P. S. Badyal, *J. Polym. Sci.: A: Polym. Chem.*, **34**, 1385 (1996).

14. S. N. Magonov and M.-H. Whangbo, *Surface Analysis with STM and AFM*, VCH, New York, 1996.

15. S. J. Limb, D. J. Edell, E. F. Gleason, and K. K. Gleason, *J. Appl. Polym. Sci.,* **67**, 1489 (1998).

16. C. B. Labelle and K. K. Gleason, *J. Vac. Sci. Technol. A,* **17**(2), 445 (1999).

17. C. B. Labelle, S. Karecki, R. Reif, and K. K. Gleason, *J. Vac. Sci. Technol. A*, (submitted) (1999).

18. R. Messier and J. E. Yehoda, *J. Appl. Phys.,* **58**(10), 3739 (1985).

19. B. A. Movchan and A. V. Demchishin, *Phys. Met. Metallogr.,* **28**, 83 (1969).

20. J. A. Thornton, *Ann. Rev. Mater. Sci.,* **7**, 239 (1977).

21. R. Messier, A. P. Giri, and R. A. Roy, *J. Vac. Sci. Technol. A,* **2**(2), 500 (1984).

22. A. W. Adamson, *Physical Chemistry of Surfaces*, 5th ed., John Wiley & Sons, Inc., New York, 1990.

23. T. A. Gengenbach and H. J. Griesser, *Surf. and Interface Anal.,* **26**, 498 (1998).

24. E. E. Johnston and B. D. Ratner, *J. Electron Spectrosc. Relat. Phenom.,* **81**, 303 (1996).

Chapter 6

Overhang Test Structure Deposition Profiles of Pulsed Plasma Fluorocarbons Films from HFPO, 1,1,2,2-$C_2H_2F_4$, and CH_2F_2

(Submitted to Chemical Vapor Deposition in 1999 as "Overhang Test Structure Deposition Profiles of Pulsed Plasma Fluorocarbons Films from Hexafluoropropylene Oxide, 1,1,2,2-Tetrafluoroethane, and Difluoromethane," Catherine B. Labelle and Karen K. Gleason.)

Section 6.1: Abstract

Films from pulsed plasmas of hexafluoropropylene oxide (HFPO), 1,1,2,2-tetrafluoroethane ($C_2H_2F_4$), and difluoromethane (CH_2F_2) were deposited onto overhang test structures to investigate the different film formation mechanisms. Four growth mechanisms were considered: direct or ion-induced deposition, low pressure chemical vapor deposition (LPCVD) from neutral species, redeposition, and sputtering. All of the films investigated were dominated by direct or ion-induced deposition, but the role of the other mechanisms varied with both pulse conditions and precursor choice. Growth from continuous plasma enhanced chemical vapor deposition (PECVD) from HFPO showed significant sputtering but little LPCVD or redeposition. The opposite behavior resulted from pulsed HFPO plasma films, which showed considerable contributions from LPCVD and redeposition growth, but no obvious sputtering. As with the pulsed HFPO films, 10/100 pulsed plasma films from $C_2H_2F_4$ and CH_2F_2 also exhibit LPCVD and redeposition growth, but little sputtering. However, redeposition was found to play a smaller role in the HFPO system than that of the other two precursors. The similarity of the $C_2H_2F_4$ and CH_2F_2 film profiles can be attributed to their similar pulsed plasma chemistries, whereas the non-hydrofluorocarbon HFPO has a significantly different pulsed plasma chemistry, and therefore, a different profile. In all cases, systematic trends in the film growth profiles were observed with the dimension of the opening separating the two cantilevers of the test structure. Tensile stress on the order of 1.3 GPa was observed for the continuous HFPO film, whereas compressive stresses of –1.2 and –1.8 GPa were seen in the $C_2H_2F_4$ and CH_2F_2 films, respectively.

Section 6.2: Introduction

Fluorocarbon thin films are being considered for use in a variety of applications including semiconductor low dielectric constant films and biopassivation coatings.[1-3] These films are grown primarily by plasma-enhanced chemical vapor deposition (PECVD), which incorporates many different parallel deposition pathways. It has been argued that for a vacuum process, the only way to explain the observed rapid polymer film growth is by means of ion-induced deposition.[3] Although neutral species pathways are believed to be possible, it is not generally acknowledged that they contribute significantly to the overall deposition process.[3] However, pyrolytic[4,5] and downstream[2,6,7] fluorocarbon CVD must have neutral pathways as a primary growth mechanism. The relative importance of neutral pathways in comparison to ion-induced or additional pathways in PECVD, however, has not been examined.

Pulsed PECVD fluorocarbon thin films from hexafluoropropylene oxide (HFPO), 1,1,2,2-tetrafluoroethane ($C_2H_2F_4$) and difluoromethane (CH_2F_2) have been studied extensively.[8-14] Carbon 1s x-ray photoelectron spectroscopy (XPS) and ^{19}F nuclear magnetic resonance (NMR) show that a range of fluorocarbon film compositions can be achieved by varying the pulse condition and/or precursor.[10,11,13,14] Gas-phase Fourier Transform Infrared Spectroscopy (FTIR) of the pulsed plasma effluents also reveals vast differences in the pulsed plasma chemistry occurring in each system, which correlate to the observed differences in film composition.[12]

Figure 6-1 shows a schematic of the overhang test structure used in this work. This structure has been described in detail previously.[15-17] It basically consists of a trench isotropically etched in SiO_2 with polycrystalline silicon overhangs, where the

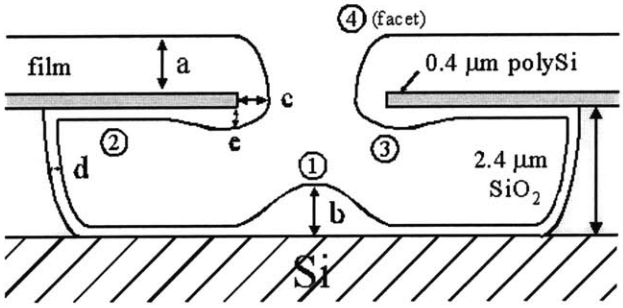

Figure 6-1: Schematic of overhang test structure used in depositions. Structure consists of polycrystalline silicon cantilevers over a trench. Numbers 1 - 4 indicate regions typically dominated by a particular growth mechanism: (1) direct or ion-induced deposition, (2) LPCVD, (3) redeposition, and (4) sputtering. Letters a – e mark points at which thickness measurements were taken.

opening between the overhangs can be varied from 1 – 8 μm.[15] Specific regions of this geometry allow for distinction of the various mechanisms involved in CVD processes.[15-17] The main mechanisms of interest here are direct or ion-induced deposition (Region 1 in Fig. 6-1), low-pressure chemical vapor deposition (LPCVD, Region 2), redeposition (Region 3), and sputtering (Region 4).[16,18]

Region 1, consisting of film grown directly beneath the cantilever opening, is dominated by growth from direct or ion-induced deposition. This area is directly exposed to the plasma and therefore is subject to both ion and neutral fluxes. However, this region will have reduced growth from neutrals since their isotropic flux is reduced relative to the anisotropic ion flux. Region 2, consisting of growth near the sides of the trench, including the surfaces beneath the base of the overhang (both on the underside of the polysilicon overhang itself and the bottom of the trench it shades) and on the sidewalls of the trench, is dominated by LPCVD. The flux of ions to Region 2 is insignificant compared to that in Region 1, and therefore any growth is primarily due to diffusion of reactive neutrals into Region 2. Region 3, comprised of growth laterally from the cantilever edge and on its underside near the opening, is dominated by redeposition, principally from the ion-induced film forming under the overhang opening (Region 1). Many of the ions impacting the film beneath the overhang opening will eject reactive neutral species that subsequently deposit in other areas of the structure. Due to the cantilevers, many of these ejected species cannot escape the trench structure and deposit on the underside of the cantilever, primarily near the opening edge, thus producing the "bulbous" appearance of the growth at the edges of the cantilevers. LPCVD also contributes partially to the lateral growth from the cantilever edge, but

cannot account for the bulbous shape to the underside of that growth. Finally, Region 4 consists of any faceting in the sidewall of the film on top of the overhang and is caused by sputtering of the growing film. Due to the presence of the overhangs, the sputter yield will be angle-dependent, and therefore an angled facet will form. Geometrical factors will cause the appearance of the facet to change as the opening size varies.

This work will examine the growth profiles resulting from fluorocarbon CVD onto the overhang test structure. Profiles from continuous and pulsed PECVD films from HFPO will be compared. Results for pulsed PECVD from $C_2H_2F_4$ and CH_2F_2 will also be reported. For each case, the relative importance of the different mechanisms is discussed.

Section 6.3: Experimental

Pulsed PECVD films were deposited from HFPO (C_3F_6O) on overhang test structures using a pulse on time of 10 ms and pulse off times of 50, 100, and 400 ms. Pulsed plasma films were also deposited from 1,1,2,2-$C_2H_2F_4$ and CH_2F_2 at a pulse condition of 10 ms on/100 ms off (10/100). In all cases, the peak rf power was 2.7 W/cm^2. Additionally, one 0.48 W/cm^2 continuous PECVD film was grown from HFPO using the same deposition system. Note that the continuous and 10/50 pulsed depositions both used approximately the same power (50 W continuous vs. 280 W * (1/6 duty cycle) = 46.7 W). All films were grown in a parallel plate reactor operating at 1 Torr. A flow rate of 12.5 sccm was used for 1,1,2,2-$C_2H_2F_4$ and CH_2F_2, whereas 23 sccm was used for HFPO. Previous work shows changing the HFPO flow rate from 12.5 to 23 sccm has little impact on film deposition rate and composition.[10] Details of the reactor

configuration have been presented elsewhere.[10] The substrates were cooled on the backside with water at ~23°C.

Overhang test structures were used as received from Dr. James P. McVittie's group at Stanford University. These structures, shown schematically in Fig. 6-1, are fabricated in arrays on silicon wafer substrates.[15] Within the array, the dimensions of the openings are intentionally varied between 1 and 8 microns. The polysilicon overhangs are ~ 0.4 μm thick. The trenches are formed in a 2.4 μm thick silicon dioxide layer deposited on bare silicon.

Cross-sectional scanning electron microscope (SEM) photos were taken of the overhang test structures at each deposition condition using a JEOL 6320FV Field Emission Scanning Electron Microscope. Samples were sputter-coated with ~100 Å of a gold/palladium mixture prior to scanning to prevent charging and damage to the fluorocarbon surface. The 10/50 deposition from HFPO was examined with an Electroscan Environmental Scanning Electron Microscope (ESEM) instead of the SEM. The ESEM operates with a water vapor environment at 1-10 Torr in order to mitigate charging effects, and therefore it was not necessary to gold-coat that sample prior to imaging. However, the higher electron beam power on this instrument was found to damage some films at higher magnifications, and therefore all of the other films discussed in this work were gold-coated and imaged with the lower power SEM. In addition, the traditional SEM provided higher resolution micrographs.

Section 6.4: Results and Discussion

Figures 6-2(a) – (d) show cross-sectional micrographs of a series of films deposited from hexafluoropropylene oxide (HFPO) onto the overhang test structures. The images shown are all for overhangs with an 8 μm opening. Fig. 6-2(a) shows the film deposited from a 0.48 W/cm^2 continuous plasma, whereas Figs. 6-2(b) – (d) show pulsed plasma films with pulse conditions of 10/50, 10/100, and 10/400 (ms on/ms off), respectively. As can be clearly seen in this series of images, the deposition profiles vary considerably as the pulse conditions are changed. As indicated by the dominant growth in Region 1, all four films show a predominance of direct or ion-induced deposition, but they differ significantly with respect to the other mechanisms. The continuous plasma film has a noticeable facet in the sidewall of the film on top of the polysilicon overhang, indicating sputtering. However, there is no indication of any deposition laterally from the overhang or under it (dimensions c, d, and e in Fig. 6-1 are zero within the resolution of the SEM), implying that LPCVD and redeposition are not significant. It should also be noted that the growth under the opening has a flattened top, which is different from any of the other films discussed here. This feature may also be due to sputtering.

In contrast, Figs. 6-2(b) – (d) all show deposition under the overhang as well as laterally from it. Also, no faceting of the film on top of the overhang is apparent. Thus, LPCVD and redeposition become relatively more important mechanisms for these films, whereas sputtering becomes relatively less significant. One of the other interesting features of films deposited from HFPO is the appearance of "string-like" fibers as the pulse off time is increased. These fibers affect the deposition profile by blocking access to the areas directly next to and under the overhangs, and thus restrict film growth. The origin of these fibers is unknown, but may be due to either long-chain molecules and/or

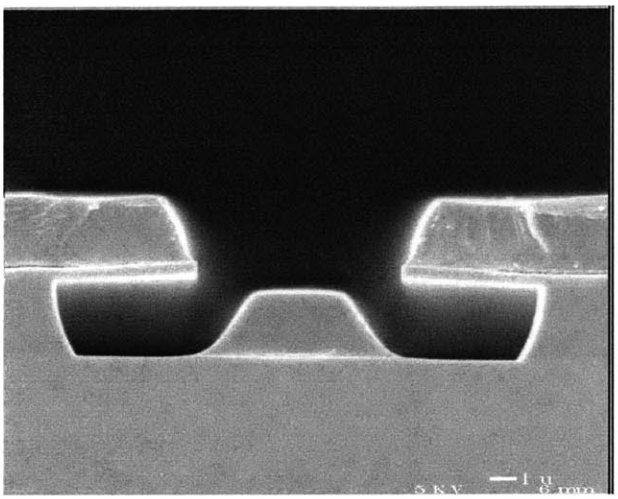

(a)

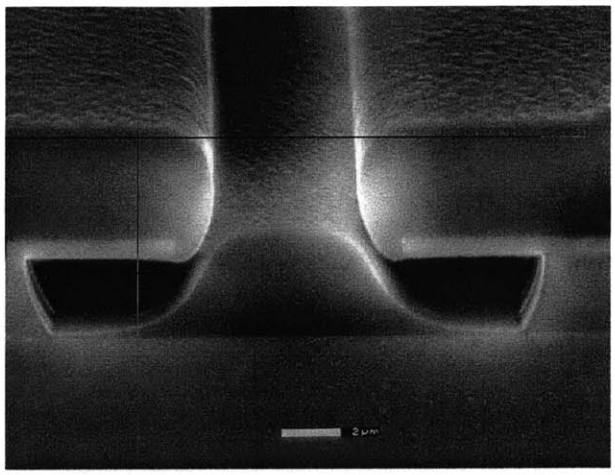

(b)

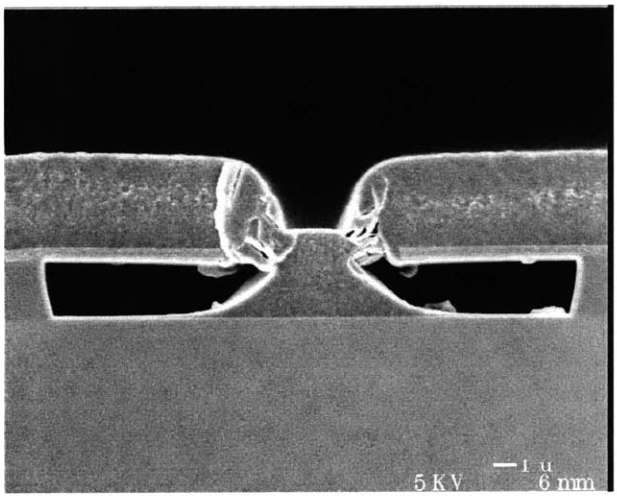

(c)

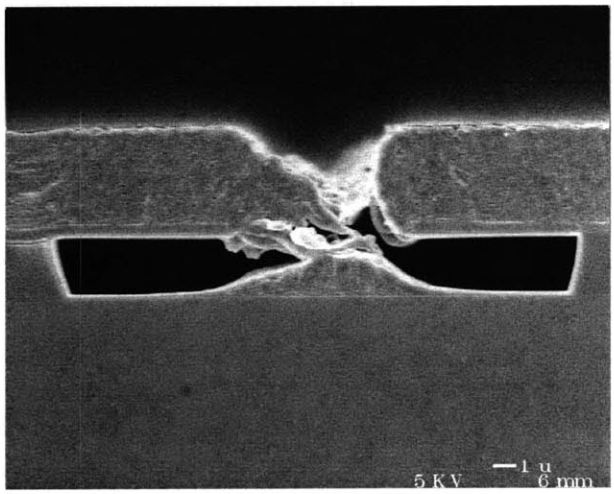

(d)

Figure 6-2: Cross-sectional micrographs of films deposited from HFPO. (a) Continuous PECVD (50 W), (b) 10/50, (c) 10/100, and (d) 10/400. Significant growth under the central opening reveals that all of the films are dominated by ion-induced dominated growth. However, the continuous PECVD image (6-2(a)) contains a facet on the upper sidewall indicative of sputtering whereas the pulsed PECVD pictures 6-2(b) – (d) do not. Also, in 2(a) no sidewall deposition can be resolved while in 6-2(b) – (d) LPCVD and redeposition growth lead to detectable deposition in regions 2 and 3.

particles formed in the gas phase as a result of the CF_2-rich gas phase chemistry,[12] or bridges being formed between the two growth surfaces due to the large nodule formation characteristics of these films.[19] The absence of these fibers in the 10/50 deposition (Fig. 6-2(b)) may indicate that the duty cycle is high enough to promote sputtering sufficient to eliminate the fibrous growth between the film on top of the overhang and that forming under the opening, but not to produce obvious faceting in the upper film.

Both the continuous and 10/50 films are exposed to approximately the same amount of power during deposition, which might lead one to expect the films to have similar deposition profiles. Comparing Figs. 6-2(a) and 6-2(b), however, it is clear that there are distinct differences between the two. Although both films show a majority of deposition on top of the overhangs and beneath the cantilever opening, the 10/50 film deposits both laterally from and under the polysilicon overhangs, and the growth under the opening has a rounded surface (vs. flat top of continuous film). The 10/50 profile also does not show any of the faceting seen in the continuous film. All of these observations emphasize the fact that pulsing of the plasma does not produce an average power effect. Rather, the pulsed plasma chemistry is determined by the absolute pulse on and off times, and is distinctly different from that obtained in a continuous plasma system.[10]

Figure 6-3 shows the ratio of film thickness under the center of the opening ("b") to that on top of the overhang ("a," see Fig. 6-1) as a function of the cantilever separation for all four of the HFPO depositions. A generally monotonic increase in the b/a ratio is seen as the spacing increases. For the smaller openings, the lateral growth emanating from the side of both cantilevers connects, obstructing access of any deposition species to

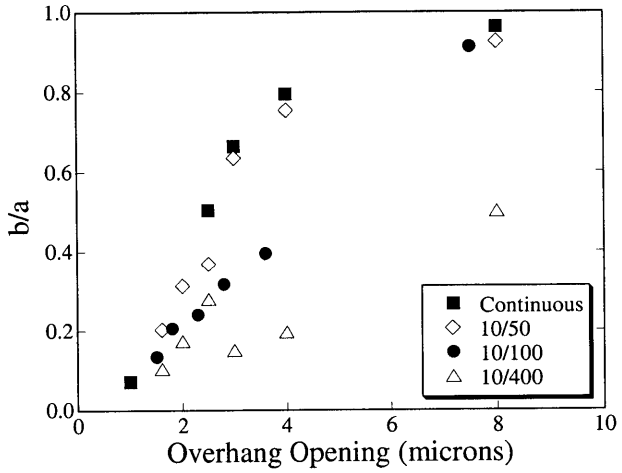

Figure 6-3: Ratio of thicknesses b and a (see Fig. 6-1) versus cantilever separation for both continuous and pulsed PECVD films from HFPO. Three of the four films show a monotonic increase in b:a as the spacing is increased. In the remaining case, the minor decrease in b:a at 3 μm for the 10/400 film is due to restriction of access to the area under the opening as a result of "string-like" fibers forming between the film on top of the overhang and that forming under the opening. These fibers appear in the 10/100 case as well, but do not hinder the growth as severely as in the 10/400 case.

the trench structure. The gap usually remains open when the spacing exceeds 2.5 μm. One exception to this is the 10/400 film, where, although clear at 2.5 μm, the 3 μm opening is significantly blocked by fiber formation. This blockage results in a sharp decrease in the observed film thickness under the opening, which is reflected by the decrease in b/a in Fig. 6-3. Although fiber formation is also observed in the 10/100 film, the effect is less detrimental, as the gap remains largely unblocked for all of the opening lengths > 2.5 μm.

Even when the openings remain unblocked, b/a < 1 because the overhangs restrict the angles at which depositing species can enter, thus lowering the growth rate under the opening. As the cantilever spacing increases, this restriction is reduced, leading to thicker films under the opening. At 8 μm, b/a is ~ 0.95 for all of the HFPO films except for the 10/400, indicating almost completely unrestricted growth at the center point under the opening. Using a diffusivity of 43 cm^2/s at 1 Torr,[20] the mean free path of CF_2 was calculated to be 36 μm,[21] which is much longer than any of the overhang structure dimensions. Taking this value as an average for all of the depositing species, gas-gas collisions should not significantly influence the trajectory of any of the incoming depositing species.

Figures 6-4(a) and (b) show cross-sectional SEM micrographs of 10/100 pulsed plasma films deposited from 1,1,2,2-tetrafluoroethane ($C_2H_2F_4$) and difluoromethane (CH_2F_2) on overhang test structures with 8 μm openings. Both figures are similar to Fig. 6-2(b) in appearance, showing growth under the opening, under the overhang, and laterally from the cantilevers. As before, this indicates that direct or ion-induced deposition, LPCVD, and redeposition mechanisms all contribute to these deposition

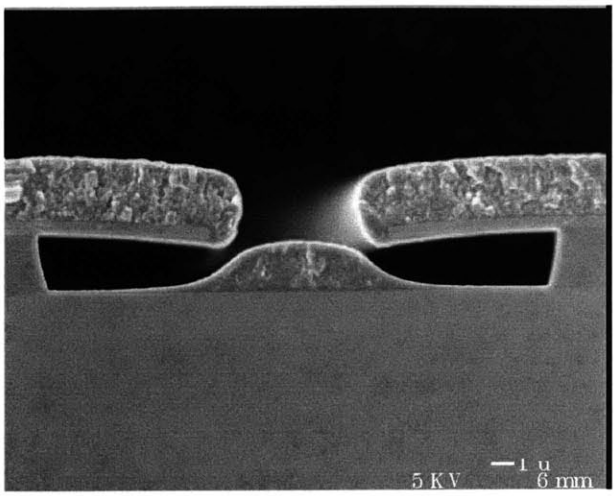

(a)

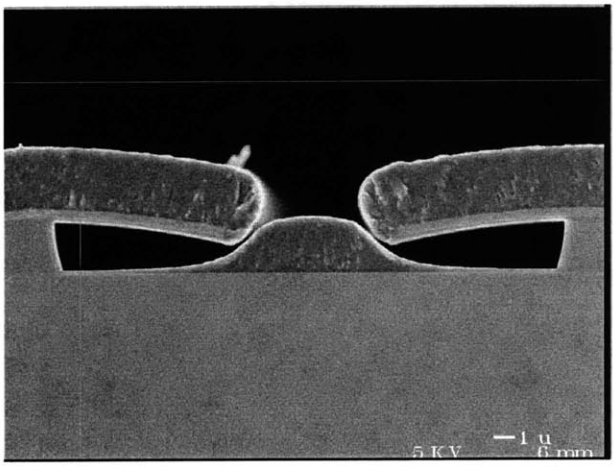

(b)

Figure 6-4: Cross-sectional SEM micrographs of 10/100 pulsed plasma films from (a) $C_2H_2F_4$ and (b) CH_2F_2. Both films show profiles similar to those seen in Fig. 6-2(b) – (d), indicating that ion-induced deposition, LPCVD, and redeposition are all involved in film growth. These films also have significant compressive stress (~ -1.2 and -1.8 GPa, respectively), as evidenced by the bowing of the polysilicon cantilevers. In comparison, HFPO pulsed plasma films (Figs. 6-2(b) – (d)) do not show any observable stress, whereas the continuous HFPO plasma film (Fig 6-2(a)) displays some tensile stress (~ 1.3 GPa).

processes, while the lack of faceting indicates that sputtering is not significant. In contrast to the films shown in Fig. 6-2, however, these films also display a high degree of compressive stress, as indicated by the bowing of the overhangs. The pulsed plasma films from HFPO do not deform the polysilicon overhangs observably, while the continuous HFPO plasma film shows a slight deformation upward, indicating tensile stress. Calculation of the film stress from the degree of deformation of the polysilicon overhang[22] provides rough values of –1.2 and –1.8 GPa (compressive) for the films from $C_2H_2F_4$ and CH_2F_2, and 1.3 GPa for the continuous PECVD film from HFPO (tensile). This calculation assumes a Young's modulus of 160 GPa for polysilicon.[23] All of these values are quite high compared to TEOS-deposited SiO_2 and some fluorinated SiO_2 films.[24,25]

Both tensile and compressive stresses have been widely seen in plasma-deposited polymers, and although their origins are not fully understood, it is generally thought that compressive stresses are induced by reactive plasma species impinging upon the growing film and inserting into existing polymer chain segments.[2,3] These insertions could act as nucleation sites, which would then account for the increased number of nucleation sites which have been observed for the more heavily stressed films from CH_2F_2 and $C_2H_2F_4$.[19]

The degree of cross-linking in the film also influences the stress. Random covalent networks have been used to examine the compositional point at which percolation of rigidity occurs.[26] Above the percolation of rigidity, the network is overconstrained, while below it the system is underconstrained. This point has been linked to the connectivity number of a network, and it has been found that the percolation

of rigidity occurs at an optimal connectivity number of 2.4.[27,28] For the films under consideration here, C 1s XPS[10] and ^{19}F and ^{13}C NMR[13,14] results show the connectivity numbers for the pulsed HFPO plasma films were ≤ 2.4, while the continuous film's connectivity number was 2.5, indicating a constrained network. This constrained network is evident in the tensile stress observed in Fig. 6-2(a). Similarly, the connectivity numbers for 10/100 films from $C_2H_2F_4$ and CH_2F_2 are 2.6 and 2.9, respectively, indicating even more highly constrained networks than the continuous HFPO case. These numbers track well with the magnitudes of the calculated stresses (HFPO, $C_2H_2F_4$ similar, CH_2F_2 more strained).

Figure 6-5 shows the ratio of film thicknesses b to a as a function of the overhang spacing for the 10/100 pulsed plasma depositions from all three precursors. All three precursors show a linear increase in b/a as the spacing is increased. Deposition from $C_2H_2F_4$ generally shows the highest degree of growth under the opening versus on top of the overhang, whereas growth from HFPO shows the lowest. However, considering the differences in the deposition profiles (i.e., fibers vs. no fibers, stress vs. no stress) it is actually quite surprising that all three precursors give such similar numbers at each cantilever separation.

It is of interest to take a closer look at the edge and underside of the overhang for these three 10/100 films. Figure 6-6(a) shows a close-up view of the edge of the overhang for a 10/100 pulsed plasma film from CH_2F_2, whereas Fig. 6-6(b) shows a close-up of the underside of the overhang near the edge of the trench for the same film. Similar profiles were observed for 10/100 films from both $C_2H_2F_4$ and HFPO. Fig. 6-6(a)

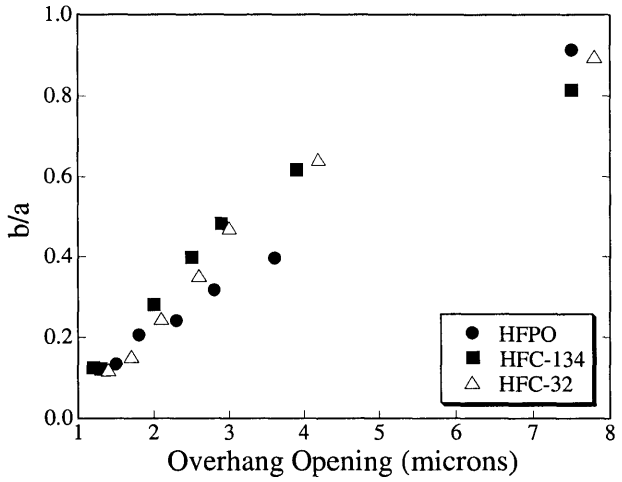

Figure 6-5: Ratio of thicknesses b and a versus cantilever separation for 10/100 pulsed films from all three precursors. All show a linear increase in b/a as the spacing is increased. Considering the differences in the deposition profiles (i.e., fibers vs. no fibers, stress vs. no stress) it is actually quite surprising that all three precursors give such similar numbers at each cantilever separation.

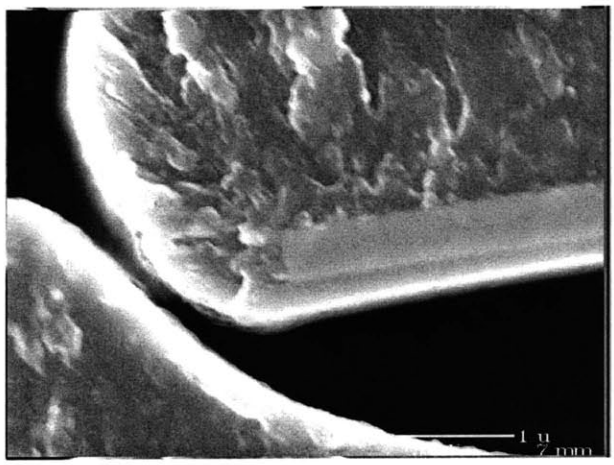

(a)

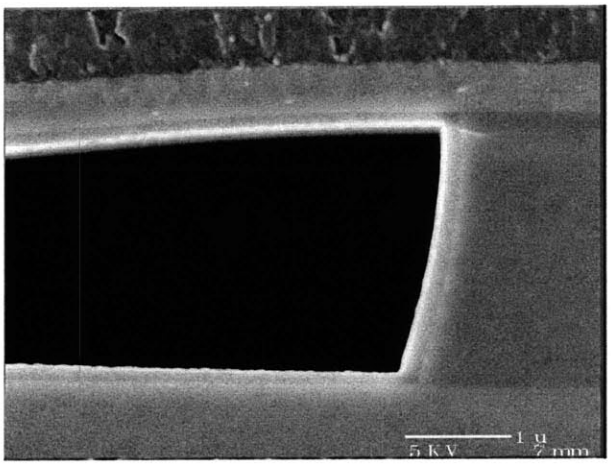

(b)

Figure 6-6: Cross-sectional SEM micrograph of 10/100 pulsed CH_2F_2 film showing (a) region at edge of cantilever and (b) region at edge of trench under cantilever. Similar profiles were observed for 10/100 films from both $C_2H_2F_4$ and HFPO. Fig. 6-6(a) clearly shows the lateral growth of the film out from the overhang resulting from both redeposition and LPCVD mechanisms. Fig. 6-6(b) similarly shows the liner of film grown under the overhang due to LPCVD. This liner specifically demonstrates the existence of a neutral pathway for film growth.

clearly shows the lateral growth of the film out from the polysilicon overhang resulting partially from redeposition mechanisms.

Fig. 6-6(b) similarly shows the liner of film which has grown under the overhang due to LPCVD. This liner specifically demonstrates the existence of a neutral pathway for film growth. As evidenced by the much thicker film in Region 1, pulsed PECVD is dominated by the ion-induced deposition pathway. In most vacuum polymerization systems it is thought that ions are the source of the observed rapid film growth. Systems such as parylene CVD are seen as exceptions to this rule.[3] However, by eliminating the role of ions from the plasma using techniques such as the overhang structure, downstream deposition,[2,6,7] or pyrolytic CVD,[4,5] it is possible to establish fluorocarbon film growth where the neutral pathway dominates. From Fig. 6-6(b) it is clear that for the 10/100 pulsed plasma systems from all three precursors, although ion-induced deposition is primary, the LPCVD component does contribute significantly to the overall growth.

Several key thicknesses were measured from these figures and have been identified as letters c, d, and e in Fig. 6-1. These correspond to: c = lateral growth from overhang, measured at midpoint of overhang, d = liner on wall of trench, measured at the midpoint, and e = growth under overhang, measured at edge of overhang adjacent to the overhang opening. A series of ratios of these dimensions are plotted in Fig. 6-7.

For all of these ratios, films from $C_2H_2F_4$ and CH_2F_2 appear to show the same deposition profiles, while the film from HFPO differs significantly. With respect to the film grown on top of the overhang, the HFPO pulsed plasma film shows a lesser degree of deposition at dimensions c, d, and e than the other two precursors. The film from HFPO also shows less growth directly under the overhang ("e") compared to the lateral

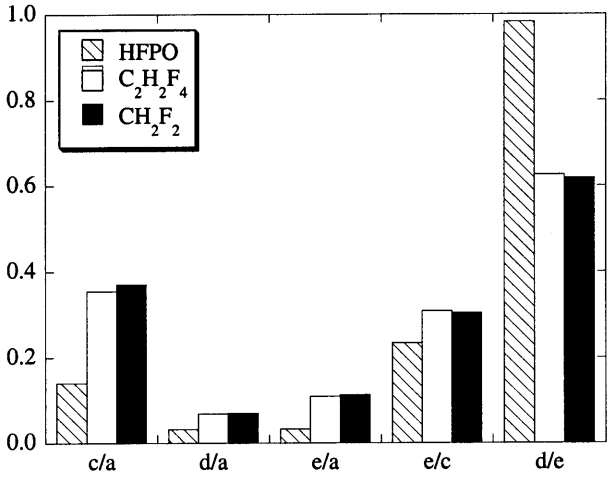

Figure 6-7: Ratios c/a, d/a, e/a, e/c, and d/e (see Fig. 6-1) for 10/100 pulsed films from all three precursors. Deposition from HFPO has smaller LPCVD and redeposition components than the $C_2H_2F_4$ and CH_2F_2 precursors. Redeposition is also less prevalent than LPCVD for growth from HFPO (d/e ~ 1). The similarity of the $C_2H_2F_4$ and CH_2F_2 film profiles can be attributed to their similar pulsed plasma chemistries, whereas the non-hydrofluorocarbon HFPO has a significantly different pulsed plasma chemistry, and therefore, a different profile.

dimension ("c") than the other precursors. However, as a result of this, the film from HFPO also has an almost 1:1 relation between the thickness directly under the overhang and that on the edge of the trench (d/e). This trend could indicate that although LPCVD appears to have a smaller role in the overall deposition mechanism for HFPO pulsed plasmas, redeposition is also present to a much smaller extent in this system versus the other two systems. The relative importance of each deposition mechanism in the PECVD cases discussed is summarized in Table 6-1.

The similarity between the profiles of the films from $C_2H_2F_4$ and CH_2F_2 can be attributed to the fact that their pulsed plasma chemistries share many similarities.[12] Both systems are known to be characterized by a competition between two dissociation pathways for the initial precursor: CF_2 formation and HF elimination.[12] These two pathways will yield many of the same deposition species for each plasma, thus resulting in the similar profiles. The minor differences in the profiles could be due to the different levels of that competition in each system. In contrast, the HFPO pulsed plasma system does not have an HF elimination pathway and is heavily dominated by its primary CF_2 decomposition pathway.[12] Therefore, this pulsed plasma lacks significant HF and free fluorine and does not have many of the other reactive species present in the hydrofluorocarbon systems of $C_2H_2F_4$ and CH_2F_2. Thus, the different reactive species generated in the HFPO pulsed plasma system result in a different deposition profile.

Section 6.5: Conclusions

Films from pulsed plasmas of HFPO, 1,1,2,2-$C_2H_2F_4$, and CH_2F_2 deposited onto overhang test structures revealed differences in the relative importance of mechanisms

Table 6-1. Summary of the relative importance of each deposition mechanism in the pulsed plasma systems from HFPO, $C_2H_2F_4$, and CH_2F_2, as well as the continuous HFPO plasma case. All show a predominance of ion-induced deposition, but the role of LPCVD, redeposition, and sputtering changes with the precursor and plasma conditions.

	Ion-induced deposition	LPCVD	Redeposition	Sputtering
Continuous PECVD HFPO	+++++	-	-	++
10/100 pulsed PECVD HFPO	++++	+	+	-
10/100 pulsed PECVD $C_2H_2F_4$	++++	+	++	-
10/100 pulsed PECVD CH_2F_2	++++	+	++	-

contributing to the overall fluorocarbon film growth process. Four growth mechanisms were considered: direct or ion-induced deposition, LPCVD, redeposition, and sputtering. All of the films investigated were dominated by direct or ion-induced deposition, but the role of the other mechanisms varied with the pulse conditions and precursor choice. In particular, deposition from neutral pathways becomes evident. Growth from continuous PECVD of HFPO showed significant sputtering but no LPCVD or redeposition, whereas pulsed plasma films from HFPO displayed the inverse behavior. Pulsed HFPO plasma films with longer pulse off times (100 and 400 ms) also show the formation of "string-like" fibers connecting the growth on top of the overhang with that beneath the overhang opening. These fibers may be due to either gas-phase or nucleation characteristics particular to these pulsed plasma conditions. As with the pulsed HFPO films, 10/100 pulsed plasma films from $C_2H_2F_4$ and CH_2F_2 also exhibit LPCVD and redeposition growth but no sputtering. However, redeposition was found to play a smaller role in the HFPO system than that of the other two precursors. The similarity of the $C_2H_2F_4$ and CH_2F_2 film profiles can be attributed to the similar pulsed plasma decomposition chemistries of these two hydrofluorocarbon precursors. HFPO, which contains no hydrogen, results in a significantly different pulsed plasma reaction network, and hence, a different growth profile. Tensile stress on the order of 1.3 GPa was observed for the continuous PECVD HFPO film, whereas compressive stresses of –1.2 and –1.8 GPa were seen in the 10/100 pulsed PECVD $C_2H_2F_4$ and CH_2F_2 films, respectively.

Section 6.6: Acknowledgments

The authors gratefully acknowledge the support of the Office of Naval Research, Lucent Technologies Bell Laboratories Graduate Research Program for Women, DuPont, and the NSF/SRC Engineering Research Center for Environmentally Benign Semiconductor Manufacturing. We would also like to thank James P. McVittie of Stanford University for providing us with the overhang test structures. This work made use of MRSEC Shared Facilities supported by the National Science Foundation under Award Number DMR-9400334.

Section 6.7: References

[1] K. Endo, *MRS Bull.* **1997**, **22**(10), 55.

[2] *Plasma Deposition, Treatment, and Etching of Polymers* (Ed: R. d'Agostino), Academic Press, Boston **1990**.

[3] H. Yasuda, *Plasma Polymerization*, Academic Press, New York **1985**.

[4] S. J. Limb, K. K. S. Lau, D. J. Edell, E. F. Gleason, K. K. Gleason, *Plasmas and Polymers* **1999**, (submitted).

[5] S. J. Limb, C. B. Labelle, K. K. Gleason, D. J. Edell, E. F. Gleason, *Appl. Phys. Lett.* **1996**, **68**(20), 2810.

[6] D. F. O'Kane, D. W. Rice, *J. Macromol. Sci.--Chem.* **1976**, **A10**(3), 567.

[7] D. G. Castner, K. B. Lewis, Jr., D. A. Fischer, B. D. Ratner, J. L. Gland, *Langmuir* **1993**, **9**, 537.

[8] C. R. Savage, R. B. Timmons, J. W. Lin, *Chem. Mater.* **1991**, **3**(4), 575.

[9] C. R. Savage, R. B. Timmons, J. W. Lin, in *Structure-Property Relations in Polymers: Spectroscopy and Performance,* Advances in Chemistry Series, Vol. 236, (Eds: M. W. Urban, C. D. Craver) ACS, Washington **1993**.

[10] S. J. Limb, D. J. Edell, E. F. Gleason, K. K. Gleason, *J. Appl. Polym. Sci.* **1998**, **67**, 1489.

[11] C. B. Labelle, K. K. Gleason, *J. Vac. Sci. Technol. A* **1999**, **17**(2), 445.

[12] C. B. Labelle, S. Karecki, R. Reif, K. K. Gleason, *J. Vac. Sci. Technol. A* **1999**, (submitted).

[13] K. K. S. Lau, K. K. Gleason, *J. Phys. Chem. B* **1998**, **102**(31), 5977.

[14] K. K. S. Lau, K. K. Gleason, *J. Electrochem. Soc.* **1999**, (in press).

[15] L.-Y. Cheng, J. P. McVittie, K. C. Saraswat, *Appl. Phys. Lett.* **1991**, **58**(19), 2147.

[16] C. Y. Chang, J. P. McVittie, J. Li, K. C. Saraswat, S. E. Lassig, J. Dong,*"Profile Simulation of Plasma Enhanced and ECR Oxide Deposition with Sputtering"*, IEDM Tech. Digest, **1993** (IEEE) 853.

[17] A. Burke, G. Braeckelmann, D. Manger, E. Eisenbraun, J. P. McVittie, J. Han, D. Bang, J. F. Loan, J. J. Sullivan, *J. Appl. Phys.* **1997**, **82**(9), 4651.

[18] J. Li, J. P. McVittie, J. Ferziger, K. C. Saraswat, J. Dong, *J. Vac. Sci. Technol. B* **1995**, **13**(4), 1867.

[19] C. B. Labelle, K. K. Gleason, *J. Appl. Polym. Sci.* **1999**, (submitted).

[20] R. C. Reid, J. M. Prausnitz, T. K. Sherwood, *The Properties of Gases and Liquids*, 3rd ed., McGraw-Hill, New York **1977**.

[21] P. W. Atkins, *Physical Chemistry*, 4th ed., W. H. Freeman and Company, New York **1990**.

[22] *Standard Handbook for Mechanical Engineers* (Ed: T. Baumeister), McGraw-Hill, New York **1967**.

[23] W. N. Sharpe, Jr.,*"Variation in mechanical properties of polysilicon"*, Proc. Int. Instrum. Symp., **1997**.

[24] M. T. Weise, S. C. Selbrede, L. J. Arias, D. Carl, *J. Vac. Sci. Technol. A* **1997**, **15**(3), 1399.

[25] D. R. Denison, J. C. Barbour, J. H. Brukhart, *J. Vac. Sci. Technol. A* **1996**, **14**(3), 1124.

[26] J. C. Phillips, *J. Non-Cryst. Solids* **1979**, **34**, 153.

[27] G. H. Dohler, R. Dandoloff, H. Bilz, *J. Non-Cryst. Solids* **1980**, **42**, 87.

[28] S. J. Limb, K. K. Gleason, D. J. Edell, E. F. Gleason, *J. Vac. Sci. Technol. A* **1997**, **15**(4), 1814.

Chapter 7

Pulsed Plasma Deposition from 1,1,2,2-$C_2H_2F_4$, CHF_3, and HFPO by Electron Cyclotron Resonance

Section 7.1: Abstract

High/low and on/off pulsed ECR plasmas from 1,1,2,2-$C_2H_2F_4$, CHF_3, and HFPO have been used to deposit fluorocarbon films. Films deposited from $C_2H_2F_4$ by both pulsing techniques have similar compositions, but the on/off pulsed plasma films tend to be less fluorinated, and defluorination occurs within the high/low pulsed plasma films as precursor flow rate increases. High/low pulsed CHF_3 ECR plasma films are more heavily dominated by CF_2, while there is no detectable growth from high/low pulsed HFPO ECR plasmas. Optical emission spectroscopy (OES) of all of these plasmas shows high intensity peaks for H, C_2, and C_3, with lower intensity CF_2 and F peaks. The dominant OES peak shifts from H_α to C_2 when the pressure is reduced for on/off pulsing from $C_2H_2F_4$, most likely a result of the increased electron temperature at the lower pressure. The presence of etch-related species such as CO and F in the HFPO pulsed plasma likely accounts for the lack of growth. Gas-phase recombination reactions may be occurring between the OES sampling region and the deposition substrate, producing fluorocarbon molecular deposition species, and thus accounting for the high degree of fluorination seen in the deposited films. Comparison with the corresponding pulsed parallel plate plasma systems shows significant differences in both plasma species and deposited film composition. Parallel plate plasmas are characterized by high intensity CF_2 peaks, with only low intensity peaks for C_2 and H species. Surprisingly, the ECR plasmas produce more highly fluorinated films than the parallel plate plasmas. Fundamental differences between high and low density plasmas (i.e., electron temperature, fractional ionization, etc.) may account for these differences.

Section 7.2: Introduction

Fluorocarbon plasmas are used extensively throughout the semiconductor industry in both etching and cleaning processes.[1,2] The plasma deposition of fluorocarbon films has been studied for many years,[3,4] and only recently has been considered for use in low κ applications.[5] These low-κ materials would yield reductions in propagation delay, power consumption, and cross-coupling noise between adjacent lines, all of which would enable the implementation of future generations of integrated circuit design rules.[6-9] In order to implement these new materials, however, a host of film property and processing requirements, some of which conflict, must be met. [6-8] Therefore, the ability to tailor a process to produce films with a specific set of properties is much desired.

A variety of different precursors are currently used in plasma enhanced chemical vapor deposition (PECVD), including CF_4, C_2F_4, C_2F_6, C_3F_8, c-C_4F_8, C_6F_6, CHF_3, CH_2F_2, $C_2H_2F_4$, and C_3F_6O (hexafluoropropylene oxide), to name a few.[3,10-12] Surprisingly, however, it has been found that films of similar composition can be deposited from dissimilar precursors. For example, films having F:C ratios between 1.0 and 1.3 have been grown from CF_4, C_2F_6, C_4F_8, C_9F_{18}, and CHF_3 using both conventional parallel plate and high density plasma sources.[10,13-16] In an effort to expand the range of film compositions which can be deposited, many researchers have investigated gas mixtures in order to tailor film composition. Typical additives include H_2 and O_2,[17,18] while mixtures of hydrofluorocarbons with pure fluorocarbons (e.g., $C_4F_8 + CH_4$)[19,20] or linear fluorocarbons with cyclic fluorocarbons (e.g., $C_2F_6 + C_6F_6$) are also being studied.[21,22]

More recently, the use of pulsed plasmas as a means to control the plasma deposition environment has gained recognition.[11,16,23,24] In this process, rf power is

applied for a specified "on" time, followed by an "off" period during which no excitation is used. During the "on" time, both ions and reactive neutrals are produced. However, since ions often have shorter lifetimes than neutrals, during the "off" time the ratio of neutrals to ions will increase, and thus, the process equilibrium will be shifted to favor film deposition from reactive neutrals. Therefore, the overall chemistry of these plasmas should be much more sensitive to the original precursor molecules than their continuous counterparts, and it should be possible to develop a range of fluorocarbon films with different film properties from a single precursor.

Several pulsed plasma chemistries employing capacitively coupled plasma sources (i.e., parallel plate reactors) have been studied in detail.[11,16,23,25,26] Typically, pulse modulation on the millisecond scale is used for these low density plasmas. For hexafluoropropylene oxide (HFPO, 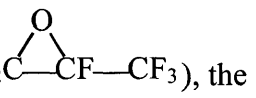), the film changes dramatically with pulse off time. At very short pulse off times (10 ms on, 20 - 60 ms off time), films contain almost equal fractions of CF_3, CF_2, CF, and quaternary carbon (C-CF), whereas at longer pulse off times, the film composition becomes increasingly dominated by CF_2.[11,23,27,28] Similar control for CF_3 has been observed for pulsed plasma deposition from a trimer of C_9F_{18} compounds.[16] Deposition from other feed gases such as 1,1,2,2-$C_2H_2F_4$ and CH_2F_2 is less influenced by the pulse on and off times, but their pulsed plasma chemistries are significantly influenced by the neutral reactions occurring during the pulse off time.[25,26] Specifically, for these two precursors, the influence of two competing dissociation pathways on the generated pulsed plasmas, and, hence, the deposited films is clearly seen.[26]

The use of pulsed power modulation in high density plasma (HDP) systems has been less widely investigated. Two different pulse timing regimes are employed for HDP processes. Typically, microsecond pulsing is used in etching applications where it has been found to be very effective at reducing notching effects, both in electron cyclotron resonance (ECR)[29-31] and inductively coupled plasmas (ICP).[32] Periods of 10 – 100 μs are used for both on and off pulse times. For deposition, some researchers use μs pulsing, usually with ICP sources,[33,34] while others use ms pulsing, usually with ECR sources.[14,35] Pulse times for the deposition processes range from 10 – 400 μs and 10 – 20 ms for on times, and 5 – 400 μs and 10 – 100 ms for off times. Takahashi et. al.,[14,17,18,35-37] have closely examined the gas phase characteristics of ms-pulsed ECR plasmas from CHF_3, as well as the resulting films. As in the parallel plate pulsed plasma systems, films deposited in the ECR system also displayed a variation in composition due both to pulse conditions and the addition of either H_2 or O_2 to the feed gas.[17,18] However, it should be noted that CHF_3 is the only (hydro)fluorocarbon precursor which has been studied in detail in a ms-pulsed ECR plasma.

In this work, millisecond-pulsed ECR plasmas from 1,1,2,2-$C_2H_2F_4$, CHF_3, and HFPO have been used to deposit fluorocarbon films. The composition of each film was determined by Carbon 1s x-ray photoelectron spectroscopy (C1s XPS), while optical emission spectroscopy (OES) was employed during deposition to identify the primary optically excited species present in the pulsed plasmas. The deposited film compositions were found to vary with precursor flow rate and chamber pressure, and were distinctly different from the corresponding films deposited in a conventional parallel plate reactor.

The differences in deposition environments between the parallel plate reactor and the ECR reactor were clearly evident in the OES spectra from each reactor.

Section 7.3: Experimental

Figure 7-1 shows a schematic of the high density plasma system, which is equipped with a Wavemat MPDR 325i electron cyclotron resonance (ECR) source employing cavity tuning. The plasma is generated in a quartz bell jar and confined by a set of permanent magnets which extend 5" below the bell jar. The gas inlet is located directly under the quartz bell jar. Five inch diameter silicon (Si) wafers were placed in the mechanically clamping wafer chuck via a load lock equipped with a transfer arm. The deposition surface is ~ 5" below the magnetic confinement ring. The wafer chuck is equipped for independent biasing and He backside cooling; however, neither bias nor cooling was utilized in these experiments since it was found that there was insignificant wafer heating when bias was not employed. The ECR system was evacuated using a 3300 L/s turbomolecular pump (TH3000M, Osaka Vacuum) backed by a 50 cubic feet per minute (CFM) roughing pump (2063, Alcatel). Typical base pressures of ~ 10^{-7} Torr were achieved with the elastomer (Viton) o-ring seals used in the system. Operating pressures ranged from 2 – 10 mTorr.

Two different microwave power supplies were used to generate pulsed plasma excitation. The large majority of the experiments were performed using an ASTeX/Gerling Laboratories (AGL) Model GL134 2.45 GHz 1 kW Low Ripple Variable Power Supply which was capable of "high/low" pulsing. This high/low pulsing consists of modulating between low and high power levels. The AGL unit can be modulated on

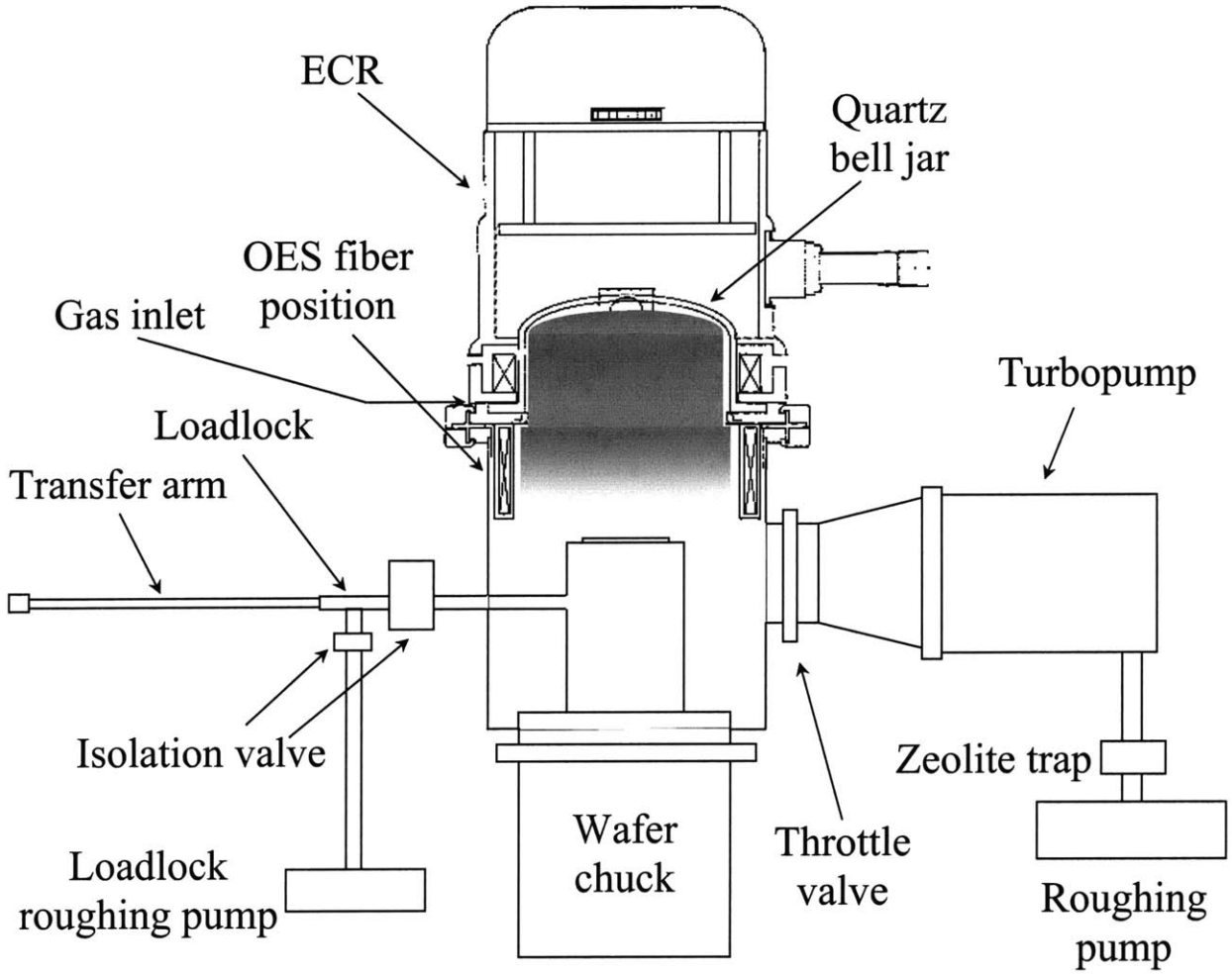

Figure 7-1: Schematic of Electron Cyclotron Resonance (ECR) deposition system. It is equipped with a Wavemat MPDR 325i ECR source employing cavity tuning, a 5" diameter mechanically clamping wafer chuck, and a load lock entry system. Pulsed microwave excitation is provided by either an ASTeX/Gerling Laboratories (AGL) Model GL134 2.45 GHz 1 kW Low Ripple Variable Power Supply capable of "high/low" pulsing, or a Muegge Electronics Model ML1250D-100TE 2.45 GHz 1.25 kW Low Ripple Pulsable Power Supply capable of true "on/off" pulsing. Both supplies are pulsed on the millisecond time scale.

the ms time scale from a minimum power of 300 W (low power level) to powers of up to 1000 W (high power level). Further experiments used a Muegge Electronics Model ML1250D-100TE 2.45 GHz 1.25 kW Low Ripple, Pulsable Power Supply, which was capable of true "on/off" pulsing on the ms time scale. The timing for both microwave supplies was driven by a variable DC voltage signal from a Systron-Donner Model 110 C pulse generator.

Plasmas were generated from 1,1,2,2-$C_2H_2F_4$, CHF_3, and hexafluoropropylene oxide (HFPO) using a pulse on (or high) time of 10 ms and pulse off (or low) times of 20, 50, and 400 ms. Precursor flow rates varied from 20 to 70 sccm. All of the high/low pulsing experiments were performed at 10 mTorr; on/off pulsing experiments used either 5 or 10 mTorr. High/low pulsed ECR plasma films were obtained from $C_2H_2F_4$ and CHF_3, but no deposition was observed from HFPO. On/off pulsing yielded films from $C_2H_2F_4$; the other two precursors have not been tried yet.

Film thicknesses and refractive indices were determined by single-wavelength ellipsometry (Rudolph Research AutoEl II Ellipsometer, Gaertner Scientific Corporation L116A Ellipsometer). Single wavelength ellipsometry was done with a He-Ne laser (6328 Å) at an angle of incidence of 70°. The magnitude of the film thicknesses was confirmed by profilometry (Tencor P-10 Surface Profilometer). *In situ* laser interferometry was used to monitor film growth during deposition.

Carbon-1s x-ray photoelectron spectroscopy (C-1s XPS, Physical Electronics Model 5200C employing a Mg $K\alpha_{1,2}$ exciting radiation source) was used to determine the relative concentrations of CF_3, CF_2, CF, and $\underline{C}$-CF in each deposited film using the same

analysis method techniques as Limb et al.[23] F:C ratios were calculated from the regressed CF_x concentrations.

Plasma species were monitored by optical emission spectroscopy (OES). An Ocean Optics S2000 OES configured with a 10 μm slit, 200 – 800 nm grating, and UV/VIS upgrade was used in conjunction with a 600 μm optical fiber equipped with a UV collimating lens. The OES was operated in scope mode, in which the raw light intensity from the plasma was sampled. A dark spectrum was subtracted from each spectrum. Spectral integration times were optimized for each plasma condition to obtain a strong signal. Typical integration times varied from 1000 – 2000 ms.

Actinometry involves comparing the emission intensity of a species of interest with that of an inert species added to the feed gas.[38] Only a small amount of the inert gas is added in order to minimize its effect on the plasma as a whole. The emission intensity for species *i* from a particular excited state can be expressed as:

$$I_i = \Gamma_i k_i [e-][i] \qquad (1)$$

where I_i is the intensity of the emission from species *i* (either the species of interest, X, or the actinometer), Γ_i is the branching ratio for emission relative to all other de-excitation paths, k_i is the excitation efficiency for species *i*, [e-] is the electron density, and [*i*] is the concentration of species *i*.[39] The excitation efficiency, k_i, is a function of the electron energy distribution and the excitation cross section:

$$k_i = \int_0^\infty v(\varepsilon)\sigma_i(\varepsilon)f(\varepsilon)d\varepsilon \qquad (2)$$

where ε is the electron energy, v(ε) is the electron velocity, $\sigma_i(\varepsilon)$ is the collision cross section for the excitation of *i*, and f(ε) is the electron energy distribution.[39] Actinometry

allows calculation of unknown species densities by scaling the emission intensity of a particular species of interest, X, with the emission intensity of the actinometer:

$$\frac{I_X}{I_{Act}} = \frac{\Gamma_X k_X [e-][X]}{\Gamma_{Act} k_{Act} [e-][Act]}. \qquad (3)$$

For the emission intensities to be directly proportional to the species concentrations, $\frac{\Gamma_X k_X}{\Gamma_{Act} k_{Act}}$ must be constant. Therefore, valid actinometry requires that the actinometer and species X undergo the same excitation path (electron impact), the relaxation occurs exclusively by photoemission or by photoemission plus a parallel de-excitation pathway with a constant branching ratio, and that both species have similar cross-section functionality with energy.[38,39]

Actinometry is commonly used to measure F concentrations in fluorocarbon plasmas using an Ar actinometer, where these conditions are met.[38,40,41] However, application of actinometry to molecular species such as CF_2 is more complicated, since the molecular and actinometer threshold energies are typically significantly different. For example, the excitation threshold of CF_2^* is ~ 4.5 eV, while that of Ar^* is 13.5 eV (for the 750.4 nm emission line).[39] Molecular actinometers such as N_2 have been used,[42] but the system is complicated by the potential dissociation of N_2. Recent work by Kiss et al. has suggested relaxing the excitation threshold matching requirement in cases where the electron energy distributions can be assumed constant.[39] They have found for a CF_4 plasma system that this assumption is valid over a range of process conditions (500 – 1000 mTorr, 20 – 100 W), and that actinometry can be applied to the molecular species present in order to compare two different spectra.

A small percentage of Ar (2 sccm) was added to most runs discussed in this work in order to allow normalization of the spectra via actinometry. It is assumed that the electron energy distributions remain relatively constant for the parameter space investigated. Table 7-1 lists OES emission assignments used in this work.[43,44]

Section 7.4: Results and Discussion

Section 7.4.1: Deposition Rates

Figure 7-2 shows deposition rates (Å/min) as a function of precursor flow rate for films deposited from $C_2H_2F_4$ and CHF_3. No deposition was observed for HFPO under the conditions tested. Open circles represent films deposited from $C_2H_2F_4$ using high/low pulsing with a pulse high time (i.e., high power plasma) of 10 ms and pulse low times (i.e., low power plasma) of 20, 50, and 400 ms. Since the plasma never completely extinguished, the length of the pulse low time did not significantly affect the observed deposition rates. At a low power of 350 W, three different pulse "high" levels were used, 400, 535, and 670 W. These conditions corresponded to average applied powers of 351 – 370 W, 355 – 412 W, and 360 – 460 W, respectively. Each range reflects the variation in pulse timing. For example, 10 ms high/50 ms low (10/50) results in higher average powers than 10/400. Deposition rate was found to increase only slightly (2 – 3%) with increasing average power for a constant pulse rate, and therefore, all data for a particular flow rate are plotted on the same graph. Fig. 7-2 shows a fairly linear increase in deposition rate with $C_2H_2F_4$ flow rate. A large amount of deposition occurs on the ECR quartz bell jar during all runs, and therefore, a portion of the increase in deposition rate can be attributed to a lack of material available for deposition in the wafer region.

Table 7-1. Optical emission spectroscopy wavelength assignments used in this work.

Species	OES Wavelength (nm)	Emission Band System
CF_2	245 - 321	
C_2	516.5	Swan System
	473.7	↓ Decreasing intensity
	563.6, 558.6, 471.5	
	469.8	
	512.9	
C_3	405.1	Comet-Head Group
CH	431.4	4300 Å System
CO	561.0, 519.8, 483.5, 451.1	Ångström System
	283.3	Third Positive System
	297.7	↓ Decreasing intensity
	313.4	
	330.6	
	349.3	
H	656.2	H_α
	486.1	H_β
	434.0	H_γ
F	685.6	↓ Decreasing intensity
	703.7	
	712.8	
	775.4	
	690.2, 720.2, 731.1, 780.0	
	624.0	
	634.8, 739.9	
C	283.7, 426.7, 723.6	
Ar	811.5	↓ Decreasing intensity
	801.5, 763.5	
	810.4, 800.6, 794.8, 750.3	
	772.4	
	738.4, 706.7, 696.5	

Refs: Reader & Corliss (# 43); Pearse & Gaydon (# 44)

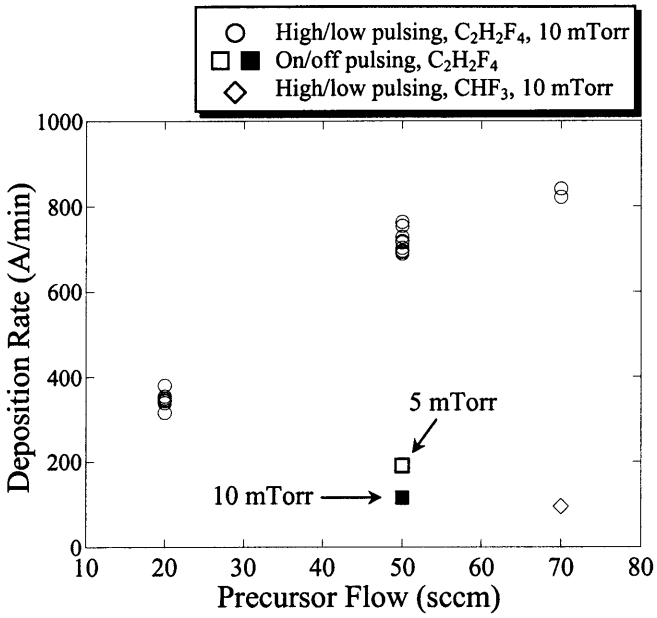

Figure 7-2: Deposition rates (Å/min) as a function of precursor flow rate for films deposited from $C_2H_2F_4$ and CHF_3. No deposition was observed for HFPO under the conditions tested. Open circles represent films deposited from $C_2H_2F_4$ using high/low pulsing for a variety of pulse cycling conditions at three different high level powers (low level power fixed). Deposition rate was found to increase only slightly (2 – 3%) with increasing average power for a constant pulse rate, and there was no significant trend with the length of the pulse low time, so all data for a particular flow rate are plotted on the same graph. The open diamond represents deposition from CHF_3 using high/low pulsing. The open and closed squares represent films deposited from $C_2H_2F_4$ plasmas using on/off pulsing. The open square represents 10/50 pulsing at 5 mTorr with a peak power of ~ 850 W (average power ~ 140 W), while the closed square is for 10/50 pulsing at 10 mTorr with a peak power of ~ 775 W (average power ~ 130 W).

Increasing the precursor flow rate mitigates this effect somewhat, allowing for increased deposition on the substrate.

The open diamond in Fig. 7-2 represents deposition from CHF_3 using high/low pulsing. A pulse rate of 10/50 was used, with a pulse high level of 400 W. Deposition rates were below the detection limit (~ 25 Å/min) at flow rates < 70 sccm.

Finally, the open and closed squares in Fig. 7-2 represent films deposited from $C_2H_2F_4$ plasmas using on/off pulsing. The open square represents 10/50 pulsing at 5 mTorr with a peak power of ~ 850 W (average power ~ 140 W), while the closed square is for 10/50 pulsing at 10 mTorr with a peak power of ~ 775 W (average power ~ 130 W). The deposition rate almost doubles when the pressure is decreased from 10 to 5 mTorr. Similar deposition rate increases with pressure decreases in high density plasma systems have been seen in the literature.[15,45]

Section 7.4.2: Deposition from $C_2H_2F_4$

Figure 7-3 shows C1s XPS spectra for10/50 high/low pulsed ECR plasma films from $C_2H_2F_4$ at three different flow rates. For these and all subsequent high/low pulsed plasma films, the high level was 400 W and the low level was 350 W. The percentage of CF_3, CF_2, CF and quaternary carbon (C-CF) species in each film is identified, along with the overall F:C ratio and film refractive index (n_f). Fourier Transform Infrared Spectroscopy (FTIR) measurements (not shown) indicate that no hydrogen is incorporated into either the films deposited from $C_2H_2F_4$, or those deposited from CHF_3 (see below).

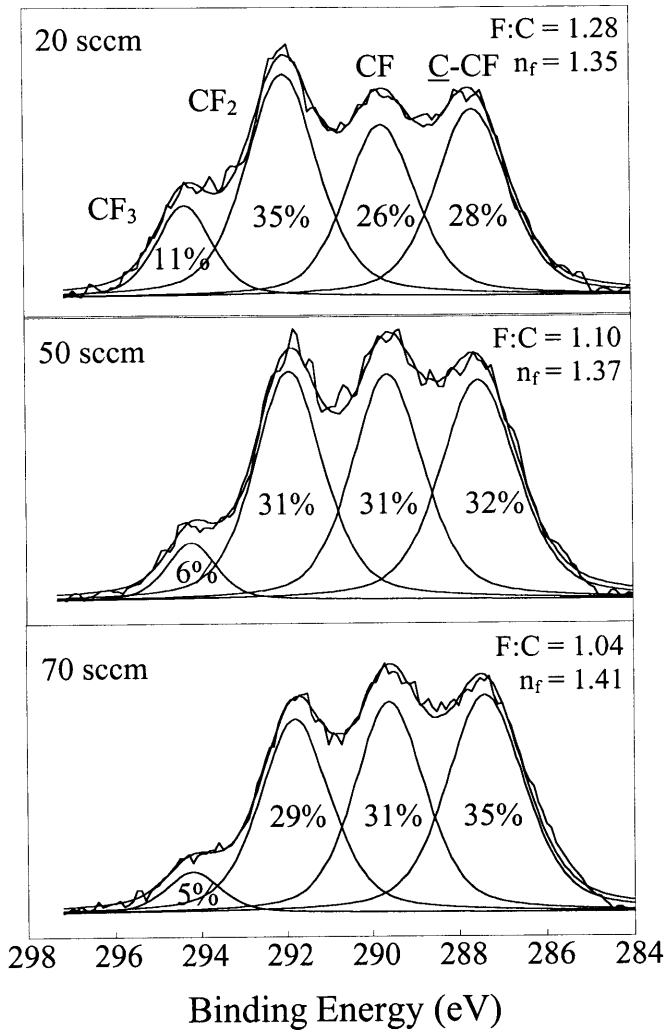

Figure 7-3: Carbon 1s XPS spectra for10/50 high/low pulsed ECR plasma films from $C_2H_2F_4$ at three different flow rates with a pulse high level of 400 W and a low level of 350 W. The percentage of CF_3, CF_2, CF and quaternary carbon (C-CF) species in each film is identified, along with the overall F:C ratio and film refractive index (n_f). Fourier Transform Infrared Spectroscopy (FTIR) measurements (not shown) did not detect hydrogen incorporation into any of these films. The three films are largely similar, but there is a shift to less fluorinated structures as the $C_2H_2F_4$ flow rate is increased.

In general, the three films are largely similar in composition. The main difference lies between 20 sccm and higher flow rates, where a shift from highly fluorinated species to less fluorinated species takes place. The largest shift occurs between 20 and 50 sccm, where the % CF_3 is reduced by half. A small decrease in CF_2 also occurs during this transition, and more CF_2 is lost when the flow rate is increased to 70 sccm. This reduction in fluorine is also reflected by the refractive index, which increases from 1.35 to 1.41 as the flow rate increases from 20 to 70 sccm (see Fig. 7-2). Further XPS analysis (not shown) revealed that film composition did not vary significantly with the magnitude of the high power level or the duration of the low power level.

Figure 7-4 shows OES data for 10/50 high/low pulsed plasmas from $C_2H_2F_4$ for all three flow rates. The spectra are dominated by C_2, C_3, and H species, with lower intensity CF_2 and F peaks. The primary peak is H_α at 656.2 nm, followed by the 516.5 nm C_2 peak. A small amount of Ar (2 sccm) was included as an actinometer and each spectrum has been normalized to the 750.3 nm Ar peak intensity. However, the validity of using this normalization to compare the 20 sccm spectrum with the higher flow rate spectra is not clear. The normalization assumes that the electron energy distributions of all the plasmas are approximately the same. However, although the intensities of H_α and H_β track consistently between the low and high flow rate spectra (H_α(high flow)/H_α(low flow) and H_β(high flow)/H_β(low flow) are both similar), the H_γ intensities do not (H_γ(high flow)/H_γ(low flow) > corresponding H_α, H_β ratios), indicating that the electron energy distributions of the 20 sccm and the higher flow rate plasmas are not similar enough to warrant direct comparison via the actinometric normalization. The three H ratios *are* approximately constant between the 50 and 70 sccm spectra, and so the normalization can

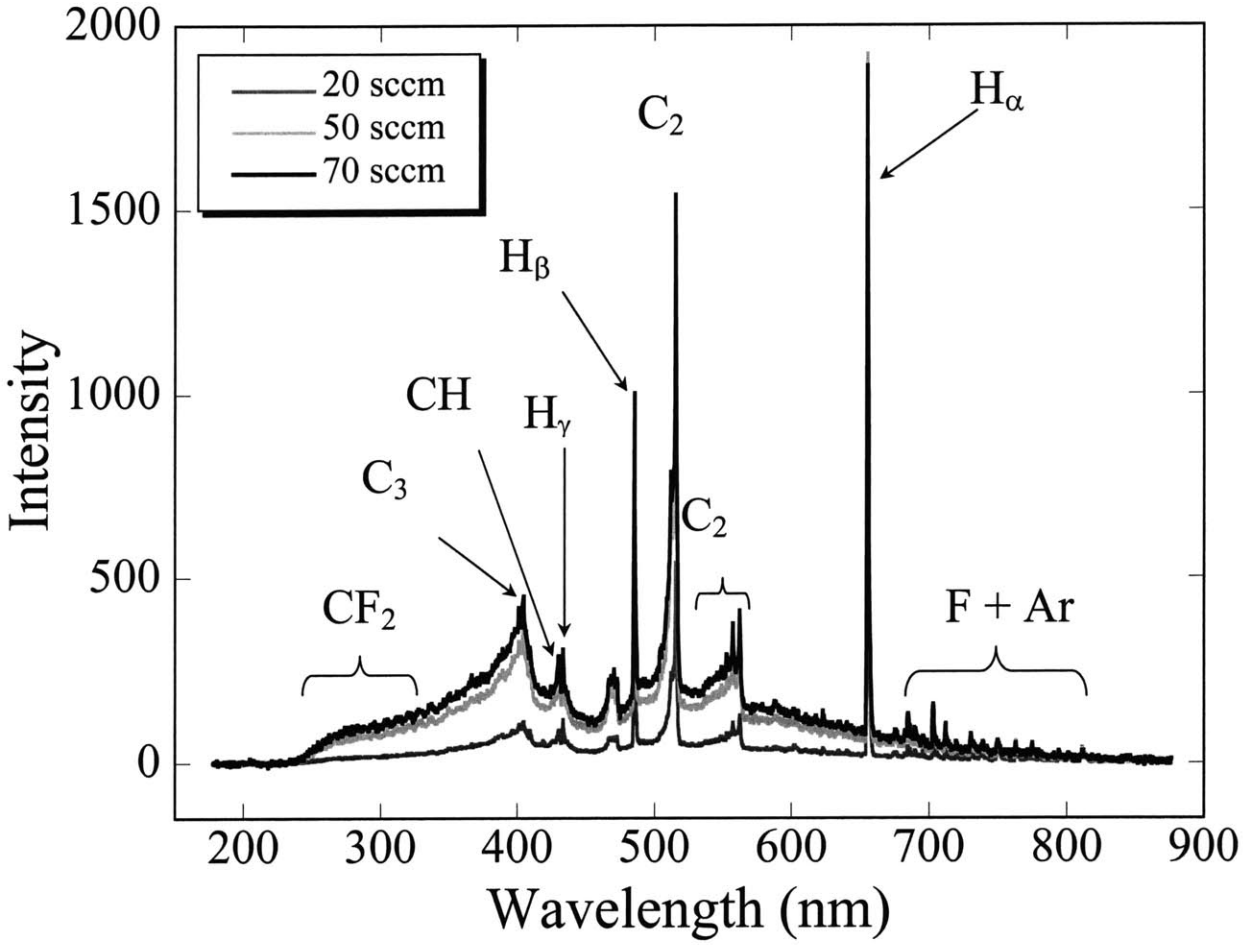

Figure 7-4: Optical emission spectra for 10/50 high/low pulsed plasmas from $C_2H_2F_4$ for precursor flow rates of 20, 50, and 70 sccm. The spectra are dominated by C_2, C_3 and H species, with low intensity CF_2 and F peaks. The primary peak is H_α at 656.2 nm, followed by the 516.5 nm C_2 peak. The overall spectral intensity increases with $C_2H_2F_4$ flow rate, most likely as a result of cavity resonance mode-hopping at the higher flow rates.

be assumed valid between those two flow rates. The main difference between the 20 sccm plasma and those at the higher flow rates was the onset of oscillation between cavity resonance modes ("mode-hopping") at the higher flow rates (oscillation period ~ 1 second). This phenomenon may have induced higher plasma-energy resonance modes than that seen for the 20 sccm plasma, thus producing a different electron energy distribution.[46] Comparing the 50 and 70 sccm spectra, there is a slight increase in spectral intensity with $C_2H_2F_4$ flow rate. As flow increases, the electron temperature is expected to decrease, theoretically resulting in decreased fragmentation and reduced OES intensity.[47,48] The minor intensity variation seen in Fig. 7-4 may be due to oscillation between slightly different resonance modes at each flow rate, which would counteract the expected decreases in fragmentation.

It is actually quite surprising that given the elemental nature of the species observed by OES, the deposited films contain relatively large concentrations of CF_2 and CF_3. These spectra were taken at a position in the chamber approximately 8 inches above the deposition substrate. Typical mean free paths at 10 mTorr are on the order of millimeters,[49] and therefore, it is possible that, rather than carbon depositing on the substrate and undergoing subsequent fluorine addition, gas-phase recombination reactions are occurring, resulting in molecular fluorocarbon deposition species. Diamond deposition from ECR plasmas of $CH_4 + H_2$ shows some evidence of this behavior, where H, CH, and C_2 species are detected in the plasma via OES, but CH_3 is acknowledged as the primary deposition species.[50-53]

A clearer picture of the differences between the spectra shown in Fig. 7-4 can be obtained by looking at the ratios of several of the dominant peaks. Figures 7-5(a) and (b)

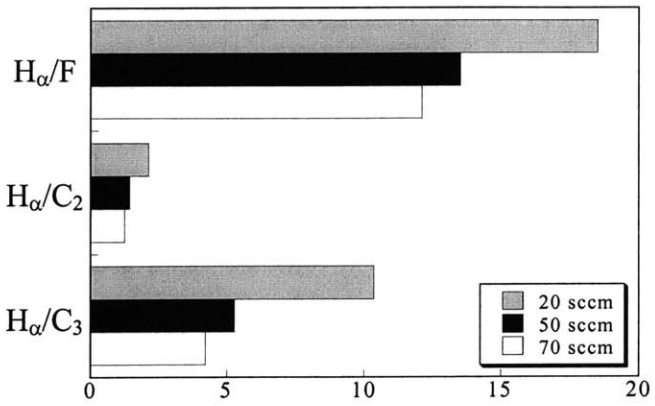

(a)

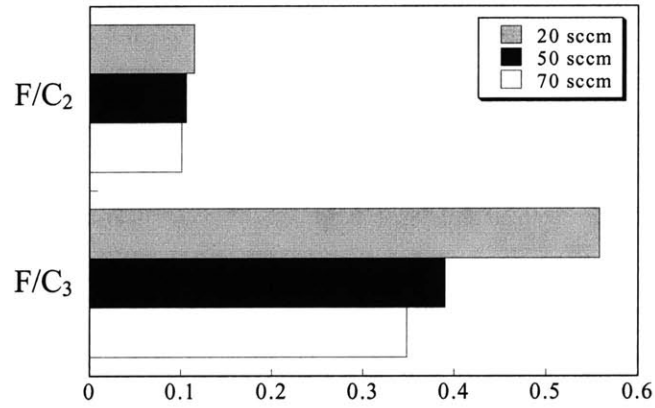

(b)

Figure 7-5: Spectral intensity ratios for several of the dominant OES peaks from Fig. 7-4 (H_α @ 656.2 nm, C_2 @ 516.5 nm, C_3 @ 405.1 nm, and F @ 703.8 nm). Generally, H_α decreases with respect to the other species, while F decreases with respect to C_2 and C_3 as the $C_2H_2F_4$ flow rate is increased. These ratios reflect the trend towards molecular vs. elemental plasma species as flow rate increases (i.e., H and F present as HF vs. elemental H & F). The energy input per molecule decreases as flow increases, leading to decreased dissociation of the excited species.

show a series of ratios for the H_α (656.2 nm), C_2 (516.5 nm), C_3 (405.1 nm), and F (703.8 nm) peaks. Generally, H_α decreases with respect to the other species, while F decreases with respect to C_2 and C_3 as the $C_2H_2F_4$ flow rate is increased. The amount of plasma energy input per precursor molecule can be quantified by the parameter $W/(F_i*M_i)$, where W is the applied power (watts), F_i is the flow rate of gas i (sccm), and M_i is the molecular weight of gas i (g/mol).[3] For an average ECR power of 360 W (10/50 high/low plasma), the values of W/FM are 2.4×10^5, 9.5×10^4, and 6.8×10^4 J/g for $C_2H_2F_4$ flow rates of 20, 50, and 70 sccm, respectively. Thus, at lower flow rates the increased energy input per molecule could result in increased dissociation, leading to a dominance of elemental vs. molecular species in the plasma. The ratios in Figs. 7-5(a) and (b) reflect this trend, with both elemental H and F having the highest concentrations at the lowest flow rate (see ratios H_α/F, F/C_2, and F/C_3). This trend may partially account for the decrease in film fluorine concentration as the flow rate is increased from 20 to 70 sccm.

Figure 7-6 shows C1s XPS spectra for three films, all deposited from 50 sccm of $C_2H_2F_4$ under 10/50 pulsed ECR excitation. At 10 mTorr, both high/low and on/off pulsing was performed. On/off pulsing was also performed at 5 mTorr. The peak powers for the 10 and 5 mTorr on/off pulsing were 775 and 850 W, respectively, corresponding to average powers of ~ 130 and ~ 140 W. The high/low pulsing power levels were the same as discussed above (400 W high/350 W low). Each spectrum has been normalized to the same total integrated area. Table 7-2 lists the percentage of each CF_x (x = 1 – 3) species, the F:C ratio, and the refractive index for each film.

Fig. 7-6 shows that at 10 mTorr, on/off pulsing results in more CF_3 and C-CF and less CF_2 and CF in the film than high/low pulsing. While the differences are small for

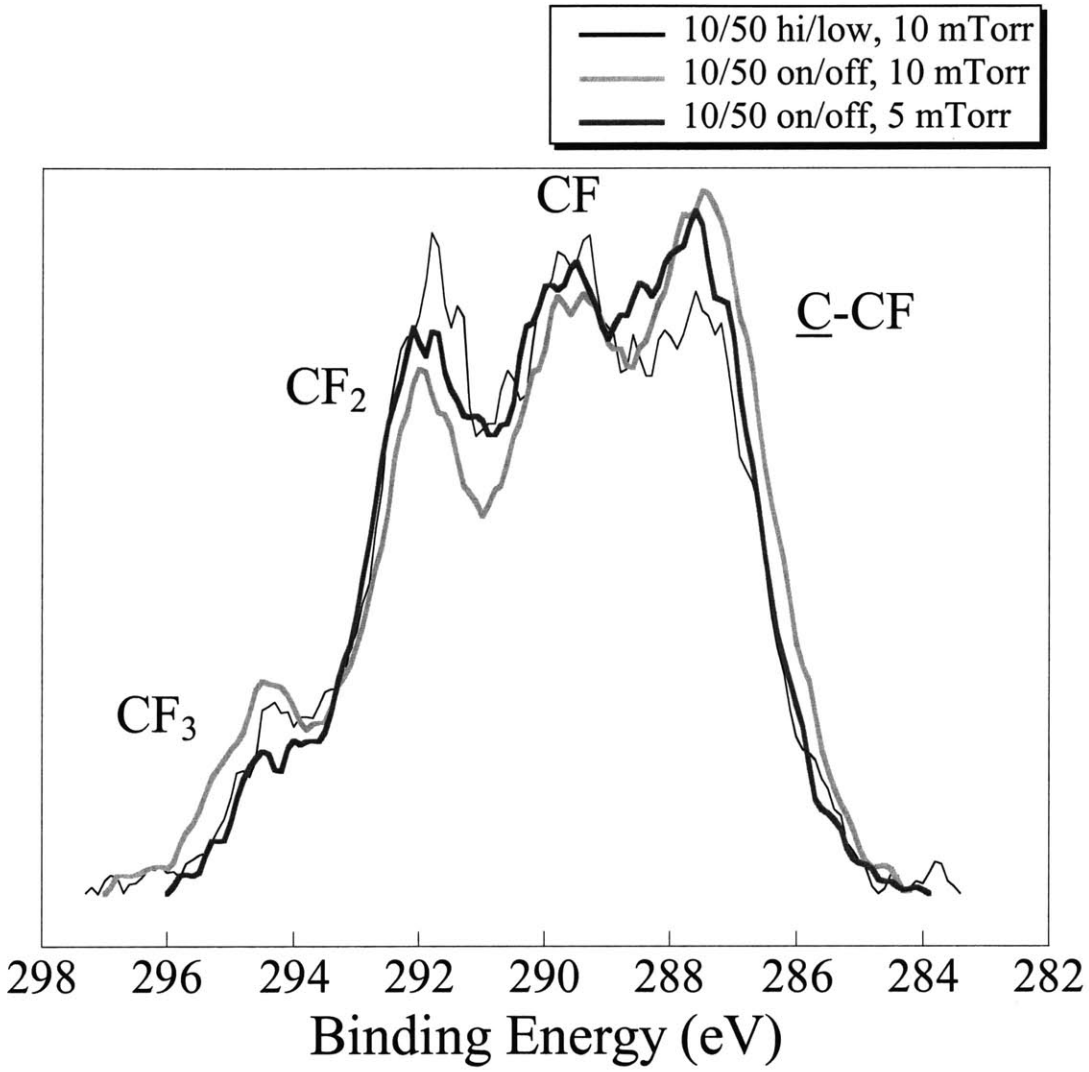

Figure 7-6: Carbon 1s XPS spectra for three films, all deposited from 50 sccm of $C_2H_2F_4$ under 10/50 pulsed ECR excitation. At 10 mTorr, both high/low and on/off pulsing was performed. On/off pulsing was also performed at 5 mTorr. Each spectrum has been normalized to the same total integrated area. A trade between CF_2 and C-CF occurs when switching from high/low to the on/off pulsing. Reducing the pressure from 10 to 5 mTorr for on/off pulsed deposition results in a slight shift from CF_3 to CF_2 and CF species.

Table 7-2. Percentages of CF_3, CF_2, CF, and C-CF species and F:C ratios as obtained from C-1s XPS for films deposited using 10/50 pulsing from $C_2H_2F_4$. The effects of high/low versus on/off pulsing as well as pressure can be seen.

Film	% CF_3	% CF_2	% CF	% C-CF	F:C	n_f
High/low, 10 mTorr	6	31	31	32	1.10	1.37
on/off, 10 mTorr	8	22	31	39	1.01	1.47
on/off, 5 mTorr	3	30	33	34	1.01	1.51

CF_3 and CF, there appears to be a definite trade between CF_2 and C-CF when switching to the on/off pulsing. The on/off pulsing also results in films with lower F:C ratios and correspondingly higher refractive indices (see Table 7-2). It is interesting to note that while mode-hopping was seen for the high flow rate high/low pulsed plasmas, no mode-hopping was observed during on/off pulsing. This distinction may account for the differences in film composition between depositions from high/low and on/off pulsed plasmas.

Reducing the pressure for on/off pulsed deposition shows a slight shift from CF_3 to CF_2 and CF species (Fig. 7-6). The F:C ratio is the same for both films, but the refractive index of the 5 mTorr film is slightly higher than that of the 10 mTorr film, reflecting the loss of CF_3 groups.[54] The slight compositional change may be due to the slightly higher peak power employed for the 5 mTorr versus the 10 mTorr deposition (~ 850 vs. ~ 775 W), which would promote increased surface rearrangement. The 5 mTorr pulsed plasma has a slightly higher peak power since it was difficult to strike at the lower power level, but the average powers are similar enough to warrant comparison of the deposited films.

Figure 7-7(a) shows OES spectra from 10/50 $C_2H_2F_4$ high/low and on/off pulsed plasmas at 10 mTorr, while Figure 7-7(b) compares 10/50 $C_2H_2F_4$ on/off pulsed plasmas at 5 and 10 mTorr, all at a $C_2H_2F_4$ flow rate of 50 sccm. As in Fig. 7-4, the most dominant species are C_2, C_3, or H, with lower intensities of CF_2 and F. A comparison of the on/off plasma to the high/low plasma (Fig. 7-7(a)) shows that the H_α, C_2, and F species are all reduced in intensity by a factor of 2, while the CF_2 region increases (CF_2 peak at 251.87 nm) doubles. Unfortunately, it is not clear that the normalization provided

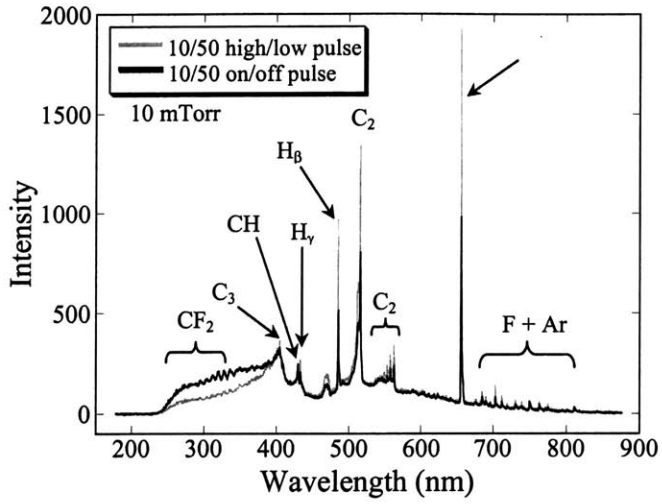

(a)

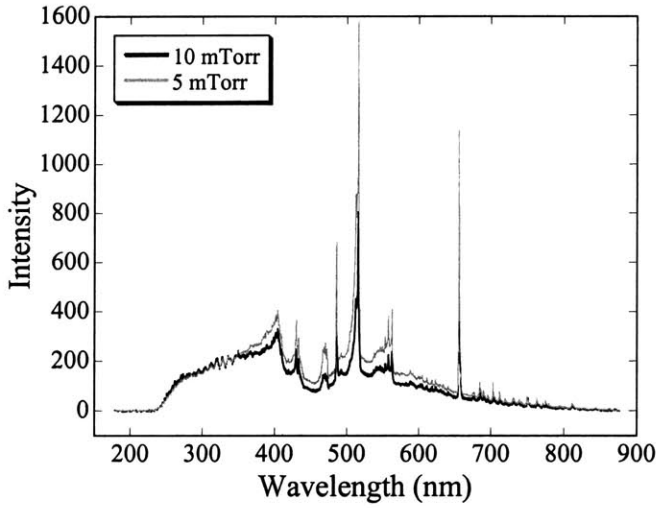

(b)

Figure 7-7: OES spectra from three pulsed plasmas, all from 50 sccm of $C_2H_2F_4$ under 10/50 pulsed ECR excitation. (a) High/low and on/off pulsed plasmas at 10 mTorr. (b) On/off pulsed plasmas at 5 and 10 mTorr. As in Fig. 7-4, most of the dominant species are C_2, C_3, or H, with lower intensities of CF_2 and F. Fig. 7-7(a) shows that the H_α, C_2, and F species are all reduced in intensity by a factor of 2, while the CF_2 region increases (CF_2 peak at 251.87 nm doubles). Unfortunately, it is not clear that the normalization provided by the Ar actinometer provides a valid comparison between these two pulsing techniques since there is some evidence that the electron energy distributions of plasmas from the two pulsing techniques are different (see H_γ peaks). In Fig. 7-7(b), the same peaks are present in each plasma, but the relative intensities have changed dramatically (actinometry is valid here). Most importantly, the dominant peak has shifted from H_α (656.2 nm) at 10 mTorr to C_2 (516.5 nm) at 5 mTorr, while the CF_2 intensity has remained constant.

by the Ar actinometer provides a valid comparison between these two pulsing techniques. As with the 20 sccm vs. higher flow rate spectra discussed above, the H_γ peaks do not show the same behavior as the H_α and H_β peaks, and therefore, these energy distributions of these two types of plasmas are not similar enough to warrant comparison via the actinometric normalization. Thus, it is not possible to make any further conjectures about the differences between these two pulsing techniques based on this data.

Figure 7-7(b) compares OES spectra from 10/50 on/off pulsed $C_2H_2F_4$ plasmas at 10 and 5 mTorr. Comparison between these two spectra via actinometric normalization has proven valid ($\frac{H_\alpha(\mathbf{5}mTorr)}{H_\alpha(\mathbf{10}mTorr)} \approx \frac{H_\beta(\mathbf{5})}{H_\beta(\mathbf{10})} \approx \frac{H_\gamma(\mathbf{5})}{H_\gamma(\mathbf{10})} \approx \mathbf{1.3}$), most likely since both are generated using the same pulsing technique. The same peaks are present in each plasma, but the relative intensities have changed dramatically. Most importantly, the dominant peak has shifted from H_α (656.2 nm) at 10 mTorr to C_2 (516.5 nm) at 5 mTorr, while the CF_2 intensity has remained constant. This dominant peak shift is seen more clearly in Figure 7-8, which shows a series of ratios for the H_α (656.2 nm), C_2 (516.5 nm), C_3 (405.1 nm), F (703.8 nm), and CH (431.4 nm) peaks. H_α decreases with respect to all four of the other peaks, with the C_2 intensity nearly doubling with respect to H_α at the lower pressure. The H_α peak intensity is approximately the same for both pressures, indicating that the F, C_2, C_3, and CH peak intensities are all increasing at the lower pressure, though to different degrees. For example, the ratio C_2/F increases by 38%, while CH/F only increases by 5% when moving from 10 mTorr to 5 mTorr. The electron temperature of ECR plasmas has been seen to increase with decreasing pressure due to the decreased number of collisions electrons undergo with neutrals.[55,56] The

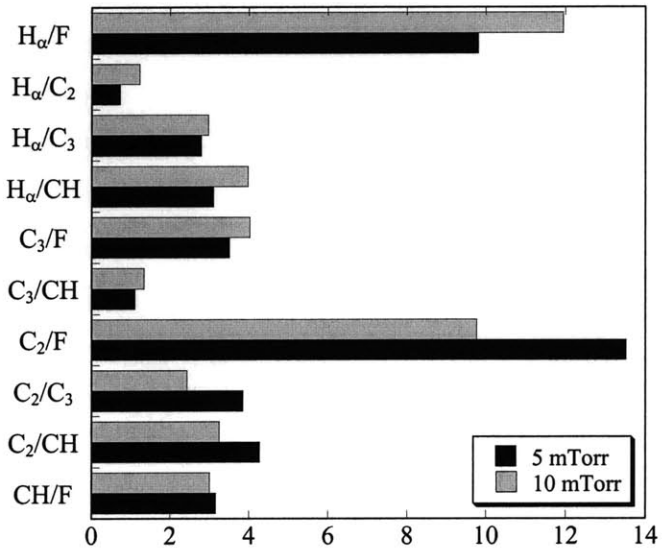

Figure 7-8: Spectral intensity ratios for several of the dominant OES peaks from Fig. 7-7(b) (H_α @ 656.2 nm, C_2 @ 516.5 nm, C_3 @ 405.1 nm, F @ 703.8 nm, and CH @ 431.4 nm). These ratios reflect the shift in dominant peaks from 10 to 5 mTorr. H_α decreases with respect to all four of the other peaks, with the C_2 intensity nearly doubling with respect to H_α at the lower pressure. The H_α peak intensity is approximately the same for both pressures, indicating that the F, C_2, C_3, and CH peak intensities are all increasing at the lower pressure, though to different degrees.

corresponding increase in high energy electrons could result in more efficient fracturing of the precursor molecule, producing the shift in dominant pulsed plasma species.

Finally, Figures 7-9(a) and (b) show the C1s XPS and OES spectra for a 10/100 $C_2H_2F_4$ pulsed plasma film deposited in a parallel plate PECVD reactor. Conventional PECVD films deposited from $C_2H_2F_4$ have been studied in detail previously (see references # 25 & 26), and a representative sample is presented here for comparison to the ECR films. Film composition was found not to change significantly with pulse off time for these films, and so the 10/100 film in Fig. 7-9 is valid for comparison to the 10/50 pulsed ECR plasma films discussed above. Comparing Fig. 7-9(a) with Figs. 7-3 and 7-6, it is clear that the parallel plate plasma film is distinctly different from those obtained by high/low and on/off pulsed ECR, most notably with a much higher C-CF fraction. The differences in the plasmas are even more pronounced, as a comparison of Fig. 7-9(b) with Fig. 7-7 shows. An Ar actinometer was not available in the parallel plate system, and therefore, Fig. 7-9(b) has not been normalized (this also applies for Figs. 7-11(b) and 7-12(c)). However, it is clear that the CF_2 OES peaks are overwhelmingly dominant in the parallel plate plasma, with comparatively small H_α and H_β peaks. Many of the peaks dominant in the ECR plasmas (C_2, C_3, F) are not present to any significant degree. Since an actinometer was not available for the parallel plate plasma, it is impossible to determine whether the CF_2 peaks in the ECR and parallel plate plasmas might actually represent the same concentration of CF_2. Nevertheless, one might expect the parallel plate plasma to produce more heavily fluorinated films than the ECR plasma since CF_2 is the dominant species in that plasma, as opposed to H and C_2 in the ECR

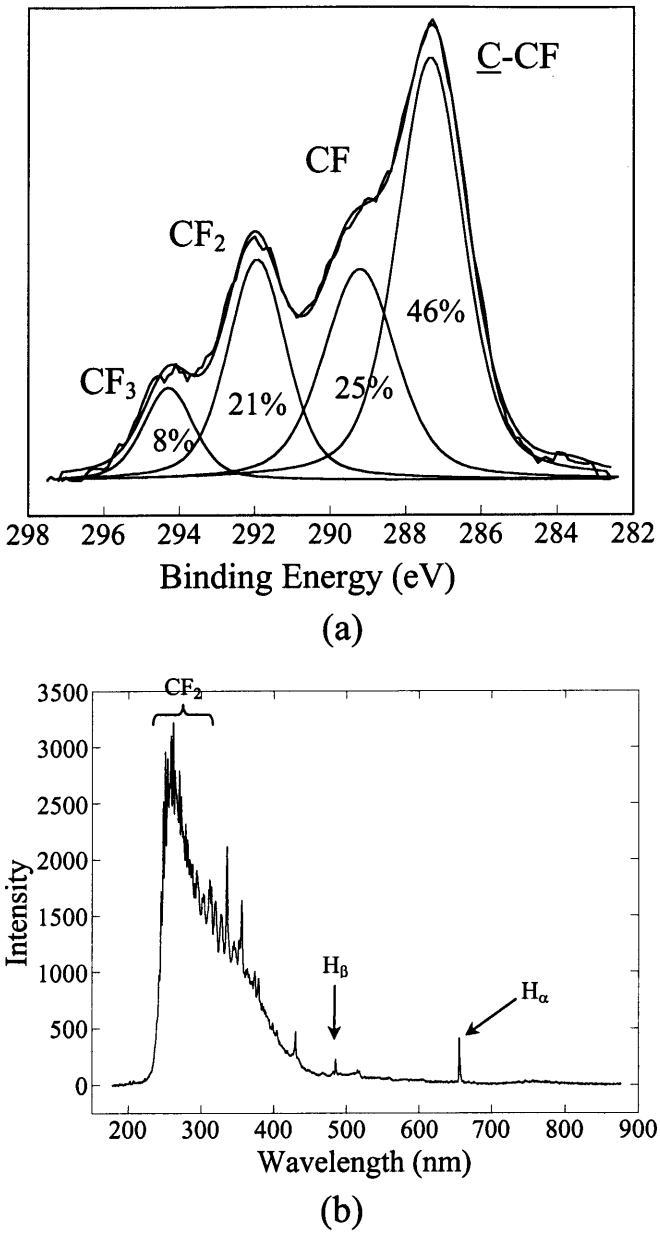

Figure 7-9: (a) Carbon 1s XPS spectrum for a 10/100 on/off $C_2H_2F_4$ pulsed plasma film deposited in a parallel plate PECVD reactor. This spectrum is representative of the parallel plate pulsed plasma films from $C_2H_2F_4$, and therefore is valid for comparison to the 10/50 pulsed ECR plasma films in Figs. 7-3 and 7-6. In comparison to the ECR pulsed plasma films, the parallel plate pulsed plasma film is distinctly different, most notably with a much higher C-CF fraction. (b) OES spectrum for a 10/100 on/off $C_2H_2F_4$ parallel plate pulsed plasma. Ar actinometry was not available in the parallel plate reactor. The CF_2 OES peaks are overwhelmingly dominant in the parallel plate plasma, with comparatively small H_α and H_β peaks. Many of the peaks dominant in the ECR plasmas (C_2, C_3, F) are not present to any significant degree. The higher fluorination of the ECR plasma vs. parallel plate plasma films is quite surprising given these spectra.

plasma. However, it is actually the pulsed ECR plasma films which have the higher F:C ratios.

These observations point to several key differences in the parallel plate versus ECR plasma deposition environments. First, since ECR plasma excitation produces a high density plasma versus the parallel plate low density plasma, the electron density will generally be ~ 10^2 greater in the ECR plasma.[57] In addition, the ECR plasma electron temperature will be ~ 2 – 3 eV higher, which implies that more efficient fracturing of molecular species in the plasma can occur due to the larger concentration of high energy electrons. Indeed, typical fractional ionizations in high density plasmas are on the order of $10^{-4} - 10^{-1}$, while those for low density plasmas are $10^{-6} - 10^{-3}$.[57] This observation can account for the strong C_2, C_3, and H peaks seen in the $C_2H_2F_4$ pulsed ECR plasmas, while molecular species dominate in the pulsed parallel plate plasma. However, this phenomenon may also partially explain the observed differences in deposited film compositions. As discussed above, it is postulated that the species approaching the deposition substrate in the ECR plasma will be significantly different from those detected via the OES fiber located ~ 8" above the substrate.[50-53] Gas-phase recombinations are expected to occur, producing fluorocarbon molecular deposition species. Since F, C_2, and CF_2 are all available to participate in these reactions, it is conceivable that significant concentrations of CF, CF_2, and CF_3 can be generated as depositing species, which would then produce the observed comparatively higher fluorinated films. In contrast, although gas-phase effluent FTIR measurements indicate that free fluorine is generated in the parallel plate pulsed plasmas,[26] most of it is likely tied up as HF (HF emission bands lie outside the available OES detection region), and the OES indicates that the free F present

is insignificant compared to CF_2. This means that only a small amount of F will available to substitute into the film, and the H detected may actually abstract F from the growing parallel plate film, producing a less fluorinated structure.

Section 7.4.3: Deposition from CHF_3 and HFPO

Figure 7-10 shows C1s XPS spectra for two films from 10/50 pulsed depositions using CHF_3 . In one case, growth occurred in the ECR reactor using high/low pulsing at a flow rate of 70 sccm and a pressure of 10 mTorr, while for the other, on/off pulsing was performed in the parallel plate reactor at a flow rate of 12.5 sccm and a pressure of 1000 mTorr). Table 7-3 lists the fraction of each CF_x (x = 1 – 3) species, the F:C ratio, and the refractive index for each film. As with growth from $C_2H_2F_4$, there are clear differences between the ECR and parallel plate films deposited from CHF_3. Both films in Fig. 7-10 have approximately the same fractions of CF_3 and CF, but the ECR plasma deposition results in a higher fraction of CF_2. This fact is surprising when one considers the OES spectrum of the corresponding pulsed plasmas, shown in Figures 7-11(a) and (b). As with the $C_2H_2F_4$ ECR plasmas, the CHF_3 ECR high/low pulsed plasma is dominated by C_2, C_3, and H peaks, with a low intensity CF_2 region. It is also worth noting that the F peak intensity in the ECR CHF_3 high/low pulsed plasma is significantly higher than that seen in the corresponding $C_2H_2F_4$ OES spectrum (Fig. 7-4), while the H peaks are lower. These observations may partially account for the differences between the $C_2H_2F_4$ and CHF_3 films when so much more of their OES spectra are similar. In stark contrast to the CHF_3 ECR plasma OES, the pulsed parallel plate plasma is dominated by CF_2, with only minor peaks for C_2 and H.

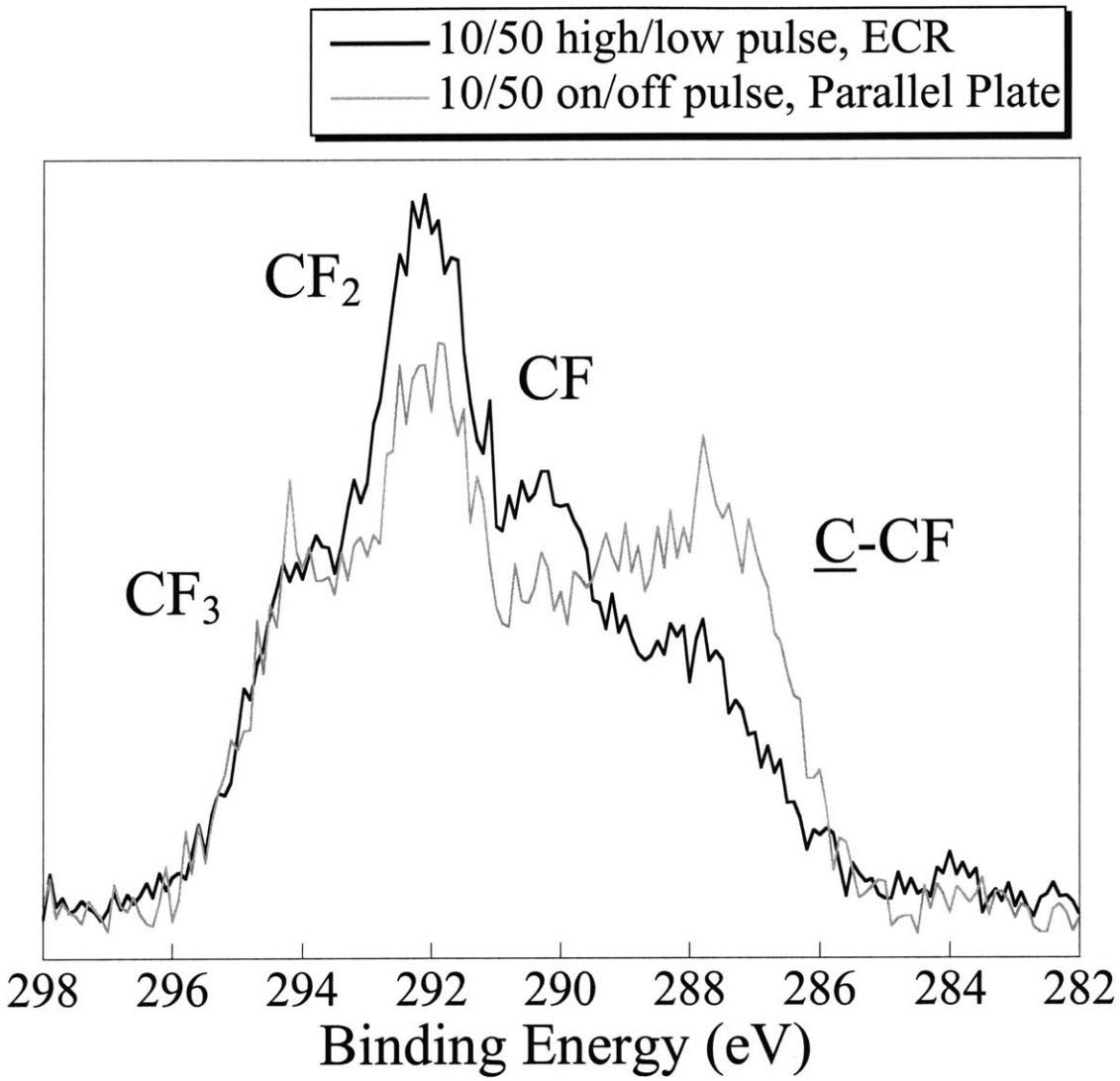

Figure 7-10: Carbon 1s XPS spectra for two films from 10/50 pulsed depositions using CHF_3. Each spectrum has been normalized to the same total integrated area. In one case, growth occurred in the ECR reactor using high/low pulsing at a flow rate of 70 sccm and a pressure of 10 mTorr, while for the other, on/off pulsing was performed in the parallel plate reactor at a flow rate of 12.5 sccm and a pressure of 1000 mTorr. Both films have approximately the same fractions of CF_3 and CF, but the ECR plasma deposition results in a higher fraction of CF_2.

Table 7-3. Percentages of CF_3, CF_2, CF, and C-CF species and F:C ratios as obtained from C-1s XPS for 10/50 CHF_3 pulsed plasma films: ECR high/low plasma (70 sccm, 10 mTorr) versus on/off parallel plate plasma (12.5 sccm, 1000 mTorr).

Film	% CF_3	% CF_2	% CF	% C-CF	F:C	n_f
high/low ECR	19	43	22	16	1.66	1.36
On/off parallel plate	16	38	19	27	1.43	1.40

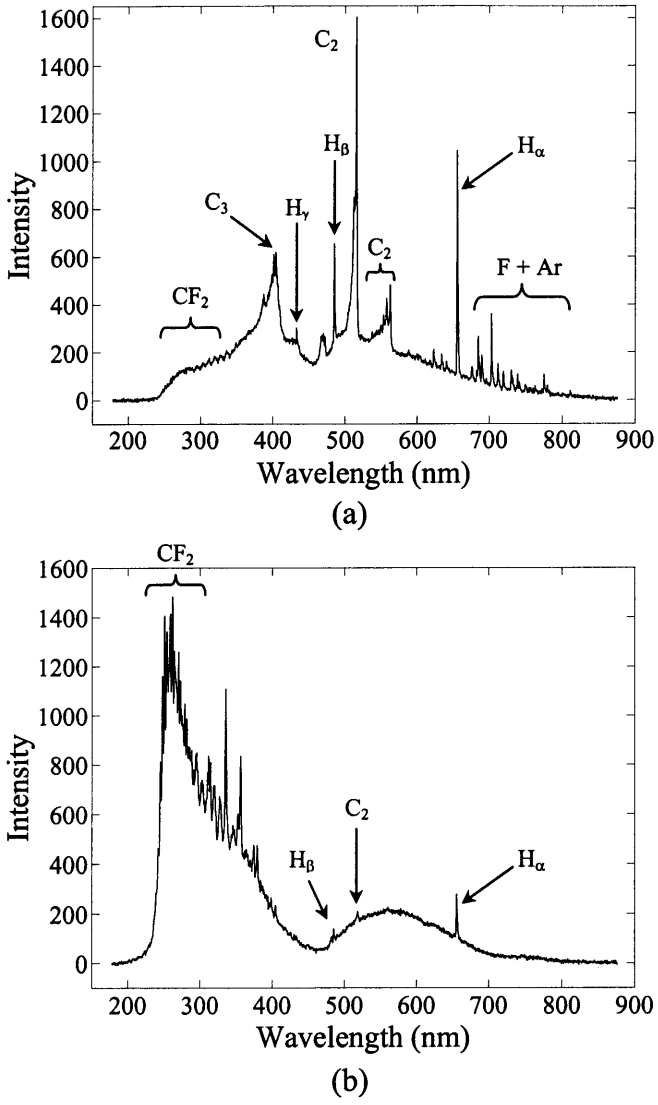

Figure 7-11: OES spectrum for (a) 10/50 high/low pulsed ECR plasma from CHF_3 (70 sccm, 10 mTorr) and (b) 10/50 on/off pulsed parallel plate plasma from CHF_3 (12.5 sccm, 1000 mTorr). As with the $C_2H_2F_4$ ECR plasmas, the CHF_3 ECR high/low pulsed plasma is dominated by C_2, C_3, and H peaks, with a low intensity CF_2 region. In stark contrast to Fig. 7-11(a), the pulsed parallel plate plasma is dominated by CF_2, with only minor peaks for C_2 and H.

It is known that the primary dissociation pathway for CHF_3 is:[58-61]

$$CHF_3 \rightarrow CF_2 + HF \qquad (4)$$

The parallel plate plasma OES spectrum shows only minor peaks for H, and almost negligible F peaks, indicating that the pulsed plasma does not further dissociate CF_2 and HF to a large extent. In contrast, there are large peaks for C_2, C_3, H, and F in the ECR OES spectrum, implying that CF_2 and HF are almost fully dissociated. These observations correlate with those seen for the parallel plate versus ECR pulsed plasmas of $C_2H_2F_4$. As with the $C_2H_2F_4$ plasmas, the lack of an actinometer makes it impossible to determine if the two CHF_3 plasmas actually contain the same concentration of CF_2 species. However, assuming CF_2 to be the primary depositing species, one might expect that the parallel plate pulsed plasma would deposit a film with a much larger CF_2 fraction than the ECR pulsed plasma could generate since CF_2 is the primary species present in that plasma. However, as Fig. 7-10 shows, this is not the case. Gas-phase reactions in the chamber downstream of the OES fiber, as well as a higher degree of surface modification due to the continuous plasma generated by the high/low ECR pulsing versus the on/off parallel plate plasma pulsing must also play an important role in the final film composition.

Finally, Figures 7-12(a) and (b) show OES spectra for 10/50 pulsed plasmas from HFPO. Fig. 7-12(a) is for a high/low pulsed ECR plasma at a flow rate of 70 sccm and a pressure of 10 mTorr, while Fig. 7-12(b) is for an on/off pulsed parallel plate plasma at a flow rate of 23 sccm and a pressure of 1000 mTorr. As with the $C_2H_2F_4$ and CHF_3 plasmas, the differences between the ECR and parallel plate pulsed plasmas are clearly evident. What is not immediately obvious is why the parallel plate pulsed plasma

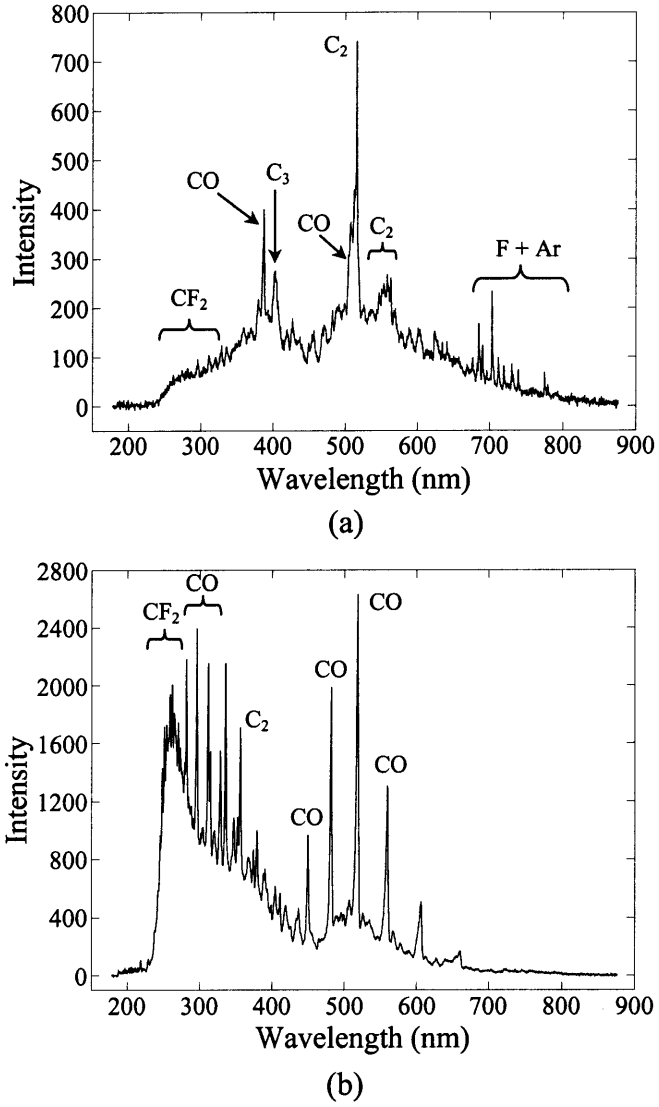

Figure 7-12: OES spectra for 10/50 pulsed plasmas from HFPO: (a) high/low pulsed ECR plasma (70 sccm, 10 mTorr), and (b) on/off pulsed parallel plate plasma (23 sccm, 1000 mTorr). The HFPO ECR OES spectrum is similar to those of the $C_2H_2F_4$ and CHF_3 high/low pulsed plasmas, but has large CO peaks, increased F peaks, and lacks H peaks. The HFPO parallel plate plasma OES spectrum compares analogously with the $C_2H_2F_4$ and CHF_3 parallel plate plasmas. Deposition does not occur from the ECR pulsed plasma, while it is easily obtainable from the parallel plate plasma.

generates films, while the ECR high/low pulsed plasma does not. The HFPO pulsed parallel plate system has been studied in detail and can produce films with a variety of CF_2 fractions.[11,23] However, even at a HFPO flow rate of 70 sccm, there was no observable deposition in the high/low pulsed ECR system. In many respects, the ECR OES spectrum in Fig. 7-12(a) is similar to those of the $C_2H_2F_4$ and CHF_3 high/low pulsed plasmas shown previously, both of which produce films. The main differences are the presence of large CO peaks, an increase in the F peaks, and the lack of any H peaks. The HFPO ECR plasma OES spectrum is most similar to that of CHF_3, which deposits a film very slowly. The increase in F (most likely due to the lack of H to scavenge F) and the presence of CO, both of which can lead to etching chemistries, may result in an etch rate that exceeds the deposition rate, and therefore no film is deposited. The parallel plate pulsed plasma also has significant quantities of CO present, but the dominance of CF_2 in the plasma, coupled with the pulse off time, during which there has been shown to be net deposition,[23,62] must overcome any etching which occurs during the pulse on time, resulting in net deposition. It is anticipated that on/off pulsing of HFPO plasmas in the ECR will result in net deposition, as well.

Section 7.5: Conclusions

High/low and on/off pulsed ECR plasmas from 1,1,2,2-$C_2H_2F_4$, CHF_3, and HFPO have been used to deposit fluorocarbon films. High/low pulsed $C_2H_2F_4$ plasma film composition varied slightly with $C_2H_2F_4$ flow rate, with a significant drop in % CF_3 occurring when the flow rate increased from 20 to 50 sccm, and a smaller degree of defluorination occurring as the flow increased further to 70 sccm. On/off pulsed $C_2H_2F_4$

plasma films were similar to those deposited by high/low pulsing, but tended to be even less fluorinated. OES spectra of both high/low and on/off pulsed $C_2H_2F_4$ plasmas showed high intensity peaks for H, C_2, and C_3, with lower intensity CF_2 and F peaks. The dominant OES peak shifts from H_α to C_2 when the pressure is reduced for on/off pulsing, most likely a result of the increased electron temperature at the lower pressure. Gas-phase recombination reactions may be occurring between the OES sampling region and the deposition substrate, producing fluorocarbon molecular deposition species, and thus accounting for the high degree of fluorination in the deposited films. High/low pulsed CHF_3 ECR plasmas produce high CF_2 concentration films. These plasmas are very similar to those from $C_2H_2F_4$, but have more intense F peaks, which may partially account for the composition differences in the corresponding deposited films. Finally, no film growth was observed from high/low pulsed HFPO ECR plasmas, despite the similarities between HFPO, CHF_3, and $C_2H_2F_4$ plasma OES spectra.

A comparison of each pulsed ECR plasma system with its corresponding pulsed parallel plate plasma system showed significant differences in both OES spectra and deposited film composition. Most striking is the fact that for HFPO, pulsed parallel plate plasmas readily deposit films, while no deposition occurs from the ECR plasma. This difference is likely due to the increased presence of etching species, such as atomic fluorine and carbon monoxide, in the high/low pulsed ECR plasma. The lower prevalence of etchants in the parallel plate plasma may be a result of using true on/off pulsing and/or the expected reduction in electron temperature. All of the parallel plate plasma OES spectra were characterized by high intensity CF_2 peaks, with only low intensity peaks for C_2 and H species. Surprisingly, for both $C_2H_2F_4$ and CHF_3 films, the

ECR plasma produces a more highly fluorinated film than the parallel plate plasma. Actinometry could not be applied, and therefore it is unclear if the CF_2 peaks in each pair of spectra might actually represent similar concentrations of CF_2. The expected higher electron temperature of the ECR high density plasma versus the low density parallel plate plasma will result in more efficient fracturing of molecular species, producing the observed intense C_2 and H OES peaks. Gas phase recombination of these same elemental species can also result in a high degree of CF_x deposition species, and combined with surface fluorination via free fluorine, produce the more fluorinated films.

In summary, Figure 7-13 plots all of the film compositions observed for both pulsed ECR and pulsed parallel plate plasmas on a ternary diagram. This diagram maps out the composition space available for fluorocarbon films. While many continuous fluorocarbon plasmas deposit similar films, regardless of precursor,[10,13-16] pulsing the plasma allows one to explore different regions of the composition space. Thus, it is possible to tailor films for a particular application by working within the appropriate region of the composition space.

Section 7.6: Acknowledgments

The authors gratefully acknowledge the support of the Lucent Technologies Bell Laboratories Graduate Research Program for Women and Tokyo Electron Limited. This work made use of MRSEC Shared Facilities supported by the National Science Foundation under Award Number DMR-9400334.

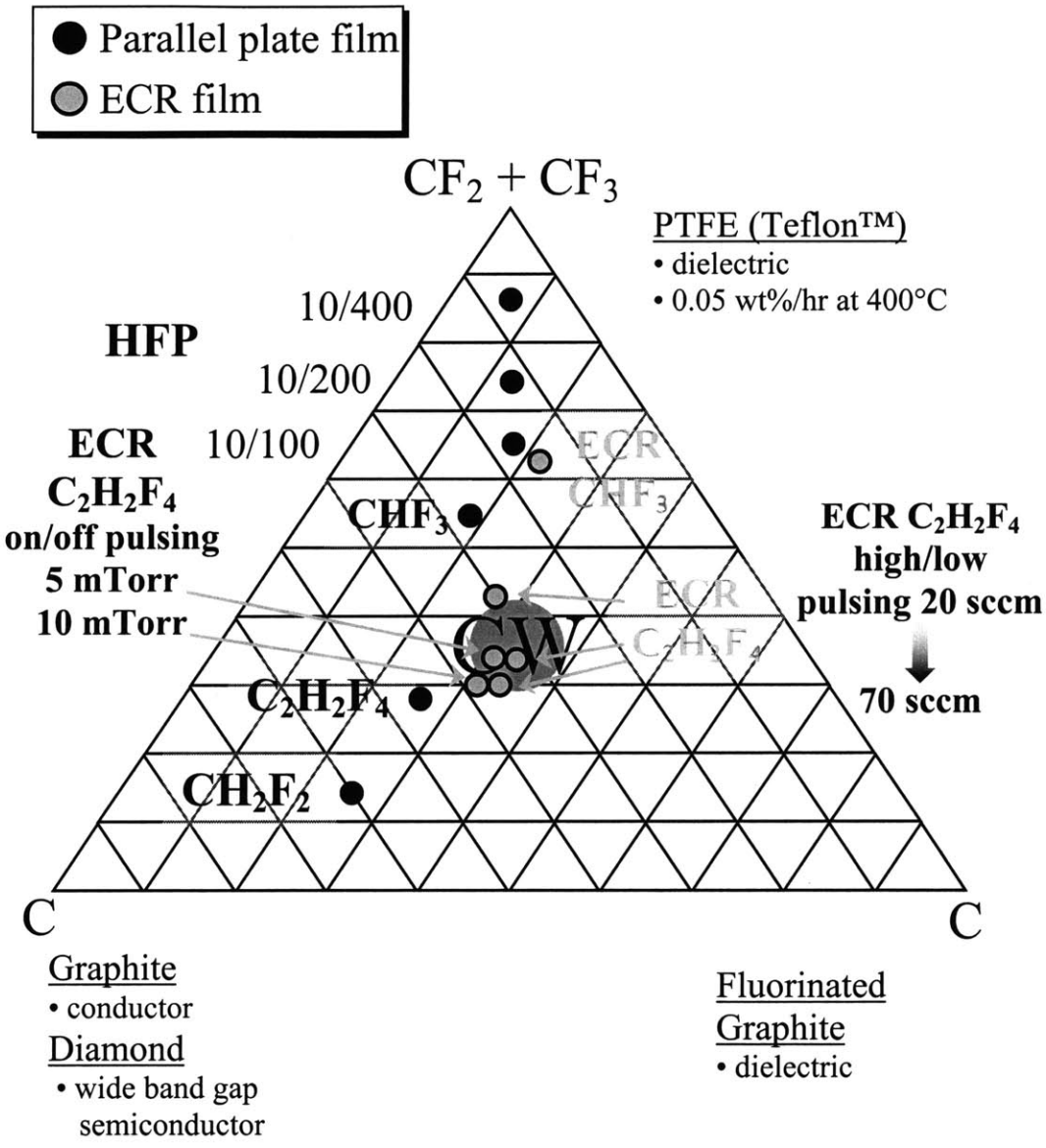

Figure 7-13: Ternary diagram showing all of the film compositions observed for both pulsed ECR and pulsed parallel plate plasmas. This diagram maps out the composition space available for fluorocarbon films. Pulsing the plasma allows one to explore different regions of the composition space.

Section 7.7: References

1. S. Wolf, *Silicon Processing for the VLSI Era*, Vol. 2 (Lattice Press, Sunset Beach, CA, 1990).

2. S. M. Sze, *VLSI Technology* (McGraw-Hill Book Company, New York, 1983).

3. H. Yasuda, *Plasma Polymerization* (Academic Press, New York, 1985).

4. *Plasma Deposition, Treatment, and Etching of Polymers*, R. d'Agostino, Ed. (Academic Press, Boston, 1990).

5. D. R. Cote, S. V. Nguyen, A. K. Stamper, D. S. Armbrust, D. Tobben, R. A. Conti, and G. Y. Lee, *IBM J. Res. Develop.* **43**(1/2), 5 (1999).

6. P. Singer, *Semicond. Intl.* **17**(13), 52 (1994).

7. R. K. Laxman, *Semicond. Intl.* **18**(5), 71 (1995).

8. P. Singer, *Semicond. Intl.* **19**(5), 88 (1996).

9. L. Peters, *Semicond. Intl.* **21**(10), 64 (1998).

10. K. Endo, *MRS Bull.* **22**(10), 55 (1997).

11. C. R. Savage, R. B. Timmons, and J. W. Lin, "Spectroscopic Characterization of Films Obtained in Pulsed Radio-Frequency Plasma Discharges of Fluorocarbon Monomers," in *Structure-Property Relations in Polymers: Spectroscopy and Performance*, Advances in Chemistry Series Vol. 236, Eds: M. W. Urban and C. D. Craver (ACS, Washington, 1993), p. 745.

12. K. K. Gleason, *History and Future of Fluorocarbon CVD Low k DielectricThin Films* (DUMIC, Santa Clara, CA, 1999), p. 11.

13. K. Endo and T. Tatsumi, *Appl. Phys. Lett.* **68**(20), 2864 (1996).

14. K. Takahashi, M. Hori, S. Kishimoto, and T. Goto, *Jpn. J. Appl. Phys. Pt. 1* **33**(7B), 4181 (1994).

15. G. S. Oehrlein, Y. Zhang, D. Vender, and M. Haverlag, *J. Vac. Sci. Technol. A* **12**(2), 323 (1994).

16. J.-H. Wang, J.-J. Chen, and R. B. Timmons, *Chem. Mater.* **8**(9), 2212 (1996).

17. K. Takahashi, M. Hori, and T. Goto, *J. Vac. Sci. Technol. A* **14**(4), 2011 (1996).

18. K. Takahashi, M. Hori, and T. Goto, *J. Vac. Sci. Technol. A* **14**(4), 2004 (1996).

19. Y. Ma, H. Yang, J. Guo, C. Sathe, A. Agui, and J. Nordgren, *Appl. Phys. Lett.* **72**(25), 3353 (1998).

20. S. Takeishi, H. Kudo, R. Shinohara, M. Hoshino, S. Fukuyama, J. Yamaguchi, and M. Yamada, *J. Electrochem. Soc.* **144**(5), 1797 (1997).

21. T. W. Mountsier and J. A. Samuels, *Thin Solid Films* **332**, 362 (1998).

22. K. Endo and T. Tatsumi, *Appl. Phys. Lett.* **70**(19), 2616 (1997).

23. S. J. Limb, D. J. Edell, E. F. Gleason, and K. K. Gleason, *J. Appl. Polym. Sci.* **67**, 1489 (1998).

24. M. Haverlag, W. W. Stoffels, E. Stoffels, G. M. W. Kroesen, and F. J. de Hoog, *J. Vac. Sci. Technol. A* **14**(2), 384 (1996).

25. C. B. Labelle and K. K. Gleason, *J. Vac. Sci. Technol. A* **17**(2), 445 (1999).

26. C. B. Labelle, S. Karecki, R. Reif, and K. K. Gleason, *J. Vac. Sci. Technol. A*, (submitted) (1999).

27. C. R. Savage, R. B. Timmons, and J. W. Lin, *Chem. Mater.* **3**(4), 575 (1991).

28. S. J. Limb, K. K. Gleason, D. J. Edell, and E. F. Gleason, *J. Vac. Sci. Technol. A* **15**(4), 1814 (1997).

29. N. Fujiwara, T. Maruyama, and H. Miyatake, *Jpn. J. Appl. Phys. Pt. 1* **37**(4B), 2302 (1998).

30. S. Samukawa, *Jpn. J. Appl. Phys. Pt. 1* **32**(12B), 6080 (1993).

31. S. Samukawa, *Appl. Phys. Lett.* **64**(25), 3398 (1994).

32. T. H. Ahn, K. Nakamura, and H. Sugai, *Plasma Sources Sci. Technol.* **5**(2), 139 (1996).

33. A. M. Hynes, M. J. Shenton, and J. P. S. Badyal, *Macromolecules* **29**(12), 4220 (1996).

34. A. Hynes and J. P. S. Badyal, *Chem. Mater.* **10**(8), 2177 (1998).

35. K. Takahashi, M. Hori, and T. Goto, *Jpn. J. Appl. Phys. Pt. 2* **32**(8A), L1088 (1993).

36. K. Takahashi, M. Hori, K. Maruyama, S. Kishimoto, and T. Goto, *Jpn. J. Appl. Phys. Pt. 2* **32**(5A), L694 (1993).

37. K. Takahashi, M. Hori, and T. Goto, *Jpn. J. Appl. Phys. Pt. 1* **33**(8), 4745 (1994).

38. J. W. Coburn and M. Chen, *J. Appl. Phys.* **51**(6), 3134 (1980).

39. L. D. B. Kiss, J.-P. Nicolai, W. T. Conner, and H. H. Sawin, *J. Appl. Phys.* **71**(7), 3186 (1992).

40. R. A. Gottscho and V. M. Donnelly, *J. Appl. Phys.* **56**(2), 245 (1984).

41. R. d'Agostino, V. Colaprico, and F. Cramarossa, *Plasma Chem. Plasma Process* **1**(4), 365 (1981).

42. R. d'Agostino, F. Cramarossa, S. De Benedictis, and G. Ferraro, *J. Appl. Phys.* **52**(3), 1259 (1981).

43. J. Reader and C. H. Corliss, *Wavelengths and Transition Probabilities for Atoms and Atomic Ions*, Vol. 1 (National Bureau of Standards, Washington, DC, 1980).

44. R. W. B. Pearse and A. G. Gaydon, *The Identification of Molecular Spectra*, 3rd ed. (Chapman & Hall, London, 1963).

45. Rusli, S. F. Yoon, H. Yang, Q. Zhang, J. Ahn, and Y. L. Fu, *J. Vac. Sci. Technol. A* **16**(2), 572 (1998).

46. *High Density Plasma Sources: Design, Physics and Performance*, O. A. Popov, Ed. (Noyes Publications, Park Ridge, NJ, 1995).

47. M. Morimoto, Y. Ueda, S. Hiejima, I. Katsumata, and Y. Kawai, *Jpn. J. Appl. Phys. Pt. 1* **36**(7B), 4659 (1997).

48. A. Raveh, J. E. Klemberg-Sapieha, L. Martinu, and M. R. Wertheimer, *J. Vac. Sci. Technol. A* **10**(4), 1723 (1992).

49. P. W. Atkins, *Physical Chemistry*, 4th ed. (W. H. Freeman and Company, New York, 1990).

50. S. Farhat, C. Findeling, F. Silva, K. Hassouni, and A. Gicquel, *Journal de Physique IV* **8**(P7), 391 (1998).

51. Y. Mitsuda, Y. Kojima, T. Yoshida, and K. Akashi, *J. Mater. Sci.* **22**, 1557 (1987).

52. Y. Saito, S. Matsuda, and S. Nogita, *J. Mater. Sci. Lett.* **5**, 565 (1986).

53. Y. Saito, K. Sato, H. Tanaka, K. Fujita, and S. Matuda, *J. Mater. Sci.* **23**, 842 (1988).

54. W. Groh and A. Zimmermann, *Macromolecules* **24**(25), 6660 (1991).

55. J. Forster and W. Holber, *J. Vac. Sci. Technol. A* **7**(3), 899 (1989).

56. S. K. Angra, P. Kumar, P. C. Banerfie, and R. P. Bajpai, *Thin Solid Films* **304**, 294 (1997).

57. D. B. Graves, *IEEE Trans. Plasma Sci.* **22**(1), 31 (1994).

58. S. F. Politanskii and V. U. Shevchuk, *Kinet. Katal.* **9**(3), 496 (1968).

59. I. C. Plumb and K. R. Ryan, *Plasma Chem. Plasma Process* **6**(1), 11 (1986).

60. K. P. Schug, H. G. Wagner, and F. Zabel, *Ber. Bunsenges. Phys. Chem.* **83**, 167 (1979).

61. Y. Hidaka, T. Nakamura, and H. Kawano, *Chem. Phys. Lett.* **187**(1,2), 40 (1991).

62. S. J. Limb, Ph.D. Thesis, MIT, 1997.

Chapter 8

FTIR Study of Thermal Annealing Behavior of ECR Pulsed Plasma Deposited Fluorocarbon Thin Films from 1,1,2,2-$C_2H_2F_4$

(Submitted to Journal of the Electrochemical Society in 1999 as "Fourier Transform Infrared Spectroscopy Study of Thermal Annealing Behavior of ECR Pulsed Plasma Deposited Fluorocarbon Thin Films from 1,1,2,2-Tetrafluoroethane" by Catherine B. Labelle and Karen K. Gleason)

Section 8.1: Abstract

Fourier Transform Infrared spectroscopy (FTIR) has been used to study structural changes in high/low and on/off pulsed $C_2H_2F_4$ ECR plasma deposited films upon thermal annealing. A significant increase in T_{stable} (~ 60°C) was achieved when the precursor flow rate was increased to 50 sccm for high/low pulsing. This increase was attributed to the reduction of CF_3 in the film at the higher flow rate, as evolution of CF_3 groups attached to unfluorinated carbons has been identified as a low temperature loss mechanism. Shifts in asymmetric vs. symmetric CF_2 stretch intensities, as well as the appearance of CH stretches, have been observed as a result of annealing. Systematic changes in peak intensity have also been observed in the 1400 – 2000 cm^{-1} range, where there appears to be a shift from carbon-carbon double bonding structures to carbon-oxygen bonding structures. These variations may be due to either additional oxygen absorption after annealing or reaction between oxygen and fluorocarbon network sites that were previously unavailable due to steric hindrance. While the thermal stability of the low flow rate high/low pulsed plasma film appears to be dominated by a low temperature CF_3 loss mechanism, the thermal stability of the other two films is dominated by oxygen and hydrogen uptake, with the film with the higher oxygen and hydrogen content after annealing also having the lower T_{stable}. Thus, minimizing both CF_3 and susceptibility to oxygen and water uptake by the deposited films would appear to be a valid strategy for increasing film thermal stability.

Section 8.2: Analysis of Pre- and Post-Anneal Film FTIR Spectra

Thermal stability is a major issue for new materials intended as low dielectric constant (κ) replacements for the standard SiO_2 interlayer dielectric in semiconductor manufacturing.[1,2] Film integrity must be maintained above the necessary threshold of 400°C needed for the final hydrogen drive-in for gate oxides. However, many of the new low κ materials under investigation do not meet this thermal requirement.[2] In fact, there is often a trade off between thermal stability and dielectric constant, with films having better thermal stability also having higher dielectric constants.[2]

One class of low κ materials where this trade off is evident is fluorocarbons. Bulk polytetrafluoroethylene (PTFE) has a dielectric constant of 2.0 with a thermal stability of 520°C,[3] seemingly making it an ideal low κ material. However, thin film processing techniques such as chemical vapor deposition (CVD) and plasma-enhanced chemical vapor deposition (PECVD) do not generally produce films composed solely of the linear CF_2 chains which give PTFE its unique properties. Amorphous fluorocarbon PECVD films generally consist of a carbon-based network with varying degrees of fluorination. Pulsed-PECVD gives more refined control over the deposited film composition, but still typically results in an amorphous fluorocarbon network.[4,5] For these types of films, thermal stability is usually improved by increasing the degree of carbon-carbon cross-linking.[6,7] However, cross-linking reduces the film fluorine content, increasing the dielectric constant;[7] hence, the trade-off.

Although many researchers have noted this trade-off, relatively little work has been done to determine the underlying causes of decreased thermal stability. Lau and Gleason have recently used ^{19}F and ^{13}C nuclear magnetic resonance (NMR) to examine

some of the structural changes which occur in fluorocarbon films deposited by PECVD of hexafluoropropylene oxide (HFPO), 1,1,2,2-tetrafluoroethane ($C_2H_2F_4$), and difluoromethane (CH_2F_2). They found that there were several different active degradation mechanisms, including loss of CF_3 terminal groups attached to unfluorinated carbons, linear CF_2-chain "unzipping," and precursor desorption.[8,9] Miyakawa et al. have also observed the elimination of CF_3 groups below 200°C using thermal desorption spectroscopy (TDS) and temperature-programmed x-ray photoelectron spectroscopy (TP-XPS).[10,11] Finally, Theil et al. have recently used Fourier Transform Infrared Spectroscopy (FTIR) to examine structural changes upon annealing of fluorocarbon films deposited by electron cyclotron resonance (ECR) high density plasma CVD (HDP CVD).[12] The results presented here continue this line of inquiry, examining fluorocarbon films deposited by pulsed ECR HDP CVD.

Pulsed ECR plasma films were deposited from 1,1,2,2-tetrafluoroethane ($C_2H_2F_4$) in an ECR high density plasma system equipped with a Wavemat MPDR 325i ECR plasma source employing cavity tuning. Five inch diameter silicon wafers were admitted into the system via a loadlock and placed on a mechanically clamping wafer chuck positioned ~ 5" below a set of magnetic confinement rings. The confinement rings are located directly beneath the ECR permanent magnets, and extend ~ 5" below the main ECR plasma region. Neither wafer cooling nor bias were used during deposition. Both high/low pulsing (modulation between high and low power plasmas) and on/off pulsing (modulation between plasma and no plasma) were generated by an ASTeX/Gerling Laboratories (AGL) Model GL134 2.45 GHz 1 kW Low Ripple Variable Power Supply) and a Muegge Electronics Model ML1250D-100TE 2.45 GHz 1.25 kW Low Ripple,

Pulsable Power Supply, respectively. Deposition parameters for the films to be discussed here are presented in Table 8-1.

Figure 8-1 shows FTIR spectra for as-deposited and post-anneal films from pulsed plasmas of $C_2H_2F_4$ using a pulse on/high time of 10 ms and a pulse off/low time of 50 ms (10/50). The spectra were obtained by averaging 64 scans taken on a Bio-Rad FTS 175 FTIR equipped with a KBr detector and compressed air purge. Each spectrum has been normalized to a film thickness of 1500 Å (Beer-Lambert Law),[13] corrected for baseline drift, and leveled to a transmittance of 100 %. Considering only the as-deposited film spectra, strong peaks are seen at 1220 and 1170 cm^{-1}, corresponding to CF_2 asymmetric and symmetric stretches, respectively. These peaks correlate with the relatively high % CF_2 detected in the films via XPS.[14] There are also broad, less intense, peaks from 1700 – 1900 cm^{-1}, indicating C=C and C=O moieties in the films. No oxygen was present in the ECR chamber, but it is known that fluorocarbon plasma films generally absorb a small amount of oxygen upon exposure to atmosphere, most likely by attachment to dangling bonds left in the film by ion bombardment during plasma exposure.[15-17] These spectra are representative of all of the as-deposited pulsed plasma films from our ECR system (i.e., other pulse rates, power levels, and flow rates), and are also typical of fluorocarbon films deposited from $C_2H_2F_4$ in a conventional parallel plate reactor in our lab.[5] One major difference between pulsed $C_2H_2F_4$ ECR plasma deposited films and parallel plate plasma films is the absence of hydrogen incorporated in the ECR plasma films. FTIR spectra of pulsed $C_2H_2F_4$ parallel plate plasma films show small peaks in the range of 2900 – 3100 cm^{-1}.[5] Within the error of the baseline correction, these peaks are not detectable for the as-deposited ECR plasma films.

Table 8-1. Deposition parameters for pulsed ECR plasma deposition from 1,1,2,2-$C_2H_2F_4$. A pulse on/high time of 10 ms and a pulse off/low time of 50 ms was used for each film. The system pressure was 10 mTorr.

Film	Pulse Type	Power Levels (W)	Average Power (W) (10/50 pulse)	$C_2H_2F_4$ Flow Rate (sccm)
1	High/Low	535/350	380	20
2	High/Low	535/350	380	50
3	On/Off	775/0	130	50

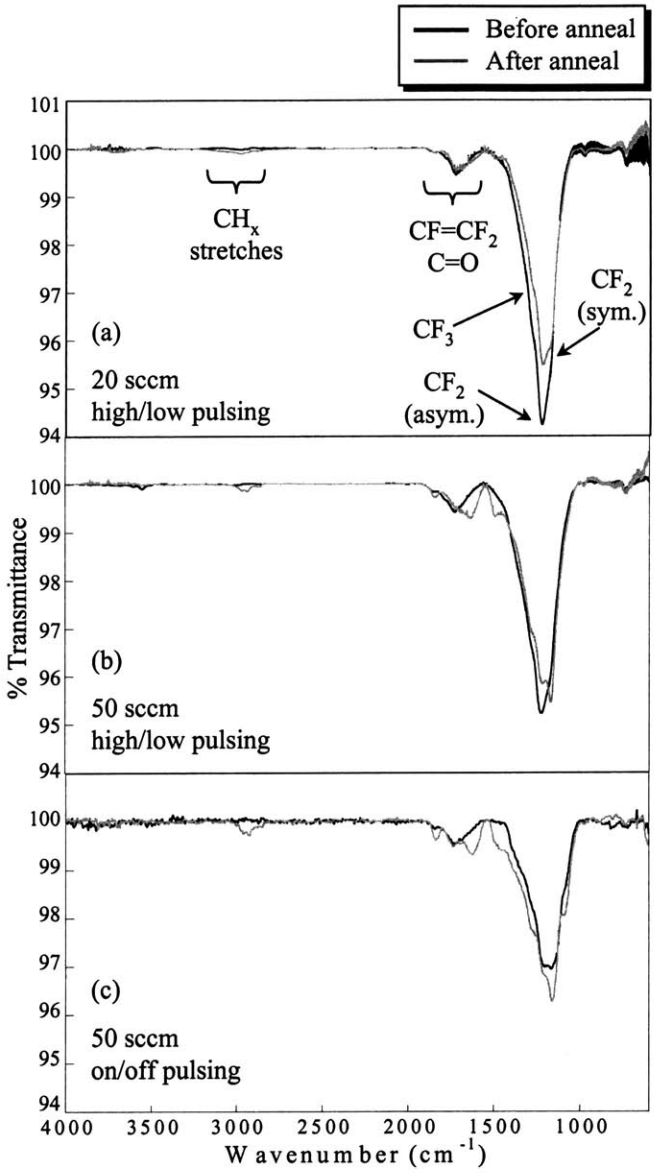

Figure 8-1: FTIR spectra for as-deposited and post-anneal films from 10/50 pulsed plasmas of 1,1,2,2-$C_2H_2F_4$. Precursor flow rates and the type of pulsing used in each deposition are indicated on the figure. Each spectrum has been normalized to a film thickness of 1500 Å. Each sample was ramped to 400°C over 1 hour under a N_2 purge. In each case there are shifts in the 1100 – 1300, 1400 – 2000, and 2900 – 3000 cm^{-1} regions as a result of annealing.

The films were annealed during the course of measurement by Interferometry for Thermal Stability (ITS).[18] In this technique, the films, intact on their silicon substrate, are placed inside a heated aluminum block equipped with a nitrogen purge. The reflectivity of the film is monitored during the temperature ramp by an interferometer system consisting of a He-Ne laser (6328 Å) and photodetector. Both the temperature and interferometer signal are computer monitored. Typical annealing runs for the fluorocarbon films discussed here consisted of a ramp to 400°C over 1 hour, followed by a bake at 400°C for ~ 10 – 20 min., and then a rapid cooling (10 – 20 min. to reach room temperature). The temperature at which each film started to degrade (T_{stable}) as determined from the ITS measurements is listed in Table 8-2. The largest shift in T_{stable} occurs between 20 and 50 sccm high/low pulsed plasma films. This increase may be attributed to the large decrease in % CF_3 as determined by XPS when moving to the higher flow rate.[14] The film deposited at 20 sccm has 11% CF_2, while at 50 sccm the film contains 6% CF_2. Evolution of CF_3 groups attached to unfluorinated carbons, with the resulting tertiary radical being stabilized at a highly substituted carbon site, has been identified as a low temperature loss mechanism for $C_2H_2F_4$ parallel plate pulsed plasma films.[8,9] Thus, a reduction in the % CF_3 could reduce the impact of this mechanism on thermal stability.

Figure 8-1 shows FTIR spectra of the annealed 10/50 pulsed plasma samples overlaid with the as-deposited film spectra. In each case there are changes in the 1100 – 1300, 1400 – 2000, and 2900 – 3000 cm^{-1} regions as a result of the annealing. Most surprising is the appearance of hydrocarbon peaks around 2950 cm^{-1}, which is most pronounced in the spectrum of the on/off pulsed plasma film. No hydrocarbons were

Table 8-2. Shifts in FTIR peak intensities upon annealing using ITS technique. The temperature at which thermal degradation begins (T_{stable}), as determined from the ITS measurement, is also identified for each film.

Pulse Type	$C_2H_2F_4$ Flow (sccm)	T_{stable} (°C)	Wavenumber (cm^{-1}) 1845	1780	1725	1640	1490
High/Low	20	~ 245	same	↓	↓	↑	same
High/Low	50	~ 300	↑	↓	↓	↑	↑
On/Off	50	~ 260	↑	same	↑	↑	↑

detected prior to anneal, but hydrocarbons or water from the air may have reacted with the film network to form these species. All three spectra show changes in the CF_2 region, with the asymmetric peak remaining dominant for the 20 sccm pulsed plasma film, while the symmetric peak becomes dominant for both 50 sccm annealed pulsed plasma films. This suggests the local environment has changed after annealing, resulting in different steric constraints on CF2 vibrations. A CF_3 peak at 1285 cm^{-1} can also be resolved in all of the annealed spectra, as well as CF at 1090 cm^{-1} in the on/off pulsed sample. Noticably, the CF_3 peak intensity at 1285 cm^{-1} reduces significantly in the 20 sccm sample, correlating with the proposed CF_3 loss mechanism. The major area of interest, however, is 1400 – 2000 cm^{-1}, where there are intensity shifts in existing peaks as well as the appearance of a new peak at 1490 cm^{-1}.

Figure 8-2 shows an expanded view of the 1400 – 2000 cm^{-1} region, with as-deposited and annealed spectra overlaid. All of the shifts identified in these spectra are summarized in Table 8-2. Fig. 8-2(a) shows only small changes in the 1400-2000 cm^{-1} region resulting from annealing. However, in Figs. 8-2(b) and 8-2(c), large increases in intensity are observed at 1845, 1640, and 1490 cm^{-1}. Smaller decreases in intensity at 1780 and 1725 cm^{-1} are seen in Fig 8-2(a) and 8-2(b), but these regions remain approximately constant in Fig. 8-2(c). The changes seen in Figs. 8-2(a) and 8-2(b) are typical of 9 other high/low pulsed plasma films which have been grown at various flow rates, regardless of pulse rate and power level, and therefore can be considered trends. Similar peak shifts have been seen by Theil et al.,[12] Yang et al.,[19] and Banerjee et al.[20] for their continuous conventional and high density plasma deposited fluorocarbon films.

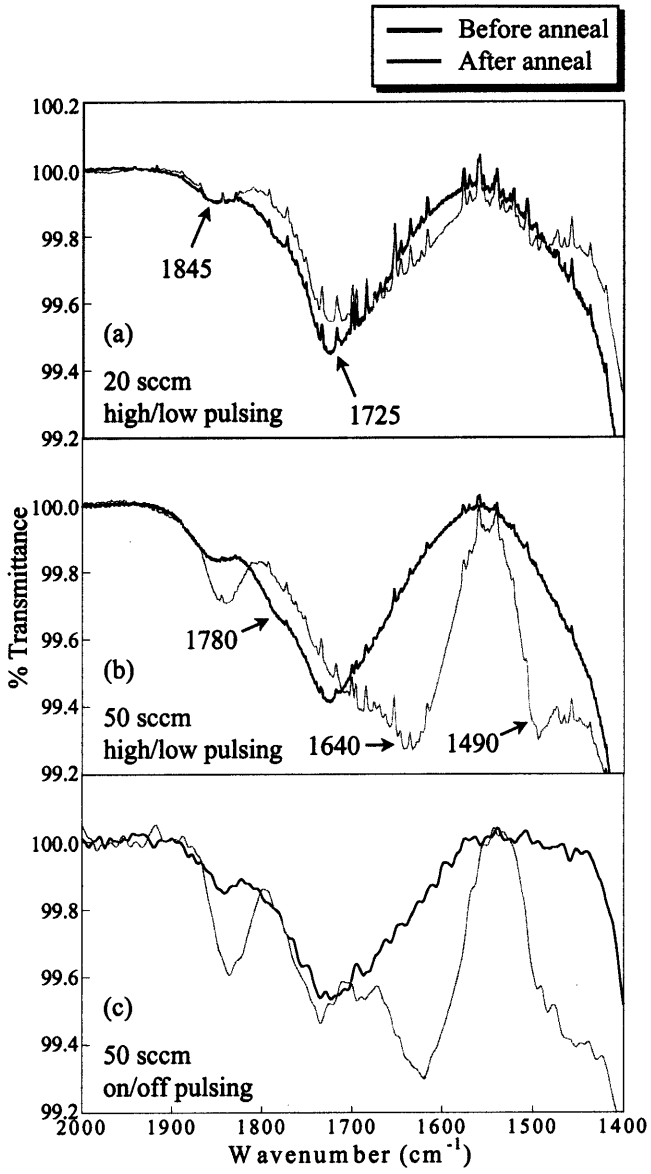

Figure 8-2: Expanded view of the 1400 – 2000 cm^{-1} region of the FTIR spectra shown in Fig. 8-1, with as-deposited and annealed spectra overlaid. Shifts in peak intensity can be seen at 1845, 1780, 1725, 1640, and 1490 cm^{-1}.

Generally, it is difficult to make specific assignments for the 1400 – 2000 cm^{-1} region since there is large overlap between C=C and C=O containing groups. However, identification of specific functional groups will be made, since the shifts are so pronounced and consistent. A review of several literature sources has resulted in the assignments given in Table 8-3.[21-27] Many of these sources deal with irradiation of PTFE, and thus provide a good baseline for comparison to the plasma deposited fluorocarbon films.[21,22,24,26] The peak at 1490 cm^{-1} could be a weak asymmetric CF_2 stretch,[28] or CF stretches shifted to higher wavenumbers by H incorporation. Such shifts are typical in both hydrofluorocarbon polymers[29] and small molecules.[30] Table 8-4 gives a more complete listing of the FTIR peak assignments used in this work.

The thermal behavior of irradiated PTFE is actually quite sensitive to oxygen incorporation. In contrast to undamaged PTFE, irradiated PTFE pyrolyzes in multiple stages.[31] PTFE irradiated in air evolves CO_2, HF, and fluorocarbon fragments upon heating. The evolution of both CO_2 and HF shows low temperature and high temperature maximums in thermal gravimetric analysis (TGA). This can be attributed to the radicals formed in PTFE upon irradiation, which have been identified and quantified by electron spin resonance (ESR).[32] Both alkyl radicals, $-F_2C-FC\bullet-CF_2-$, and chain end radicals, $-F_2C-F_2C\bullet$, are produced by irradiation under vacuum. Such radicals are analogous to "dangling bond" defects in as-deposited PECVD fluorocarbon films. Exposure of irradiated PTFE to oxygen results in peroxyradicals, $-F_2C-FC(OO\bullet)-CF_2-$ and $-F_2C-F_2COO\bullet$. Heating of peroxyradicals to 250 °C in trace water results in the low temperature evolution of CO_2 and HF. Further reactions of ambient oxygen and water with irradiated PTFE result in acid fluoride groups (-COF) and carboxylic acid (-COOH)

Table 8-3. Peak assignments for 1400 – 2000 cm^{-1} region of FTIR spectra.

Wavenumber (cm^{-1})	Assignment
1490	Unassigned in literature
1640	$CF_xCO_2^-$
1725	C=O
1780	$CF=CF_2$ and COOH
1845	$CF_xC(=O)F$

Table 8-4. General FTIR peak assignments for fluorocarbon films.

Wavenumber (cm^{-1})	Assignment	Reference
1315 ± 105	CF_3-CX_y stretch (X = F on high wavenumber side)	Roeges (23)
1270 ± 70	CF_3-CX_y stretch (X = F on high wavenumber side)	Roeges (23)
1190 ± 80	CF_3-CX_y stretch (X = F on high wavenumber side)	Roeges (23)
982	CF_3	Fisher & Corelli (21)
715 ± 95	CF_3 wagging	Roeges (23)
1450	CF_2 asymmetric stretch (weak), CF_2 shifted by nearby H	Liang (28) Kuptsov (29) & Pouchert (30)
1195 ± 85	CF_2 asymmetric stretch	Roeges (23)
1130 ± 70	CF_2 symmetric stretch	Roeges (23)
625	CF_2 wagging	Fisher & Corelli (21)
1050 ± 60	CF stretch in CH_2F	Roeges (23)
955 ± 15	CF stretch	Roeges (23)
1845 ± 55	C=O stretch in $CF_xC(=O)F$	Roeges (23)
1810	C=O in COOH, isolated	Bürger (26)
1770 – 80	C=O in COOH, associated	Bürger (26)
1730 ± 25	C=O	Roeges (23)
1630 ± 45	CO_2 asymmetric stretch in $CF_xCO_2^-$	Roeges (23)
1870 – 1890	COF	Fischer (24) Fisher & Corelli (23)
1780 – 1790	C=C in $CF=CF_2$	Bürger (26) Fisher & Corelli (23)
3020 – 3100	CH in $CH=CH_x$	McMurray (25) Roeges (23)
2879 – 2994	CH in hydrofluorocarbon	Danilich (27)
2850 – 2960	CH in saturated hydrocarbons	McMurray (25)

groups.[21] Heating above 300°C results in decarboxylation, a second, higher temperature production mechanism for CO_2 and HF evolution.[31]

From the peak assignments given in Table 8-3, Fig. 8-2 shows an increase in oxygen-bonded structures after annealing, while carbon-carbon double bonding decreases slightly or remains unchanged. These changes in oxygen content are only moderate for the 20 sccm samples, but become much more pronounced at higher flow rates. The samples are annealed under a positive N_2 pressure, which should prevent any oxygen contamination during the anneal. However, it is possible that upon atmospheric exposure after the anneal, more oxygen is absorbed, resulting in the observed shifts. A true test of this theory would be to perform the anneal and FTIR measurements *in situ*, thus avoiding atmospheric exposure. Another possibility is that the fluorocarbon network can relax at elevated temperatures, allowing reactions between unstable sites in the film and O_2 already present in the film to proceed that were once sterically hindered. The high temperatures during annealing will also enable oxygen to undergo reactions not possible at room temperature (i.e., different CO_2 evolution mechanisms at < 250 and > 300°C, see above).

Relating these results to the overall film thermal stability, these observations can be made: first, significant CF_3 film concentrations can enable a low temperature CF_3 loss mechanism; second, the presence of oxygen in a film will result in oxygen-bonded structural changes upon anneal; and third, hydrogen from H_2O or adventitious hydrocarbons can be incorporated after anneal. CF_3, CO_2 and HF outgassing has been observed for fluorocarbon plasma deposited films, supporting these observations.[20] Loss of CF_3 dominates Fig 8-2(a), leading to the lowest thermal stability of the films studied

here. However, this film is relatively resistant to oxidation and hydrogenation. Figs. 8-2(b) and 8-2(c) show the thermal stability of the remaining two films is dominated by oxygen and hydrogen uptake. Of this pair, the film with the higher oxygen and hydrogen content after annealing (Fig. 8-2(c)) also has the lower T_{stable} (Table 8-2).

In conclusion, FTIR has been used to study structural changes in pulsed $C_2H_2F_4$ ECR plasma deposited films upon thermal annealing. A significant increase in T_{stable} (~ 60°C) was achieved when the precursor flow rate was increased to 50 sccm for high/low pulsing. This increase was attributed to the reduction of CF_3 in the film at the higher flow rate, as evolution of CF_3 groups attached to unfluorinated carbons has been identified as a low temperature loss mechanism. Shifts in asymmetric vs. symmetric CF_2 stretch intensities, as well as the appearance of CH stretches, have been observed as a result of annealing. Systematic changes in peak intensity have also been observed in the 1400 – 2000 cm^{-1} range, where there appears to be a shift from carbon-carbon double bonding structures to carbon-oxygen bonding structures. These variations may be due to either additional oxygen absorption after annealing or reaction between oxygen and fluorocarbon network sites that were previously unavailable due to steric hindrance. While the thermal stability of the low flow rate high/low pulsed plasma film appears to be dominated by a low temperature CF_3 loss mechanism, the thermal stability of the other two films is dominated by oxygen and hydrogen uptake, with the film with the higher oxygen and hydrogen content after annealing also having the lower T_{stable}. Thus, minimizing both CF_3 and susceptibility to oxygen and water uptake by the deposited films would appear to be a valid strategy for increasing film thermal stability.

Section 8.3: Acknowledgments

The authors gratefully acknowledge the support of the Lucent Technologies Bell Laboratories Graduate Research Program for Women and Tokyo Electron Limited. We would also like to thank Brett Cruden for his assistance with the ITS measurements.

Section 8.4: References

1. P. Singer, *Semicond. Intl.* **20**(13), 67 (1997).

2. L. Peters, *Semicond. Intl.* **21**(10), 64 (1998).

3. *Fluoropolymers*; *Vol. XXV*, L. A. Wall, Ed. (Wiley-Interscience, New York, 1972).

4. S. J. Limb, D. J. Edell, E. F. Gleason, and K. K. Gleason, *J. Appl. Polym. Sci.* **67**, 1489 (1998).

5. C. B. Labelle and K. K. Gleason, *J. Vac. Sci. Technol. A* **17**(2), 445 (1999).

6. K. Endo and T. Tatsumi, *Jpn. J. Appl. Phys. Pt. 2* **36**(11B), L1531 (1997).

7. K. Endo, *MRS Bull.* **22**(10), 55 (1997).

8. K. K. S. Lau and K. K. Gleason, *J. Phys. Chem. B* **102**(31), 5977 (1998).

9. K. K. S. Lau and K. K. Gleason, *J. Electrochem. Soc.*, (in press) (1999).

10. Y. Miyakawa, K. Fujita, N. Hirashita, N. Ikegami, J. Hashimoto, T. Matsui, and J. Kanamori, *Jpn. J. Appl. Phys. Pt. 1* **33**(12B), 7047 (1994).

11. N. Hirashita, Y. Miyakwa, K. Fujita, and J. Kanamori, *Jpn. J. Appl. Phys. Pt. 1* **34**(4B), 2137 (1995).

12. J. A. Theil, F. Mertz, M. Yairi, K. Seaward, G. Ray, and G. Kooi, *Thermal Stability of a-C:F,H Films Deposited by Electron Cyclotron Resonance Plasma Enhanced Chemical Vapor Deposition* (MRS Symp. Proc., San Francisco, CA, 1997).

13. P. W. Atkins, *Physical Chemistry*, 4th ed. (W. H. Freeman and Company, New York, 1990).

14. C. B. Labelle and K. K. Gleason, , (in progress) (1999).

15. K. Endo and T. Tatsumi, *Appl. Phys. Lett.* **68**(20), 2864 (1996).

16. N. Amyot, J. E. Klemberg-Sapieha, M. R. Wertheimer, Y. Segui, and M. Moisan, *IEEE Trans. Elect. Insul.* **27**(6), 1101 (1992).

17. R. d'Agostino, R. Cramarossa, F. Fracassi, E. Desimoni, L. Sabbatini, P. G. Zambonin, and G. Caporiccio, *Thin Solid Films* **143**, 163 (1986).

18. B. Cruden, K. Chu, K. Gleason, and H. Sawin, *J. Electrochem. Soc.*, (submitted) (1999).

19. H. Yang, D. J. Tweet, Y. Ma, and T. Nguyen, *Appl. Phys. Lett.* **73**(11), 1514 (1998).

20. I. Banerjee, M. Harker, L. Wong, P. A. Coon, and K. K. Gleason, *J. Electrochem. Soc.* **146**(6), 2219 (1999).

21. W. K. Fisher and J. C. Corelli, *J. Polym. Sci.: Polym. Chem. Ed.* **19**, 2465 (1981).

22. J. S. Forsythe, D. J. T. Hill, A. L. Logothetis, and A. K. Whittaker, *Polym. Degrad. Stabil.* **63**, 95 (1998).

23. N. P. G. Roeges, *A Guide to the Complete Interpretation of Infrared Spectra of Organic Structures* (Wiley, New York, 1994).

24. D. Fischer, U. Lappan, I. Hopfe, K.-J. Eichhorn, and K. Lunkwitz, *Polymer* **39**(3), 573 (1998).

25. J. McMurry, *Organic Chemistry*, 3rd ed. (Brooks/Cole, Pacific Grove, CA, 1992).

26. W. Bürger, K. Lunkwitz, G. Pompe, A. Petr, and D. Jehnichen, *J. Appl. Polym. Sci.* **48**, 1973 (1993).

27. M. J. Danilich, D. J. Burton, and R. E. Marchant, *Vib. Spectrosc.* **9**, 229 (1995).

28. C. Y. Liang and S. Krimm, *J. Chem. Phys.* **25**(3), 563 (1956).

29. A. H. Kuptsov and G. N. Zhizhin, *Handbook of Fourier Transform Raman and Infrared Spectra of Polymers*, Vol. 25 (Elsevier, New York, 1998).

30. C. J. Pouchert, *The Aldrich Library of FT-IR Spectra* (Aldrich Chemical Co., Milwaukee, WI, 1985).

31. U. Lappan, L. Haubler, G. Pompe, and K. Lunkwitz, *J. Appl. Polym. Sci.* **66**, 2287 (1997).

32. A. Oshima, T. Seguchi, and Y. Tabata, *Radiat. Phys. Chem.* **50**(6), 601 (1997).

Appendix A

Electron Cyclotron Resonance High Density Plasma Deposition System Design and Operation

Figure A-1 shows a schematic of the Electron Cyclotron Resonance (ECR) high density plasma deposition system. Its major components are a Wavemat Microwave Plasma Disk Reactor (MPDR) 325i microwave plasma source with magnetic confinement rings, a 5" mechanically clamping wafer chuck capable of being cooled to -40°C, a vacuum isolated loadlock for sample transfer, and a vacuum system comprised of a 3200 L/s magnetically levitated turbomolecular pump backed by a 50 CFM mechanical pump. The system has a base pressure of $\sim 10^{-7}$ Torr and is typically operated at 10 mTorr. This appendix will detail the design and operation of this system.

Section A.1: ECR Source

The ECR source is a 2.45 GHz Wavemat MPDR 325i microwave plasma source which utilizes cavity tuning.(see Wavemat 325i manual) Figure A-2 shows a schematic of the ECR source. The main items to notice are the microwave tuning probe and short tuning adjustment knob, the quartz bell jar, the water and N_2 purge ports, and the two magnet assemblies (ECR and confinement ring).

The microwave tuning probe and short tuning adjustment knob are both used to match the generated microwave plasma. The short tuning knob is used to change the size of the resonance cavity, which in turn controls the operating mode of the cavity. The microwave tuning probe position determines the electromagnetic fields near the cavity wall, and thus, the coupling of energy into the cavity. Both of these elements are coupled, and therefore, to match a plasma, it is necessary to first adjust the tuning probe, then the tuning short, and then repeat this sequence until the plasma is well matched. In practice, it has been found that for this system the short tuning knob does not need to be

adjusted significantly; a good match can be achieved solely through adjustment of the tuning probe. Typical matching conditions have the tuning probe at position 11 and the short tuning knob centered on the black mark. It is important to note that multiple cavity tuning modes are possible for a particular plasma and that several of these modes may be used during a single plasma run (see appendix to ECR manual). This phenomenon is known as "mode hopping" and manifests as a visible cycling of plasma intensity. The period of the mode hopping is usually on the order of 1 – 2 seconds, and therefore is much longer than the pulse signal being sent to the microwave power supply (millisecond pulsing). Mode hopping has generally been observed at any microwave power or pulse condition when the gas feed flow rate is $\geq$ 50 sccm. The chamber pressure also fluctuates with the plasma intensity when mode hopping occurs (generally $\pm$ 3 sccm for a set pressure of 10 mTorr).

The quartz bell jar contains the plasma discharge area and is the only part of the ECR plasma source held under vacuum. Extreme care must be taken when moving or transporting the ECR source as mishandling can result in fracturing of the bell jar. In addition, proper support must be provided for the waveguides attached to the ECR source in order to prevent stress on the waveguide side of the bell jar that could lead to fracture. It is recommended that if the bell jar is fractured it should be returned to Wavemat (Plymouth, MI, Phone: (313) 454-0020) for repair and re-assembly as the re-assembly process is extremely sensitive to the sealing flange tolerances and the magnitude and sequence of applying torque to the sealing bolts. A local glass blower, G. Finkenbeiner Inc., can handle repairs of small chips or fractures of the bell jar (Tom Hession, Waltham,

MA, Phone: (781) 899-3138), but extreme care must be taken when reassembling the ECR after the bell jar has been repaired.

There are several considerations to keep in mind about the bell jar during operation. First, due to the plasma excitation, the bell jar will heat up significantly while the plasma is on. A water cooling channel encircles the base of the bell jar and is used to cool the cavity walls, magnet ring, and ECR base plate. Cooling water at $\leq 20^{\circ}C$ with a minimum flow rate of 1 gal/min. should be used. Connections to the ECR cooling channel are made with ¼" NPT fittings. Currently, ¼" NPT → ¼" Swagelock adapters are in place, allowing connection of ¼" PFA (polyfluoroacetate) tubing that goes to the chilled water supply from the Neslab System I chiller. The pressure differential between inlet and outlet from the ECR should be at least 20 psi, while the inlet pressure should not exceed 60 psi. The inlet water pressure can be changed by adjusting the Nibco 75CL stop valve located on the water chilling line near the end of the forward circulation path (near turbopump). The water comes in contact with aluminum, nickel-plated soft iron, and stainless steel in the ECR and therefore it is recommended that it be filtered and treated to prevent corrosion. Due to the water chiller setup available, it has not been possible to follow these recommendations. The chiller currently circulates deionized water. It is expected that over an extended period of the time, the water channels may become corroded to the point where sealing tolerances are exceeded and the baseplate will need to be replaced. Upon installation of the source on this system, both the bell jar and baseplate were replaced. A second source of cooling is provided by a nitrogen purge which circulates through the magnets and is directed at the base of the quartz bell jar. Dry nitrogen should be used to prevent formation of ozone during plasma operation. A

minimum flow rate of 3 ft^3/min. is required. Connections to the ECR N_2 purge channel are made with ¼" NPT fittings. Currently, ¼" NPT → ¼" Swagelock adapters are in place, allowing connection of ¼" PFA (polyfluoroacetate) tubing that goes to a 240 L liquid N_2 dewar. On this system, the purge is operated at near maximum flow for a N_2 source held at 80 psi (one turn short of full open on N_2 purge valve). It is normal to feel some leakage from several of the ECR joints when the N_2 purge is in operation. It is estimated that approximately 5½ hours of purge time can be expected from the 240 L dewar.

Both water and N_2 cooling MUST be turned on before attempting to strike a plasma. Since the N_2 is provided by a liquid N_2 dewar, a maximum plasma operation time of ~30 min. must be observed. Exceeding this limit will result in icing of the N_2 lines. Both the water and N_2 cooling must remain on after a plasma has been extinguished since the bell jar remains hot. The cooling water is typically circulated for at least 30 min. after the last plasma if plasma operation was brief. For long plasma runs, the cooling water should be circulated at least 50-60 min. after the last plasma. The N_2 purge should remain on ~10 min. after extinguishing a plasma, but a reduced flow rate can be used. Typically, the N_2 purge valve is left 1.5 – 2 turns open during this phase of operation.

A second consideration with the bell jar during deposition runs is coating of the bell jar vacuum surface. Excessive coating of the jar will result in flakes of film peeling off from the surface and falling onto the deposition substrate. Progressive coating of the bell jar can be observed through two quartz viewports on the ECR source. Proper eye protection must be worn when viewing through these viewports as they will emit UV.

When a majority of the visible area is coated (usually a brown film), the bell jar should be cleaned with an O_2/Ar plasma. The cleaning parameters are: 40/20 pulse, 10 sccm O_2/20 sccm Ar, 10 mTorr, ~800 W plasma. Depending on the bell jar coating, cleaning runs are typically 15 – 30 min. Thick coatings can be removed through sequential 30 min. cleaning runs, where the N_2 lines are allowed to de-ice in between runs. The bell jar is considered "clean" when a coating is no longer visible through the ECR viewports. NOTE: The effectiveness of the O_2/Ar plasma clean on the main chamber is not directly known. It is anticipated that there is a gradual buildup of film on the chamber walls that is not entirely removed in these cleaning runs.

The magnetic confinement rings below the quartz bell jar are used to confine the plasma below the generation region. The deposition substrate is held ~ 5 in. below the confinement rings. The substrate is removed from the plasma in order to prevent excessive ion bombardment. Four vertical slits in the confinement rings allow for the four upper viewports on the chamber. Twelve rare earth permanent magnets are used to produce the magnetic fields for the electron cyclotron resonance condition. The magnets on this source generate a field of 875 G within the quartz bell jar. As with all systems utilizing magnets, care must taken that all instrumentation around the magnets are compatible. The turbomolecular pump used in this system is sufficiently removed from the ECR source to prevent any interference from the ECR magnets with the magnetic levitation system used by the pump.

Feed gas is introduced through a ¼" VCR fitting connected to the gas control panel (see Section A.6) by ¼" stainless steel tubing. There is no gas distribution ring as described in the ECR manual since the magnetic confinement ring option is present. The

gas inlet is directly above the magnetic confinement ring. Since this connection is normally under vacuum, it must always be capped or lead to a shutoff valve.

Section A.2: Microwave Power Supplies

Two microwave power supplies have been used with the ECR plasma source: ASTeX/Gerling Laboratories (AGL) Model GL134 2.45 GHz 1 kW Low Ripple Variable Power Supply (ASTeX, Woburn, MA: Bob Shivis @ (781) 937-6237) and Muegge Electronics Model ML1250D-100TE 2.45 GHz 1.25 kW Low Ripple, Pulsable Power Supply (Muegge, Reichelsheim, Germany: Rolf Winter @ 49-6164-93070). Both power supplies are capable of "pulsing", but in different modes.

The AGL power supply operates in either continuous and pulse mode depending on the position of an internal switch (see manual pg. 14 for details). In continuous mode, a 10-turn potentiometer on the front panel controls the microwave power output from 0 – 1000 W. In pulse mode, a 6 – 10 V signal to pin 6 of connector J4 controls the output power level from 300 – 1000 W. A minimum signal of 6 V must be supplied at all times or a system interlock will trip and the power supply will shut down. Since the 6 V signal generates a 300 W plasma, this system is not capable of true on/off pulsing. Rather, it is capable of high/low power pulsing, with the plasma never turning completely off. Typically, a lower level signal of ~ 6.1 V is used to prevent inadvertent shutdown due to a dip in signal below 6 V. The power supply and corresponding magnetron both require sufficient ventilation for forced-air cooling. A series of interlocks protect the power supply from overloads. The manual should be consulted when any of these trip.

The AGL power supply is not equipped to detect and display the reflected power from the system, and therefore, a separate detection and monitoring system was established. A directional coupler located directly before the ECR chamber in the waveguide line was used to sample the reflected power. The coupler signal was displayed on a digital oscilloscope and minimized using the tuning procedure. Good matches for fluorocarbon plasmas were obtained in the 50 – 100 mW range, while Ar plasmas were well matched at ~ 200 mW. The degree of matching usually improves over the length of a run as the bell jar heats up. A water-cooled dummy load (Astex Model LS) capable of dissipating 500 W continuously or 1 kW for up to 1 minute attached to a 3-port circulator is used to protect the magnetron from any reflected power. Any reflected power which reaches the magnetron will cause damage that reduces the lifetime of the magnetron. The extent of lifetime reduction is somewhat dependent on the level of reflected power, ranging from 5 – 10% for modest levels, to a total life span measured in seconds if all 1 kW of power is reflected back to the magnetron. For proper operation, the total reflected power from the plasma should not exceed 200 W.

The Muegge power supply can also operate in either continuous or pulsed mode. However, the Muegge power supply is capable of true on/off pulsing (up to 25 KHz), whereas the AGL power supply can not turn completely off during the "off" portion of the pulsing. In both continuous and pulsed modes, a potentiometer on the front panel controls the microwave output from 0 – 1250 W. An on/off switch on the front control panel starts and shuts down the production of microwaves. With the proper connections (see manual), it is possible to operate the power supply remotely (i.e., via computer). To initiate pulse mode, a +24 VDC signal must be sent to pin #5 on connector X5 at the back

of the power supply, telling the power supply that it is now in pulse mode. A reference (ground) signal must also be supplied to pin #4 on connector X5 for this + 24 VDC signal (+24 V = pin #5 - pin #4). A Lambda Model RWS15A +24 VDC power supply installed in a separate box has been configured to supply the Muegge supply with the "pulse mode" signal. This +24 VDC power supply operates off of 110 VAC power (wall plug). In addition to the "pulse mode" signal, the pulse sequence must also be fed to the microwave power supply. The manual states that a $10 < V < 24$ VDC pulse signal (typically from a pulse generator) must be sent to pin #6 on connector X5 at the back of the power supply. However, due to the relatively slow pulsing (milliseconds) used for our deposition processes, a 0 – 9 V signal was deemed adequate to trigger the pulse sequence by the Muegge engineers. If faster pulsing is desired using the same power supply, Muegge should be contacted for instructions. A reference or ground signal must also be sent to pin #7 on the same connector. The current setup has the internal wire of the BNC connector from the pulse generator connected to pin #6, while the BNC grounding shield is connected to pin #7. The "off" time signal level must be set to 0 V, while the "on" time level must be set as high as possible ($\geq$ + 9 V). Both the "pulse mode" and the pulse sequence connections are currently wired through a single DB25 male connector that mates with connector X5 on the back of the microwave power supply. Connector X4 on the back of the power supply is an external interlock provided for the water cooling line, and must have pins 1 & 2, 3 & 4, and 5 & 6 connected to one another (in those pairs) in order for the power supply to turn on. The first two pairs are safety intelocks, while the last pair is for the water cooling. All of these connections are currently set up on a blank connector. Pins 5 and 6 DO NOT actually connect to the

magnetron water cooling lines. Care must be taken to ensure that water cooling is always turned on before attempting to run the power supply.

Whereas the microwave power supply has forced air cooling, and thus requires adequate ventilation, the accompanying magnetron requires water cooling at a rate of 2 L/min. ***Water cooling must always be turned on before operating the microwave power supply.*** The lab chiller is already being operated at maximum capacity since it is connected to both parallel plate reactors and is supplying chilled water to the ECR cooling channel (dummy load is removed from waveguide line for Muegge supply since Muegge isolater performs same function). Therefore, the cooling lines originally installed for the Mydax Galden fluid chiller (see Section A.4) have been diverted to the magnetron. Since the Mydax chiller is not regularly used for chuck cooling, this arrangement should not cause any problems unless cooling of the wafer chuck is deemed necessary. Since these cooling lines are connected to a lab sink versus a closed circuit chiller, the water temperature is not controllable. If the magnetron is to be used extensively, more permanent, temperature controlled water cooling lines should be set up (i.e., buy an additional water chiller). The magnetron is also placed on a high shelf and extreme care must be taken not to shift it from its position on the shelf. The shelf provides the primary support for the length of waveguide connecting the magnetron with the ECR chamber, and improper alignment of the magnetron will induce stress on the bell jar, which will result in fracturing of the bell jar. The reflected power is sampled by an isolator directly before the magnetron and displayed on the front panel of the power supply.

When first operating the Muegge power supply, an internal fuse on transformer T3 (208 V $\rightarrow$ 220 V transformer) blew due to power surges when the main switch is turned on. This problem has been corrected by replacing the original 1.6 A slo-blo fuse with a 3.0 A slo-blo fuse. If main power fails to come on after turning the main switch, however, this fuse should be the first thing to check. Muegge Electronic's US partner, Cober Electronics in South Norwalk, CT (Marius Negluchi, (203) 855-8755 x322) can be contacted for further repair assistance.

In general, whenever generating microwave power there exists the possibility of microwave leakage from the system. The maximum acceptable leakage rate is 10 mW/cm^2. The system should be checked for microwave leakage whenever any of the microwave components or large sections of the reactor (i.e., chuck, ECR source) are disassembled or moved. The MIT Radiation Protection Office (Donald Haes, 258-5640) will do microwave leak checks upon request.

Section A.3: Deposition Chamber

Figures A-3 – A-14 show the design schematics used to construct the deposition chamber. Figs. A-3 – A-7 show progressive top-down cross sections of the chamber detailing the placement of all view and access ports, while Figs. A-7 – A-11 show front and side views of the reactor giving complete sizing specifications for all of the ports. The NW 16 ports have sapphire windows whereas the NW 50 ports have 7056 glass windows (MDC Vacuum Products). The NW 40 ports are for pressure sensors. Figs. A-12 and A-13 are details of the wafer chuck mating flange and the rectangular port for the loadlock, respectively, while Fig. A-14 demonstrates how horizontal distances were

calculated for all of the ports. The chamber was constructed at MDC Vacuum Products (Roy Andrews, 800-443-8817) in Hayward, CA.

Section A.4: Wafer Handling

Five inch wafers are introduced to the vacuum chamber via an MDC Vacuum Products Rectangular *Fast Entry* Load-Lock System (Model #RFEL-824G) with a 24" transfer arm and precision X-Y manipulator (see Figs. A-15 – A-17). The loadlock is pumped down with a Leybold Trivac D4A roughing pump which can maintain a base pressure of ~ 20 mTorr. An MKS Instruments Baratron Type 622A pressure transducer connected to Channel #1 of an MKS PDR-C-2C power supply/readout is used to monitor the loadlock pressure (see Section A.6). Five inch wafers are placed on a custom sample holder (see Fig. A-18) which orients the wafer via its primary flat. The sample holder was initially made of solid stainless steel; however, the weight of the holder bowed the transfer arm excessively, so the bulk of the steel was removed. Wafers are then translated horizontally into the vacuum chamber where they are placed on a small ledge inside a 5" mechanically clamping wafer chuck (Lucas Labs, Paul Leeman, (650) 347-1293). The transfer arm is lowered until the wafer is supported only by the ledge and then withdrawn. A pneumatically driven piston lifts the wafer and clamps it to the top of the chuck. A removable quartz ring is placed on top of the aluminum clamping ring at the top of the chuck in order to prevent chamber contamination due to sputtering of the aluminum ring. Proper placement of the wafer upon clamping can be verified by directing the interferometry laser onto the quartz ring. The wafer should be visible in the scattered laser light. The wafer is retrieved by attaching a removable clamp to the

transfer arm, which then secures the wafer onto the transfer arm. Detailed procedures for wafer loading and unloading are given in Sections A.8.1 and A.8.3.

The 5" wafer chuck is shown schematically in Figs. A-19 – A-21. The chuck is capable of being rf biased via the N-type rf connector on the back side of the chuck. However, due to design flaws in the chuck, a successful bias has not be achieved while the chuck has been attached to this system. Paul Leeman of Lucas Labs should be consulted if proper operation of the chuck bias is desired. The chuck is also equipped for backside helium cooling of the wafer with HT-135 Galden heat transfer fluid (a dielectric perfluoroether) acting as the He heat sink. The backside He flow is controlled via a needle valve and a MKS Instruments Baratron Type 122A pressure gauge with a full scale reading of 10 Torr. The He backside pressure should be set to ~ 1 Torr. Care must be taken not to apply too much pressure to the wafer backside as the wafer can break. The Galden fluid is circulated through the main chuck column and is maintained at a temperature between –40 and 30°C via a Mydax Model 1VL10W water cooled chiller (Mydax, Auburn, CA: Sandie Smith, (530) 888-6662). ¾" PTFE (polytetrafluoroethylene) tubing is used to connect the chuck to the Mydax chiller. Flaretek fittings (Harbor Controls, Chelmsford, MA, (978) 453-2323) are used to connect the PTFE tubing to both the wafer chuck and the chiller. Care should be taken whenever filling the Mydax chiller with Galden fluid as it has a high vapor pressure and is very expensive (~$400/gal, can be obtained from Modoc Engineering, Santa Clara, CA, 800-237-7111). The chiller has a 2 gallon reservoir of Galden fluid which is pumped at 4 GPM @ 60 psi through the wafer chuck. Extreme care should be taken never to bend the PTFE tubing as it can easily develop leaks. A PTFE flaring mandril is available for

expanding the PTFE tubing when making repairs to the tubing. Over time, the reservoir in the chiller may become depleted due to small leaks from the inlet port. Refer to the chiller manual instructions for procedures to fill and start up the chilling unit. The water lines for the chiller are currently connected to one of the lab sinks, and thus, the water is not actually continuously circulated. If the chiller is to be operated for long periods of time, it is recommended that provisions be made to connect it to the building water chilling system. The cooling water for the chiller must have a minimum flow of 2.5 GPM with an inlet to outlet pressure differential of 20 psi for optimal performance. It has been found through the use of Temp-Plate temperature recording decals (Wahl Instruments, Ashville, NC, 800-421-2853) that there is no significant heating of the wafer when bias is not applied to the chuck. All of the films currently deposited have not utilized chuck biasing, and therefore, the chuck chilling system has not been used. Compressed air for the pneumatic piston is controlled with a 4-way valve located on the reactor support system near the base of the chuck. The orientation of the valve for raising and lowering the chuck is clearly indicated near the valve. Building compressed air is used to operate the chuck.

Section A.5: Vacuum System

An Osaka Vacuum 3200 L/s Model TH3003M turbomolecular pump (Osaka Vacuum, San Jose, CA: John Norton, (408) 441-7658) backed by a 50 CFM Alcatel Model 2063 roughing pump (Alcatel Vacuum Products, Hingham, MA: Glenn Melanson, (781) 331-4200) is used to maintain vacuum in the deposition chamber. A base pressure of $\sim 10^{-7}$ Torr is typical for the elastomer (Viton) seals used in the system.

General operating procedure calls for the two pumps to be running continuously, only to be shut down for pump or system maintenance. The turbopump was originally owned by Lucent Technologies Bell Laboratories and was donated to the lab after ~ 6 years of continuous operation. Several problems were encountered during startup of the system that eventually led to the replacement of the pump by a spare that Osaka Vacuum secured for us. The pump power supply was undamaged, so the power supply was tuned to the replacement pump. Thus, although the serial numbers on the pump and power supply do not match (as usually required for these types of pumps), they are fully tuned to each other. It should be noted that the original turbopump was a "chemical" pump, intended for use with corrosives such as fluorine. The replacement pump is NOT a chemical pump, and so greater care should be taken in exposing it to large quantities of extremely corrosive gases, as the rotor will eventually be corroded.

The turbopump is magnetically suspended during operation, rotating at 200 rps when at full speed. The pump makes no noticable noise during normal operation; however, during deceleration and shutdown, a slight noise indicates the rotor is braking and eventual release of the magnetic suspension gives a clicking sound. Both the turbopump power supply and pump utilize forced air cooling, and so sufficient ventilation must be available. Several considerations must be kept in mind during operation of the turbopump. First, the maximum backing pressure (pressure at turbopump outlet) is 150 mTorr. Exceeding this pressure will result in a full-speed touchdown of the magnetically suspended rotor onto ceramic bearings. The bearings are designed to withstand 5 full-speed touchdowns before replacement, and once the rotor is stopped, after the cause of the touchdown is determined, the pump can usually be started

up again with no problem. A log of touchdowns is maintained on the turbopump power supply. The dry bearings should be replaced upon the 5th high speed touchdown. The CSB light on the front panel of the power supply will light up at the 5th touchdown (sometimes it lights up before the 5th touchdown, in which case contact Osaka Vacuum to learn how to reset it—the log sheet should be the most accurate tally of touchdowns). Contact Osaka Vacuum for dry bearing replacement.

The backing pressure is monitored by an MKS Instruments Baratron Type 626A pressure transducer with a full scale reading of 1 Torr. With the current turbo/backing pump arrangement, a maximum gas flowrate of 100 sccm is possible; however, the backing pressure should always be used to determine if a particular flow rate is compatible with the turbopump requirements. In addition, it is important to be cautious when opening the system throttle valve after maintaining a mTorr pressure in the chamber. Full opening of the valve may lead to a rapid rise in the backing pressure, potentially exceeding the 150 mTorr limit. The throttle valve should be opened gradually, allowing the gas to evacuate with a safe backing pressure before opening completely.

Touchdown on the dry bearings involves a great deal of force. If the turbopump was not properly secured and something went wrong during touchdown (i.e., rotor blade breaking), the turbopump could easily shear itself off from the deposition chamber. Therefore, the turbopump has been bolted to its support frame, which is in turn bolted to the cement floor. In any instance where the turbopump must be removed from the frame, it is ***vital*** that the bolts securing the pump to the frame be reattached upon reassembly ***before*** the pump is started.

Second, the turbopump power supply requires an input voltage of 200 V (± 10%). The input power line is rated to 208 V (single phase, 4.5 A), and is passed through a Controlled Power Company Model LT-R uninterruptable power supply (UPS) (Controlled Power, Troy, MI: Jason Verlinde, (800) 521-4792 x255) modified to act solely as a power conditioner to ensure a constant, clean 208 V signal to the turbopump power supply. A drop or spike in the input power voltage will cause the pump to touchdown on the dry bearings. In the case of a power outage, the turbopump power supply is equipped with a battery which will initiate a controlled shutdown of the turbopump. Since the roughing pump is not connected to a UPS, it was necessary to rewire the turbopump UPS so that it acts solely as a power conditioner and does not attempt to keep the turbopump running when the roughing pump has shut off (see Fig. A-22 for changes in electrical schematics). In the current configuration, during a power outage the roughing pump will shut off and the turbopump will go through a controlled shutdown. If there are no large vacuum leaks, the turbopump backing pressure should not rise high enough to cause a high-speed touchdown during the shutdown procedure. When power is restored, the roughing pump will start up again (its circuit breaker does not trip off), while the turbopump will remain off until manually started up again. An indicator on the power supply front panel shows the status of the power supply battery. This battery should be replaced approximately every two years. The current battery was installed 6/18/97. See the turbopump manual for instructions on changing the battery.

Third, the turbopump system is sensitive to any stray rf or dc signals that may interrupt communication between the power supply and the pump. All rf cables in the vicinity of the turbopump should be shielded and checked to make sure that any leakage

is minimzed. The main cable connecting the power supply to the pump has been wrapped in aluminum foil to deflect any signals. Any BNC cabling used in powered lines should be replaced with double-shielded rf cabling, and additional shielding should be added if there is still leakage from these cables.

Finally, during startup and shutdown of the turbopump, the roughing pump should always be running. The turbopump can be started at atmospheric pressure, but in order for it to reach full speed, the backing pressure must be < 150 mTorr by the time the rotor acceleration period has stopped (~ 20 min.). Therefore, normal operating procedure has the roughing pump started first, and then the turbopump. At shutdown, the turbopump manual indicates the roughing pump can be shut down while the turbopump is decelerating, but in practice the roughing pump should be left on until the turbopump has come to a complete stop. Shutting the roughing pump off while the turbopump decelerates is intended to prevent backstreaming of the roughing pump hydrocarbon oil into the turbopump. However, a MDC Vacuum Products Model KMST-100-Z molecular sieve using Type 13X synthetic zeolite has been placed between the roughing pump and the turbopump, so oil backstreaming is not an issue.

The Alcatel roughing pump is separated from the turbopump by a right-angle valve that is generally left open. This valve should be closed when baking out the molecular sieve. The molecular sieve should be baked out every time the pump oil is changed (i.e., every couple of months), and the zeolite charge should be replaced periodically (baking only removes trapped water vapor, not trapped oil). It should be noted that, as with the replacement turbopump, the roughing pump is not a chemical pump. For roughing pumps, exposure to corrosive gases will eventually damage both the

rotor and the seals, with the seals most likely to fail first. Hence, the seals in the roughing pump may need to be replaced at more frequent intervals than those of the corresponding chemical pump. A good pump repair/maintenance company is Mass-Vac in North Billerica, MA (978-667-2393).

Section A.6: Instrumentation

The ECR deposition system is equipped with a variety of instrumentation for monitoring and control. A series of 5 vacuum pressure gauges are used to monitor the pressure in various parts of the system. Four Baratron pressure transducers from MKS Instruments (Andover, MA; Matt Kosakowski, (978) 975-2350) monitor the main operating pressures and their configurations are listed in Table A-1.

Table A-1: Pressure transducer configurations for ECR reactor.

Model	Pressure Range (full scale, Torr)	Power Supply/ Readout	Pressure
127A	0.1 heated @ 45°C	651C pressure controller	Main chamber
626A	1	PDR-D-1	Turbopump backside
622A	10	PDR-C-2C, Channel #1	Loadlock
122A	10	PDR-C-2C, Channel #2	He backside

The Model 127A gauge on the main chamber is used in a feedback loop with a MKS Instruments Model 653B Exhaust Throttle Valve (NW 200 flange, non-sealing) to control the chamber pressure (via 651C pressure controller). The Model 651C pressure controller has 5 programmable setpoints which are currently assigned: A = 10 mTorr, B = 5 mTorr, C = 30 mTorr, D = 80 mTorr, E = throttle valve 15% open. The PID control

parameters can be set for each channel to obtain the desired response time for a particular setting to be reached. The Model 127A, 122A, and 622A transducers are each isolated from the system by Nupro Model SS-8BK bellows sealed valves (Cambridge Valve & Fitting, Billerica, MA, (781) 272-8270). In addition, a MKS Instruments HPS Division Low-Power Nude Sensor Y_2O_3-coated Ir hot filament ion gauge controlled by a SensaVac™ Series 919 Hot Cathode Ioniziation High Vacuum Sensor System is used to check the chamber base pressure (HPS, Boulder, CO, Mark Thompson, (800) 345-1967). This ion gauge was inadvertently coated with fluorocarbon film during initial depositions and ceased to operate. HPS (Eric Bopp) indicated that the gauge can be baked at 400°C without damaging any of its components. For safety, the gauge was repeatedly baked at 350°C (total time ~ 6 hrs) until the gauge started working again. A 90° turn has been added to the ion gauge port to prevent additional coating of the gauge in the future.

Since the Model 653B Exhaust Throttle Valve is non-sealing, it is not possible to measure the reactor volume directly by sealing the chamber, releasing a known amount of gas, and measuring the pressure rise. A rough calculation of the volume has been made based on the chamber geometry, which gives a value of ~ 37 L.

A gas panel with five gas inlets controls the flow of gases into the deposition chamber. Gas feed flows into the deposition chamber from one ¼" VCR port directly beneath the quartz bell jar. The gas panel consists of four mass flow controllers (MFCs) and one needle valve, each of which is isolated on both sides by Nupro Model SS-4BKT bellows sealed valves. The MFCs configurations are given in Table A-2. (Note: 1,1,2,2-$C_2H_2F_4$ will be listed as $C_2H_2F_4$)

Table A-2: MFC configurations on ECR gas panel.

Manufacturer	Model	Calibration Gas	Range (sccm)	Process Gas	MFC Channel
Unit Inst.	UFC-1200A	C_3F_6	200	HFPO	5
Unit Inst.	UFC-1100A	Ar	20	Ar	4
Unit Inst.	UFC-1100A	H_2	100	O_2	3
Brooks Inst.	5850E	$C_2H_2F_4$	100	$C_2H_2F_4$, CH_2F_2, CHF_3	2

A Unit Instruments URS-100 five-channel controller controls all of the MFCs. Flows of process gases different from an MFC's calibration gas are determined by the ratio of the respective gas correction factors: $\frac{Q_1}{Q_2} = \frac{C_1}{C_2}$, where Q_i = flow of gas i and C_i = correction factor for i. The correction factors for each process gas with the corresponding maximum flow for the assigned MFC are listed in Table A-3. (Note: 1,1,2,2-$C_2H_2F_4$ will be listed as $C_2H_2F_4$)

Table A-3: Gas correction factors and maximum process flows for ECR gas panel.

Process Gas	Correction Factor	MFC Gas	MFC Correction Factor	Max. Process Gas Flow (sccm)
HFPO	0.2	C_3F_6	0.347	115
$C_2H_2F_4$	0.295	$C_2H_2F_4$	0.295	100
CH_2F_2	0.627	$C_2H_2F_4$	0.295	213
CHF_3	0.528	$C_2H_2F_4$	0.295	179
Ar	1.398	Ar	1.398	20
O_2	0.994	H_2	1.024	97

The fifth inlet channel is for nitrogen, and is controlled by a needle valve. This inlet should never be used when the turbopump is in operation as the uncontrolled flow can easily exceed the pumping capabilities of the turbo/roughing pump system. Finally, the

HFPO MFC has a slight leak, and therefore, the top isolation valve for that MFC should remain closed unless flowing HFPO. Normally, all of the isolation valves (except top HFPO and top N_2) are left open. Pressurized sections of the gas panel could potentially contain too much gas for the turbopump backing pressure to remain < 150 mTorr if opened fully in one step. Therefore, if the system is pressurized, all valves up to the MFCs (and needle valve for N_2) should be open when initial pump-down occurs.

On/off pulse conditions are set using a Systron-Donner Model 110C Pulse Generator (obtained through BID Service, Freehold, NJ, (732) 863-9500). This pulse generator is capable of controlling both the upper and lower level voltages of the pulse with minimum and maximum voltages of ± 9 V (max separation between levels = 18 V). The pulse generator signal is monitored on a Nicolet Model 4094 Digital Oscilloscope (Nicolet, Madison, WI, (608) 276-5600). The pulse on time is controlled by the "pulse width" dial on the pulse generator, while the pulse off time is set by the "repetition rate" dial. In the current configuration, the pulse generator signal is monitored on channel A, while the ECR reflected microwave power diode signal is monitored on channel B. The oscilloscope and pulse generator should be allowed to warm up for at least 15 min. prior to setting any pulse conditions.

Section A.7: *In situ* Diagnostics

Two in situ diagnostic techniques are used with the ECR deposition system: optical emission spectroscopy (OES) and laser interferometry. An Ocean Optics Model S2000 OES (Dunedin, FL, (727) 733-2447) configured with a 10 μm slit, 200 – 800 nm grating, and UV/VIS upgrade is used in conjunction with a 600 mm optical fiber with a

UV collimating lens provides information about the chemical species present in the plasma phase. The spectrometer is used in "scope" mode, where the light from the plasma is the source of the OES signal. The length of time over which a signal is sampled ("integration" time) is controlled via the Ocean Optics OES software (OOIBase). The lower limit of the integration time is determined by the PC A/D board used with the spectrometer. A 1 MHz, 8 channel A/D board with a minimum integration time of 3 ms. has been installed with this spectrometer. A typical integration time for a continuous plasma in the ECR chamber is 1076 ms. Care must be taken to keep both the optical fiber position and integration time constant in order to make proper comparisons between data which do not incorporate an actinometer. These requirements are not as stringent when an actinometer is used. The optical fibers are quite fragile and should be treated with care to prevent breakage due to rough handling or excessive bending. The fibers also have a limited lifetime and should be replaced every few years. The optical fiber should be mounted on one of the NW16 sapphire viewports since the sapphire does not significantly block UV light. The fiber is currently held in position by taping it to a clamp attached to the NW16 port. NOTE: Proper eye protection should be worn when viewing the plasma from one of the sapphire viewports in order to prevent UV damage to the eye. In general, plastic covers are placed over all of the viewports (glass, quartz & sapphire) not in use to prevent inadvertant UV exposure, but proper eye protection should be worn, regardless.

A laser interferometer for *in situ* film thickness measurements has been constructed from a Uniphase Model 1507P-1 0.8 mW polarized He-Ne laser (Uniphase, San Jose, CA, (408) 434-1800) and a Metrologic Model 45-545 Digital Laser Power

Meter (Metrologic, Blackwood, NJ, 800-436-3876). The laser is reflected by a mirror into the deposition chamber and onto the wafer through one of the NW50 glass viewports. When properly aligned, the laser exits the opposite glass viewport and is detected by the laser power meter. The laser strikes the wafer at an approximate angle of 69° from the normal. Holders have been designed to attach to the NW50 windows and hold the optical components. Alignment is achieved by moving the mirror and detector within their holders until a maximum laser signal is detected. The maximum signal is usually ~0.2 on the 2 mW scale (some signal is lost due to reflections off the windows). The interferometer signal is fed to an A/D board on a PC which is controlled by a LabView program called Laser (written by Brett Cruden). The rate of signal acquisition and the maximum number of data points to acquire are set by this program, which shows a real-time trace of the interferometer signal. Oscillatory fringes in the signal indicate a change in film thickness. Originally, an analog laser meter was used, but proximity to the ECR magnets caused that meter to go out of alignment. The laser power meter is unaffected by the magnets. Both the laser interferometry and OES acquisition programs can be run simultaneously under Windows.

Section A.8: Operating Procedure

Section A.8.1: Wafer Loading

Steps: (assumes starting with atmospheric-pressurized loadlock, valve between loadlock & chamber CLOSED)

1. Check to make sure the XY manipulator settings are: vertical = 6.0, horizontal = 3.716 (black micrometer scale)

2. Check to make sure wafer chuck is in the DOWN position (4-way valve pointing to the RIGHT).
3. Place 5" wafer on sample holder, orienting the primary wafer flat with the base of the holder.
4. Close loadlock access door and tighten knob.
5. Making sure the green shutoff valve under the loadlock is OFF, open valve between loadlock and loadlock roughing pump (pump should be ON)
6. Let loadlock pump down until reaches ~ 30 mTorr (channel #1 on PDR-C-2C pressure readout).
7. Flowing Ar or another inert gas, set chamber pressure to 80 mTorr (Setpoint D on 651C pressure controller).
8. When both pressures reached (30 mTorr for loadlock, 80 mTorr for chamber), slowly open slit valve between loadlock and chamber. A pressure rise should be seen on the loadlock side (channel #1 on PDR-C-2C pressure readout). Always keep an eye on the backing pressure for the turbopump (should not exceed 150 mTorr). Open slit valve fully.
9. Push transfer arm in until the guide marker on the arm reaches the 1st black mark on the guide pole (a hole in the transfer arm should be roughly centered in the loadlock access port window).
10. Slowly raise the transfer arm height to 7.75 with the vertical knob of the XY manipulator.
11. Push transfer arm in until the guide marker reaches the 2nd black mark on the guide pole. You should feel the wafer reaching the inside wall of the chuck.

If the arm does not go to the 2nd mark, the wafer is not fully in—pull the arm out slightly, try again, raising the arm **slightly** if necessary. *****NEVER TRY TO RAISE THE CHUCK IF THE 2ND BLACK MARK IS NOT REACHED DURING TRANSFER—THE WAFER WILL BREAK*****

12. Lower the transfer arm height to 6.5 using the vertical knob of the XY manipulator. The wafer is now being supported on a ledge inside the chuck.
13. Carefully back the transfer arm out to the 1st black mark on the guide pole.
14. Lower the transfer arm height to 6.0.
15. Back the transfer arm out fully. Make sure that the wafer is not still on the sample holder. If it is, repeat steps 9 – 15.
16. **CLOSE THE GATE VALVE.**
17. Raise the chuck by turning the 4-way valve towards the floor (pointing DOWN). Pressurized air will leak out of the 4-way valve making an audible hiss.
18. Turn the Ar (or inert gas) flow off. DO NOT open the chamber throttle valve.
19. When the chamber pressure is ~ 20 – 30 mTorr, open the chamber throttle valve to 15% (Setpoint E on the 651C pressure controller). *****WATCH THE TURBOPUMP BACKING PRESSURE; IT SHOULD NOT EXCEED 150 mTorr.*****
20. When the chamber pressure is ~ 5 mTorr, fully open the chamber throttle valve.

Section A.8.2: Plasma Ignition Setup

NOTE: In general, DO NOT strike a plasma without a wafer loaded onto the chuck—microwave leakage can result (see Section A.2).

Steps:

1. Turn on pulse generator and digital oscilloscope (allow at least 20 min. warm up time; power switch for oscilloscope is on back of instrument).
2. Start chiller cooling water (wait at least 10 min. before striking plasma)
3. If taking interferometry and/or OES data, start up computer and load appropriate program.
4. Power up microwave power supply (just turn power supply on, do not turn microwaves on).
5. Set pulse rate on/off times and voltage levels using pulse generator and oscilloscope (see Section A.6 for details). **If using the AGL microwave power supply, after setting the pulse rate, switch the oscilloscope to Channel B and level the horizontal guideline to ~ 200 mV**.
6. Set gas flow rates using URS-100 MFC controller. Channel assignments are listed in Table A-2. Maximum flow rates are listed in Table A-3.

   ALWAYS MONITOR THE TURBOPUMP BACKING PRESSURE WHEN SETTING FLOW RATES; IT SHOULD NOT EXCEED 150 mTorr AT ANY TIME*
7. Set chamber pressure using MKS 651C pressure controller. Setpoint A is configured for 10 mTorr.

8. When the flow rates, pulse rate, and chamber pressure are stabilized, start the interferometry data acquisition.
9. Turn ECR N_2 purge on (1 turn from full open).
10. Double check that wafer chuck is in the UP position, the cooling water is flowing normally (check chiller to see if stopped due to high temp/low level), the N_2 purge is flowing, pulse rate is set, flow rates are set, and system pressure is stabilized.
11. Turn microwave power ON.
12. Using the ECR microwave tuning probe and short tuning adjustment knob (see Section A.1), tune the plasma until a good match is achieved (for AGL power supply, minimized diode signal on oscilloscope; for Muegge power supply, minimize displayed reflected power).
13. Deposit for up to 30 min. – N_2 purge will ice up lines if allowed to run longer.
14. Take OES measurements as needed during deposition. Growth can be monitored via real-time *in situ* interferometry.
15. When finished deposition run, turn microwave power OFF.
16. Reduce N_2 purge flow until valve is ~1 – 2 turns open.
17. Shut off process gas flows.
18. Open throttle valve SLOWLY, monitoring turbopump backing pressure at all times (should not exceed 150 mTorr).
19. Let chamber pump down for 2 – 3 minutes.
20. Unload wafer → SEE Section A.8.3.
21. Check if bell jar needs cleaning (see Section A.1 and Section A.8.5).

22. If doing another deposition run, load another wafer (see Section A.8.1) and go to Step 5.
23. If done for day, see Section A.8.4.

Section A.8.3: Wafer Unloading

NOTE: Chuck should remain in the UP position until specified. When there is a wafer in the chuck NEVER have the chuck in the DOWN position during pressure equalization and valve opening steps.

Steps:

1. Check to make sure isolation valve between loadlock and deposition chamber is closed.
2. Close valve between loadlock and loadlock roughing pump.
3. Slowly open green valve under loadlock (next to roughing pump isolation valve) to vent loadlock access port to atmosphere.
4. When at atmospheric pressure, open access door and attach custom wafer clamp to the sample holder, being careful not to bend the clamp or move the transfer arm significantly.
5. Close access door and tighten knob.
6. Close green venting valve and open valve between loadlock and loadlock roughing pump.
7. Let loadlock pump down until reaches ~ 30 mTorr (channel #1 on PDR-C-2C pressure readout).

8. Flowing Ar or another inert gas, set chamber pressure to 80 mTorr (Setpoint D on 651C pressure controller).
9. When both pressures reached (30 mTorr for loadlock, 80 mTorr for chamber), slowly open slit valve between loadlock and chamber. A pressure rise should be seen on the loadlock side (channel #1 on PDR-C-2C pressure readout). Always keep an eye on the backing pressure for the turbopump (should not exceed 150 mTorr). Open slit valve fully.
10. Lower the wafer chuck by turning the 4-way valve so that it points to the RIGHT. A hissing sound will accompany the release of pressurized air.
11. Check to make sure the XY manipulator settings are: vertical = 6.0, horizontal = 3.716 (black micrometer scale)
12. Push transfer arm in until the guide marker on the arm reaches the 1st black mark on the guide pole (a hole in the transfer arm should be roughly centered in the loadlock access port window).
13. Slowly raise the transfer arm height to 7.0 with the vertical knob of the XY manipulator.
14. ***Slowly*** push the transfer arm into the chamber. You should feel the clamp on the sample holder meet the edge of the wafer. Push gently, and if there is no resistance, push the transfer arm in until the guide marker reaches the 2nd black mark on the guide pole.
15. ***If there is resistance:*** back the transfer arm out slightly and try again. If there is still resistance (i.e., can't feel the clamp taking hold of the wafer), when backing the transfer arm out, raise or lower it slightly before trying to

engage the wafer again. Through careful trial and error, the clamp should eventually take hold of the wafer. ***DO NOT TRY TO FORCE THE CLAMP TO TAKE HOLD – THE WAFER WILL BREAK****

16. Once the clamp has taken hold of the wafer, back the transfer arm out a little (an inch or two).
17. Lower the transfer arm to 6.5 using the vertical knob of the XY manipulator.
18. Carefully back the transfer arm out to the 1st black mark on the guide pole.
19. Lower the transfer arm height to 6.0.
20. Back the transfer arm out fully. Make sure the wafer is on the sample holder. If it is not, repeat steps 11 – 20. If the wafer cannot be retrieved, the system will have to be shut down and pressurized so that either the ECR source or the loadlock can be disconnected and the wafer manually retrieved. The same applies if it is suspected that the wafer has broken.
21. **CLOSE THE GATE VALVE.**
22. Close the valve between the loadlock and the loadlock roughing pump.
23. Slowly open green valve under loadlock (next to roughing pump isolation valve) to vent loadlock access port to atmosphere.
24. Open access port and retrieve wafer from sample holder.
25. Remove custom wafer clamp by pulling from the *underside* of the clamp. DO NOT pull on the top part of the clamp, as that will deform the clamp over time.

26. If not loading another wafer, turn the Ar (or inert gas) flow off. DO NOT open the chamber throttle valve. If doing another deposition run, see Section A.8.1 for the wafer loading procedure.
27. When the chamber pressure is ~ 20 – 30 mTorr, open the chamber throttle valve to 15% (Setpoint E on the 651C pressure controller). ***WATCH THE TURBOPUMP BACKING PRESSURE; IT SHOULD NOT EXCEED 150 mTorr.****
28. When the chamber pressure is ~ 5 mTorr, fully open the chamber throttle valve.

Section A.8.4: Shutdown and Vacuum Startup

Section A.8.4.1: Normal Shutdown

Normal shutdown implies shutdown of all of the reactor components involved in deposition, with the exception of the pumping system. Normal procedure is for the vacuum system to be running continuously (24 hrs a day, 7 days a week). Shutdown of the vacuum system is described in Section A.8.4.2.

Steps: (assumes wafer has been unloaded)

1. Shut off any gases used at the source (i.e., Ar cylinder, HFPO cylinder, etc.).
2. Observing guidelines for maximum flow allowed for turbopump, pump out each pressurized line ONE AT A TIME. ***WATCH THE TURBOPUMP BACKING PRESSURE; IT SHOULD NOT EXCEED 150 mTorr.**** Depending on the gas, line pump down should take 5 – 15 minutes.

3. Wait until at least 10 min. after the last plasma was extinguished, then turn the N_2 purge line off. During that 10 min., the N_2 purge should have been set to its lower flow rate (1 – 2 turns open).
4. Chamber throttle valve should be left in the full open position, continuously pumping down the chamber.
5. Power down microwave power supply (main on/off switch; microwave power should already be turned off).
6. Turn off pulse generator and oscilloscope (power switch for oscilloscope is on back of instrument).
7. If plasma operation was brief, wait at least 30 min. after last plasma was extinguished, then turn cooling water off. If plasmas were on for a long time ($\geq$ 20 min.), then wait at least 50 – 60 min., then turn cooling water off. Check the temperature of the ECR source walls about 5 min. after cooling water shutdown. If the walls are warm, turn cooling water back on for another 30 minutes.

Section A.8.4.2: Complete Shutdown

Complete shutdown involves shutdown of all reactor components including the vacuum components (turbo and roughing pumps) and pressurization of the system.

Steps:

1. Follow normal shutdown procedure in Section A.8.4.1.
2. Wait at least 30 min. after normal shutdown procedure to allow for complete pumping of the chamber.

3. Press STOP button (green) on turbopump power supply. A slight whining noise will be heard as the rotor decelerates. Full deceleration will take ~ 20 minutes. A slight pressure rise may be seen in the chamber during the latter part of the deceleration. When the pump has fully decelerated, the magnetic levitation will be released, producing a slight shock noise.
4. When turbopump has come to a COMPLETE STOP, turn off the roughing pump.
5. Close the isolation valve between the chamber and the Model 127A pressure transducer. A pressure rise will still be seen over time as the isolation valve leaks slightly.
6. Close the isolation valve between the chamber and the Model 122A pressure transducer on the He backside cooling line.
7. Disconnect the needle valve on the He backside cooling line from the He cylinder (disconnect the UltraTorr fitting).
8. Fully open needle valve on He backside cooling line. This gives the system a path to vent to atmosphere if the system is pressurized too much.
9. Fully open the N_2 needle valve on the gas panel to pressurize the system. NOTE: Chamber throttle valve should be left fully open during pressurization so that pumps are pressurized as well.
10. Let N_2 run about 5 – 10 min., then CLOSE N_2 needle valve.
11. System will complete pressurization through He backside cooling needle valve. Check periodically to see if system is at atmosphere (put finger on

opening at He backside cooling needle valve). Pressurization typically takes ~ 20 min after N_2 is turned off.

Section A.8.4.3: Vacuum Startup

After the vacuum system has been shutdown according to Section A.8.4.2, follow the procedure detailed below for pump startup.

Steps:

1. Reconnect needle valve on He backside cooling line to He cylinder.
2. CLOSE He backside cooling needle valve.
3. Make sure all process gas flows are OFF.
4. Make sure all of the gas panel isolation valves *downstream* of the MFCs (needle valve for N_2) are open.
5. Make sure that any other seals opened while system was pressurized are sealed again.
6. Turn on roughing pump.
7. Open isolation valves for Model 127A and Model 122A pressure transducers.
8. Wait until chamber pressure (as measured by Model 127A transducer, viewed on 651C pressure controller) is < 100 mTorr.
9. Press START button (red) on turbopump power supply. Magnetic levitation will turn on and the rotor will start accelerating. There should be no noise from this startup. The turbopump will take ~ 20 min. to reach full speed.

10. Check base pressure after turbopump has been operating at full speed for ~ 30 min. by turning on ion gauge. After lengthy pumping, the base pressure can eventually reach ~ 10-^{7} Torr.

Section A.8.5: Maintenance

The roughing pump oil should be changed approximately every two months, sooner if the oil in the roughing pump viewport turns increasingly brown. The roughing pump uses ~ 1.5 gallons of Alcatel 300 pump oil, which is a clear, hydrocarbon-based oil. A complete system shutdown (see Section A.8.4.2) must be initiated to change the roughing pump oil. The loadlock roughing pump oil should also be changed at the same time. A log of pump oil changes should be kept. See the roughing pump manual for instructions on how to change the pump oil. NOTE: The pump oil should be hot when draining from the pump, as the oil is less viscous when hot.

The molecular sieve trap should be baked out whenever the roughing pump oil is changed. The valve between the turbopump and the roughing pump should be closed for the bake out. The bake out should also occur **before** the pump oil is changed so that the cleanest oil possible is being used when the full vacuum system is started up again. A cartridge heater placed in the center hole of the molecular sieve trap is used to bake out the sieve. Always make sure to connect the grounding cable of the cartridge heater to the post on top of the trap before turning on the heater. The roughing pump should be on during the bakeout, and the sieve should be baked out for ~ 1 – 2 hours. The bakeout will remove any trapped water vapor in the sieve; however, it will not remove any trapped oil. Hence, the sieve charge should be replaced periodically (~ 2 times a year).

If the ion gauge becomes coated with film again, it can be baked out at 350°C for as long as necessary to remove the film. The Laibinis lab has an oven large enough to hold the gauge at the appropriate temperature. Gale Petrich (x3-5020, Rm. 13-3061) has allowed me to do a quick check on whether the ion gauge is working (and has been baked enough) by attaching it to a He leak detector in his lab.

The quartz bell jar will need to be cleaned periodically due to deposition on the bell jar. Typically, the bell jar needs to be cleaned every 3 – 4 runs when depositing ~ 5000 Å per run. The cleaning procedure consists of striking an O_2/Ar plasma with the following parameters: 40/20 pulse, 10 sccm O_2/20 sccm Ar, 10 mTorr, ~800 W. Follow the operating procedure detailed in Section A.8.3 for operating the plasma. NOTE: A wafer MUST be loaded during cleaning. See Section A.1 for more information about cleaning the bell jar.

If the ECR source needs to be removed from the chamber (to retrieve a broken wafer or other maintenance), it can be lifted off the chamber using a pulley (get from Sawin lab) attached to the chain hanging from the ceiling directly above the source. The microwave waveguides should be disconnected from the source before moving it. A series of 3 chains are used to attach the source to the pulley. Two of the chains are anchored on the cooling water Swagelock fittings, while the third circles the diameter of the source, securing the other two chains in place. The two chains on the fittings are connected by a C-clamp over the top of the source, which is in turn clipped to the pulley. **At least 3 people are needed to remove the ECR source from the chamber.** Obtain the pneumatic lift from Steve Wetzel in the sub-basement of Bldg. 66. Place this lift, with a thick cushion on the raised platform, on the equipment rack side of the chamber.

After removing the double-claw clamps from the source/chamber seal, lift the ECR slowly using the pulley. One person should be guiding the ECR on each side, while another operates the pulley. Lift the source until the magnetic confinement rings clear the top of the chamber, and then slowly lower the source onto the cushion on the raised platform. The source can then be carefully lowered and disconnected from the pulley. The source can be placed back on the chamber using the same technique. Care must be taken to align the slots in the magnetic confinement rings to the viewports on the chamber when replacing the source.

Extreme care must be taken when removing or replacing the source as any stress can result in fracture of the quartz bell jar.

Section A.8.6: Summary of Crucial Points

Although emphasized in the sections above, it is essential to follow the procedures listed below in order to avoid damage to the reactor and those operating it.

- **NEVER LET THE TURBOPUMP BACKING PRESSURE EXCEED 150 mTorr WHEN PUMP IS AT FULL SPEED**
- **NEVER STRIKE A PLASMA WITHOUT COOLING WATER AND N_2 PURGE FLOWING TO ECR SOURCE AND WAVEGUIDE DUMMY LOAD**
- **ALWAYS ALLOW AT LEAST 30 MINUTES FOR THE COOLING WATER TO COOL THE ECR BELL JAR AFTER PLASMA HAS BEEN EXTINGUISHED; LONGER IF PLASMA RUN TIMES WERE > 20 MIN.**

- **BE EXTREMELY CAREFUL NOT TO PUT UNEVEN STRESS ON THE ECR BELL JAR** (either when moving the ECR or attaching waveguides) **AS THAT CAN RESULT IN FRACTURE OF THE BELL JAR**
- **NEVER OPEN ISOLATION VALVE BETWEEN LOADLOCK AND CHAMBER WITHOUT EQUALIZING PRESSURES** (chamber P should be > loadlock P)
- **ALWAYS WEAR APPROPRIATE UV EYE PROTECTION WHEN PLASMA IS ON TO PREVENT UV DAMAGE TO EYES**
- **NEVER LOOK DIRECTLY INTO THE INTERFEROMETRY LASER BEAM**

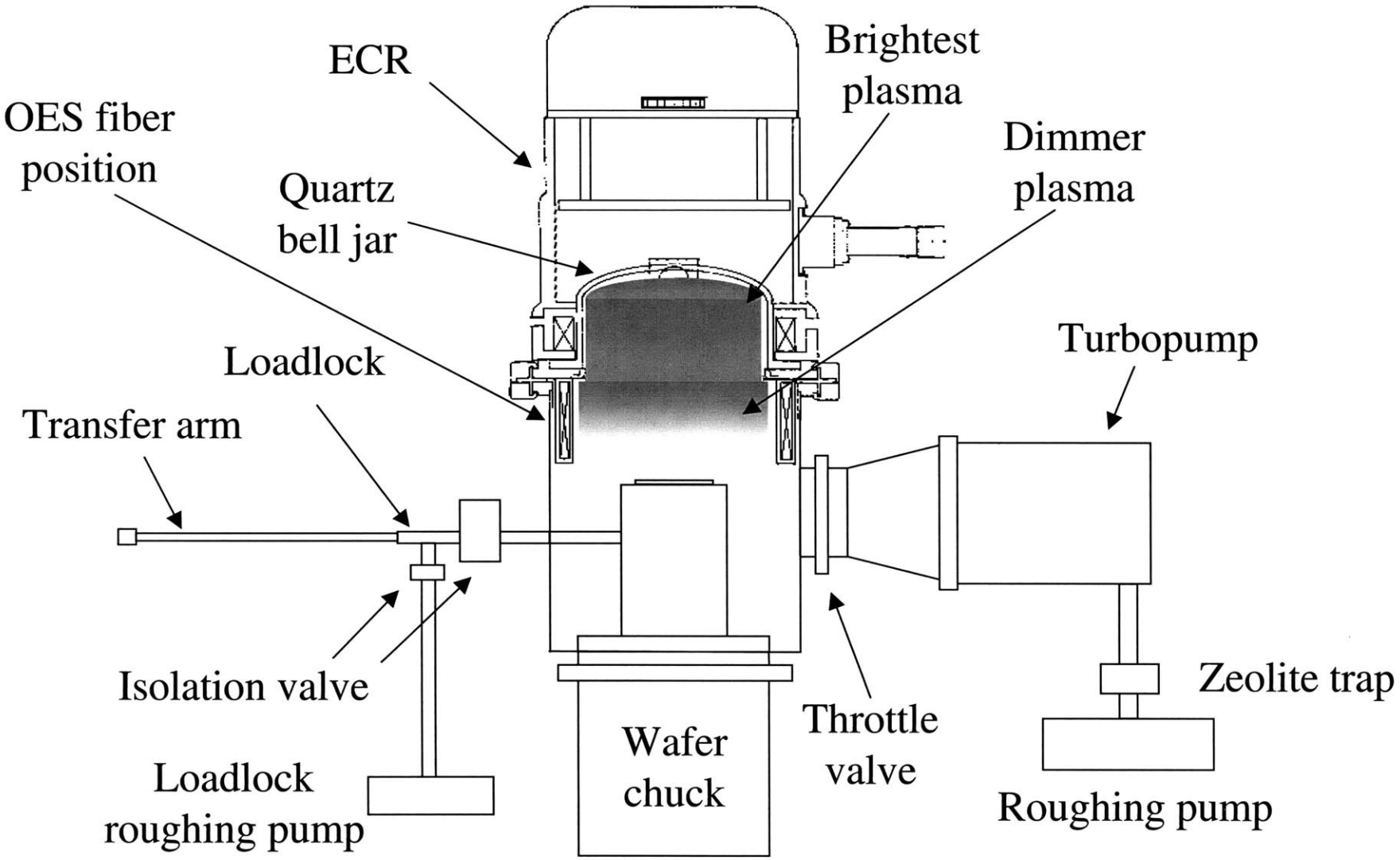

Figure A-1: Schematic of ECR Deposition System

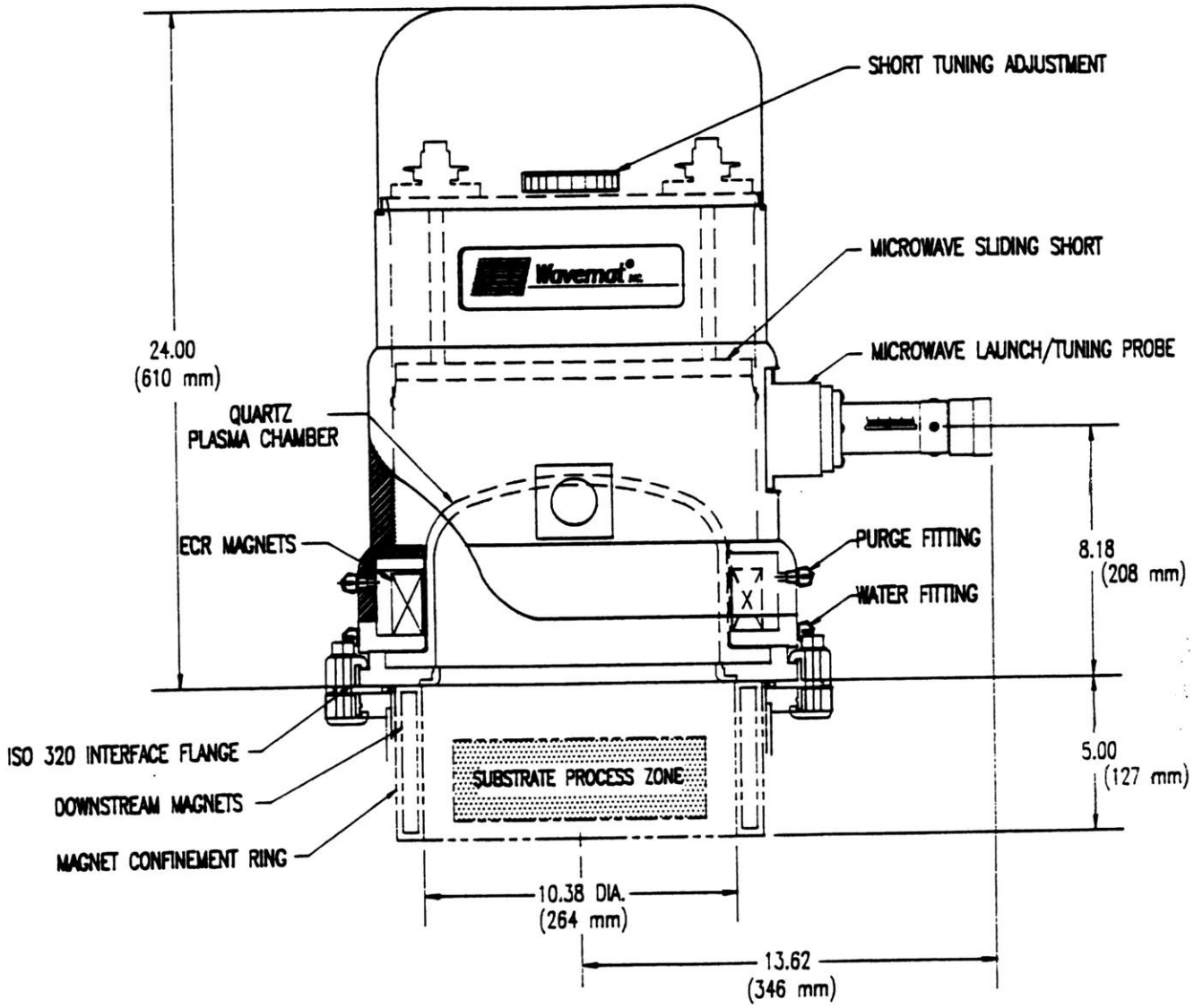

Figure A-2

(courtesy of Wavemat, Inc.)

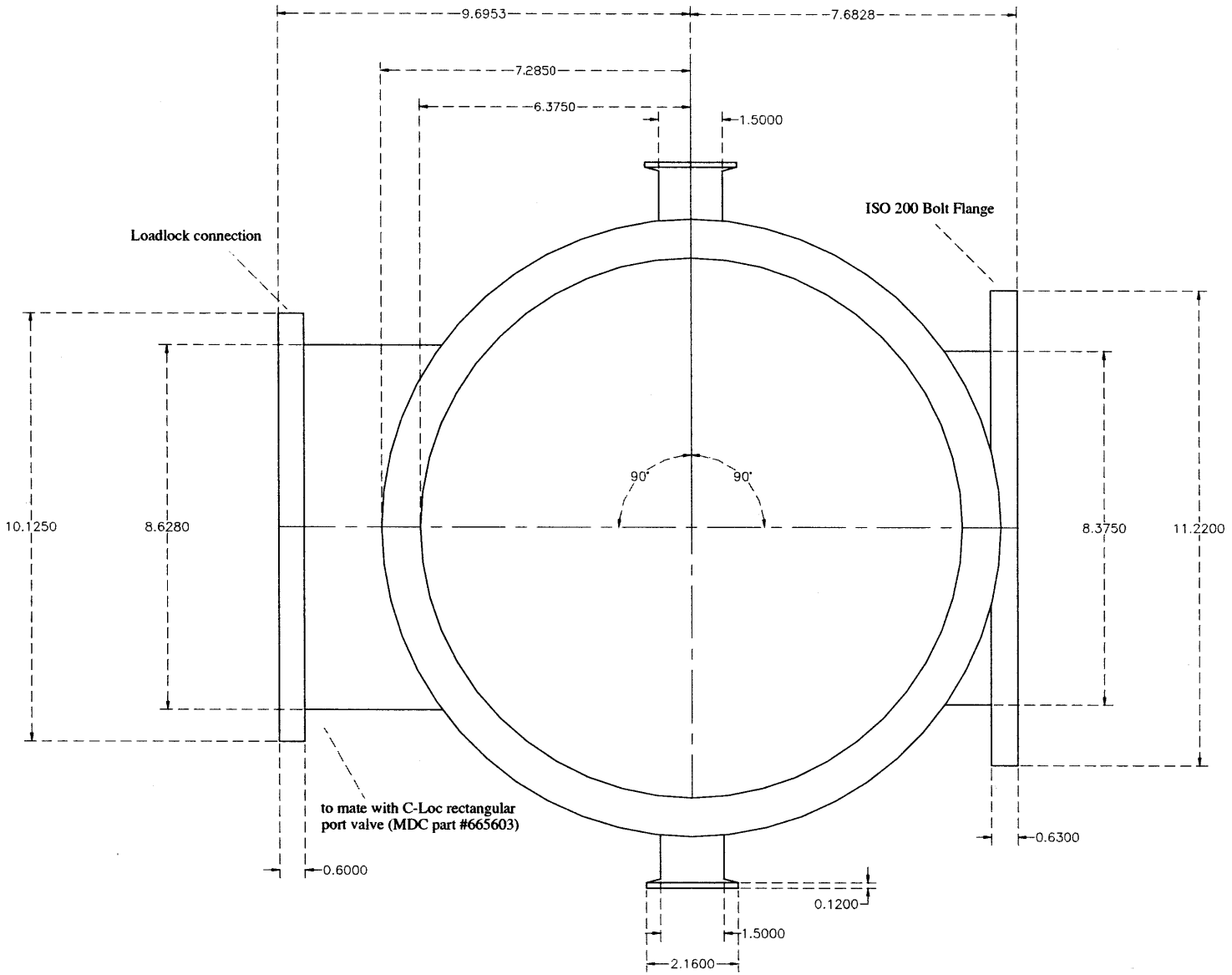

Figure A-3: Top down view (5 viewports not visible under top flange)

****Unless otherwise indicated, all walls are 3/16" thick****

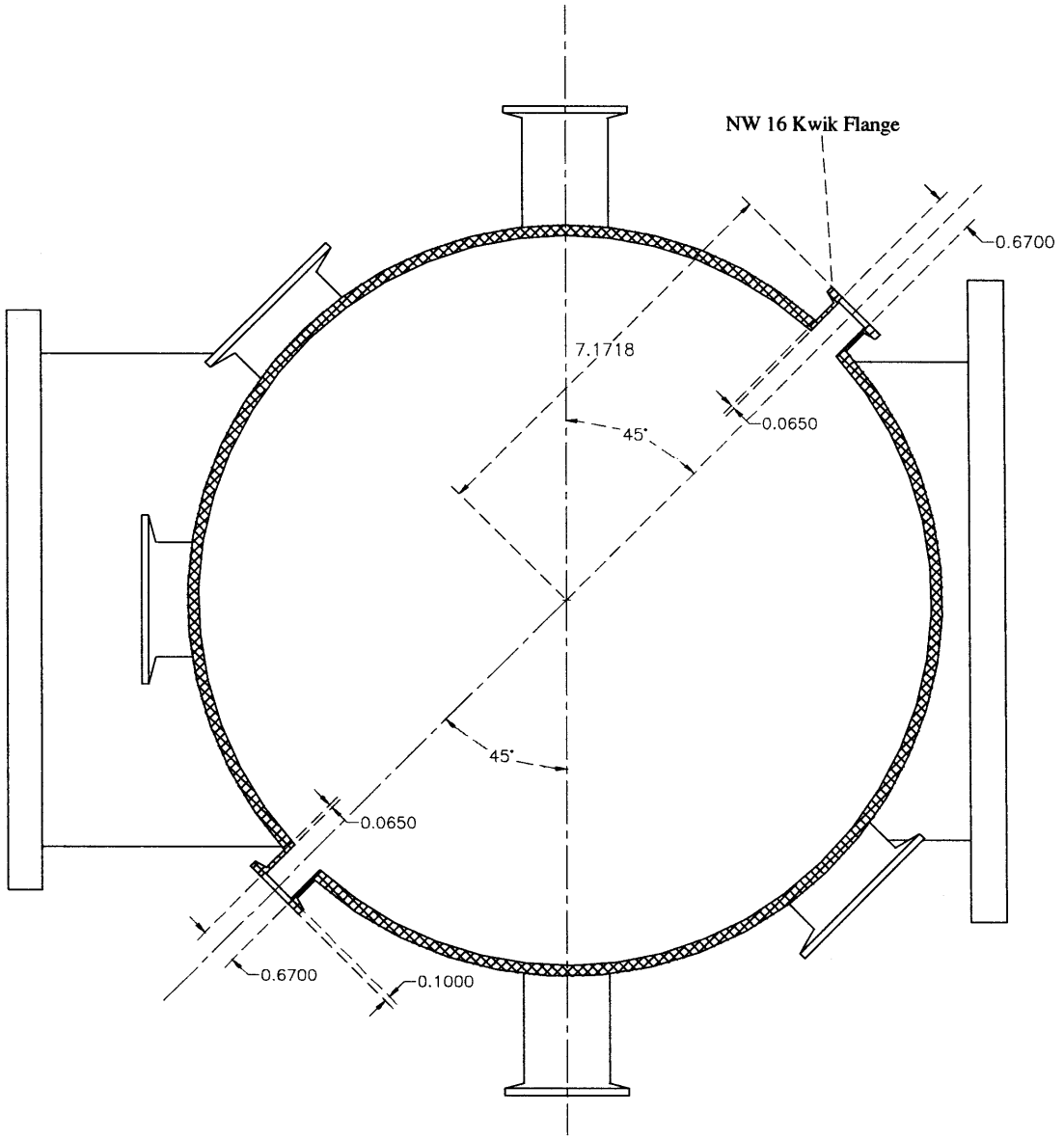

Figure A-4: Top down cross-section @ 1.375 in. down from bottom of top flange

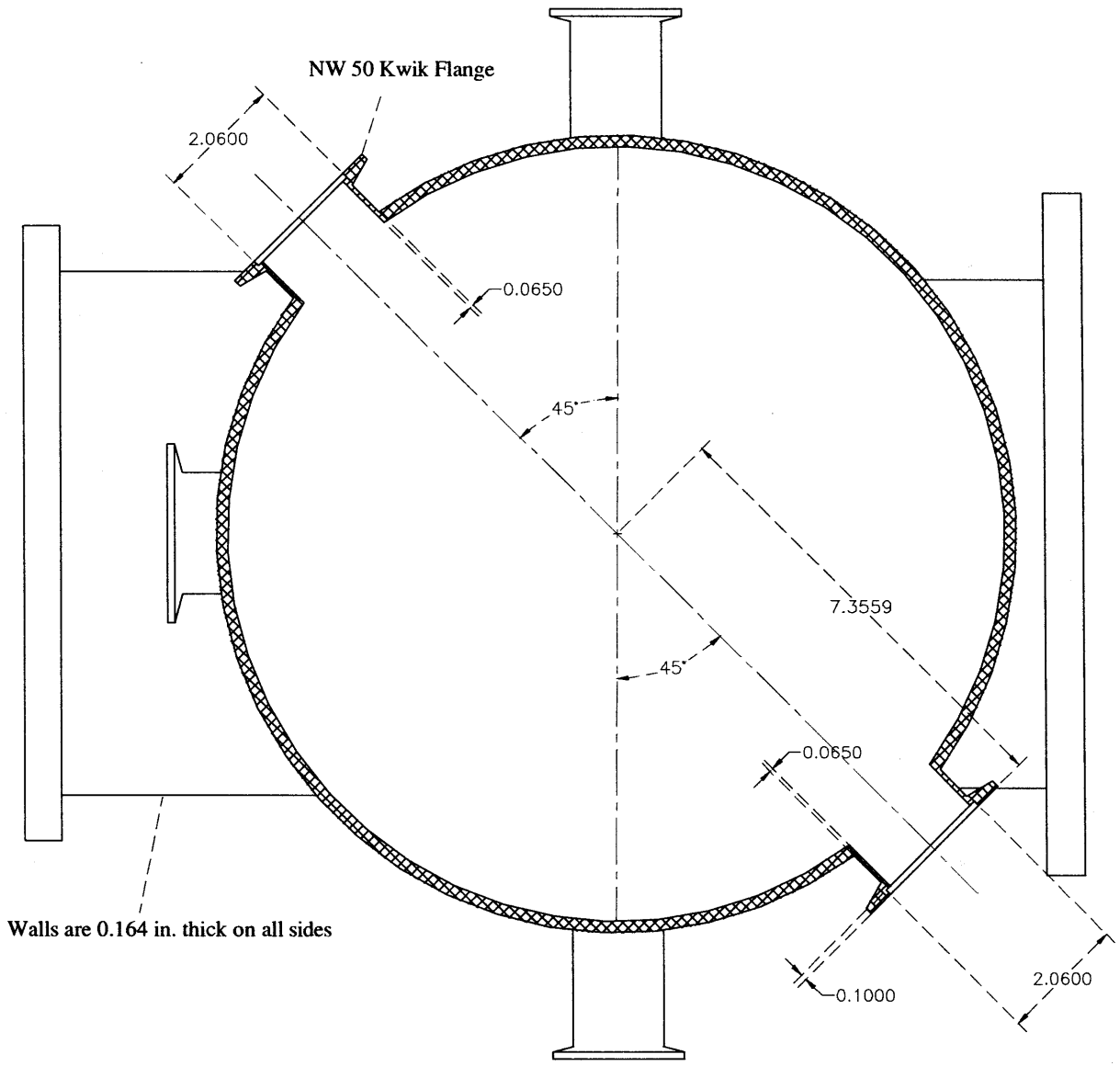

Figure A-5: Top down cross-section @ 2.5 in. down from bottom of top flange

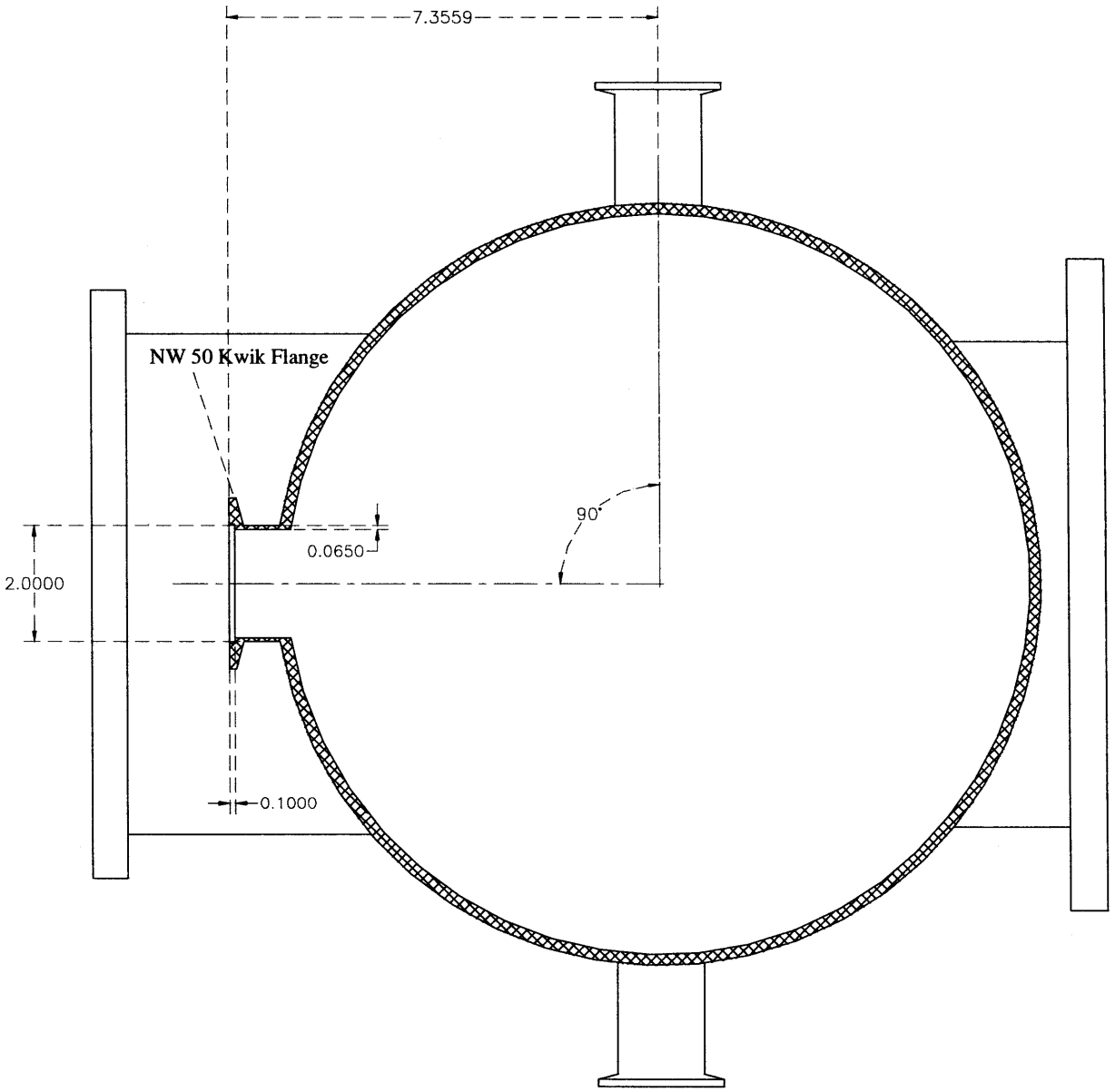

Figure A-6: Top down cross-section @ 6.5 in. down from bottom of top flange

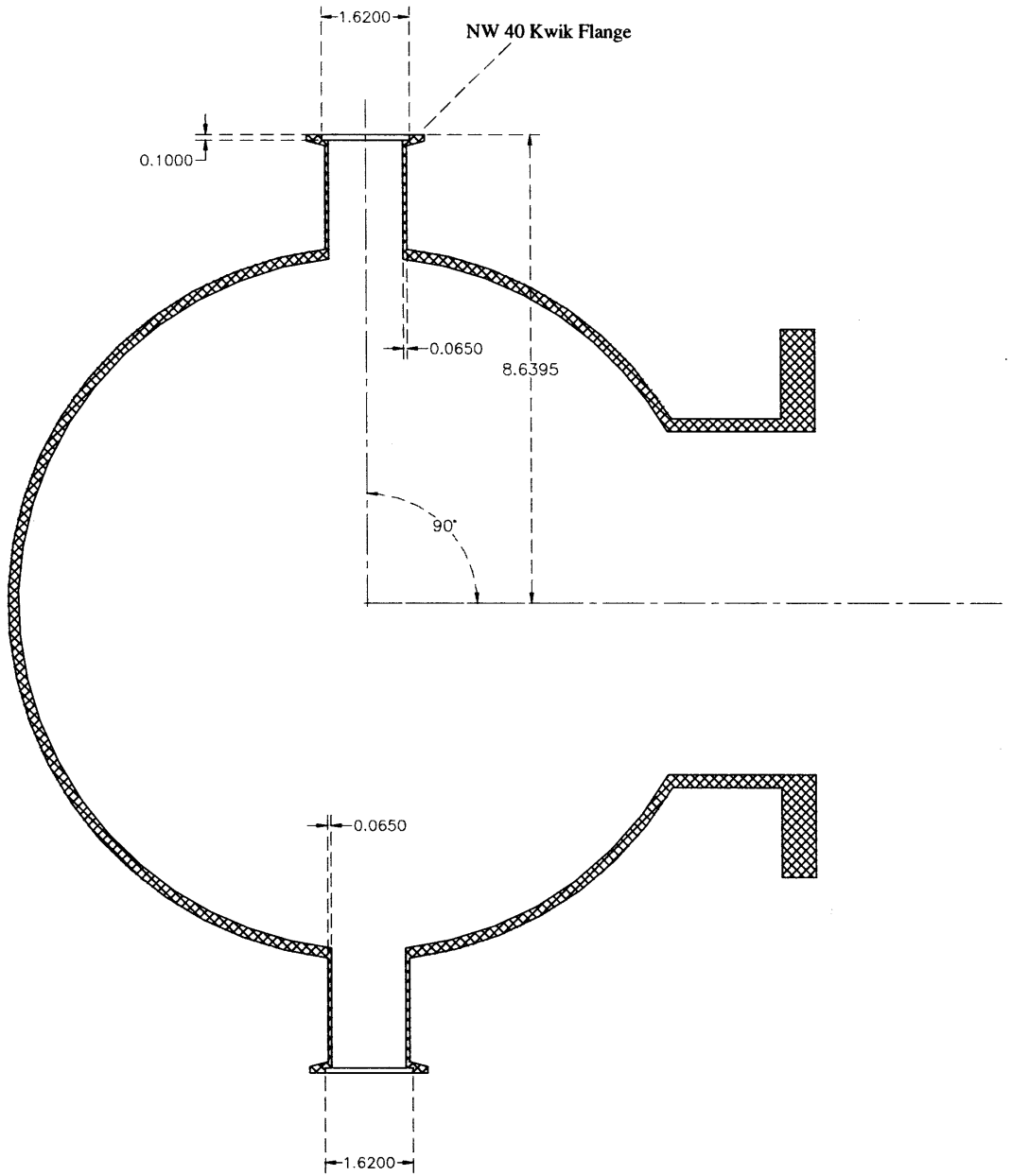

Figure A-7: Top down cross-section @ 13.4375 in. down from bottom of top flange

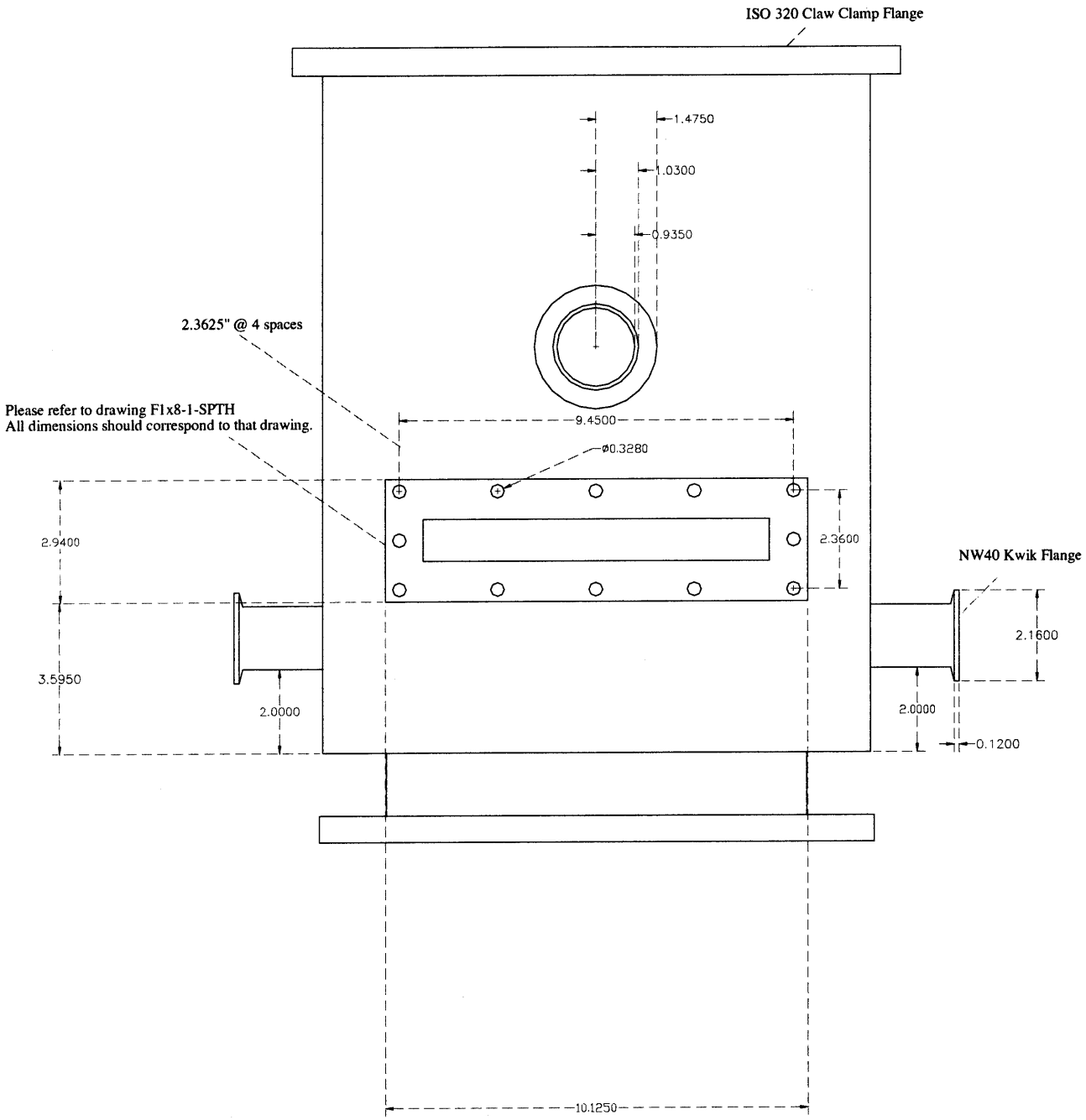

Figure A-8: Front view (facing loadlock connection, 4 top viewports not shown)

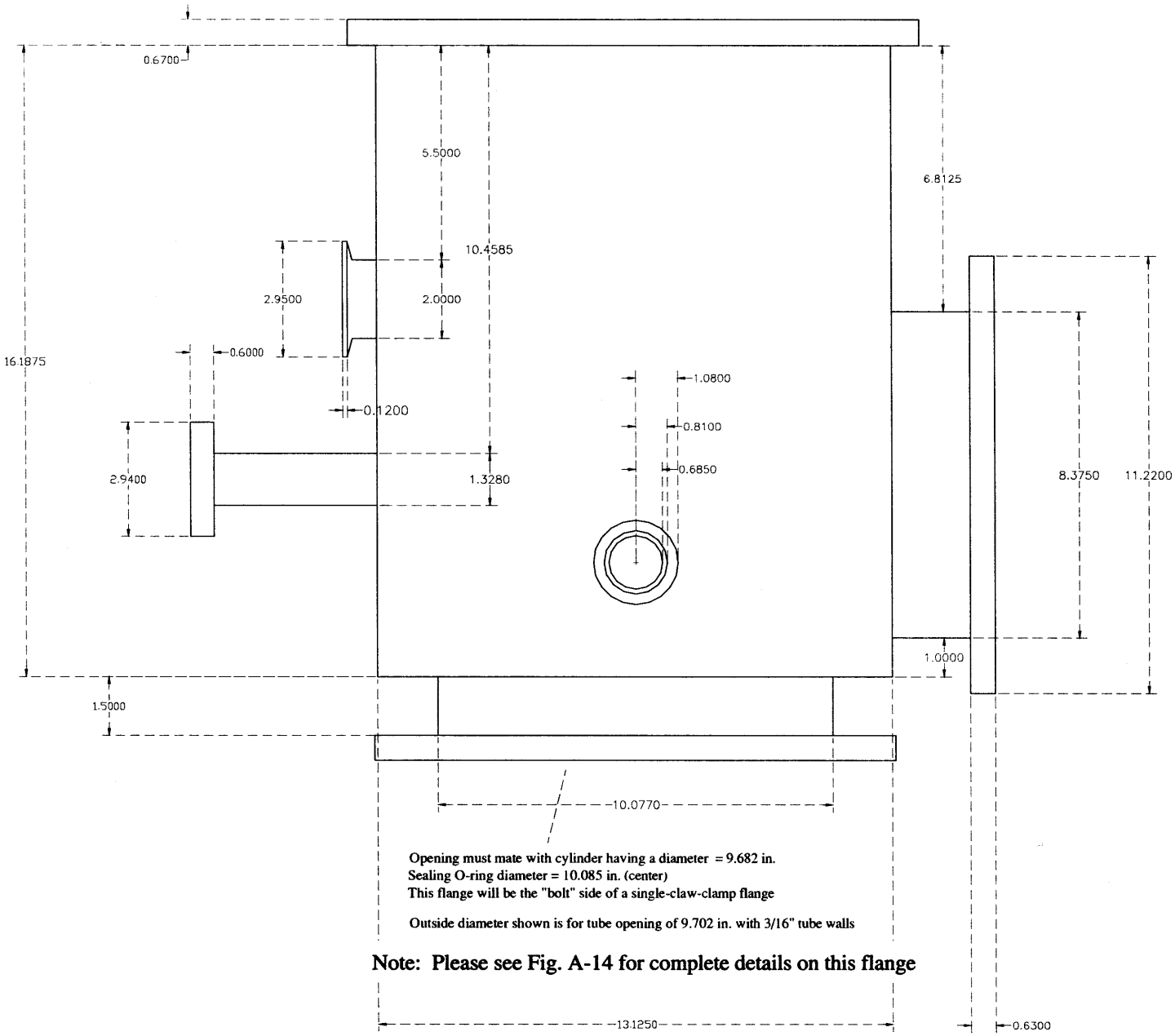

Figure A-9: Side view, rotated 90° cw from front (4 top viewports not shown)

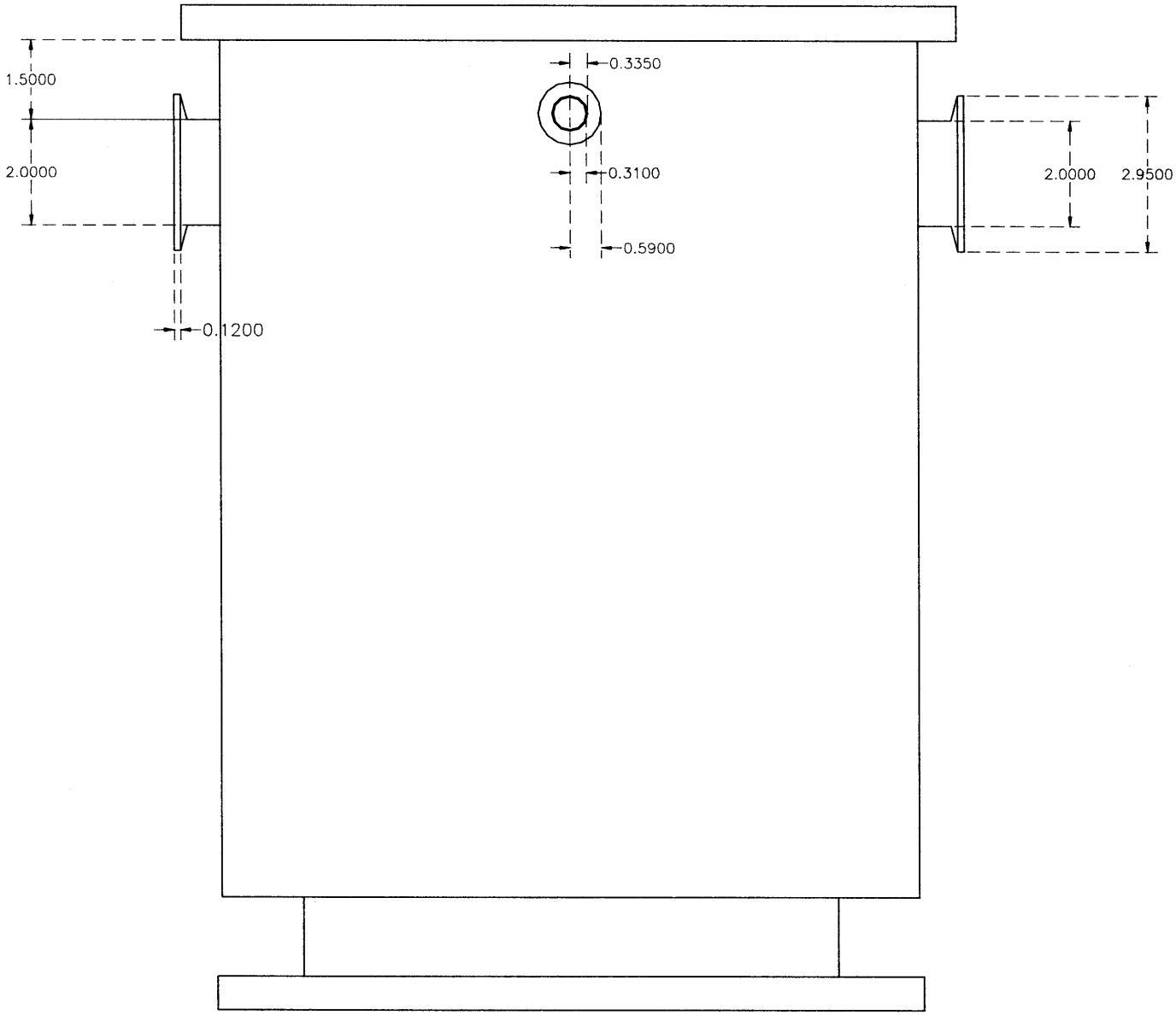

Figure A-10: Side view, rotated 45° cw from front, displaying 4 top viewports only

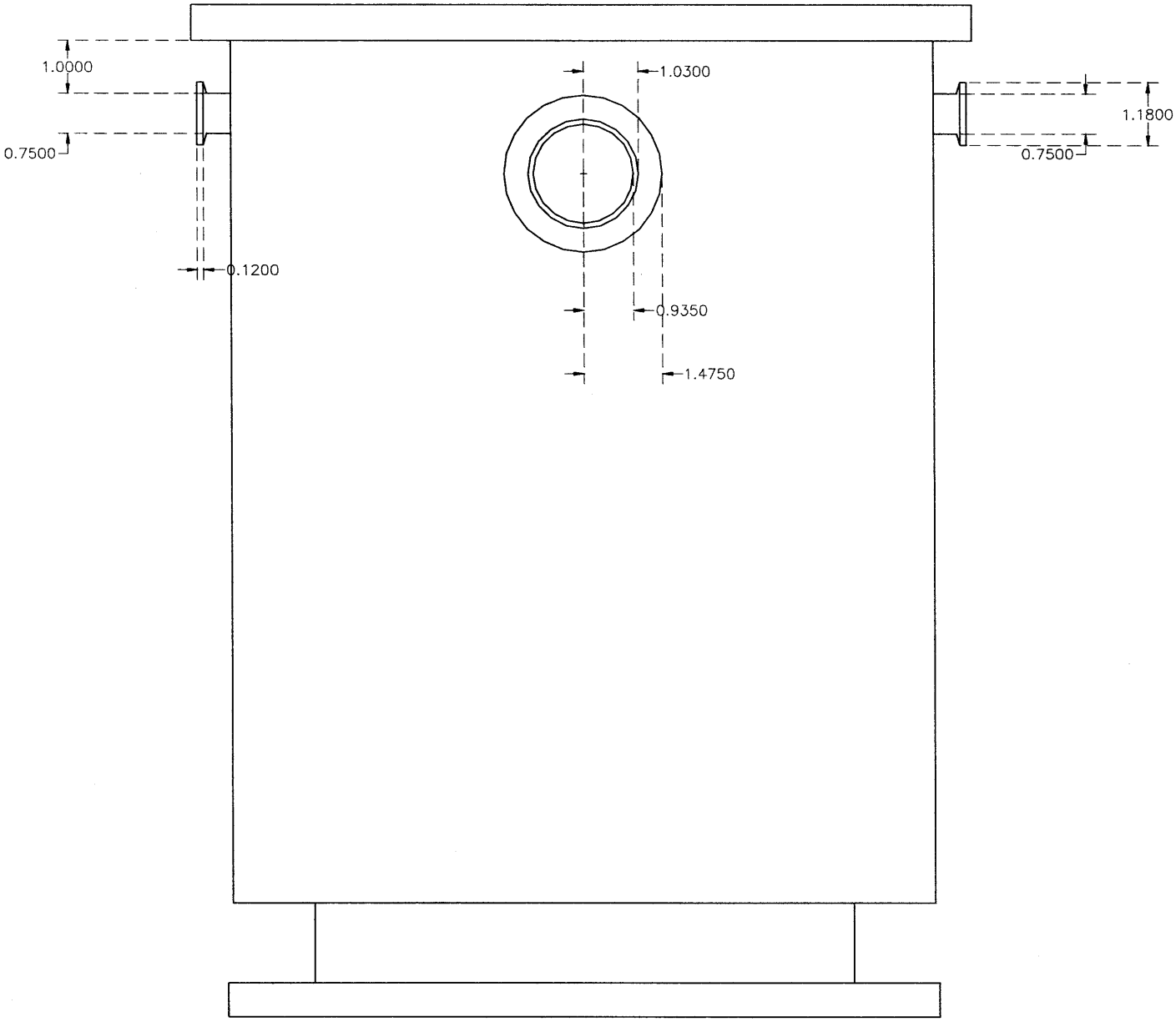

Figure A-11: Side view, rotated 45° ccw from front, displaying 4 top viewports only

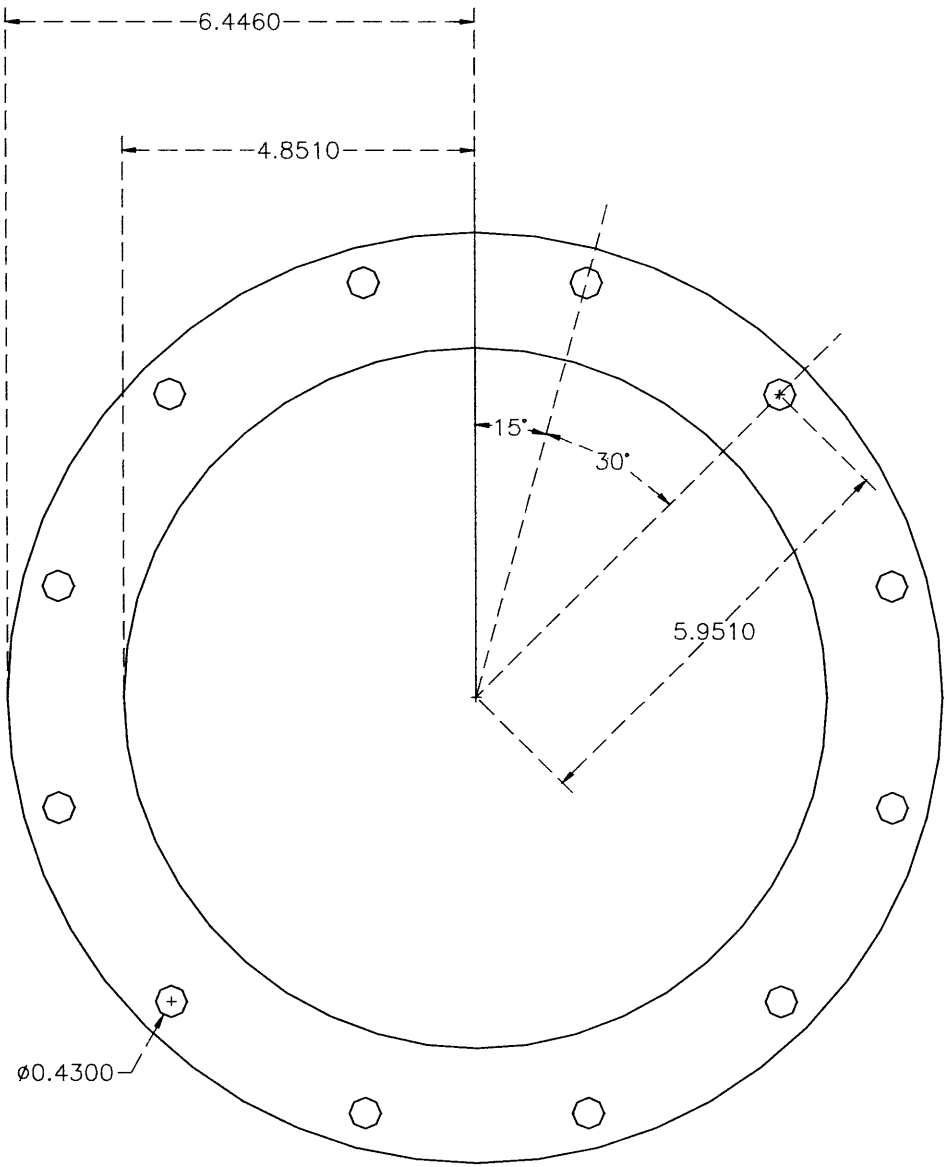

Figure A-12: Detail of bottom flange (mates to wafer chuck flange)

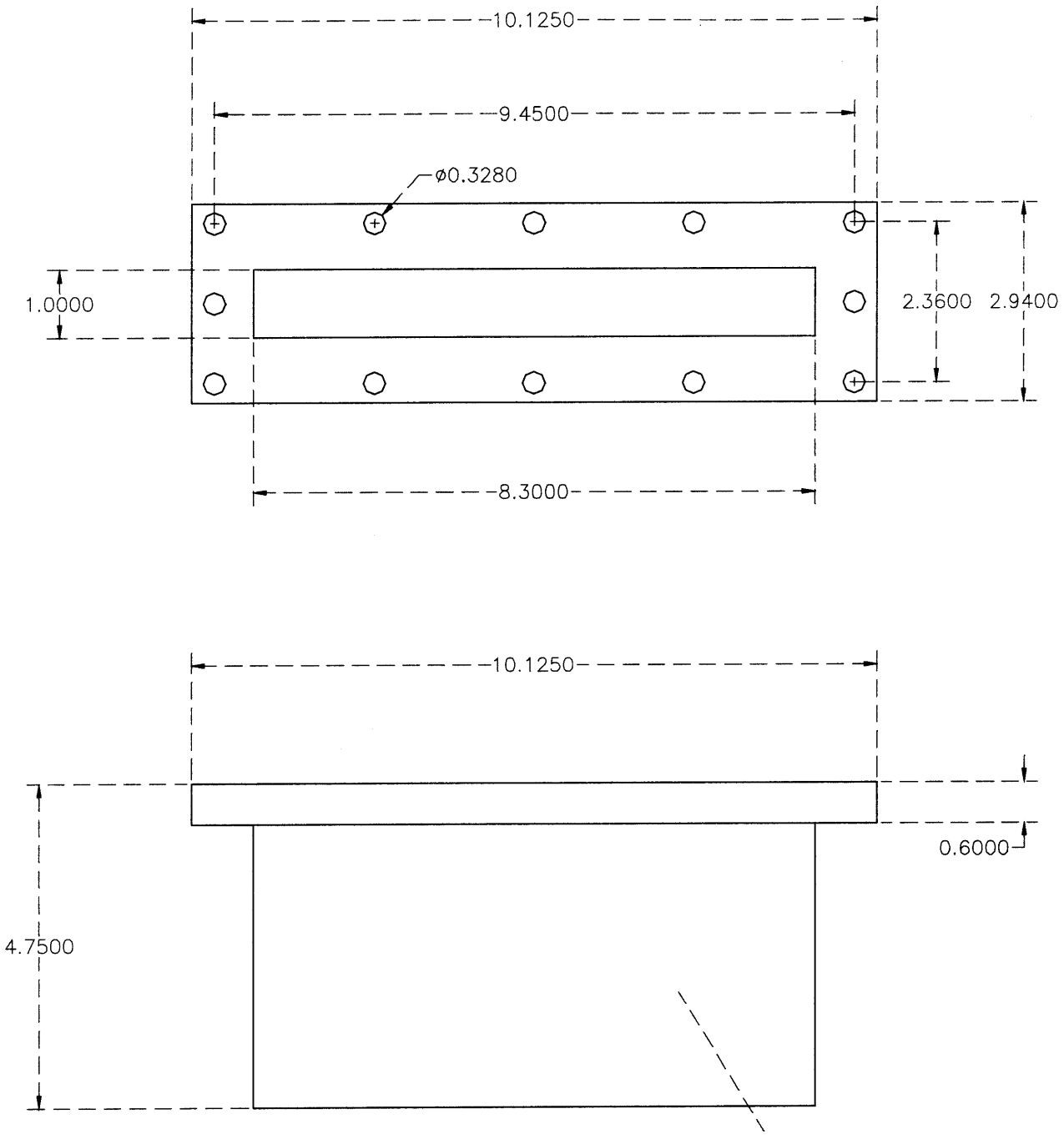

Rectangular tubing w/ 1.0" x 8.3"
inside dimen., 8 ga., 0.164" thk

Figure A-13: Rectangular port for loadlock (Recreation of MDC Drawing # F1x8-1-SPTH)

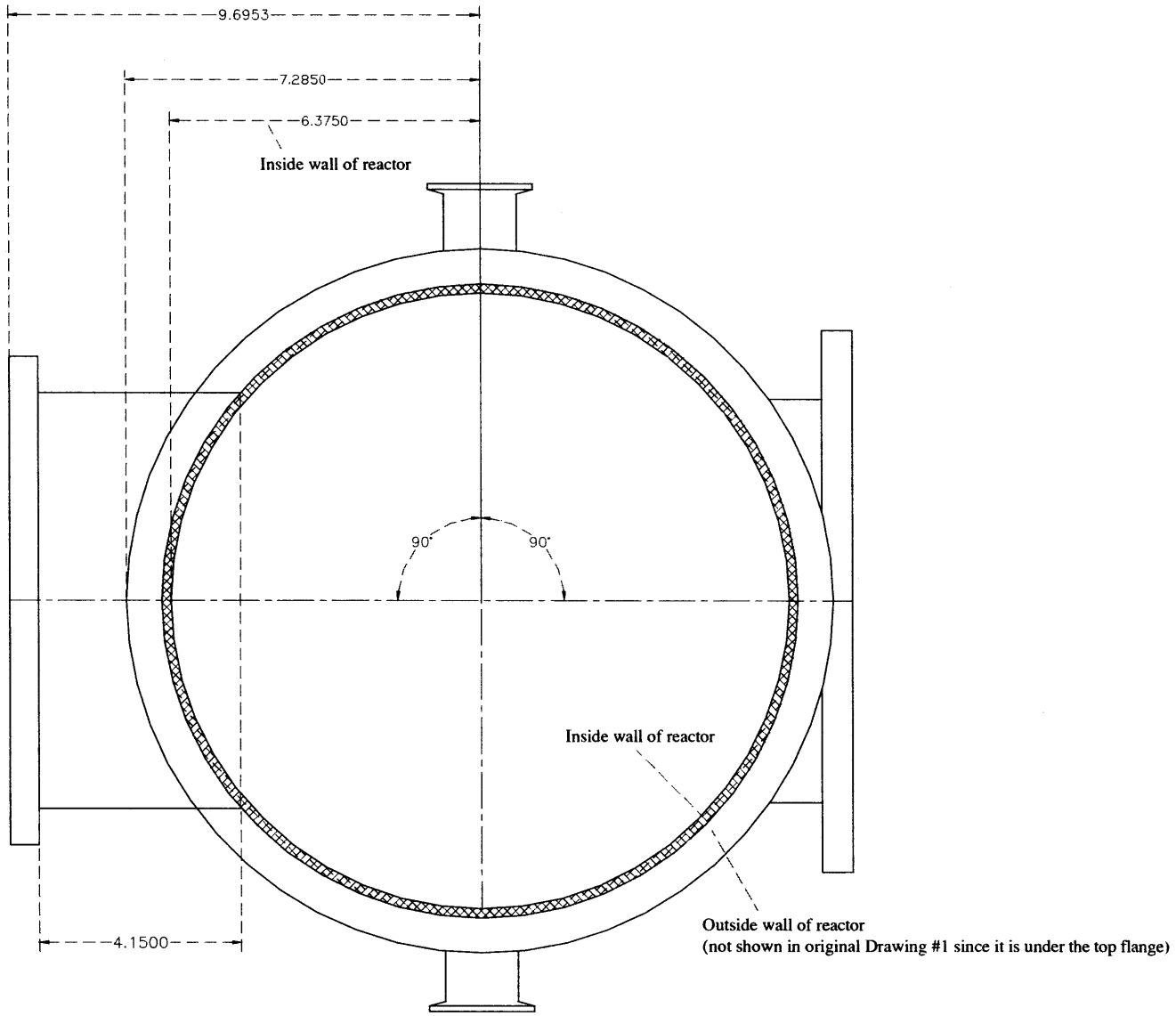

Figure A-14 (modified A-3): Top down view showing calculation of horizontal distance of left flange from center
Please note: All horizontal distances have been calculated in this manner, and dimensions should be taken from Figs. A-3 - A-7 for these features

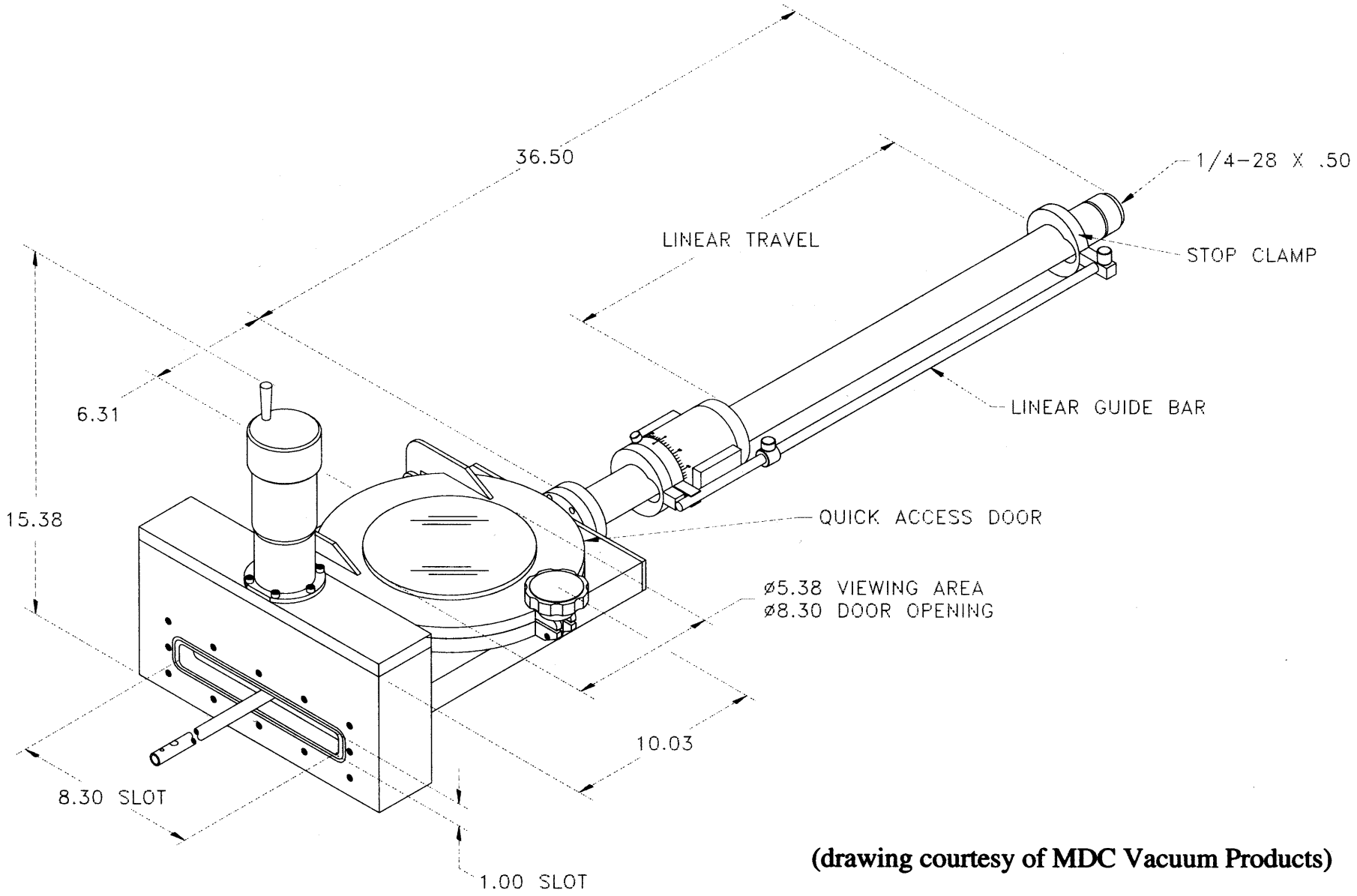

(drawing courtesy of MDC Vacuum Products)

Figure A-15: MDC Rectangular *Fast Entry* Load-Lock System

(drawing courtesy of MDC Vacuum Products)

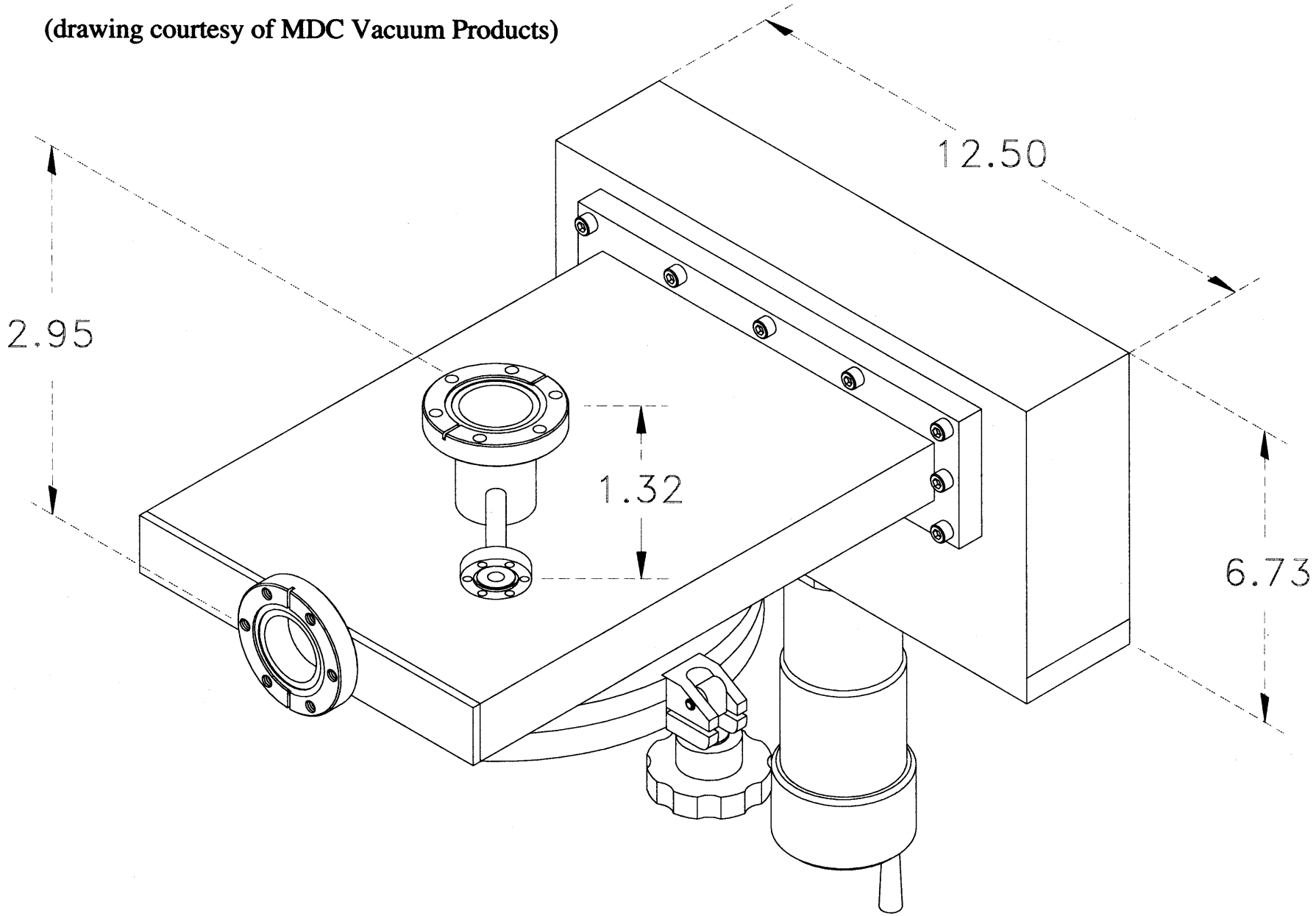

Figure A-16: Loadlock, view of bottom side of entry port

(drawings courtesy of MDC Vacuum Products)

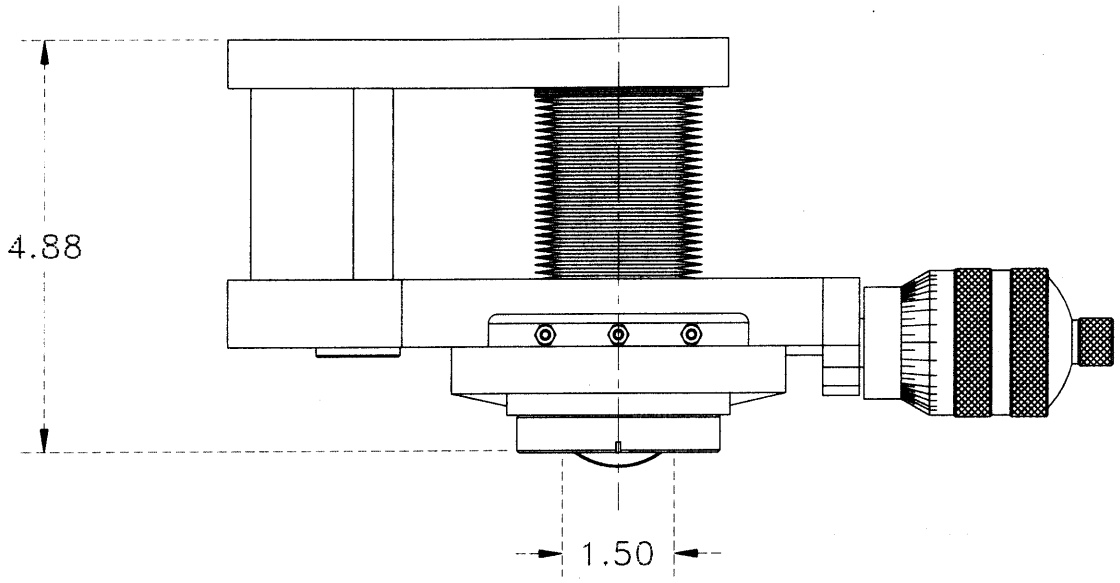

Side View

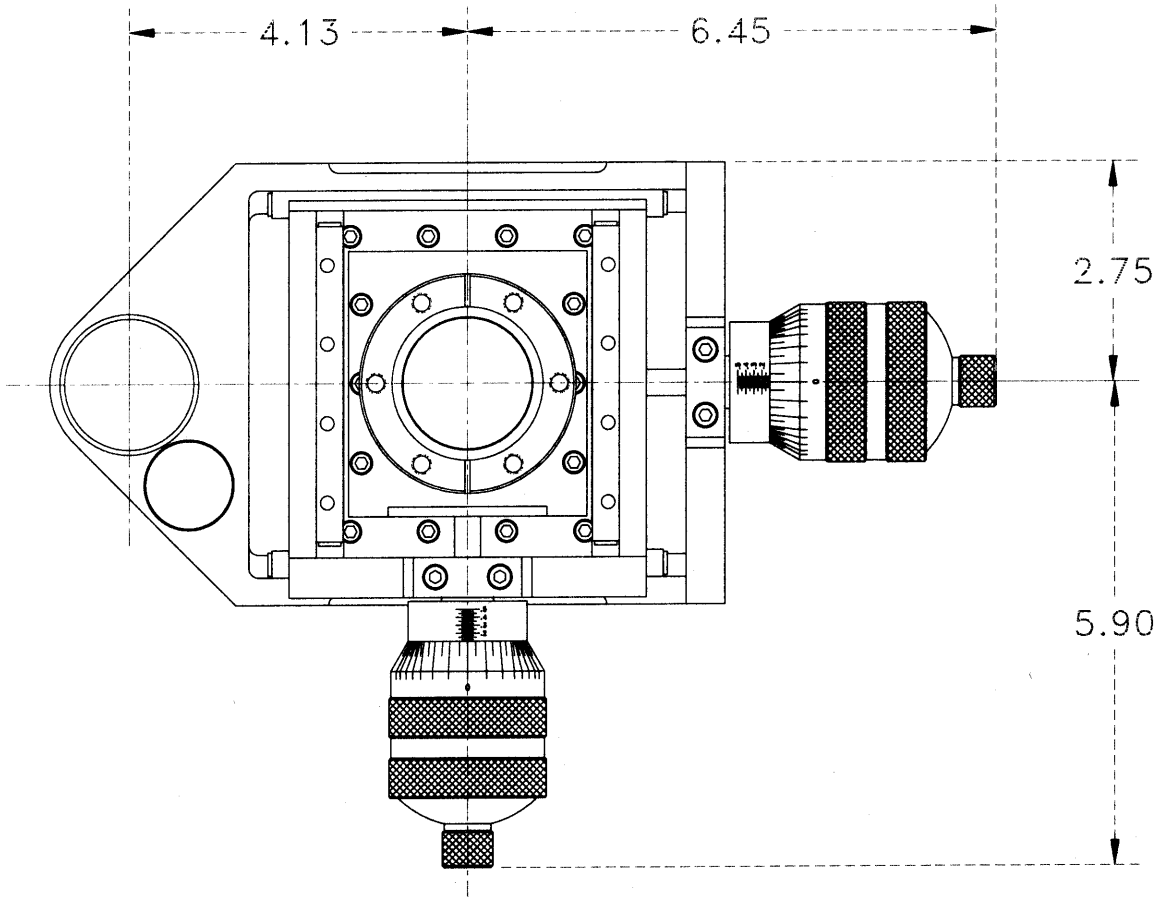

Bottom View

Figure A-17: Side & Bottom views of XY manipulator

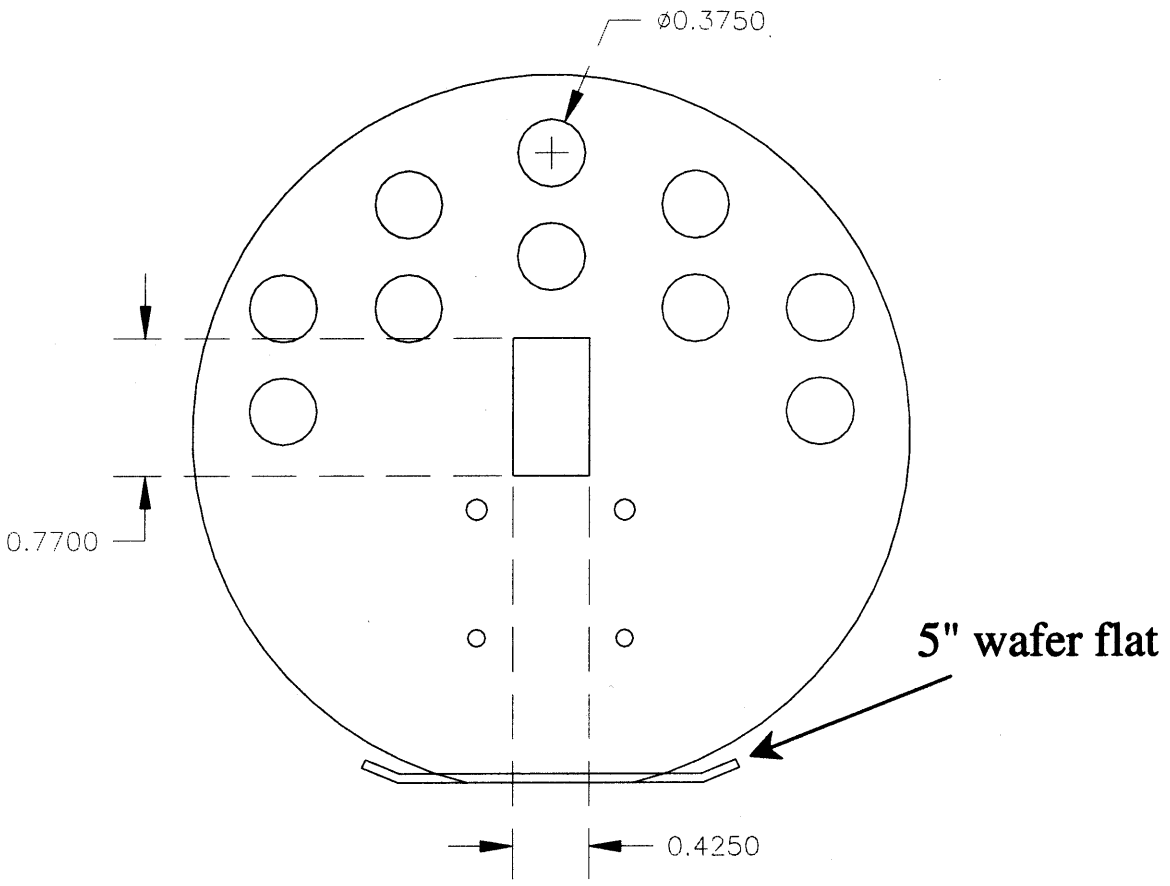

Top view

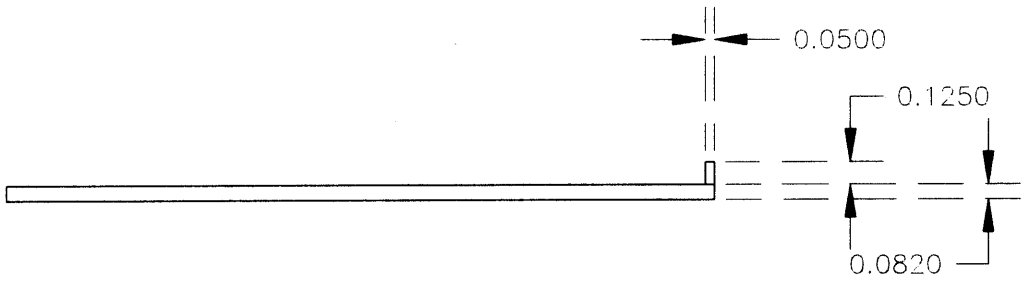

Side view

Figure A-18: 5" wafer sample holder

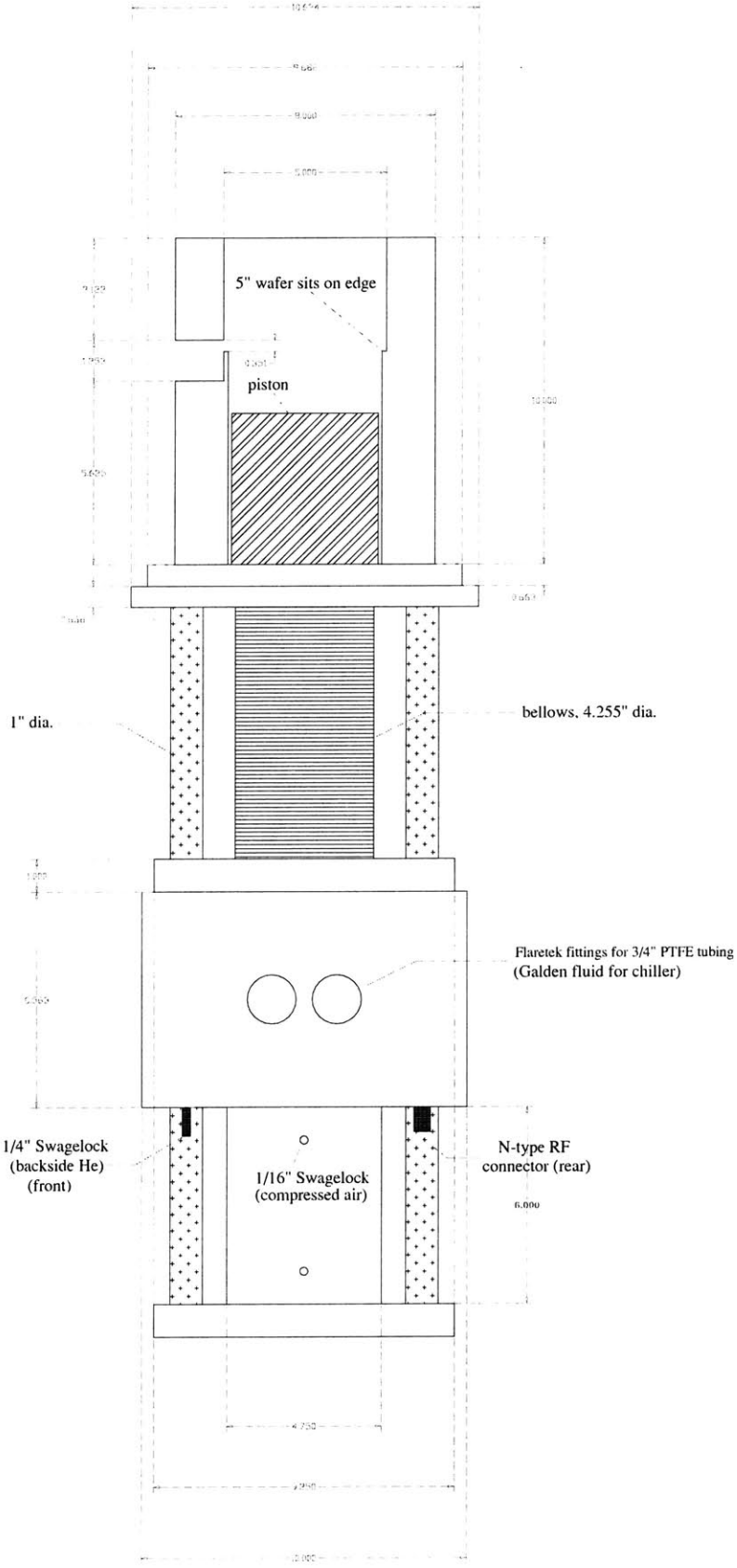

Figure A-19: Front view of 5" Lucas Labs wafer chuck

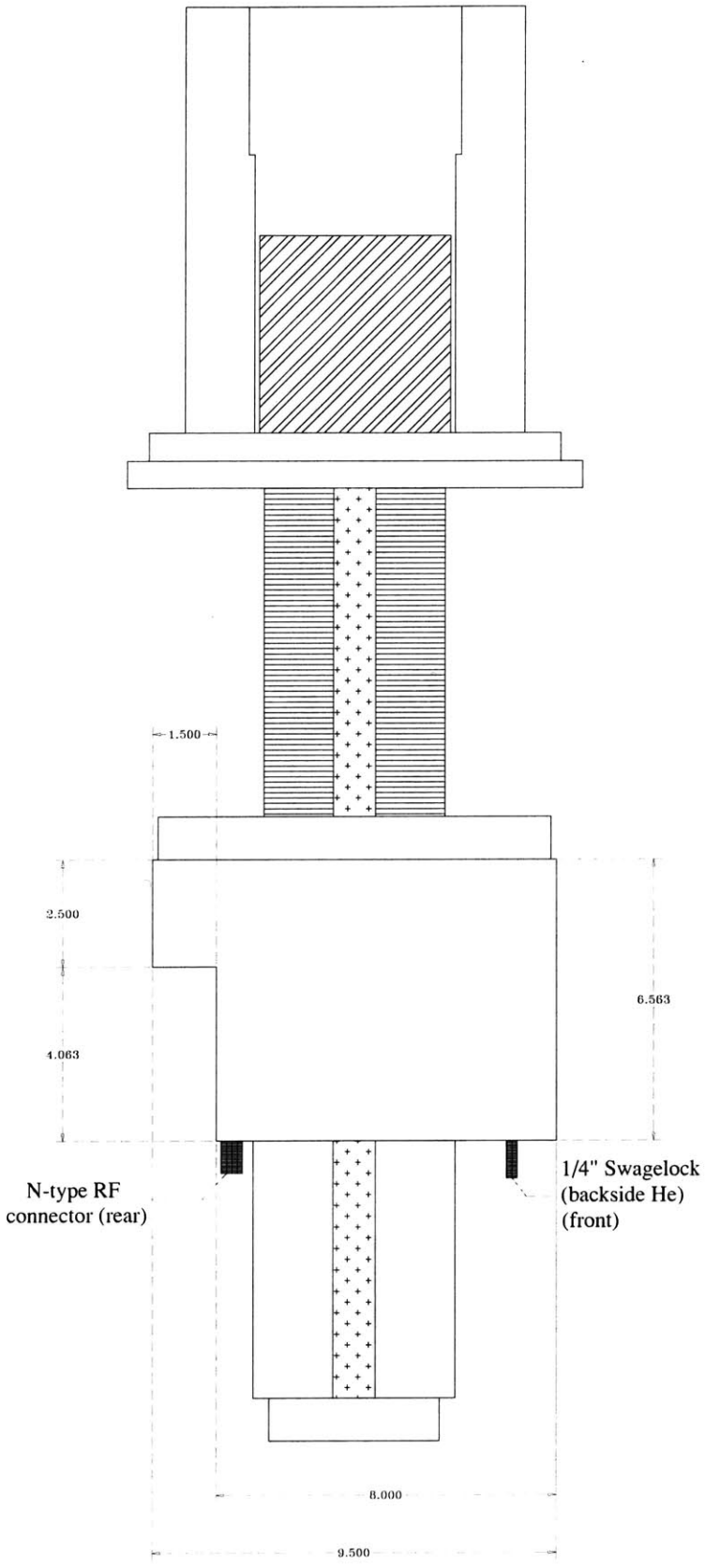

Figure A-20: Side view of 5" Lucas Labs wafer chuck

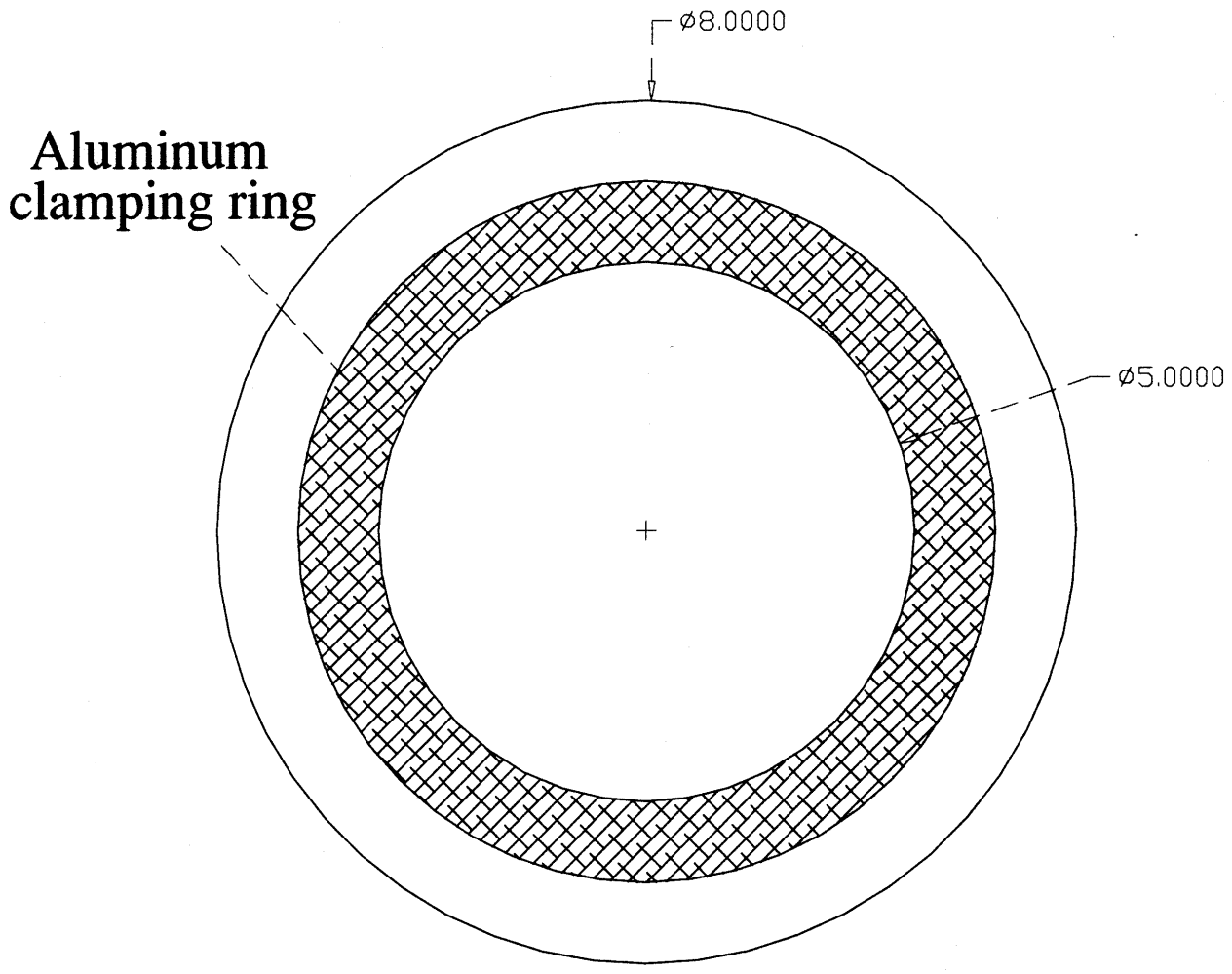

Figure A-21: Top view of 5" Lucas Labs wafer chuck
(quartz ring covers top to prevent Al sputtering)

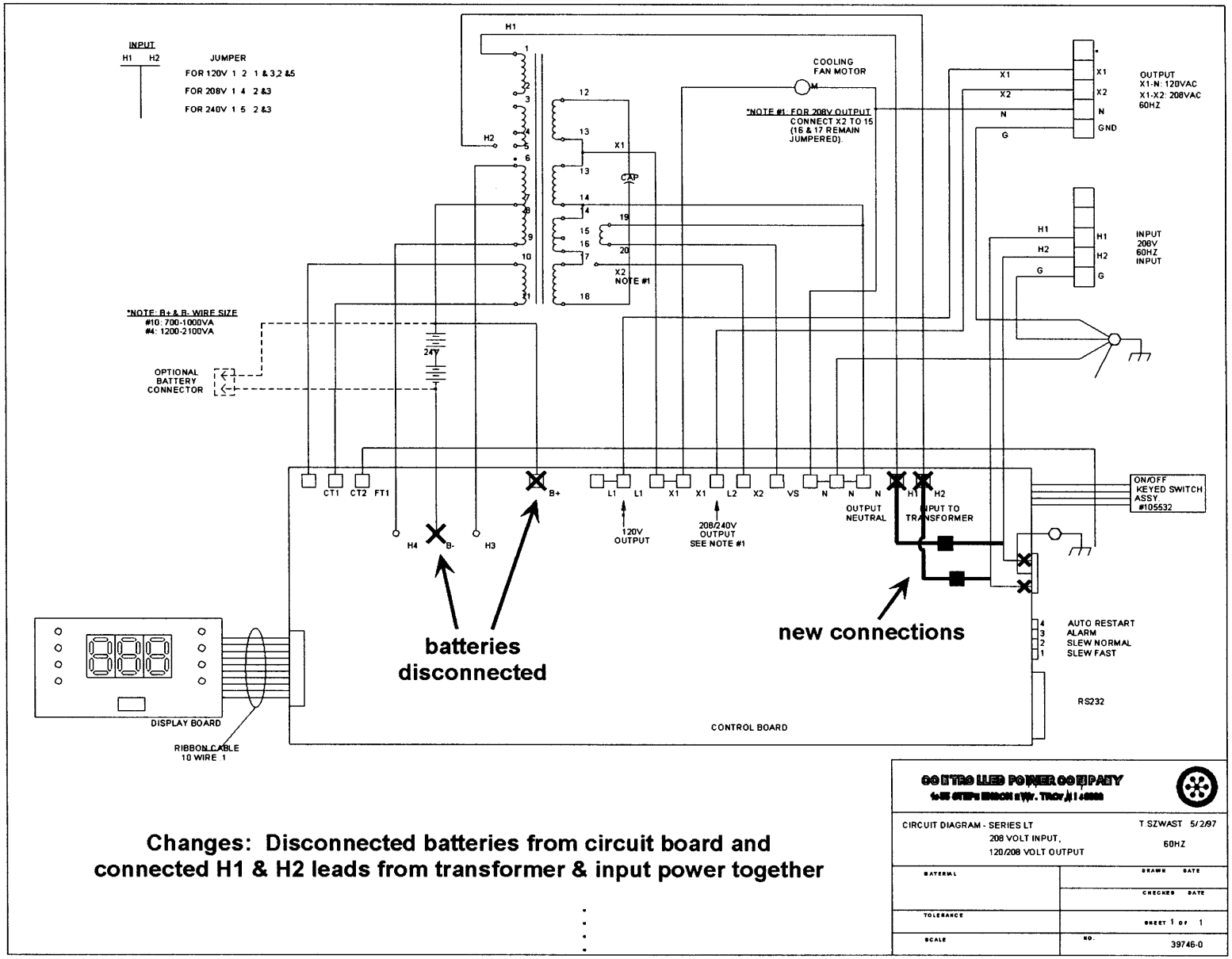

Changes: Disconnected batteries from circuit board and connected H1 & H2 leads from transformer & input power together

Figure A-22: Electrical schematics for UPS